Dissertation
submitted to the
Combined Faculty of Natural Sciences and Mathematics
of Heidelberg University, Germany
for the degree of
Doctor of Natural Sciences

Put forward by
Francesco Conte
born in Rome, Italy
Oral examination: 01.02.2024

Gamma-ray emission and absorption in the inner few parsecs of the Galactic Centre

Referees:
Prof. Dr. James A. Hinton
Prof. Dr. Saskia Hekker

Candidate:
Francesco Conte

ABSTRACT

Located 8 kpc away, the Galactic Centre is a rich environment for observing non-thermal phenomena such as a supermassive black hole, potential dark matter accumulations, supernova remnants, pulsar wind nebulae, clustered massive stars, and many more. It is a key target for both operational and next-generation TeV observatories like H.E.S.S., MAGIC, and CTA. Current telescopes, limited by a full-width half-maximum of 5 arcminutes, struggle to pinpoint the nature of gamma-ray sources amidst the Galactic Centre's complexity. UV/visible observations are also compromised due to dust absorption and infrared re-emission. However, this study leverages the infrared radiation's ability to absorb high-energy photons, using a model of the infrared field for spatial and spectral gamma-ray analyses. In this thesis I present the first 3D model for the infrared radiation field in the inner few parsecs. By studying the high-energy absorption, I find that if the central gamma-ray source and the large scale gamma-ray emission share the same cosmic-ray accelerator, then the central emitter is a ring of outer radius 2.5 pc that CTA will see as an extended source. In that case, the diffuse gamma-ray emission is expected to show a turn-off around 20 TeV rather than a power-law to 100 TeV.

ZUSAMMENFASSUNG

Das 8 kpc entfernte Galaktische Zentrum (GZ) ist ein reichhaltiges Umfeld zur Beobachtung nicht-thermischer Phänomene wie das supermassiven Schwarzen Lochs Sgr A*, potenzieller Dunkler Materie-Anhäufungen, Supernova-Überresten, Pulsarwindnebeln, gebündelten massiven Sternen und vielem mehr. Es ist ein Schlüsselziel sowohl für bestehende als auch für die nächste Generation von TeV-Observatorien wie H.E.S.S., MAGIC und CTA. Aktuelle Teleskope, begrenzt durch eine Winkelauflösung von 5 Bogenminuten, kämpfen darum, die Natur der Gammastrahlenquellen inmitten der Komplexität des GZ zu bestimmen. UV/sichtbare Beobachtungen werden ebenfalls durch Staubabsorption und Infrarot-Reemission beeinträchtigt. Diese Studie nutzt jedoch die Fähigkeit der Infrarotstrahlung, hochenergetische Photonen zu absorbieren, und verwendet ein Modell des Infrarotfeldes für räumliche und spektrale Gammastrahlenanalysen. In dieser Arbeit präsentiere ich das erste 3D-Modell für das Infrarotstrahlungsfeld in den inneren paar Parsecs. Durch die Untersuchung der Hochenergieabsorption stelle ich fest, dass, wenn die zentrale Gammastrahlenquelle und die großräumige Gammastrahlenemission denselben kosmischen Strahlenbeschleuniger teilen, der zentrale Emitter ein Ring mit einem äußeren Radius von 2.5 pc ist, den CTA als ausgedehnte Quelle sehen wird. In diesem Fall wird erwartet, dass die diffuse Gammastrahlenemission um 20 TeV herum abbricht, anstatt einem Potenzgesetz bis 100 TeV zu folgen.

"Anche se il disegno generale è stato minuziosamente progettato, ciò che conta non è il suo chiudersi in una figura armoniosa, ma la forza centrifuga che da esso sprigiona, la pluralità dei linguaggi come garanzia d'una verità non parziale."
– Italo Calvino, Le lezioni americane

"Even if the overall design has been minutely planned, what matters is not the enclosure of the work within a harmonious figure, but the centrifugal force produced by it – a plurality of language as a guarantee of a truth that is not merely partial."
– Italo Calvino, Six memos for the next millennium

LIST OF ABBREVIATIONS

AGB	Asymptotic Giant Branch
AGN	Active Galactic Nucleus
B/P	Boxy/Peanut
CC	Central Cavity
CMB	Cosmic Microwave Background
CMZ	Central Molecular Zone
CND	Circum-Nuclear Disk
CNG	Circum-Nuclear Gas
CNR	Circum-Nuclear Ring
CoG	Curve of Growth
CoM	Center of Momentum
CR	Cosmic Ray
CWB	Colliding Wind Binary
DM	Dark Matter
DoF	Degree of Freedom
DSA	Diffusive Shock Acceleration
EBL	Extragalactic Background Light
ECSN	Electron-Capture Supernova
F11	Fritz et al. 2011
FIR	Far-Infrared
FoV	Field of View
GC	Galactic Centre
GCE	Galactic Centre Excess
GMC	Giant Molecular Cloud
GP	Galactic Plane
GRB	Gamma-Ray Burst
GRBR	Gamma-Ray Background Region
GZK	Greisen-Zatsepin-Kuz’min
HAC	Hydrogenated Amorphous Carbon
HB	Horizontal Branch
IACT	Imaging Atmospheric Cherenkov Telescope
IC	Inverse Compton
IMF	Initial Mass Function
IR	Infrared
IRBR	Infrared Background Region

IRF	Instrument Response Function
IRS	Infrared Source
ISM	Interstellar Medium
KN	Klein-Nishina
KSP	Key Science Project
LBV	Luminous Blue Variable
LISM	Local Interstellar Medium
LoS	Line of Sight
LTE	Local Thermodynamic Equilibrium
MHD	Magneto-Hydrodynamic
MIR	Mid-Infrared
MW	Milky Way
NA	Northern Arm
NIR	Near-Infrared
NLTE	Non-Local Thermodynamic Equilibrium
NRF	Non-thermal Radio Filament
NSC	Nuclear Star Cluster
NSD	Nuclear Stellar Disk
P&T13	Popescu and Tuffs 2013
P&T17	Popescu et al. 2017
PAH	Polycyclic Aromatic Hydrocarbon
PF	Planck Fit
PISN	Pair-Instability Supernova
pp	proton-proton
PSF	Point Spread Function
PWN	Pulsar Wind Nebula
QSO	Quasi-Stellar Object
RJ	Rayleigh-Jeans
RMS	Root Mean Square
SED	Spectral Energy Distribution
SMBH	Supermassive Black Hole
SN	Supernova
SNR	Supernova Remnant
TS	Termination Shock
TSC	Tidally Stretched Cloud
UV	Ultraviolet
VHE	Very-High-Energy
W&D	Weingartner and Draine
WA	Western Arm
WR	Wolf-Rayet
YMSC	Young Massive Star Cluster
YSO	Young Stellar Object

LIST OF FIGURES

LIST OF TABLES

TABLE OF CONTENTS

INTRODUCTION

Despite a certain degree of chance, the physics and the astrophysics of cosmic rays (CRs) are commonly assumed to begin with Victor Hess experiments in the distant 1911 (see details on page 7). Keeping in mind that the experiment's objective was to show that the "unknown ionising radiation" had a terrestrial origin, he would have probably never expected that the CR astrophysics would remain a vital field more than a century afterwards – perhaps the most vital branch of astrophysics among the ones born before the mid-20th century. In hindsight, this fact is not surprising: CRs are not directly detectable from the ground, and the same goes for gamma rays – so the birth of high-energy astrophysics had to wait for the technology to reach a sufficient level to allow the installation of detectors in orbit around our planet. As it is well known, such technology was exclusively military and focused mostly on spying on international nuclear activities.

This is just one of the reasons why high-energy astronomy (studying the highest energies of the electromagnetic spectrum) has always been considered closer to particle physics than to astronomy in its common meaning (the study of extraterrestrial phenomena).

Among the many reasons, one in particular illustrates the distance between the two fields: the absence of adequate laboratories. While, in all other electromagnetic bands, astrophysics can rely on the results of targeted experiments to study the physics connected to celestial phenomena[1], it is exactly the opposite for gamma radiation: there are no laboratories on Earth capable of reproducing gamma-ray experiments at PeV or EeV energies – the current record holder, the LHC, barely surpasses 10 TeV. Consequently, it is rather high-energy astrophysics providing valuable information to particle physics, with an obvious downside – we have no control over our "laboratories".

The effects of such unique characteristics are manifold; here I will mention three:

---

[1] Speaking of casual discoveries, the story goes that Herschel diffracted the light with a prism in order to measure the temperatures of different parts of the visible light spectrum, and left a spare thermometer where he thought there was no light – next to the red end of the visible band. Much to his surprise, the thermometer temperature went a bit up: he discovered the IR radiation.

- Despite significant technological advancements in gamma-ray detection in the last 30 years, the angular resolution and energy sensitivity of gamma-ray detectors are not comparable to those of other electromagnetic bands – the point spread function (PSF) extension of instruments like MAGIC or H.E.S.S. at TeV energies is on the order of $5'$, which means that even physically small regions emitting high-energy photons have a large angular size, making their geometrical investigation very hard (excluding objects that are very close or very extended in size like Galactic phenomena and nearby galaxies). Furthermore, the size of the gamma-ray source could be several orders of magnitude larger than the region of CR acceleration. All of this means that studying the detailed morphology of a gamma-ray source is often extremely complex, while studying the morphology of the CR accelerator is virtually unachievable at the moment.

- Many very high-energy transient events that we are able to detect (e.g. GRBs) are often of extragalactic origin or not clearly Galactic. As a result, in addition to the obvious experimental bias (we can only study the most luminous events), it is often challenging to associate a gamma-ray source to a clear astrophysical counterpart studied at significantly different resolutions in other electromagnetic bands, whose physics we have a much better understanding of and on much smaller spatial scales.

- Most of the time, we cannot choose the physical phenomena to study, and especially their temporal evolution because high-energy events are often impossible to predict (with some exceptions often related to transients or recurrent events, such as novae [10, 97], binaries [206], GRBs [96]). As a result, some questions remain unanswered because we cannot find suitable study subjects to answer them. As a useful example for later, the distribution of Local CRs suggests that the acceleration of protons up to the PeV range is rather common in our Galaxy (no break is observed in the proton spectrum up to those energies). However, as mentioned above, high-energy hadronic sources showing an emission that could suggest proton acceleration to the PeV range – so-called PeVatrons – are quite elusive (although at the time of this thesis submission, the LHAASO observatory has released a catalogue [50] showing more than 40 gamma-ray sources consistent with a PeVatron scenario).

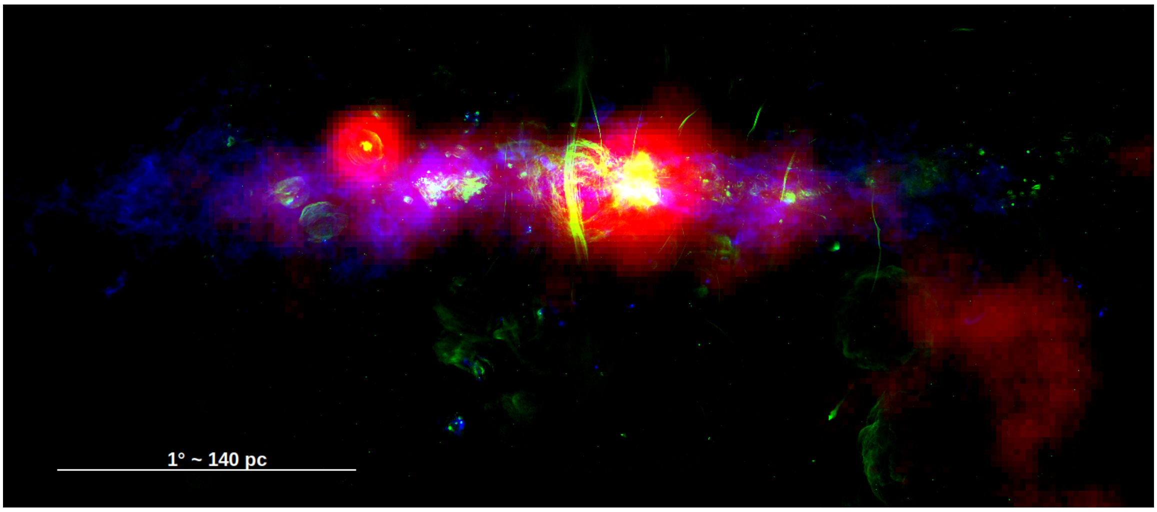

Figure 1: Composite RGB image of the Galactic Centre. The MeerKAT radio map (1.28 GHz) [104] is shown in green, the Herschel SPIRE FIR map (250 μm) [145] in blue, and the H.E.S.S. map above 0.4 TeV [95] in red. The maps used are shown singularly in Fig. 2.1.

Keeping in mind everything mentioned above, the importance of finding a suitable test case to investigate high-energy processes becomes rather clear – a nearby, extended, non-transient astrophysical object that is a gamma-ray source but also provides information in other bands: a "celestial laboratory". If we want to discuss a PeVatron scenario, it is also important that the source, when of hadronic nature, emits at sufficiently high energies.

The Galactic Centre (GC) offers all of this. Located at a distance just over 8 kpc ([89]), where one parsec corresponds to approximately 25″, it is a fascinating environment where numerous non-thermal events can be observed (as seen in the MeerKAT green radio structures shown in the Fig. 1). It has been extensively investigated in all bands except the visible/UV range, as the extinction in that band is on the order of 40 magnitudes. Showcasing a supermassive black hole (Sgr A*), highly magnetised filaments, supernova remnants (SNRs), pulsar wind nebulae (PWNe), highly star-forming clouds, possible accumulation of dark matter (DM), and other structures that cannot be easily categorised, the GC represents a wonderful laboratory for studying Galactic non-thermal phenomena. It is not surprising that it is a favoured source for operational TeV observatories in both hemispheres (H.E.S.S., MAGIC, VERITAS, HAWC) and is one of the main focuses for next-generation observatories (SWGO, CTA).

In particular, the first observations of the GC above the TeV range were carried out by H.E.S.S. [16]. Among the various identified sources, two in particular are the

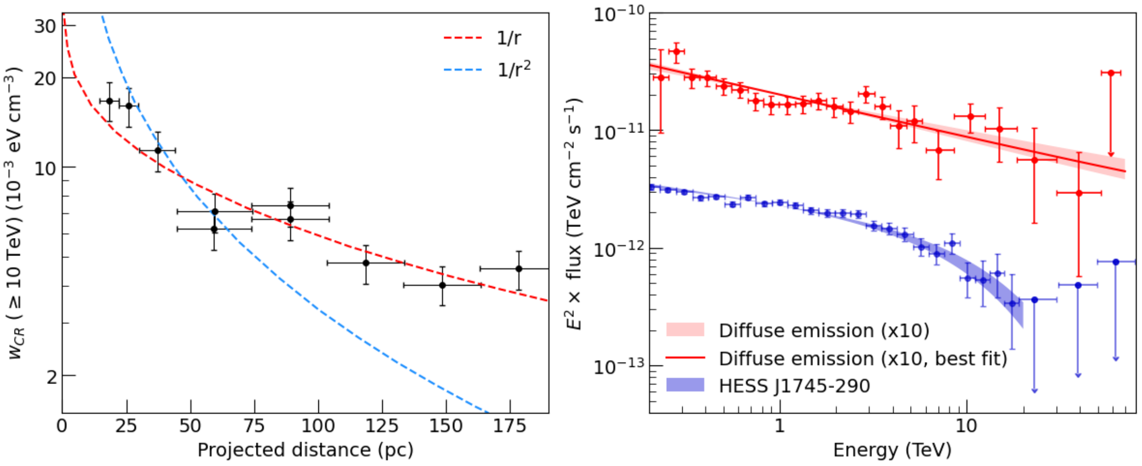

Figure 2: Left panel: radial profile of the CR energy density in the Galactic ridge inferred by H.E.S.S. The radial profiles are also shown and discussed in Fig. 2.5. Right panel: SED of central and diffuse component emission. Adapted from [93].

focus of this thesis: the central source (HESS J1745–290 [19], the central bright red spot in Fig. 1), which coincides with the position of Sgr A*, and the extended diffuse emission on a scale of ∼ 2.5° ([94], the large red glow in the same figure). The diffuse emission, in particular, exhibits very peculiar characteristics:

- It shows a significant spatial correlation with the gas and dust in the central molecular zone (CMZ), strongly suggesting a hadronic origin. The red glow tracing the blue dust distribution can be easily seen in Fig. 1.
- According to the data published by H.E.S.S., its spectrum shows a power-law behaviour without any cut-off up to ∼ 50 TeV (see the red curve in Fig. 2, right panel), suggesting a photon emission up to 100 TeV (although the point is up for debate, see for example MAGIC [139]). Being a hadronic source, this would make the GC the first Galactic PeVatron.
- The inferred spatial profile of the CR density suggests that protons are accelerated in the central ∼ 10 parsecs (Fig. 2, left panel), ideally connecting the diffuse emission with the central source – assuming that the central source is hadronic, that they share the same accelerator, and that the protons can propagate to such length.

However, the spectrum of the central source is quite different: although the spectral index below 5 TeV is very similar to the diffuse emission, its spectrum exhibits a

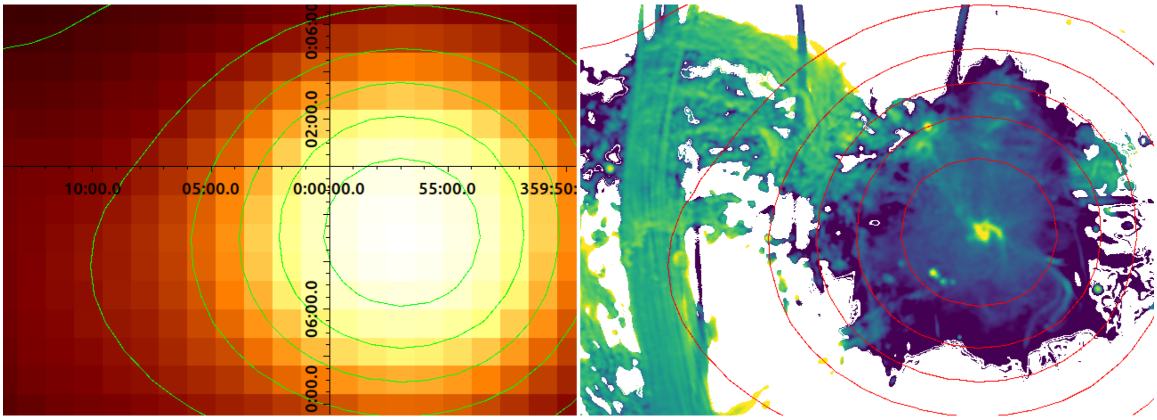

Figure 3: H.E.S.S. (left panel) and MeerKAT (right panel) maps of the region around HESS J1745–290. The H.E.S.S. contours are overplotted in both panels.

clear cut-off around 10 TeV (the blue curve in Fig. 2, right panel). The most obvious conclusion is that the two sources are not directly correlated: the central source could have a leptonic origin or, even if it were hadronic, the energy of the parent nuclei would not exceed 100–150 TeV.

Yet, there are possible explanations for the aforementioned break that would be compatible with central particle acceleration to higher energies. For example, assuming that the proton diffusion coefficient is strongly time- and energy-dependent (see discussion in Section 1.1.4, and for instance [15]) could explain the absence of photons at higher energies (the protons that would generate them can escape more easily from the confinement zone).

In this thesis I explore a different solution.

The central ∼ 5 pc around Sgr A* host one of the most intense infrared radiation fields in our Galaxy. This is possible due to the simultaneous presence of two factors: the abundance of interstellar dust and the presence of an extremely intense UV/optical radiation field that powers the dust emission. Such an intense infrared radiation field is capable of absorbing gamma radiation through the creation of electron-positron pairs. Being dependent on the energy of both IR and gamma-ray photons, this mechanism would leave a signature in the intrinsic spectrum of the gamma-ray source. The hypothesis my thesis is based on is that the cut-off in the spectrum of the central source, HESS J1745–290, is an absorption feature, and that the intrinsic spectrum of the source extends to higher energies – for example, it could resemble the spectrum of the diffuse emission, therefore strongly suggesting that they share the central CR accelerator.

Since the pair production opacity strongly depends on the 3D spatial position, we can use it to investigate the geometry of the gamma-ray source. For example, we can ask which combination of source spectrum, centre position, and morphology is consistent with the H.E.S.S. data after calculating the absorption. The great advantage of this analysis is that the 3D map of the pair production opacity has the same angular resolution as the infrared maps from which it is derived, which is on the order of arcseconds (refer to Fig. 3 for a visual understanding of the H.E.S.S. angular resolution). Therefore, such investigation can potentially constrain the gamma-ray source geometry with a resolution (~ 1–$2''$) that is normally unthinkable in high-energy astronomy.
To verify the absorption hypothesis, observations at energies around 100 TeV are needed, which current observatories cannot reach – while LHAASO and HAWC, the only observatories capable of detecting photons at those energies, cannot effectively observe the Galactic Centre due to their location too far north of the equator. But with observations from both CTA and SWGO, the next-generation gamma-ray observatories, we will be able to characterise both the spectrum and geometry of the central source in greater detail and thus test this hypothesis.

In this thesis I present my model for the gamma-ray absorption by the 3D infrared radiation field and discuss the results. Introductions to high-energy astrophysics and to the Galactic Centre seen in gamma rays are respectively in Chapter 1 and Chapter 2. Chapter 3 deals with the development of the 3D infrared radiation model in the inner 6 parsecs of the Galactic Centre, and in Chapter 4 I study the resulting gamma-ray absorption and its implications on the CR source geometry and on the physics of the gamma-ray emission. The results are discussed in Chapter 4.4.4.

1

INTRODUCTION TO HIGH-ENERGY ASTROPHYSICS

1.1 Cosmic rays

History

While studying the discharge rate of his electroscopes in the proximity of ionising sources, in 1896 Henry Becquerel found out that he could not completely shield the electroscopes from ionisation regardless of where he performed his experiments. This opened up an enigma which challenged both radiation and particle physics models at the time: where does this “spontaneous radioactivity” come from, seemingly present everywhere? The most common belief, also thanks to the identification of radioactive materials by Marie and Pierre Curie in 1898, was that the radiation originated from the ground. It was a Jesuit priest, Father Theodor Wulf, who perfected a portable electroscope and thus allowed targeted experiments far from the ground. While his experiments from the top of the Eiffel Tower ($\sim 300\,\mathrm{m}$) did not show any variation compared to ground level, Domenico Pacini’s experiments in 1911 yielded quite the opposite results, clearly demonstrating that radiation decreased drastically already a few meters underwater – indicating absorption at the water surface and thus strongly suggesting that whatever was discharging the electroscopes was coming from above.

It is within this context that the famous nine balloon flights (with dozens of Wulf electroscopes) by Victor Hess come into play. During his last flight, he reached an altitude of $5200\,\mathrm{m}$ above sea level and finally observed a significant increase in ionisation with altitude, confirming Pacini’s findings. It was the 7th August 1912, and this is commonly regarded as the date of the discovery of cosmic rays. By the time Victor Hess won the Nobel Prize in 1936, it was already clear that CRs were charged particles originating from beyond the solar system.

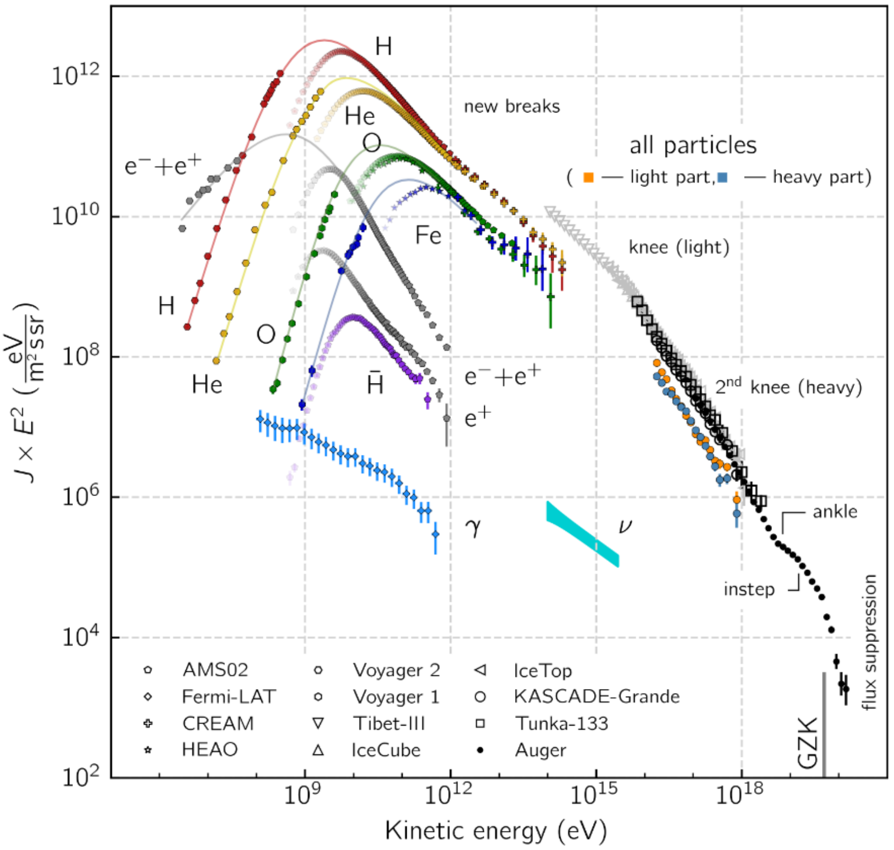

Figure 1.1: The all-particle spectrum, including the flux measured or inferred for the main chemical elements, electrons, positrons, antiprotons, and estimates for the astrophysical neutrinos (figure taken from [174]). References for all the data used are reported in the text.

More than a century later, CR astrophysics has seen new enigmas replace the old ones. We have learnt a great deal about their nature, their composition, and their behaviour in the vicinity of Earth, but key questions such as their origin or the physics of their emission process remain open.

1.1.1 *Spectrum and composition*

Being charged particles, CRs are subject to continuous deflections by Galactic magnetic fields and do not provide any directional information about their origin, except for extremely energetic particles. Such information is instead conveyed by neutral particles like photons and neutrinos[1]. The mechanisms of high-energy

---

[1] Technically, being neutral, neutrons also carry positional information, but they decay in approximately 15 minutes and thus are not useful messengers – unless at very high Lorentz factors ($\sim 10^9$),

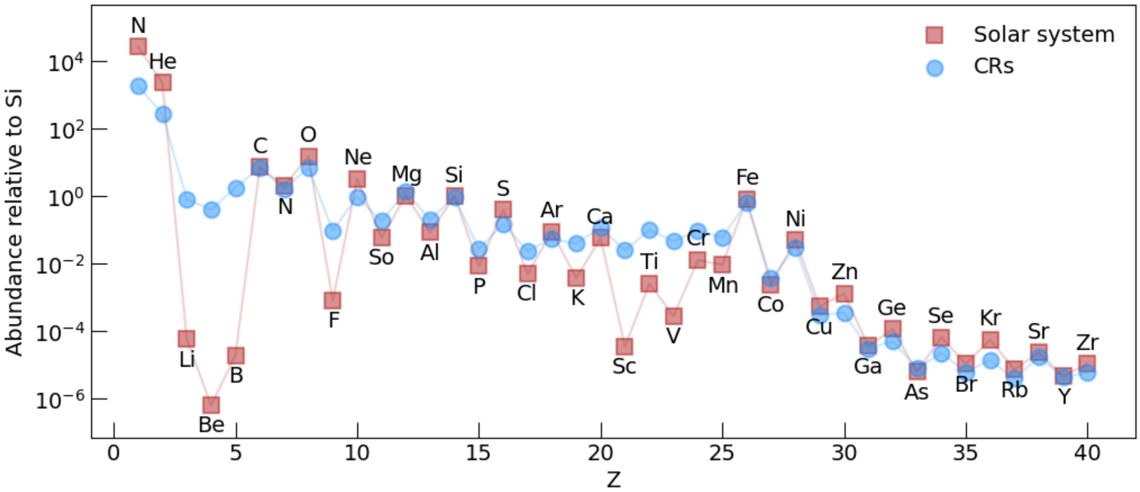

Figure 1.2: Chemical abundances in the Solar system and local CR composition, both normalised to the observed Si abundance.

photon production are the focus of Section 1.2, while a discussion of neutrino astrophysics is not relevant for the purposes of this thesis.

The CR energy spectrum and composition have been extensively studied since the 1960s by numerous detectors on the ground, underwater and mounted on balloons and satellites. A comprehensive list of CR flux data can be found in databases such as the Cosmic-Ray Database [142] and the KASCADE Cosmic-Ray Data Centre [117].

A very limited selection of flux data, enough to cover 12 orders of magnitude in energy for a few particles and antiparticles (AMS-02 [13], Auger [2], CREAM [211], Fermi-LAT [32], HEAO [40], IceCube and IceTop [4], KASCADE-Grande [29], Tibet-III [27], Tunka-133 [172], Voyager 1 [61] and Voyager 2 [185]) is shown in Fig. 1.1. An estimate of the astrophysical neutrino flux from the IceCube observations [3] is also shown.

The CR composition is dominated by hydrogen (generally referred to as protons) and to a lesser extent by helium nuclei, with a much smaller contribution from heavier elements, electrons, and their antiparticles. Additionally, at 10 GeV, the ratio of electrons to protons is about 2% (and at that energy it should not be affected much by solar activity). It closely follows the one inferred for the gas in the solar system (see Fig. 1.2), except for elements such as lithium, beryllium, and boron – which

---

which would allow for mean free paths of Galactic scale. However, at such high energies we would observe an anisotropy in the CR sky, which has been excluded [9].

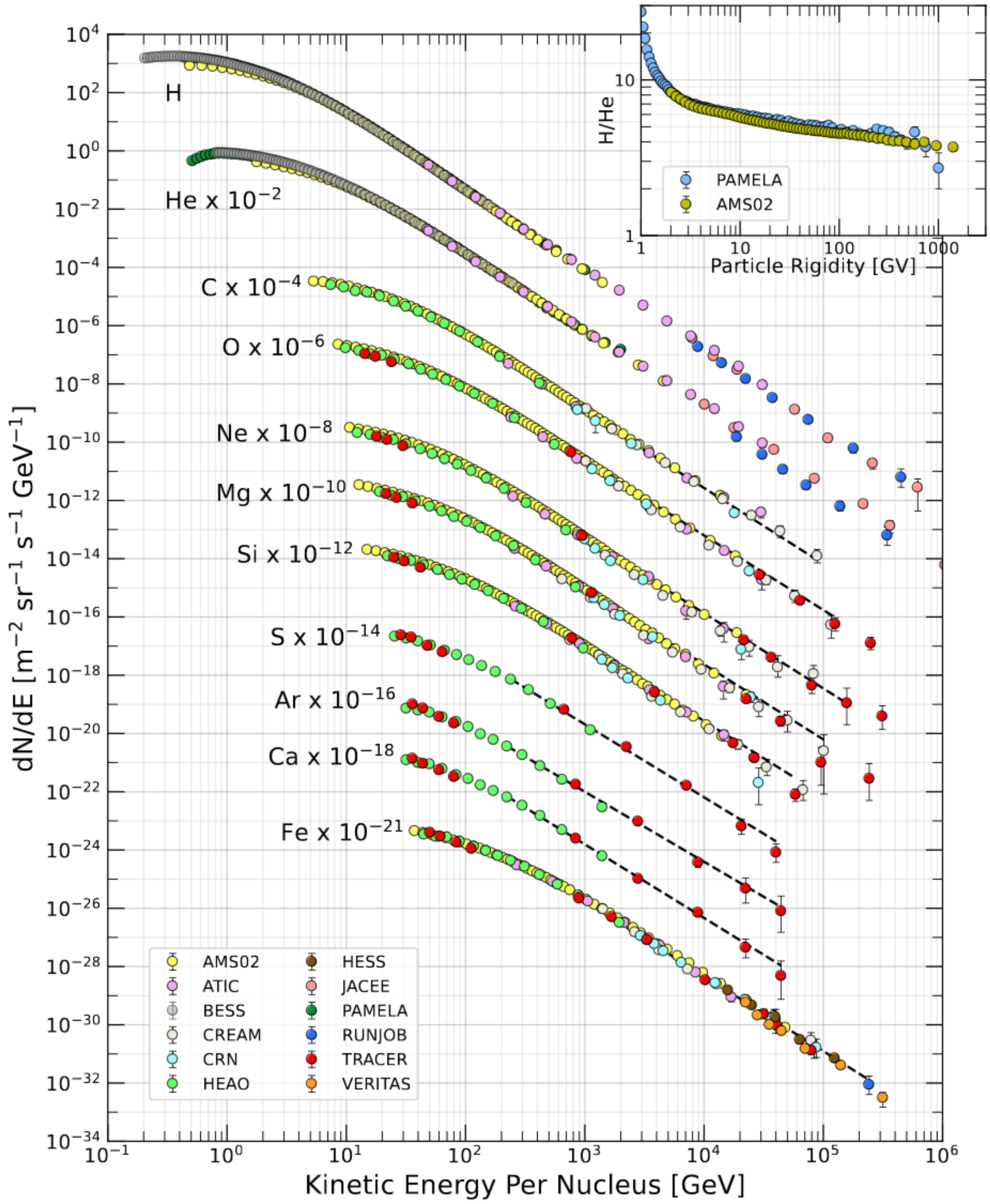

Figure 1.3: CR fluxes for different chemical elements. The energy is per nucleus. The inset shows the H/He ratio as a function of rigidity. Figure taken from [209], their figure 30.1.

are primary products of spallation[2] of high-energy carbon, nitrogen, and oxygen nuclei interacting with the interstellar medium (ISM) – as well as heavier elements

---

[2] *Spallation* refers to an inelastic nuclear reaction in which a high-energy particle collides with an atomic nucleus. In CR physics, the term is practically used as a synonym for *fragmentation*, although formally it is not completely correct.

that result from the spallation of iron nuclei. As shown in Fig. 1.3, all elements exhibit the same spectral index at least up to the “knee” (labelled in Fig. 1.1 together with the “ankle” and the flux cut-off), indicating that at those energies both CR acceleration and diffusion do not depend drastically on their composition.

Across the entire gamma-ray energy range the physics of CR acceleration and diffusion varies significantly, resulting in different spectral features, many of which have not yet been completely understood. To understand the qualitative behaviour of the spectrum, it is necessary to link its observable characteristics, in particular the spectral index α, to the physical mechanisms of particle acceleration and diffusion. It is assumed that the spectrum in a given range (particles per unit energy, time, area, and solid angle) can be described by a power-law function:

$$\phi(E) = \frac{\mathrm{d}n}{\mathrm{d}E} = K\left(\frac{E}{E_0}\right)^{-\alpha} \tag{1.1.1}$$

where K and E_0 define the flux normalisation. If we assume that both the acceleration and the diffusion mechanisms imprint power-law signatures onto the particle spectrum (with spectral indices α_A and α_D respectively), the total spectral index accounts for them in a very simple manner:

$$\frac{\mathrm{d}n}{\mathrm{d}E} \propto E^{-\alpha_\mathrm{A}} \cdot E^{-\alpha_\mathrm{D}} \longrightarrow \alpha = \alpha_\mathrm{A} + \alpha_\mathrm{D} \tag{1.1.2}$$

although it should be noted that the power-law approximation may be somewhat simplistic (see for instance [133]).

In the following, we describe the spectral features in four separate energy bands.

$\mathbf{E \lesssim 10^9}$ eV

In this range, the particle energy is strongly influenced by the solar magnetic field, which is highly variable and creates considerable uncertainty in the data. However, at these energies, data is also provided by the two Voyager probes, drifting far beyond the solar system but still able to transmit invaluable information to us – such as a CR spectrum unaffected by the solar activity. α in this range is approximately 0, meaning that the flux does not depend on energy up to around 1 GeV.

Between a few GeV and the knee ($\mathbf{E \simeq 3 \times 10^{15}}$ eV)

In this range the behaviour is rather regular, following a power-law distribution with $\alpha \simeq 2.7$ without evident deviations until a known turn-off point called the *knee*.

The commonly accepted scenario assumes the majority of CRs falling in this range to have a Galactic origin. The experimental verification of theoretical models for the CR transport are limited by the uncertainties in the measurement of physical quantities (such as the global and the local Galactic magnetic field) and by the impossibility to reproduce astrophysical mechanisms (such as supernova explosions) on the Earth. However, in general, the observed spectrum can be explained by making a few simple assumptions.

The CR acceleration invokes the Diffusive Shock Acceleration (DSA) mechanism, where a particle confined by the magnetic field is accelerated repeatedly as it crosses the shock front back and forth, until it finally manages to escape. The shocks are caused by isolated supernova explosions, which provide an injection spectrum with a spectral index $\alpha_\mathrm{A} \simeq 2.2$ and a maximum particle energy ranging from around 3×10^{14} eV to 3×10^{15} eV, depending on the shock velocity, ISM conditions, energy transport, and magnetic field amplification. This maximum energy value corresponds to the CR knee, beyond which particles are no longer accelerated with the same efficiency, resulting in a softening of the spectrum (beyond the knee the observations give $\alpha \simeq 3.0$). Additional details on DSA and acceleration in supernovae are given later in Section 1.1.3.

The contribution from the diffusion translates into the probability that a particle remains confined within the Galaxy or escapes before being detected, and affects its energy via the losses it goes through along its path. Random diffusion can trap the particle – thus favouring its detection – but also drive it away from the Galaxy. This mechanism is clearly dependent on the particle's energy since more energetic particles are less deflected and are therefore more difficult to keep confined. If we can identify elements whose abundances change during the random walk, the average distance travelled by CRs (or more precisely, the amount of matter they traverse during the diffusion) can be calibrated through the discrepancy between their composition and that of the gas in the solar system. Elements created by CR spallation are suitable targets for this investigation because, knowing the process cross-section and assuming their density on the Galactic scale, we can calibrate their mean free path in the diffusive environment. Additionally, the ratio between stable and unstable isotopes with a sufficiently long half-life (e.g. $\simeq 1.5$ million years for ^{10}Be) provides an independent clock to calibrate the average CR residence time in our Galaxy [210]. The result published in [14] obtained using the B/C abundance ratio sets $\alpha_\mathrm{D} \simeq 0.5$, which gives us the observed value of $\alpha \simeq 2.7$.

As a summary, the observed characteristics of the CR spectrum in this energy range can be predicted assuming that CRs are accelerated within the Galaxy and contained for a sufficient amount of time.

Between the knee ($\mathbf{E \simeq 3 \times 10^{15}\,eV}$) and the ankle ($\mathbf{E \simeq 3 \times 10^{18}\,eV}$)

Generally, this energy range is considered a transitory phase between Galactic and extragalactic CR-dominated spectrum and is not yet fully understood, although there are models describing the Galactic CR acceleration beyond the knee energy (see for instance [202], where they model CR acceleration up to 100 PeV by local supernovae embedded in young massive star clusters).

Magnetic confinement imposes an upper limit on the energies of Galactic CRs since their trajectory cannot cross the boundary set by the Galactic disk thickness (~ 100–150 pc from the disk plane). A particle with charge q moving in a homogeneous magnetic field B follows a circular path with a Larmor radius r_{L} and an energy given by

$$E = qBr_{\mathrm{L}} \simeq 100\,q \left(\frac{B}{1\,\mu\mathrm{G}}\right)\left(\frac{r}{100\,\mathrm{pc}}\right)\mathrm{PeV}. \tag{1.1.3}$$

In the case of a proton orbiting at the edge of the disk near the Sun and assuming an average magnetic field of 4 μG [184] a maximum energy of 400 PeV is found – roughly the energy of the second knee, which could then mark the threshold for non-confinement of CRs in the Galaxy. Beyond this energy an additional softening is observed, with $\alpha \simeq 3.3$.

Another hint at the rising extragalactic origin of these particles above the second knee is that the arrival direction is quite isotropic [9], which is hardly compatible with Galactic sources located on the same plane.

Beyond the ankle ($\mathbf{E \gtrsim 3 \times 10^{18}\,eV}$)

The sudden hardening ($\alpha \simeq 2.7$ again) is considered a signature that CRs of extragalactic origin begin to dominate the flux in this energy range. There is an evident flux suppression around $\sim 5 \times 10^{19}$ eV, which can be explained as a physical limit of diffusion (due to the GZK effect [91, 212]) or acceleration (due to the maximum efficiency of the accelerator, see for instance [26]).

The GZK effect consists in the absorption of the proton flux by the cosmic microwave background (CMB) radiation through photo-pion reactions:

$$\mathrm{p} + \gamma_{\mathrm{CMB}} \rightarrow \pi^0 + \mathrm{p} \tag{1.1.4}$$

$$p + \gamma_{\mathrm{CMB}} \to \pi^+ + n. \tag{1.1.5}$$

The net effect is a sharp steepening of the proton spectrum around $\sim 5 \times 10^{19}$ eV. Heavier nuclei have higher energy thresholds in proportion to their mass number, because what matters in the reaction is the energy per nucleon (therefore the limit for an iron nucleus is approximately 56 times higher than for protons[3]).
If we also consider the contribution from the extragalactic background light (EBL) high-energy nuclei can undergo photo-disintegration, resulting in the creation of lighter nuclei:

$$A + \gamma \to (A - nN) + nN. \tag{1.1.6}$$

Since the cut-off is evident in the all-particle spectrum around $\sim 5 \times 10^{19}$ eV, it might seem a strong hint of a GZK-induced suppression. But such a claim (like the one in [5]) implies that the spectrum at those energies is dominated by protons[4]. However, the claim by the Pierre Auger Observatory goes in the opposite direction: the composition above 5×10^{18} eV seems to clearly shift towards heavier nuclei [1]. Solving this enigma (and many others) requires a multi-messenger approach. Indeed, we get additional information from the secondary products of the aforementioned reactions:

- the neutral pions produced in Equation 1.1.4 decay into photons:

$$\pi^0 \to \gamma + \gamma \tag{1.1.7}$$

- the charged pions produced in Equation 1.1.5 decay into neutrinos:

$$\pi^+ \to \mu^+ + \nu_\mu \qquad \text{followed by} \qquad \mu^+ \to e^+ + \nu_e + \bar{\nu}_\mu \tag{1.1.8}$$

Therefore, the detection of cosmogenic neutrinos and photons would strongly indicate a predominance of hydrogen in the CR composition. Unfortunately, the dominant process at those energies is photo-disintegration (Equation 1.1.6), which generates neutrinos through the decay of unstable nN nuclei but yields a much lower neutrino flux compared to the charged pion decay from GZK photo-pion production.

---

[3] The same kinetic energy of a tennis ball flying at 430 km/h – except it is a single atom.

[4] We do not have certainty of the CR composition at those energies, since no detector in space could ever be sensitive to CRs in that range, and ground-based detectors do not directly measure the composition but infer it from other parameters with large uncertainties.

1.1.2 *CR energetics*

How important are CRs for the energy balance of the Galaxy? This question is critical and the answer is by no means simple. In order to assess it at first order, we need to calculate the CR energy density on Galactic scale and compare it to radiation and magnetic fields.

Going back to Equation 1.1.1, let us now investigate the spectrum quantitatively. Locally, for $E_0 = 1\,\mathrm{GeV}$ and $\alpha = 2.7$, we obtain from observations [13]:

$$K = 1.8\,\mathrm{cm}^{-2}\,\mathrm{s}^{-1}\,\mathrm{sr}^{-1}\,\mathrm{GeV}^{-1}. \tag{1.1.9}$$

Defining $E_1 = 1\,\mathrm{GeV}$ and $E_2 = 100\,\mathrm{PeV}$, the total integrated flux above 1 GeV is then

$$F(E > 1\,\mathrm{GeV}) = \int_{E_1}^{E_2} \phi(E)\mathrm{d}E = \left.\frac{K}{(1-\alpha)E_0^{-\alpha}}\right|_{E_1}^{E_2} \simeq 1\,\mathrm{cm}^{-2}\,\mathrm{s}^{-1}\,\mathrm{sr}^{-1} \tag{1.1.10}$$

with a CR number density of

$$n_{\mathrm{CR}} = \frac{4\pi}{c} F(E > 1\,\mathrm{GeV}) \simeq 4 \times 10^{-10}\,\mathrm{cm}^3. \tag{1.1.11}$$

Therefore, we find the CR energy density:

$$w_{\mathrm{CR}}(E > 1\,\mathrm{GeV}) = \int_{E_1}^{E2} E\,\frac{\mathrm{d}n(E)}{\mathrm{d}E}\,\mathrm{d}E = K\frac{4\pi K}{c\,E_0^{-\alpha}} \int_{E_1}^{E_2} E\,E^{-\alpha}\,\mathrm{d}E = K\left.\frac{4\pi K}{c\,(2-\alpha)E_0^{-\alpha}}\right|_{E_1}^{E_2} \tag{1.1.12}$$

which finally yields

$$w_{\mathrm{CR}} \simeq 1.1\,\mathrm{eV/cm}^3. \tag{1.1.13}$$

In order to understand the weight of the CRs for the energy balance in the Galaxy, we can compare w_{CR} to:

- the energy density of the magnetic field:

$$w_{\mathrm{B}} = \frac{B^2}{8\pi} \simeq 0.4\,\mathrm{eV/cm}^3, \tag{1.1.14}$$

- the energy density of the CMB:

$$w_{\mathrm{CMB}} = a\,T_{\mathrm{CMB}}^4 = 0.26\,\mathrm{eV/cm}^3, \tag{1.1.15}$$

- and the energy density of the diffuse starlight:

$$w_{\mathrm{SL}} \simeq 3 - 4 \times 10^{-1}\,\mathrm{eV/cm^3} \tag{1.1.16}$$

with $T_{\mathrm{CMB}} = 2.73\,\mathrm{K}$ [76], and where we assumed a magnetic field value $B = 4 \times 10^{-6}\,\mu\mathrm{G}$ [184]. The value provided for the stellar light energy density is evaluated on its peak around 1 μm[168].

It is quite evident that the CR energy budget is far from negligible on Galactic scales – quite the opposite, CRs might very well be a key factor regulating the physical processes in the Galaxy. In the last 15 years the community has experienced continuous advancements in the derivation of theoretical models for CR transport, however no current cosmological high-resolution simulation can deal with the physics behind CR feedback on both small and large scales yet. A review on the role of CR feedback in the Galaxy can be found in [174].

1.1.3 *Acceleration*

The fact that the entire CR spectrum can be approximately described as a broken power-law between 2.7 and 3.3 suggests the existence of a global acceleration mechanism, with the major differences in the spectrum arising from diffusion and absorption processes.

Today it is commonly believed that the underlying mechanism for CR acceleration in astrophysical phenomena (e.g. supernovae, young massive star clusters) is Diffusive Shock Acceleration (DSA) [42]. In 1949 Enrico Fermi had devised a theory in which moving magnetic fields could accelerate particles with scaled velocity $\beta = v/c < 1$, but only when the collision was head-on [73]. Such condition greatly limited its effectiveness, making it a second-order process since the energy gain for each collision was proportional to β^2. In DSA, on the other hand, the plasma moves with a velocity U_1 greater than the shock velocity U_2. In the rest frame of the shock, the upstream plasma impacts the shock with a velocity $U_1 - U_2$ and exits downstream with a velocity $(U_1 - U_2)/r$, where r is the density compression ratio at the shock. The interaction with the surrounding magnetic field causes the particle to re-cross the shock – this time downstream – and this cycle can be repeated many times until the particle escapes the shocked region. In the appropriate reference frame, each subsequent shock (both downstream and upstream) is always head-on, and the net energy gain is always positive and proportional to β – making it a first-order Fermi acceleration mechanism. In the end, DSA is able to explain the CR power-law

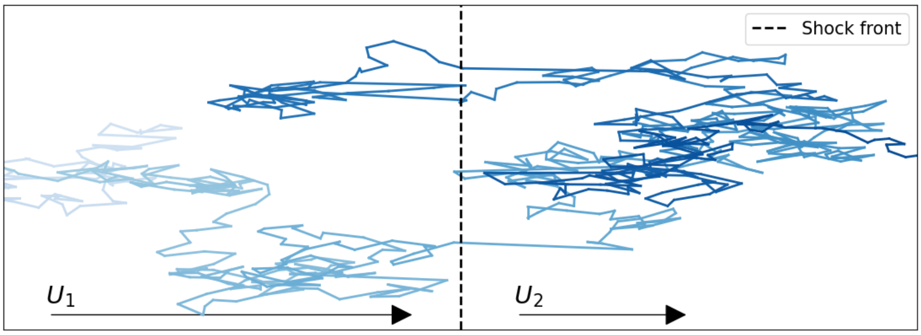

Figure 1.4: Depiction of the DSA mechanism. The incoming plasma travels from the left (*upstream*) with velocity U_1, while the shock moves with velocity U_2.

behaviour: the imprint of the acceleration onto the spectrum is proportional to E^{-2}. However, DSA relies on three fundamental conditions:

1. downstream particles must be able to return upstream;
2. the particles cannot propagate freely because magnetic field lines would quickly guide them away from the shock;
3. the particles must be able to escape from the shock when their energy is sufficiently high, or the energy transfer could smear the shock quickly.

The solution presented by DSA to the first two conditions is that the trajectories are stochastically curved by fluctuations in the magnetic field [42]. Indeed, as particles move in a plasma, they create Alfvén waves which propagate along the magnetic field lines, with length scales of the order of the particle Larmor radius. The interaction between the Alfvén waves and the typical plasma diffusion length creates a resonance capable of scattering the CRs, giving them a diffusive motion and thus hindering their escape along the field lines [65].

The third point is instead related to the physics of the specific accelerator that influences the initial conditions of the plasma, including velocity, density, and magnetic field with which the upstream plasma approaches the shock. In other words, the details of the CR injection into the DSA mechanism and the dynamics of the shock determine the maximum acceleration energy of the particles while keeping the shock “functional”, and can slightly alter the spectral index with which the particles escape from the shocked region (with respect to the “standard” $\alpha_{\mathrm{A}} = 2$ from DSA, keeping in mind that the observed one is $\alpha_{\mathrm{A}} \simeq 2.2$).

CR source candidates

The obvious follow-up question is: which astrophysical objects satisfy both the conditions on initial CR injection and the presence of an appropriate shock and magnetic field? A few examples of good candidates are:

- Massive and compact multiple stellar systems, where the shock is caused by the collision of stellar winds (e.g., η Carinae [206]).
- Young massive star clusters (YMSCs), where the high density of massive stars and the resulting concentration of stellar winds create the conditions for the formation of a hot "superbubble"-like magnetised shock around the cluster [131, 43].
- Recurrent novae, where a star A transfers hydrogen onto a companion white dwarf, causing a thermonuclear explosion and a subsequent shockwave that collides with the stellar wind of the star A [10, 97].
- Pulsar wind nebulae (PWNe), where fast-rotating neutron stars with an extreme magnetosphere accelerate electrons up to several tens of GeV, forming a "nebula" of relativistic electrons.
- Supernova remnants (SNRs), which can accelerate the material ejected by the explosion itself but can also accelerate further the relativistic nebula created by the pulsar at its centre. The most well-known example is the Crab Nebula, one of the standard sources in gamma-ray astronomy, capable of accelerating particles up to several PeV [128].

While all of these sources can contribute to some extent to the CR spectrum, the SNRs are excellent candidates because, besides providing a magnetised shock and continuous high-energy injection, they meet two key requirements:

1. they can account for the observed Galactic CR flux;
2. they can accelerate particles up to energies near the CR knee.

Therefore, SNRs are considered to be "working" candidates, albeit with a few critical points (see, for example, [66, 35, 60]).

Demonstrating that SNRs can account for the Galactic CR energy is quite straightforward. Following the idea of Walter Baade and Fritz Zwicky back in 1934 [33], the total power in the form of CRs contained within the Galactic disk is

$$P_{\mathrm{CR}} = \frac{w_{\mathrm{CR}}\, V_{\mathrm{Gal}}}{t_{\mathrm{res}}} = 2.8 \times 10^{40}\,\mathrm{erg/s} \tag{1.1.17}$$

with w_{CR} coming from Equation 1.1.13 and $V_{\mathrm{GGal}} \simeq 10^{63}\,\mathrm{cm}^3$, and with $t_{\mathrm{res}} \simeq 15\,\mathrm{Myr}$ [210] being the average CR residence time in the Galaxy calculated through the B/C ratio.

Assuming a SN explosion rate $r_{\mathrm{SN}} \simeq 0.03\,\mathrm{yr}^{-1}$ and an average energy $E_{\mathrm{SN}} \simeq 10^{51}\,\mathrm{erg}$, the total power irradiated in an explosion gives instead

$$P_{\mathrm{SN}} = E_{\mathrm{SN}}\, r_{\mathrm{SN}} = 9.5 \times 10^{41}\,\mathrm{erg/s} \tag{1.1.18}$$

which indicates that SN explosions converting $\sim 3\%$ of their energy into CR acceleration (which we will refer to as CR conversion efficiency ϵ_{SN}) would justify the observed CR flux. However, it is important to note that the total CR energy, and hence the value of ϵ_{SN}, is proportional to the calculated residence time. Different models yield significantly different estimates (e.g., Lipari et al. [132] provides a t_{res} of approximately 200 Myr, which reduces the required efficiency by a factor of 10). Moreover, the average energy E_{SN} is not a precisely known value either.

To address the second point, which pertains to the maximum particle energy achievable, we need to delve into the details of the physics of the explosion. The expanding ejecta act as a shock, being hot ($T \sim 10^6\,\mathrm{K}$) and under-dense ($n \sim 1\,\mathrm{cm}^{-3}$). As it expands into the interstellar medium (ISM), it decelerates. Consequently, the resonant interaction of Alfvén waves and magnetic field fluctuations weakens, leading to a diminishing efficiency in confining particles. This, in turn, limits the maximum energy of accelerated particles to approximately [36]):

$$E_{\max} = 0.03 \left(\frac{B}{\mu\mathrm{G}}\right) \left(\frac{u}{10^4\,\mathrm{km/s}}\right) \left(\frac{t}{10^3\,\mathrm{yr}}\right)\ \mathrm{PeV} \tag{1.1.19}$$

which can hardly reach 100 TeV even for the most convenient combinations (as it has been confirmed by observations [80]), let alone the knee energy *on average*. To reach PeV and higher energies additional mechanisms need to be invoked – such as the amplification of the magnetic field by CRs [137] and the interaction of the accelerated CRs with an additional shock created by the stellar wind of massive stars in YMSCs [202].

This point should be stressed once again: since magnetic fields on all scales – interstellar and intergalactic – deflect CRs along their paths, directional information is lost: they do not provide us with any information about the source location. This means that the only way to trace back the acceleration sites, assuming we find astrophysical objects in which shocks and magnetic fields play a role, is to model their acceleration physics, their subsequent gamma-ray emission (see Section 1.2.2), and then constrain the results with gamma-ray observations.

1.1.4 *Diffusion and escape*

As described in Section 1.1.1, by studying the abundances of elements created through spallation processes it is possible to infer the grammage, which represents the average amount of gas crossed by a high-energy nucleus. Assuming a value for the average gas density, one can deduce the distance travelled by the nucleus and the residence time in the Galaxy. If the isotope is also radioactive with very long decay times, the residence time can be calculated from its relative abundance to the stable isotope, without the need to make assumptions about the gas density (which is not homogeneous at all). The two techniques yield discordant values, but both significantly exceed 1 million years – which would already be sufficient for a weakly deflected particle to escape the Galaxy (travelling at approximately the speed of light, it would cover 300 kpc). It is evident that the assumption of small deflections is inadequate.

The solution invokes again an amplification of magnetic field perturbations due to magneto-hydro-dynamic (MHD) waves and local discontinuities, which result in a random distribution of deflection angles and, consequently, a completely diffusive environment. In such a case, the evolution of a quantity is described by the second Fick's law or *diffusion equation*:

$$\frac{\partial f(x,t)}{\partial t} = D_{\mathrm{xx}} \nabla^2 f(x,t) \tag{1.1.20}$$

D_{xx} being the spatial diffusion coefficient. Following [186], the diffusion coefficient for a charged nucleus can be expressed as

$$D \sim 3-5 \times 10^{28} \left(\frac{E}{1\,\mathrm{GeV}}\right)^{1/3} \mathrm{cm}^2/\mathrm{s} \tag{1.1.21}$$

valid for particles with $E \lesssim 10^{17}\,\mathrm{eV}$. The relation $D \propto E^{1/3}$ is typical of the Kolmogorov spectrum and is in good agreement with diffusion models for Galactic CRs – even though, towards the higher end of the energy range, one would expect a Kraichnan-type turbulence spectrum, where $D \propto E^{1/2}$.

In a diffusive environment, the length that a proton can travel before interacting via pp (or *diffusion radius*) is roughly

$$R_\mathrm{D} \approx 2\sqrt{Dt} \tag{1.1.22}$$

which is valid for times smaller than the typical pp timescales. In 1 million years, the diffusion length for a 1 GeV particle is approximately 35 pc, while for a 100 TeV particle it increases to $\sim 250\,\mathrm{pc}$. This means that the diffusion length is highly variable but always comparable to the thickness of the Galactic disk.

In summary:

- the distance travelled by CRs indicates that their motion is diffusive;
- the diffusion distance is a function of the particle's energy.

These two points are more than enough to expect CR diffusion to play a major role in shaping the all-particle spectrum. The contribution of diffusion to the local CR spectrum represents how the particle energy changes between acceleration and detection. On the other hand, their escape probability depends on the diffusion properties such as the type of accelerator (continuous or impulsive), the physics of the medium being traversed (e.g., the magnetic field), as well as its geometrical features (e.g., the presence of gas inhomogeneities).

We introduced CR escape as a critical factor on Galactic scales, but it is also important on smaller length scales. For example, the region surrounding an accelerator (assuming a sphere with a radius R_A) can contain CRs up to a certain energy $E_\mathrm{max}(R_\mathrm{A})$, while more energetic particles are more likely to escape according to Equation 1.1.22, since $R_\mathrm{D} > R_\mathrm{A}$. This would reflect in the inferred CR spectrum of a given source (see Section 1.2) as a gradient in E_max. This gradient could potentially explain why the CR spectrum sometimes exhibits a cut-off at lower energies than expected ([93]). A case study will be presented in Section 4.4.

Let the particle spectrum be $f_i(x, p, t)$ for a given species i. From a formal standpoint, the equation describing its evolution in a diffusive environment, taking into account energy losses and continuous injection of particles from all species, is known as the *diffusion-loss equation* (compare it to Equation 1.1.20 and see [135] for a detailed derivation):

$$\frac{\mathrm{d}f_i}{\mathrm{d}t} = D_{\mathrm{xx}}\nabla^2 f_i + \frac{\partial}{\partial p}\left(\frac{\mathrm{d}p}{\mathrm{d}t} f_i\right) + S_i \tag{1.1.23}$$

with the first term describing the spatial diffusion and the second term describing the temporal evolution of the energy spectrum, while $S_i(E)$ represents the generalised injection term. In the case of CRs, the injection term can generally include all sources and sinks of particles:

$$S_i = Q_i - \frac{N_i}{\tau_i^{\mathrm{d}}} - \frac{N_i}{\tau_i^{\mathrm{in}}} + \sum_{j>i} \frac{P_{ji}}{\tau_j} N_j \tag{1.1.24}$$

where, from left to right, we have the continuous injection term, the loss due to decay with timescale τ_i^{d}, the loss due to spallation with timescale τ_i^{in}, and the gain from the spallation of other species j.

By adding the advection term (transport due to the field velocity), we obtain the transport equation [161], which describes the evolution of the particle distribution function under the assumption of near-isotropy in velocity space. Introducing the field velocity $\vec{v}$ and the diffusion coefficient in momentum space D_{pp}, the equation is written as follows:

$$\frac{\mathrm{d}f_i}{\mathrm{d}t} + \vec{v}\cdot\nabla f_i = D_{\mathrm{xx}}\nabla^2 f_i + \frac{p}{3}(\nabla\cdot\vec{v})\frac{\partial f_i}{\partial p} + \frac{1}{p^2}\frac{\partial}{\partial p}\left(p^2 D_{\mathrm{pp}}\frac{\partial f_i}{\partial p}\right) + S_i \tag{1.1.25}$$

where, from left to right, we have the temporal evolution, the contribution of advection, spatial diffusion, energy changes due to compressive flow (first-order Fermi acceleration), energy changes due to the motion of magnetic field variations (second-order Fermi acceleration), and the source term.

1.2 HIGH-ENERGY GAMMA-RAY EMISSION

History

The discovery of spontaneous radioactivity by Henry Becquerel in 1896 – although the term "radioactivity" would only be coined two years later by the Curies – prompted a young Ernest Rutherford to study the tendency of uranium to spontaneously ionise the air in 1899. The chain of reactions he was investigating in his experiment was most likely:

$$^{238}\mathrm{U} \rightarrow^{234} \mathrm{Th} +^{4} \mathrm{He} + \gamma$$

$$^{234}\mathrm{Th} \rightarrow^{234} \mathrm{Pa} + \mathrm{e}^{-} + \bar{\nu}_{\mathrm{e}}.$$

Obviously, he was unaware of the details of the chemistry behind his experiments[5]. Evidently being a systematic man, he referred to the highly ionising but less penetrating radiation (the helium nucleus ^{4}He) as "alpha" and the more penetrating but less ionising radiation (the electron, that was Becquerel's radiation) as "beta". Unfortunately, his scientific apparatus did not allow him to recognise the third radiation (in red in the formula and which, incidentally, was the only true *radiation*), whose discovery was achieved one year later by Paul Villard. Nevertheless, apparently this did not prevent Rutherford from giving it the official name "gamma".

But precisely because gamma radiation was associated with spontaneous decay reactions on non-cosmological timescales, questioning whether it played a role in astronomy was not at all natural (in a sense, it would have been like asking whether the Earth was surrounded by radium or uranium). The major change came only ten years later, when William Bragg found out that gamma radiation is capable of ionising the air. It almost immediately triggered the fortuitous discovery of CRs by Victor Hess (see Section 1.1 above) who indeed was looking for gamma rays coming from below, excluding an extraterrestrial origin. And after the particle nature of CRs was clarified, any idea of pursuing gamma astronomy was set aside – there was no physical theory of gamma-ray emission that was also of astrophysical interest.

---

[5] To give an idea of the understanding of nuclear physics at that time: when Rutherford and Soddy realised that radioactivity caused an element to naturally change into another, Soddy wrote that he yelled, "This is transmutation: the thorium is disintegrating and transmuting itself into argon (sic) gas!" Rutherford replied, "For Mike's sake, Soddy, don't call it transmutation. They'll have our heads off as alchemists!".

As a matter of fact, the end of World War II and the new geopolitical situation changed everything – especially after the world had witnessed the military applications of atomic energy. High-energy physics went through an intense phase of development, with an unusually high density of fundamental theories and discoveries in just over 5 years. To name just a few:

- the prediction of a diffuse gamma-ray emission due to inverse Compton scattering by energetic electrons on low-energy photons by Eugene Feenberg and Henry Primakoff in 1948 [70];
- the first measurement of gamma-ray flux on a balloon by Robert Hulsizer and Bruno Rossi in 1948 [108];
- the discovery of the neutral pion and its rapid decay into two gamma-ray photons by R. Bjorklund in 1950 [41];
- the measurement of MeV gamma-ray flux on a rocket by Gilbert Perlow and Charles Kissinger in 1951 [162];
- the prediction of a diffuse gamma-ray emission due to the decay of neutral pions produced by the interaction of CRs with interstellar gas by Satio Hayakawa in 1952 [100];
- the prediction of a diffuse gamma-ray emission due to the bremsstrahlung of high-energy electrons on interstellar gas by George Hutchinson, also in 1952 [110].

However, what motivated the deployment of multiple American gamma-ray detectors into orbit during the height of the Cold War was not astrophysical research – they were meant to be used to spy on Russian nuclear activity on Earth[6]. Curiously, what propelled the birth of gamma-ray astronomy was the nascent field of radio astronomy[7]. The discovery of radio emission from the Cygnus A galaxy and its radio lobes in 1953 played a crucial role: assuming it was synchrotron radiation, the calculations of the energy of both magnetic field and relativistic electrons in such an environment yielded more than 10^{60} ergs [48]. In fact, this result brought to light

---

[6] We can picture the astonishment of the scientists operating the Vela satellites when they recorded a clearly extraterrestrial strong signal. This marked yet another serendipitous discovery: gamma-ray bursts (GRBs) [121]).

[7] Another rather accidental discovery: Karl Jansky was an engineer working on the interference of intercontinental transmission – he ended up discovering astrophysical radio emission coming from the Galactic Centre [113].

the existence of two new astrophysical subjects: magnetic fields and astrophysical plasma [160], paving the way for non-thermal astrophysics and the first targeted gamma-ray observations. These included the Sun in 1959 [163], Cygnus A itself in 1960 [44], and most importantly the Galactic Centre: in 1968 George Clark, Gordon Garmire and William Kraushaar announced the detection of the Galactic Centre and the Galactic plane above 50 MeV by the OSO-3 satellite detector. In addition, they revealed an isotropic high-energy component that was correctly interpreted as extragalactic. Gamma-ray astrophysics had now come alive.

1.2.1 *Gamma-ray detection techniques*

The gamma-ray range falls within the highest energy range of the electromagnetic spectrum, but there is no clear experimental boundary between gamma rays and X rays. Theoretical definitions state that X rays arise from highly energetic processes involving the redistribution of electron energy, while gamma rays arise from the redistribution of nucleon energy. However, these phenomena occur within overlapping energy ranges. Photons with energies above 1 MeV obtained by accelerating electrons are commonly used in medical radiotherapy (and are defined as X rays), while gamma rays in the decay reaction studied by Rutherford have energies around 50 keV. In astrophysics, due to the chronic lack of information about the photon emission mechanism, the boundary is much looser: any photon with a wavelength shorter than 0.01 nm, corresponding to energies greater than 124 keV, is considered a gamma ray.

Gamma-ray astronomy is peculiar for three reasons at the very least:

- At those energies, photons cannot be effectively focused using lenses, so determining their arrival direction is a non-trivial task. The techniques behind the detection of a gamma-ray photon descend from the ways it interacts with matter – in other words, gamma-ray detection relies on particle physics' principles rather than optics. This has obvious implications for the efficiency of the detector, which depends on the probability of the photon interacting with matter and the probability of that interaction being recognisable, and affects the angular sensitivity of the detector, as accurately determining the direction of gamma rays becomes more challenging.

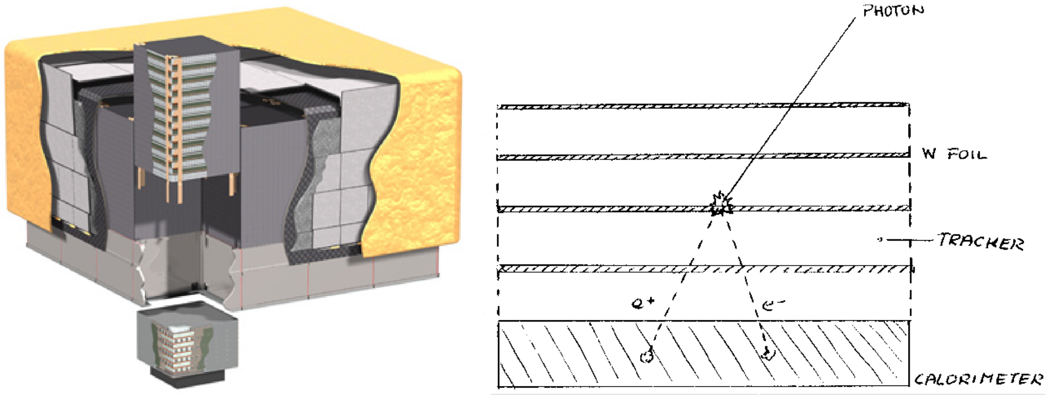

Figure 1.5: Left: depiction of the Large Area Telescope on the Fermi satellite. Starting from the outer layers: the thermal blanket (yellow layer); the anticoincidence shields (the grey panes); the 16 "towers" (dark grey + light grey boxes). One of the towers is depicted in exploded view showing the particle tracker (upper segment) and the calorimeter (lower segment). Adapted from [32]. Right: schematics of the photon detection (taken from [77]).

- Gamma rays do not penetrate the atmosphere (fortunately, see footnote 3), but they interact with the materials that make up the atmosphere. This effect can be exploited to indirectly reconstruct the photon but it limits the possibilities of direct detection to detectors on balloons or satellites.

- The electromagnetic flux is highly energy-dependent and gamma-ray detection typically occurs in a photon-starved regime, so in order to achieve a decent significance detectors must cover the largest possible area, and the integration time must be very long. However, a satellite size is limited by its deployment cost, which has two obvious consequences: first, the detectors are only useful at energies where there is a sufficient flux for small equivalent areas (typically at energies $\ll$TeV); second, there is an upper limit to the energy of gamma rays set by the amount of matter needed for their detection.

Concerning direct gamma-ray detection tecnhiques, a gamma-ray spectrometer, the photon passes through the material, creating a current (mainly through the photoelectric effect, Compton scattering, and pair production) that can be measured. In a scintillator, the crystalline material emits light proportional to the energy of the gamma ray, which can be measured using photo-multipliers. At energies higher than MeV, the primary mechanism is the production of an electron-positron pair, as the rest mass of an electron is 511 keV. The basic idea is that the gamma ray passes through some material, creating pairs of electrons and positrons that are tracked with their energies measured using a calorimeter. This system allows for

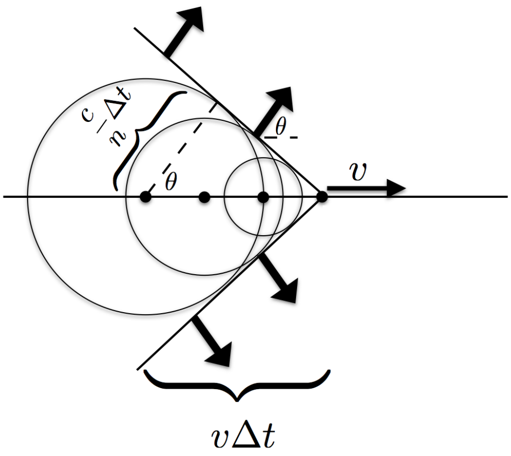

Figure 1.6: Cherenkov light cone emitted by a particle moving at v in a medium with refractive index n. The geometry is confined into a cone because the particle moves faster than the wavefront. Taken from https://casper.astro.berkeley.edu/.

the reconstruction of both the gamma-ray energy and its arrival direction, obtained by analysing the tracks of the created pairs.

Despite the apparent simplicity of such a system, discerning the energy deposited by a photon from that deposited by a CR is a non-trivial problem: the diffuse CR flux exceeds the diffuse gamma-ray flux by many orders of magnitude. For this reason, a gamma-ray detector typically employs anticoincidence shields – additional detectors specifically sensitive to charged particles – placed outside the main detector to flag a background event. Such a system, although simple in concept, requires extremely fast timing and materials that do not rapidly decay despite the high energies involved.

Direct detection on the ground is not possible: when a high-energy gamma-ray photon[8] penetrates the atmosphere, between 10 and 20 km above sea level, it interacts with the Earth's radiation field and with charged particles (nuclei and electrons), accelerating them to relativistic velocities and initiating a cascade of e^+/e^- pairs creation and their subsequent bremsstrahlung (see the following section). The net effect is the development of an atmospheric shower that exhausts when the photon energy falls below the threshold for further pair creation. If the charged particles that make up the shower have speeds greater than the speed of light in the medium (which is not c but rather c/n, where n is the refractive index, and for air is equal to 1.00029 at ground level), they emit Cherenkov radiation: flashes of a few ns, directed

---

[8] In the following labelled as the "primary" photon.

along the original axis of arrival of the gamma-ray, in a cone with an opening angle that is smaller the faster the individual charged particle is. The greater the energy of the primary photon, the more extensive is the shower and the broader is the collective lateral dimension of the total Cherenkov light emitted. The spectrum of Cherenkov light, peaking between blue and UV, can be collected to trace back to the direction and energy of the primary gamma-ray.

A ground-based Cherenkov gamma-ray detector must therefore have certain characteristics: it must be sensitive to blue/UV light; it must be able to process a signal that lasts a few nanoseconds (it is not a time-integrable signal) and that is buried in noise (Night Sky Background); it must be able to collect enough light. A cone with an aperture of 1° with its vertex at 15 km and with a vertical axis subtends a circle with a radius of 180 m at 5 km above ground level. If the axis of the cone is inclined, the geometry changes and the area increases. Fortunately, it is not necessary to collect all the light to reconstruct the primary gamma-ray: the light can be sampled by an array of telescopes spread over the illuminated area, with a filling factor that decreases with the energy of the gamma-ray (in other words, the greater the primary particle energy, the smaller the fraction of Cherenkov light that must be collected to achieve an effective detection). This technique is the basis of the current IACT observatories (H.E.S.S., MAGIC, VERITAS) and of the next generation – the Cherenkov Telescope Array (CTA).

Another possibility for the detection of astrophysical gamma-rays consists in directly measuring the shower of charged particles instead of collecting the Cherenkov light they emit in the air – for example, by placing a large number of water tanks[9] at the altitude where the shower is expected to still be “alive”, to intercept the largest number of electrons. The above applies also in this case: the number of detectable particles increases with the energy of the primary gamma-ray – the higher it is, the smaller the fraction needed for a correct identification, and the larger the spacing between the detectors can be. This second technique is the basis of the so-called water Cherenkov detectors, like HAWC or the next-generation SWGO.

---

[9] The refractive index in water for visible wavelengths is approximately 1.33, with possible variations due to its temperature and purity. It is therefore much easier to induce Cherenkov light, and measure it.

1.2.2 *Gamma-ray emission mechanisms and CR cooling*

Unlike other electromagnetic bands, gamma-ray emission is never thermal: an internal kinetic energy of 1 MeV corresponds to a temperature of 1.2×10^{10} K. Such temperatures can only be reached in the cores of the most massive stars, but with radiation densities so high that photons interact immediately to create electron-positron pairs, leading to the complete destruction of the star [34]. Therefore, gamma-ray astrophysics is dominated by non-thermal emission.

There are several gamma-ray production mechanisms that are of astrophysical interest. To mention the most important: synchrotron, inverse Compton (IC), relativistic bremsstrahlung, neutral pion decay, radioactive nucleus decay, and matter-antimatter annihilation – including dark matter (DM) self-annihilation.

In most cases, particularly in the gamma-ray range, the emission is attributed to relativistic charged particles. Only two elements on the list deviate from this pattern: radioactive decay and annihilation emission, including dark matter self-annihilation. However, the radioactive decay of nuclei does not exceed 15 MeV (decay of quarks can reach GeV energies, but the flux is negligible). On the other hand, the most common annihilation channel – electron-positron annihilation – still requires high-velocity particles in order to emit gamma rays above $\sim 10\,\mathrm{MeV}$. Heavier antiparticles (e.g., antiprotons) are typically produced through the interaction of CRs with the gas, and their predicted flux is very low (with a few exceptions, see for instance [53]).

In summary – with the notable exception of dark matter which has not been clearly observed so far – astrophysical gamma-ray emission above $\sim 20\,\mathrm{MeV}$ is directly or indirectly linked to CRs. This simple fact has a consequence of tremendous importance: it helps us inferring the CR properties around a gamma-ray source and thus the physics of the specific accelerator.

The following formal derivations of the emission processes reference the treatment in [135], unless otherwise specified. The emission of gamma radiation will be discussed as a consequence of energy loss by CRs. Therefore, the starting point is inevitably the *relativistic Larmor formula*, which describes the energy loss of a charged particle as a function of its Lorentz factor $\gamma_\mathrm{L} = E/mc^2$, charge q, and acceleration $\vec{a}$ in its components perpendicular and parallel to its velocity $\vec{v}$:

$$\frac{\mathrm{d}E}{\mathrm{d}t} = -\frac{q^2\gamma_\mathrm{L}^4}{6\pi\epsilon_0 c^3}(|a_\perp|^2 + \gamma_\mathrm{L}^2|a_\parallel|^2) \tag{1.2.1}$$

Synchrotron

The trajectory of a charged particle e moving in a uniform magnetic field (with a flux density of B) is curved due to centripetal acceleration, resulting in the emission of energy in a direction parallel to the velocity ($a_{\parallel} = 0$). By equating the relativistic centripetal force and the Lorentz force:

$$\gamma_{\mathrm{L}} m a_{\perp} = q(v \times B) \tag{1.2.2}$$

the energy loss rate from Equation 1.2.1 becomes

$$\frac{\mathrm{d}E}{\mathrm{d}t} = -\frac{q^2 \gamma_{\mathrm{L}}^4}{6\pi\epsilon_0 c^3} |a_{\perp}|^2 = -\frac{q^4 B^2}{6\pi\epsilon_0 c m^2} (\gamma_{\mathrm{L}}^2 - 1) \sin^2\theta \tag{1.2.3}$$

θ being the angle between the velocity and the magnetic field, or pitch angle. Therefore, synchrotron emission is proportional to the square of the energy and inversely proportional to the square of the mass (lighter particles emit more easily). Assuming that the particle is an electron ($m = m_{\mathrm{e}}$) and that the θ distribution is random due to isotropic diffusion, the power emitted finally becomes

$$\frac{\mathrm{d}E}{\mathrm{d}t} = -\frac{4}{3} \sigma_{\mathrm{T}} c (\gamma_{\mathrm{L}}^2 - 1) U_{\mathrm{mag}} \tag{1.2.4}$$

where σ_{T} is the Thomson scattering cross-section ($\sigma_{\mathrm{T}} \propto 1/m_{\mathrm{e}}^2$) and U_{mag} is the energy density of the magnetic field. In the case of synchrotron emission due to protons, a factor $(m_{\mathrm{e}}/m_{\mathrm{p}})^2 \simeq 2.5 \times 10^{-7}$ should be considered, thus synchrotron emission is typically more important for electrons than for protons (but there are models with non-negligible proton synchrotron emission, for instance for AGNs [20]). Furthermore, the emission occurs in the direction of the (relativistic) motion of the particle, resulting in beamed emission in that direction with a frequency $\nu \simeq \gamma_{\mathrm{L}}^3 \nu_{\mathrm{r}}$, ν_{r} being the relativistic gyrofrequency.

Synchrotron spectra for different magnetic field values and cut-off energies are shown in the left panel of Fig. 1.7. A larger magnetic field gives a larger flux and also a larger maximum achievable energy, but the latter is also achieved by higher energies in the electron distribution.

Our Galaxy shows a diffuse radio emission coming from its disk, which is interpreted as synchrotron radiation due to the diffuse Galactic magnetic fields (with an average flux density of $\approx 4\,\mu\mathrm{G}$). Another example of likely synchrotron emission

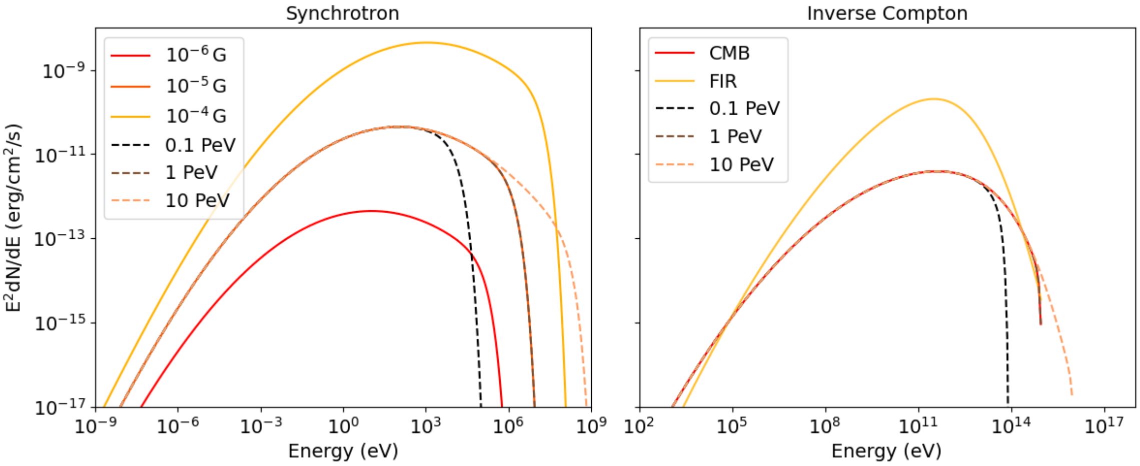

Figure 1.7: Left panel: synchrotron emission SED. The solid lines assume an electron power-law with spectral index $\alpha_e = 2.3$ and a cut-off at 1 PeV, varying the B field. The dashed lines assume a B field of 10 μG and the same electron distribution, but varying the cut-off energy. Right panel: IC emission SED. The yellow solid line assumes a MIR radiation field with a density of 100 eV/cm^3, while the red solid line assumes the CMB as target radiation field. Both use the same electron distribution as the synchrotron “solid” case. The dashed lines assume a CMB target radiation field and the same electron distribution, but varying the cut-off energy. Mind the difference in the energy scales. All the spectra in this figure as well as in figures 1.8, 1.9 and 1.10 have been calculated using GAMERA [98].

is the X-ray emission in magnetised regions close to CR accelerators observed in multiple occasions, for instance close to SNRs.

Inverse Compton

In the classical Thomson scattering theory (1906), photons can interact with free electrons, transferring to them a rather negligible fraction of their energy. When the energy differences are significant (i.e., when $E_\gamma \geq m_r c^2$), the energy of the photon changes substantially, and the relativistic treatment of Compton scattering (1922) is required. However, the inverse process exists as well and it is very relevant in non-thermal astrophysics: high-energy electrons can scatter low-energy photons (typically the CMB or infrared photons) up to gamma-ray energies. This process is known as Inverse Compton (IC) scattering [59].

Assuming an isotropic radiation field with energy density U_{rad}, the equation describing the power transferred to the photon is

$$\frac{dE}{dt} = -\frac{4}{3}\sigma_T c(\gamma_L^2 - 1)U_{\text{rad}} \tag{1.2.5}$$

and indeed, a simple comparison with the analogous Equation 1.2.4 for synchrotron emission clarifies its physical interpretation: since electric fields and magnetic fields are interchangeable under the appropriate transformation of the reference frame, synchrotron can be treated as Compton scattering of the magnetic field's virtual photons. Synchrotron and inverse Compton processes "compete" with each other in cooling down high-energy electrons – despite the different emission energies (see the different energy scale in the two panels of Fig. 1.7, and also Fig. 1.9).
The energy of the up-scattered photon in the Thomson regime is on average

$$\nu = \frac{4}{3}\gamma_{\mathrm{L}}^2 \nu_0 \tag{1.2.6}$$

hence a 10 GeV electron (with a Lorentz factor $\gamma_{\mathrm{L}} = 2 \times 10^4$) would scatter a 3 eV (visible) photon up to 1.2 GeV. Looking at it from a different perspective, a high-energy electron has a very short mean free path since low-energy photons in the Galaxy are quite abundant (starting with the CMB).
In the limit of very high energies ($\gamma_{\mathrm{L}} \gg 1$) the cross section cannot be assumed constant, but needs to account for quantum relativistic corrections. The proper formulation of the cross section is given by the Klein-Nishina formula, and at very high energies it goes down with energy:

$$\sigma_{\mathrm{KN}}(x) = \frac{3}{8}\sigma_{\mathrm{T}}\frac{1}{x}\left[\ln 2x + \frac{1}{2}\right] \qquad (x \gg 1) \tag{1.2.7}$$

where x is the product of electron and photon energies, each in units of $m_{\mathrm{e}}c^2$. The net effect is that the cross section becomes smaller when the energy increases, so that IC becomes much less efficient at cooling down the electrons, with an energy loss proportional to their energy rather than their squared energy (see Equation 1.2.5).
An example of an IC emission spectrum can be seen in the right panel of Fig. 1.7 using both the CMB and a mid-infrared (MIR) thermal target radiation field at 500 K. Different radiation fields result in very different spectra, and their intensities can vary locally by several orders of magnitude (up to even $10^5\,\mathrm{eV/cm^3}$ in the inner parsec of the Galactic Centre, as will be discussed in Section 3.8).

Bremsstrahlung

Photons and magnetic fields are not the only possible sources of interaction for a free electron. The Galaxy is filled with ionised gas and dust. When an electron

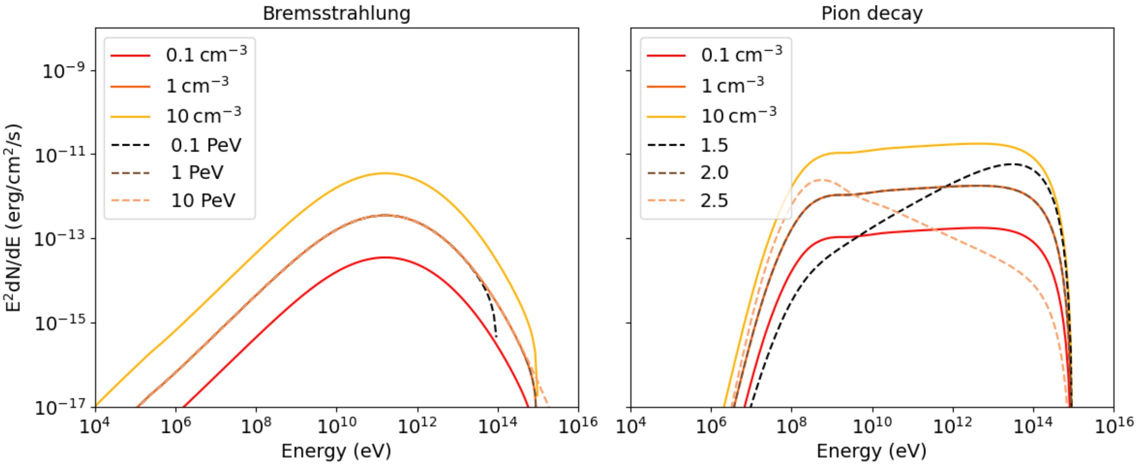

Figure 1.8: left panel: bremsstrahlung emission SED. The solid lines assume the same electron power-law as in Fig. 1.7, while varying the gas density. The dotted lines vary the electron cut-off energy as in the previous figure. Right panel: pion decay SED. The solid lines assume a proton spectral index of 2.0 for the three different gas densities. The dotted lines assume a proton density of 1 cm^{-3} with different proton spectral indices.

interacts with the Coulomb field of a nucleus, it gets deflected and consequently emits a photon. This radiation is known as "free-free" because the electron remains unbound from the atom, or it is also called bremsstrahlung, which means "braking radiation" in German.

Despite bremsstrahlung emission involving electrons of all energies, and in the case of a non-relativistic electron resulting in emission proportional to its velocity (i.e., the square root of its energy), the solution for the energy loss of a relativistic electron in an electromagnetic field is given by the Bethe-Heitler formula (1934) [39]:

$$\frac{\mathrm{d}E}{\mathrm{d}t} = -\frac{Z(Z+1/3)q^6 N}{16\pi^3 \epsilon_0^3 m_\mathrm{e}^2 c^4 \hbar} E_\mathrm{e} \left[\ln\left(\frac{183}{Z^{1/3}}\right)\right] \tag{1.2.8}$$

where the radiated energy is proportional to the photon energy E_e, other than the gas density N. Z is the charge of the nucleus.

Rarely is bremsstrahlung emission dominant in a source spectrum: it requires a high electron energy density and a high density of ionised material. However, in the first case, it is likely that electrons will cool through IC emission, while the second condition favours emission through pion decay if high-energy protons are present. Bremsstrahlung dominating would require both a low radiation field density and a low proton flux, conditions which are typically not met in the vicinity of most CR accelerators – with the notable exception of pulsars, which moreover are rather common – but for diffuse emission in the ISM the situation is different, especially at MeV energies (see, for instance, [187] for a discussion on the importance of bremsstrahlung in this case). The bremsstrahlung spectrum is plotted in Fig. 1.8 for different proton density values, and appears subdominant in a source spectrum in Fig. 1.9.

Pion decay

The three previous mechanisms are usually invoked for electrons, since the emission is proportional to the inverse square of the mass. However, relativistic protons can interact with the gas and create mesons through inelastic collisions:

$$\mathrm{p}+\mathrm{p}\rightarrow \mathrm{p}+\mathrm{p}+a_1\pi^0+a_2\pi^+ +a_2\pi^-$$

$$\mathrm{p}+\mathrm{p}\rightarrow \mathrm{p}+\mathrm{n}+a_1\pi^0+(a_2+1)\pi^+ +a_2\pi^-$$

where the amounts a_1 and a_2 of neutral and charged pions depend on the total energy of the collision in the center of momentum (CoM) frame. In this example pions, which are the lightest mesons, have been created – the reactions above account for the productions of heavier mesons like kaons later decaying into pions. As mentioned in the introduction, we cannot study a p+p reaction in the laboratory at energies higher than $\sim 15\,\mathrm{TeV}$. Therefore, at high energies, it is necessary to combine theoretical models and simulations to obtain cross sections and energy distributions of secondary particles [116].

The pions, in turn, decay into photons (see Equation 1.1.7) and leptons (Equation 1.1.8, with the appropriate antiparticles for π^-). Photons in the energy range of the pion decay, in particular the “pion bump” visible around 200 MeV when plotting $\mathrm{E}^2\mathrm{dN/dE}$, would be a clear indication of the hadronic nature of their origin if it were not for the fact that in the same energy range, leptonic emission from IC scattering is also efficient, and bremsstrahlung to a lesser extent (Fig. 1.9). The smoking gun would be the neutrinos from the decay of charged pions, but their detection presents a non-trivial challenge: the interaction cross-section is so low that it requires several years and enormous effective detection areas to build up enough statistics.

Since hadronic emission uses the gas as a target, any spatial correlation between gamma-ray emission and gas constitutes a clear evidence that the radiation is not (exclusively) of leptonic origin. However, considering the typical angular resolution of gamma-ray observatories, such a study can only be performed for very extended

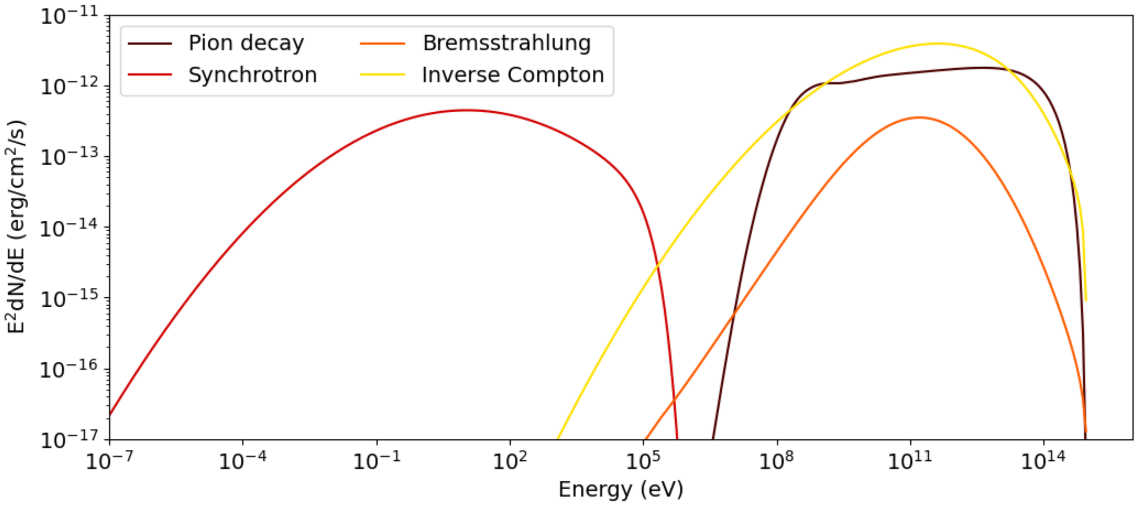

Figure 1.9: Example of a spectrum with hadronic and leptonic emissions. The proton density is 1 cm^{-3}, the B field density is 1 μG, the energy stored in the electrons amounts to 10^{47} ergs, and protons and electrons distributions extends to 1 PeV with spectral indices 2.0 and 2.3 respectively. The only low-energy radiation field considered is the CMB.

sources, i.e. Galactic sources. A rather famous example is the Galactic Centre, where gamma-ray emission closely traces the gas distribution [94].

If the hadronic nature of the emission is established, the photon spectrum gives away the proton spectrum, since on average the detected photon contains $\sim 10\%$ of the parent proton energy[10]. This is undoubtedly a powerful tool to constrain the maximum energy achievable by a local accelerator.

CR cooling

We have mentioned a few times how different mechanisms can "compete" for the energy emission from relativistic electrons. Assuming the presence of gas, radiation, and magnetic fields (both diffuse in the ISM and in specific conditions around a source), a non-trivial question arises: how much of the electron's energy is radiated and through which mechanism? To answer this question, one can define a cooling timescale, $t_{\rm cool} = E/(\mathrm{d}E/\mathrm{d}t)$, for each emission channel and determine which one dominates (i.e., has shorter timescales) in each energy band. From the formulas for $\mathrm{d}E/\mathrm{d}t$ in equations 1.2.4, 1.2.5, and 1.2.8, one finds that:

- $t_{\rm cool}^{\rm brems}$ is constant throughout the energy range;

---

[10] In hadronic models, it is usually assumed that pions are produced by the interaction of cosmic protons, even when there is no reason to ignore the CR mixed composition. This has consequences on the expected flux of both gamma rays and neutrinos, see [47].

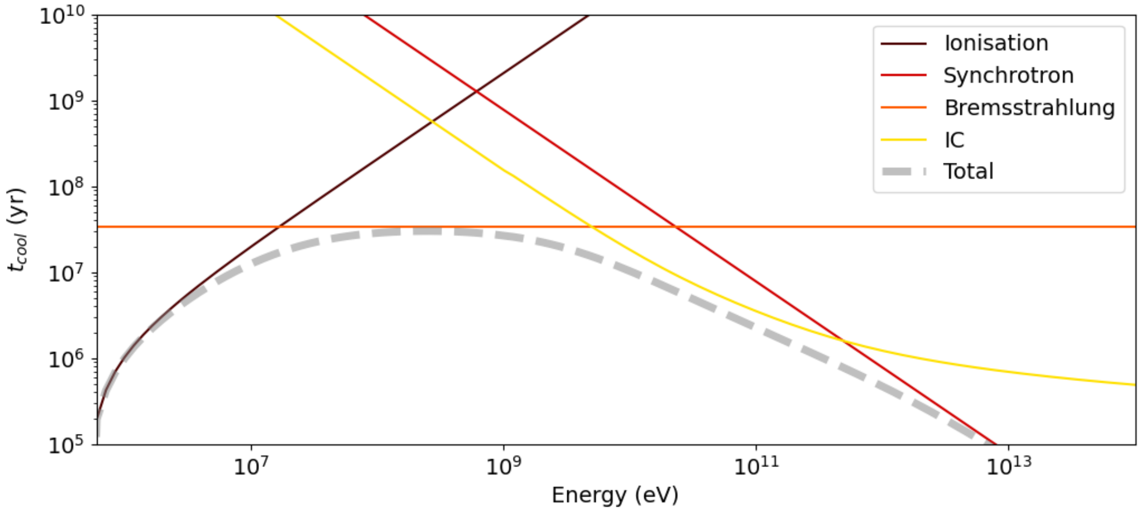

Figure 1.10: Cooling timescales for electrons traversing a region with hydrogen density $N_{\mathrm{H}} = 3\,\mathrm{cm}^{-3}$, a B field of 3 μG, and a NIR photon field with $U_{\mathrm{rad}} = 1\,\mathrm{eV/cm}^3$.

- $t^{\mathrm{syn}}_{\mathrm{cool}}$ decreases proportionally to energy;
- $t^{\mathrm{IC}}_{\mathrm{cool}}$ also decreases as $t^{\mathrm{syn}}_{\mathrm{cool}}$, but flattens in the Klein-Nishina regime;
- for completeness, the cooling processes of electrons at lower energies an be added to the list, which have not been addressed as they are not emission mechanisms: ionisation and excitation, which have a flat dE/dt profile (coming from the Bethe-Bloch formula), and therefore a linear $t^{\mathrm{ie}}_{\mathrm{cool}}$ with energy.

Keeping in mind that the cooling efficiency depends on the environmental conditions, in Fig. 1.10 a typical situation is presented where each mechanism dominates in a certain energy range – ionisation up to 10 MeV, bremsstrahlung up to 10 GeV, IC up to 1 TeV, and synchrotron after the electrons reach the Klein-Nishina regime.

Electromagnetic cascades

Each emission mechanism has a counterpart in absorption, and typically, the cross-section of the process is similar. For example, the emission of photons from pair annihilation has a cross-section similar to pair production with photon absorption. This means that if an electron interacts with a proton and emits a photon via bremsstrahlung, it is equally possible for that photon to interact with the radiation field of a nucleus and be absorbed, resulting in pair production – similar examples can be made for synchrotron and IC. Reversing this argument, if an electron-positron pair is created in matter, radiation, or a magnetic field, it is possible for these *secondary particles* to interact via bremsstrahlung, IC, or synchrotron radiation respectively before they can escape the field, re-emitting photons at lower energy than the original pair. The newly emitted photons may in turn be absorbed, and so on. This effect is known as cascading and becomes less efficient as the energy of the created particles decreases, ending when the photon energy is too low to create a new pair. In fact, it is a competition between the probability of interaction of both leptons and photons and their probability of escaping the region. See [38] for a detailed discussion.

In regions with weak fields, the probability of absorption before the particle escapes is low. However, there are astrophysical regions with extremely dense fields where self-absorption becomes highly probable. Examples include active galactic nuclei (AGNs) [22], pulsars inside supernova remnants [37], X-ray binaries [54] and in general in photon-rich regions hosting CR accelerators, like for instance the Galactic Centre. This will be discussed in Chapter 4.

2

THE GALACTIC CENTRE AT VERY-HIGH ENERGIES

Located at a distance of $8178 \pm 26\,\mathrm{pc}$ [89], so that a parsec corresponds to an angular distance of $\approx 25.2''$, the GC is a complex and varied environment with both thermal and non-thermal emission on multiple scales. At the very centre lies the supermassive black hole (SMBH) Sgr A*[1], with a mass of $(4.154 \pm 0.014) \times 10^6\,\mathrm{M}_\odot$ [89] which dominates the gravitational potential in the inner few parsecs. However, the inner $2.5°$ ($\simeq 360\,\mathrm{pc}$) are embedded in the so-called Central Molecular Zone (CMZ), a dusty cluster of Giant Molecular Clouds (GMCs) containing 30–$50 \times 10^6\,\mathrm{M}_\odot$ in gas [147] and showcasing 5–10% of the star formation of the entire Milky Way in less than 1% of its disk's volume [101]. A few open clusters with recent star forming episodes are known, including the Three Giants – the Quintuplet cluster, the Arches cluster, and the Nuclear Star Cluster (NSC) with Sgr A* lying at its centre. Also, a few massive HII regions are scattered in the CMZ (namely Sgr A, B, C, D and E), with densities of more than $10^4\,\mathrm{cm}^{-3}$ that exceed by far the typical values for Galactic clouds. While the average magnetic field strength in the ISM is not very high ($\approx 10\,\mu\mathrm{G}$), it can increase to the order of $\sim$ mG in the non-thermal radio filaments (NRFs) abundant in the region [74].

In Fig. 2.1 the CMZ region is depicted in gamma-ray ($E > 0.4\,\mathrm{TeV}$, H.E.S.S. [95], top), FIR ($250\,\mu\mathrm{m}$, Herschel SPIRE [145], middle) and radio ($23\,\mathrm{cm}$, MeerKAT [104], bottom panel). Indeed, the GC cannot be observed in the near IR/visible/UV band due to absorption by dust (details in Section 3.1), so the only windows for investigations are the radio to MIR and the (hard) X-ray to gamma-ray bands. The variety of non-thermal emitters in the CMZ region, both observed (Sgr A* and its accretion disk, massive star binaries, SNRs, ultra-compact star clusters, PWNe, hot magnetised NRFs) and expected (the peak of the Galactic dark matter distribution),

---

[1] To be precise, Sgr A* is the name of the radio source associated with the SMBH. Nowadays it has become its common name, since the identification is clear.

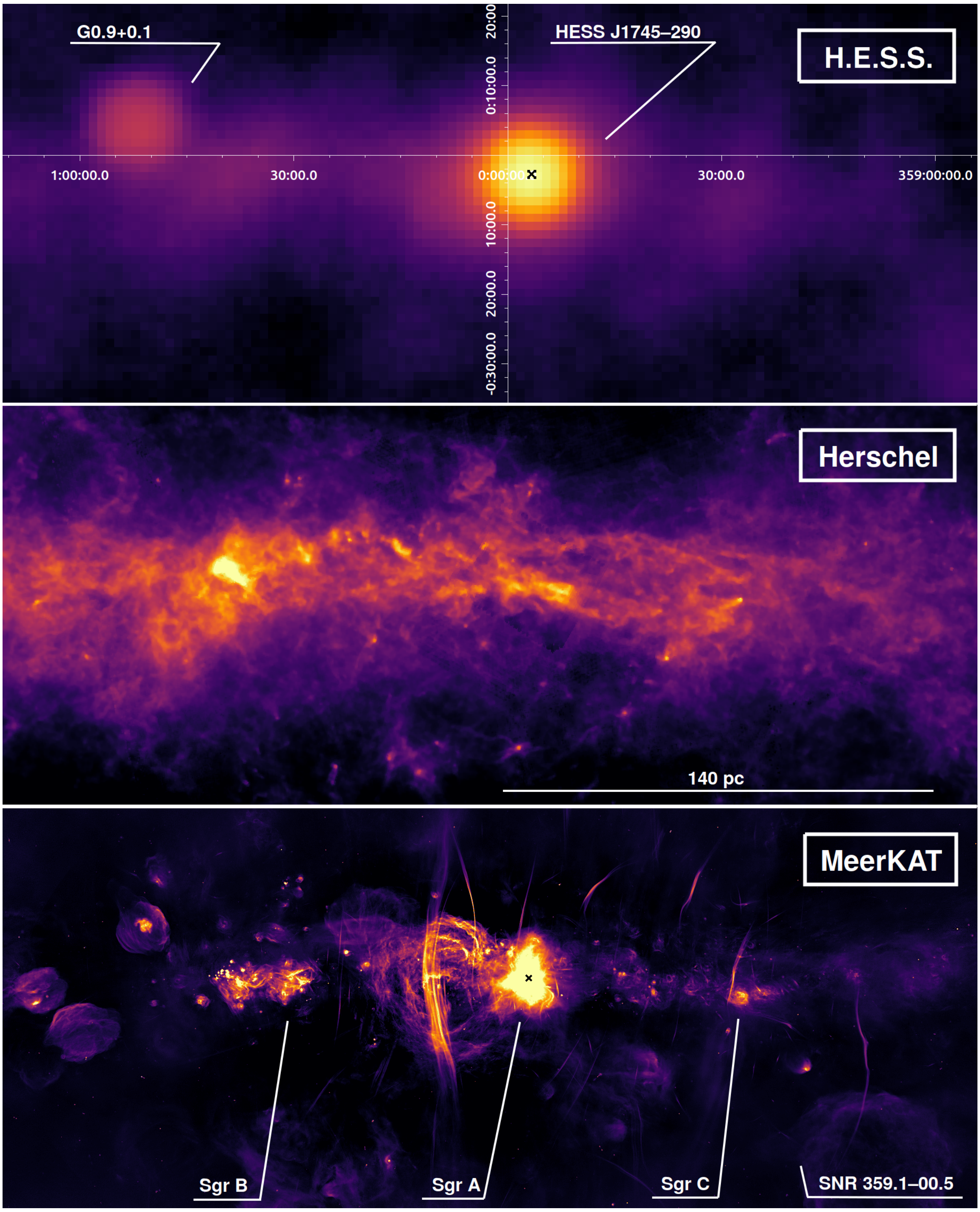

Figure 2.1: The CMZ in TeV, FIR, radio (references in text). These are the same maps used for the RGB image in Fig. 1. The H.E.S.S. map is a significance map, while the other two are flux maps. All maps share the same spatial scale indicated in the top panel grid, and are coloured in log-scale. The position of Sgr A* is marked with a black cross. The brightest two sources in the H.E.S.S. map – HESS J1745–290 and G0.9+0.1 – have been labelled. A few non-thermal features have been highlighted in the bottom panel.

makes it an exciting laboratory to improve our understanding of the physics at very-high energies and to test its limits.

Furthermore, in addition to its gravitational influence and its key role in the process of star formation and enrichment of the interstellar medium, the intense activity of the GC has clear repercussions on the energy budget of the entire Galaxy: there is little doubt that the Fermi Bubbles – large-scale structures observed at GeV energies by Fermi-LAT [188] and in X-ray by eROSITA [171] – originate from past and present high-energy CR acceleration in the GC, whether they are remnants of an AGN-like behaviour of Sgr A* or they are fuelled by the stellar winds of recently formed massive young stars.

Such a concentration of high-energy phenomena and the energies involved, coupled with its relatively short distance, make the entire region a privileged study case for gamma-ray astrophysics – and indeed, the results in both the GeV range with Fermi-LAT and the TeV range with H.E.S.S., MAGIC and VERITAS are exciting at both large and (relatively) small scales. Concerning the former, Fermi-LAT has revealed a gamma-ray excess in the GC peaking at 1–2 GeV, which has been invoked by some as proof of dark matter-induced emission – the debate is still ongoing, see for instance [150]. However, the core of this chapter will be the comparison between the central TeV source HESS J1745–290 and the TeV diffuse emission on the CMZ scale.

2.1 THE CENTRAL SOURCE HESS J1745–290

The first telescopes to detect the GC at ∼ TeV energies were CANGAROO-II, Whipple and H.E.S.S. (using only two working telescopes out of four) almost at the same time in 2003. They all saw a strong gamma-ray signal coming from the Sgr A region – however, Whipple observed the source with a large zenith angle and did not reach a 4 sigma significance. The measurements by CANGAROO-II [198] and H.E.S.S. [16] did not quite agree with each other: while the former reported a very soft power-law emission with spectral index $\alpha = 4.6 \pm 0.5$, the latter found $\alpha = 2.20 \pm 0.17$. This last trend was confirmed by the H.E.S.S. full array in 2006 [18] and then by MAGIC [25, 23] and VERITAS [30], much more in agreement on both the spectral index and the flux normalisation (see Fig. 2.2). Observations by CANGAROO-III in 2008 were finally in agreement with the other observatories, ending the debate. Since then, the bright central TeV source is commonly known as HESS J1745–290 – a point-like source included in the Sgr A region (see Fig. 2.3 to compare the sizes of the two regions).

Since the H.E.S.S. array is the only working TeV observatory located in the southern hemisphere, it provides the most sensitive view to date of the GC with enough statistics at higher energies and a low energy threshold, covering most of the desired spectral range. The spectral analysis [93] rejected a simple power-law scenario,

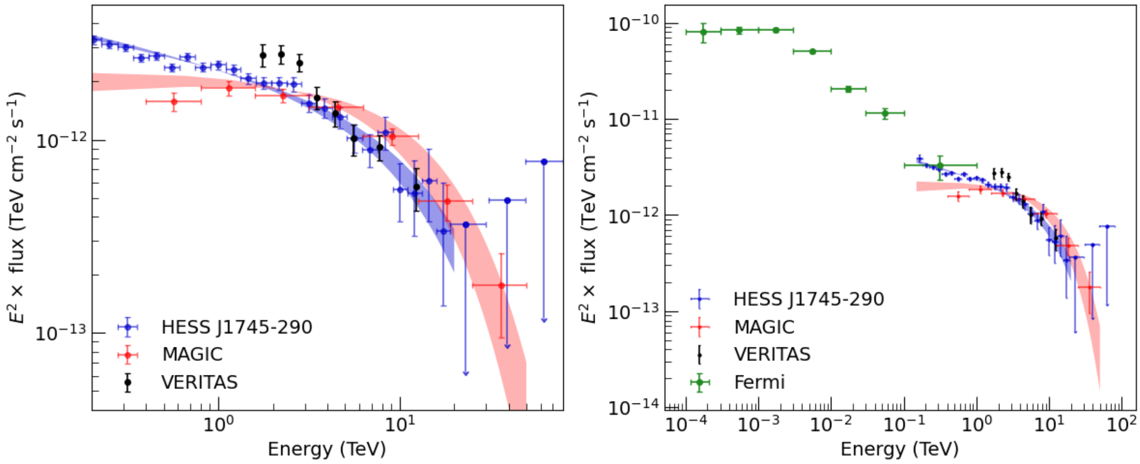

Figure 2.2: Left panel: SED of the central source HESS J1745–290 [93] in the IACTs' energy range. The fit parameters for the H.E.S.S. datapoints are given in text. Datapoints and fit results from MAGIC (taken from [139]) and VERITAS [31] are also shown. Right panel: same datapoints, but including the Fermi points in the 100 MeV–TeV range [6].

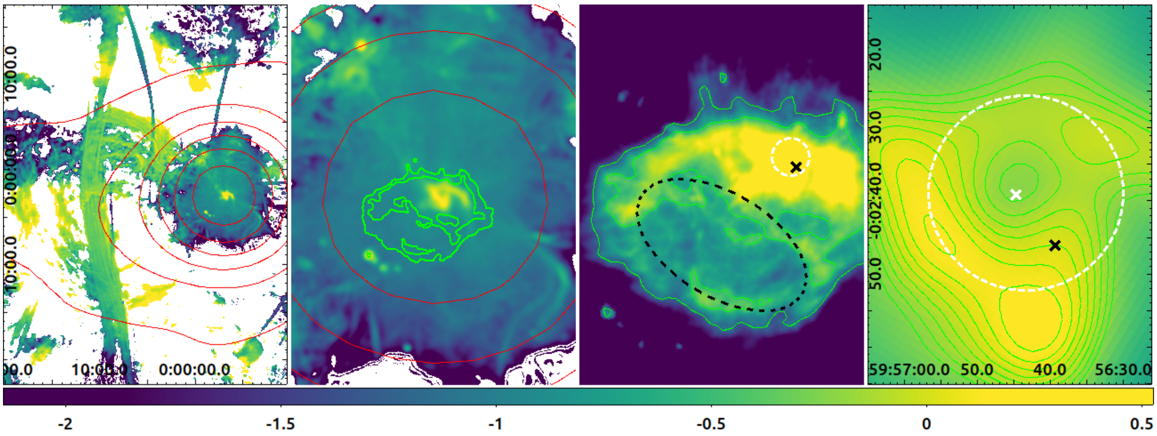

Figure 2.3: MeerKAT zoom-ins [104] from the CMZ scale to the inner few parsecs, colour-coded by the spectral index at 1 GHz except for the third panel where a flux map is shown. The colour bar refers to the spectral index. The H.E.S.S. contours [95] are overplotted in red. The green contours in the second panel show the MeerKAT flux in the Sgr A region, where the inner warm filaments (in yellow) are clearly distinguishable from their thermal emission surrounded by a (blue-green) synchrotron halo; the SNR Sgr A East lies in the lower left part and it is marked with the black dashes ellipse in the third panel. The centroid of HESS J1745–290 [11] is shown as a white dashed circle, while the position of Sgr A* is marked with a black cross. The white cross in the right panel corresponds to the position of the PWN G359.95–0.04 [203].

preferring an exponential cut-off:

$$\frac{\mathrm{d}N}{\mathrm{d}E} = \Phi_0 \left(\frac{E}{1\ \mathrm{TeV}}\right)^{-\alpha} \exp\left(-\frac{E}{E_\mathrm{c}}\right)$$

with a flux value at 1 TeV $\Phi_0 = (2.55 \pm 0.37) \times 10^{-12}\,\mathrm{TeV}^{-1}\,\mathrm{cm}^{-2}\,\mathrm{s}^{-1}$, a spectral index $\alpha = 2.14 \pm 0.10$, and a cut-off energy $E_\mathrm{c} = 10.7 \pm 2.0\,\mathrm{TeV}$. Quite in contrast to the other bands, the flux shows no sign of variability [19].

Since the angular resolution in other energy bands allows for a detailed study of astrophysical objects, the main puzzle regarding the GC lies in understanding the source of CR acceleration. In this regard, the limited angular resolution of gamma-ray astronomy (the FWHM of H.E.S.S. is approximately $5'$ at 1 TeV, corresponding to $\approx 12\,\mathrm{pc}$) makes the association with a specific putative accelerator quite challenging. Comparing the observed emission spectrum to the typical spectrum of a spatially compatible source (e.g., a PWN, a SNR, a YMSC, that could suggest a leptonic or hadronic origin and features such as an exponential cut-off in the observed energy range) could be of help. However, the gamma-ray emission model is strongly influenced by the specific characteristics of the surrounding region – like for instance the distribution, temperature, and density of the surrounding gas for hadronic sources, or the morphology and energetics of the magnetic fields for leptonic sources – therefore, such an approach is hardly decisive in a crowded environment like the GC.

The uncertainty of the source centroid position has been estimated by H.E.S.S. to be approximately 13″ [11]. It includes Sgr A*, the NSC, and the PWN G359.95–0.04 (see Fig. 2.3, fourth panel), but seems to exclude the SNR Sgr A East (same figure, third panel). Although their nature is completely different, they all could be TeV CR accelerators – hence assuming that the gamma-ray flux originates from a combination of these sources seems reasonable.

2.1.1 *Possible accelerators*

*Sgr A**

Although known since the 1970s, Sgr A* has been an ongoing subject of investigation as a radio source. It is the only Galactic object that has been studied with a resolution on the order of microarcseconds [69]. Its radio emission is believed to be due to synchrotron radiation in the strong local magnetic fields – and indeed, there is ample orbiting material. A relatively low-mass, cool accretion disk ($\sim 10^{-5}\,\mathrm{M}_\odot$) with a radius of 4×10^{-3} pc has been observed [149], with a temperature of 10^4 K. Additionally, there is a numerous group of massive stars known as the S-cluster [67], which project their stellar winds toward the black hole. Moreover, recently, new astrophysical objects have been observed in its immediate vicinity (all within a radius of 1″): the G-objects [84], compact gas structures with observational properties akin to massive stars that have a large part of their gas stripped by Sgr A*. Overall, Sgr A* generally remains in a quiescent state, but from time to time experiences brief flaring phases of synchrotron radiation showing an increase up to 2–3 orders of magnitude in the luminosity in infrared, radio, and X-rays (see, for example, [90]) – but, as mentioned, not in gamma rays.

Fermi-LAT has also observed a bright GeV source very close to Sgr A*, named 4FGL J1745.6–2859 (see the Fermi 4FGL catalogue, [6]), whose SED is shown in Fig. 2.2, right panel. It can be fitted using a broken power-law distribution with spectral indices of 2.00 ± 0.04 up to 3 GeV and 2.68 ± 0.05 beyond. Despite the good match between the Fermi and H.E.S.S. fluxes around 500 GeV, the spectral indices differ significantly (H.E.S.S. reports 2.10 ± 0.04), making a common nature of the emission in the two energy ranges unlikely. The hypothesis of lepto-hadronic emission has been studied, for example, in [57], where the GeV flux arises from hadronic interactions with the accretion disk protons as well as electron bremsstrahlung, while double-leptonic emission has been investigated in [140], assuming that the GeV flux originates from highly energetic electrons injected during past flares, while the TeV flux is due to IC emission from continuously accelerated electrons in quiescent phases. Both models work, taking into account the large intrinsic uncertainties – instead, fitting both H.E.S.S. and Fermi fluxes with hadronic emission would need two separate proton accelerators in very different energy ranges, each dominating the gamma-ray emission in either Fermi or H.E.S.S. range, with sub-dominant electron contributions despite the abundance of free electrons and the intensity of both IR and magnetic fields. This assumption seems rather unrealistic.

G359.95–0.04

Detected using Chandra observations of the GC in 2005, the PWN G359.95–0.04 [203] is 4 times brighter than Sgr A* in the 1–10 keV range ($\sim 10^{34}$ erg/s), lying at a distance of 0.3 pc (8.7″) from it. Despite having been associated with the SNR Sgr A East, its cometary tail points towards the center of the HB, in particular toward the strong NIR emitter IRS13 which is embdedded in an enhanced diffuse X-ray field [203]. The X-ray flux of G359.95–0.04 is not very high, but its spectrum is hard and likely due to synchrotron rather than thermal emission. This allows for an interpretation of the local TeV flux as IC emission powered by energetic electrons in the intense local IR field – indeed, this PWN has been considered a possible counterpart for HESS J1745–290 since its discovery and in particular since 2007 [105], also considering its position close to the very center of the H.E.S.S. centroid (Fig. 2.3). Its IR and above all its radio flux are very low. All these features can be elegantly explained with a ram-pressure-confined PWN model [203], that has the additional merit to motivate the elongation with a bow shock from the surroundings of Sgr A*, thus placing G359.95–0.04 at an actual short distance to it.

The Nuclear Star Cluster

Another potential VHE gamma-ray emitter lying at the very centre of the Galaxy is the Nuclear Star Cluster. Indeed, most galaxies host their own nuclear star cluster at their centres, but the GC is the only one that we can resolve on milliparsec scales ($\approx 0.03''$) thanks to its proximity. This resolution allows us to obtain unique information about the energetic processes of the central SMBH and the complex dynamics of feedback in galactic evolution. It also provides insights into the stellar dynamics in the presence of extreme gravitational fields.

Its effective radius is approximately $180''$ in K-band (about 7 parsecs), and it shows elongation along the Galactic plane, with an eccentricity of around 0.3 [72]. Numerous recent studies have set its total mass between $2 \times 10^7\,M_\odot$ and $4 \times 10^7\,M_\odot$ using both photometric and dynamical methods. As an example, we report the value $(2.5 \pm 0.4) \times 10^7\,M_\odot$ found in [178] and $(2.1 \pm 0.7) \times 10^7\,M_\odot$ found in [72], two papers that have been heavily used in the simulations of the 3D UV radiation field from the NSC in Section 3.4.

Its star formation history is known to be quite complex [179], with stellar populations of different metallicities co-existing (plus contamination from the stars of the NSD, a rotating disk that extends up to $\sim 120\,\mathrm{pc}$ [155]), and with about 1% of its mass formed in the last 100 Myr. In particular, the most recent burst dates back to 3–8 Myr ago, with a mass of stars above 8 solar masses ranging between 14 000 and $37\,000\,M_\odot$. These massive stars are contained in a sphere with Sgr A* at its centre and an effective radius of 0.5 pc [71], still linked to the NSC but with greater deviations from the ellipsoidal symmetry described above. The central concentration of massive stars is a strong argument in favour of in situ formation (as opposed to formation through continuous mergers of smaller star clusters), as their aggregation time is incompatible with an age of only a few Myr.

As mentioned in Section 1.1.3 YMSCs are potentially accelerators well beyond the TeV, so a compact one centred on Sgr A*, whose extension roughly matches that of the central source's centroid of H.E.S.S., cannot be ignored. However, whether it is at the base of the gamma-ray emission of HESS J1745–290 or not, the NSC is a fundamental entity for the study of this thesis: such a massive and compact cluster of young and massive stars develops a very intense UV radiation field, which, thanks also to the large amount of dust contained in the central parsecs, results in an IR radiation density exceeding $10^5\,\mathrm{eV/cm^3}$ (see Section 3.8). To model the IR radiation field, it is necessary to model the UV source (Section 3.4). In the rest of the thesis, the NSC is assumed to be the primary source of local UV photons.

2.2 The diffuse component

The field of view of IACTs – several degrees, though the peripheral region typically has poorer resolution – allows for a comprehensive investigation of a structure like the CMZ with a length scale below 3°.

H.E.S.S. first [17], and subsequently VERITAS [31] and MAGIC [139], produced a map of the entire region's gamma-ray emission (see for example Fig. 2.1, upper panel). By removing the brightest point sources (HESS J1745–290 and the composite SNR G0.9+0.1 labelled in said figure), the map of the so-called GC diffuse component shows a significant spatial correlation with the CMZ gas density (see the discussion in [94], where velocity-integrated maps of CS line emission have been used, and also see the first two panels of Fig. 2.1 for a visual correlation between gamma-ray and dust emission), demonstrating that such emission mainly has a hadronic origin (Section 1.2.2) and that somewhere proton acceleration must take place. Moreover, the total CR energy in the entire region estimated from the gamma-ray luminosity amounts to $\sim 10^{50}$ erg, which is comparable to the energy released by a single SNR thus bolstering the single accelerator scenario, while the lack of gamma-ray emission at $l > 1°$ – where the gas is still abundant – could put some constraint on the source age ($\sim 10^{4}$ yr according to H.E.S.S. estimates) and the CR transport timescale. The general aim for the investigation of the GC in gamma rays is thus twofold: to study both the acceleration region geometry (including its location) and the CR spectrum, which could be spatial-dependent.

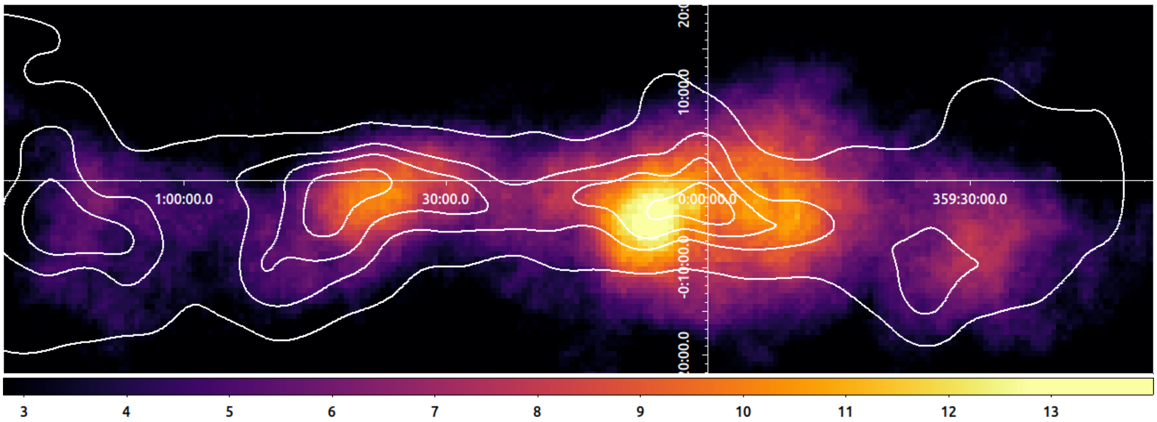

Figure 2.4: H.E.S.S. diffuse component [94] with ^{12}CO contour lines [196] overlaid, after subtracting HESS J1745–290 and G0.9+0.1. The bright additional source HESS J1746–285, coincident with the Fermi "Arc source", dominates the residual VHE emission in the region.

Regarding the first point, the GC allows us to study the accelerator's morphology in detail: from the gamma-ray brightness, we can infer the CR energy density w_{CR}, knowing both the density of molecular clouds and their location – both known given their proximity. The angular extension of the gamma-ray source allows us to resolve the radial profile of w_{CR}, providing information both on the accelerator's position and the timescale of acceleration and diffusion:

- In the case of a single burst-like event in the past, and in a diffusive environment, after enough time the CR distribution would become homogeneous across the region. In this case, the radial profile would be constant.
- In the case of a constant injection of CRs with a rate $Q_{\mathrm{CR}}(E)$, assuming a diffusive environment with a diffusion coefficient $D(E)$ and a diffusion radius r_{d}, particles are confined longer in the region and the expected profile (taken from [21]) is
$$w_{\mathrm{CR}}(E,r) = \frac{Q_{\mathrm{CR}}(E)}{4\pi D(E) r}\,\mathrm{erf}\left(\frac{r}{r_{\mathrm{d}}}\right) \propto 1/r \tag{2.2.1}$$
where the approximation holds assuming diffusion does not vary spatially and at lengthscales smaller than typical pp collision lengths.
- In the previous case, but with very fast ("ballistic") diffusion where particle deflection is negligible (wind-like advection), the expected profile is
$$w_{\mathrm{CR}}(E,r) = \frac{Q_{\mathrm{CR}}(E)}{4\pi r^2} \propto 1/r^2 \tag{2.2.2}$$

The radial profile for CRs above 10 TeV for H.E.S.S. [93] and MAGIC [139] is reported in Fig. 2.5 and shows that the single burst episode is disfavoured – the radial trend is monotonic with a peak within $\sim 15\,\mathrm{pc} \approx 6.3'$ from Sgr A*, which is why it is referred to as a "central accelerator". Furthermore, while the H.E.S.S. analysis favours a diffusive scenario with constant injection ($1/r^{\alpha}$ with $\alpha = 1.10 \pm 0.12$), the MAGIC data does not strongly favour a specific scenario ($\alpha = 1.2 \pm 0.3$).

H.E.S.S. initially extracted the spectrum of the diffuse component in the so-called "pacman region" – an annulus around the central source (0.15–0.45° ≈ 20–60 pc), excluding an opening angle of 66° [93]. This is the same spectrum shown in Fig. 2 (in red in the right panel). The claim by H.E.S.S. is that the spectrum (up to 40 TeV) can be fitted by a power-law with spectral index $\alpha = 2.32 \pm 0.12$, without any cut-off. Since the hadronic nature of the gamma-ray emission is clear, and because, as

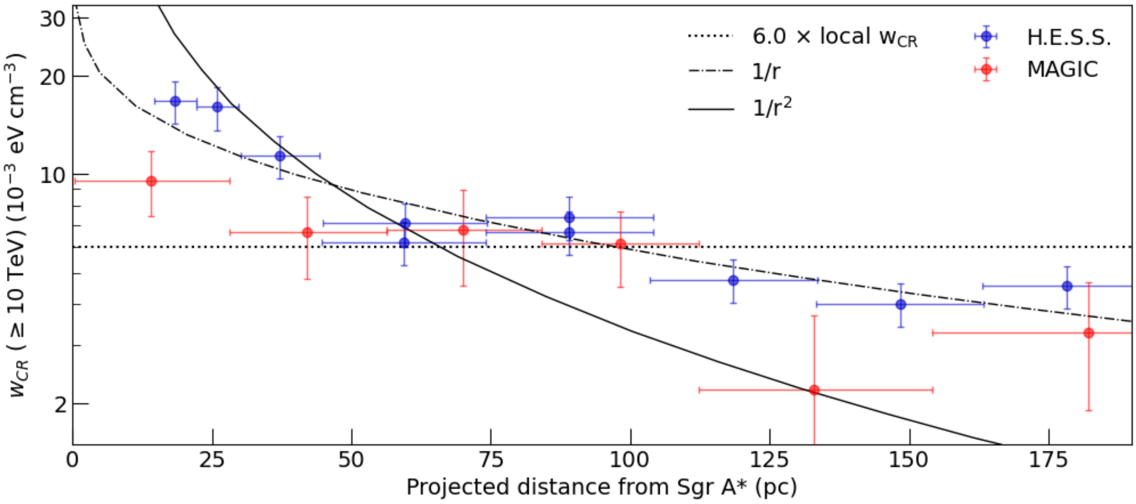

Figure 2.5: Radial profile of the CR energy density in the Galactic ridge according to H.E.S.S. [93] and MAGIC [139]. Uniform, $1/r$ and $1/r^2$ distributions are also plotted. Here "local" refers to our solar system.

mentioned in Section 1.2.2, the photon retains about 10% of the proton's energy [116], the linear spectral profile suggests a gamma-ray emission that extends up to at least 100 TeV, and thus the central accelerator is capable of accelerating nuclei to energies of 1 PeV – making it the first known "PeVatron" in our Galaxy. The observed spectral index itself constitutes an additional hint towards the presence of an accelerator in situ, since the expected gamma-ray profile from pp collisions follows approximately the same spectral index as the underlying proton population, which is around 2.7 at TeV energies in our solar system. If the emission was due to the "CR sea" pervading the Galaxy, the spectral index would be different – unless we assume that diffuse CR populations vary depending on the Galactic region, of which no proof has been found. But ultimately, there are not enough details for us to infer about the nature of the accelerator or the possible connection with the central source HESS J1745–290.

Later, H.E.S.S. [94] and MAGIC [139] extracted the spectrum in a much more extended area covering the entire Galactic ridge. The results are shown in Fig. 2.6. H.E.S.S. claims that the best fit is a single power-law with spectral index $\alpha = 2.28 \pm 0.21$. The figure also shows a fit of the H.E.S.S. data assuming an exponential cut-off at 1 PeV in the proton distribution. MAGIC's data, on the other hand, give a hard spectral index of 1.98 and an exponential cut-off at 17.4 TeV, in severe contrast with the possibility that the accelerator could reach such energies.

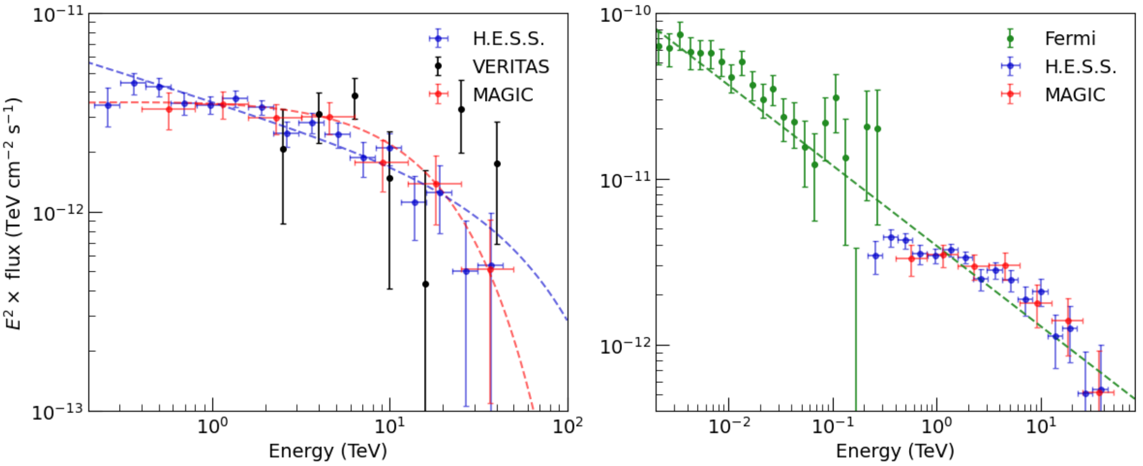

Figure 2.6: Left panel: TeV emission in the Galactic ridge with H.E.S.S. [94], MAGIC [139] and VERITAS [12]. The red dashed line is the MAGIC best-fit, while the blue-green dashed line is the expected gamma-ray profile in case of a spectral index of 2.28 and a proton cut-off at 1 PeV. Right panel: same as in left panel, but adding the Fermi SED (taken from [81]). The green dashed line is the best-fit they obtain using both Fermi and H.E.S.S. points, even though they use the early H.E.S.S. flux [17]. The parameters for all the fits shown are given in the text.

Unlike the CRs in the TeV range, the CR energetics at GeV in the GC are comparable to the values observed in our solar system. The spectrum of Fermi-LAT after subtracting the contributions from the point sources [81], extracted in the same regions as H.E.S.S., is shown in the right panel and it looks harder than the solar system's, which could explain why w_{CR} at GeV is comparable to our local values – but would then still raise the issue of the different spectral indices given the same total energy retained. Fermi and H.E.S.S. data can be fitted [81] with a single power-law with $\alpha \approx 2.49$. Even though this fit was calculated using old H.E.S.S. data [17], it still fits the data well. Whether the GeV and TeV emission are due to different accelerators or different mechanisms is still up to debate.

2.3 CENTRAL SOURCE AND DIFFUSE COMPONENT: A POSSIBLE CONNECTION

The central source HESS J1745–290 and the diffuse component have distinctly different spectra (see Fig. 2), since the central component has an exponential cut-off at around 10 TeV. The basic assumption is that the sources are unrelated, and as already discussed, the origin of the gamma-ray emission for HESS J1745–290 may be leptonic as opposed to the diffuse component. However, there are at least two observations that tend to empirically link the two sources:

- the radial distribution of w_{CR} suggests that the accelerator responsible for the diffuse emission is within a few arcminutes from Sgr A*
- their spectral indices up to a few TeV are very similar

making the hypothesis of the two sources sharing the same CR accelerator quite tempting. Clearly, the main obstacle to such a scenario lies in explaining the cut-off of the central source, or in other words, why the higher-energy emission present in the CMZ is instead suppressed at the centre. There are at least two possibilities: a) the cut-off is in the proton distribution, and b) the proton spectrum is the same throughout the region, and the cut-off is due to photon absorption.

The first point could be addressed by invoking a faster proton diffusion at higher energies, as discussed in Section 1.1.4 – such a scenario is extensively discussed in [57]. Another possible explanation is a "fading CR accelerator" [134], whose imprint in the proton spectrum is not constant over time but it has already passed the phase of injecting PeV protons into the CMZ and now is fading, injecting protons into the surrounding gas with the cut-off observed for HESS J1745–290.

The second scenario, initially hypothesised in [93] and [52], constitutes the core of this thesis and is described in detail in Chapter 4: photons with energy > 1 TeV interact with the infrared radiation field ($\lambda \gtrsim 1\,\mu$m) within a radius of a few parsecs from Sgr A*, resulting in the production of electron-positron pairs (see Section 4.1). Indeed, this region shows intense infrared activity emitted by the abundant interstellar dust it contains, powered by the strong UV radiation from the NSC. The interaction between gamma-ray radiation and IR radiation is strongly energy-dependent and produces a clear signature in the gamma-ray spectrum. However, the IR radiation field is highly anisotropic, and a detailed study of the absorption spectrum critically depends on the position of the gamma-ray source located within it. For this reason, such an investigation requires the development of a 3D model of the IR radiation field, which is discussed in Chapter 3.

On the other hand, knowing the IR radiation field allows us to study the position of the source within the field itself, in a way that it reproduces the expected absorption (that is, the observed spectrum for HESS J1745–290) assuming the same intrinsic gamma-ray spectrum of the diffuse component. The additional advantage of this approach is that the geometry of the source is resolved with the angular resolution of the field, which is a few arcseconds instead of the typical few arcminutes typical of IACTs.

3

3D IR EMISSIVITY MODEL IN THE INNER PARSECS OF THE GALACTIC CENTRE

As discussed in Chapter 2, the Galactic Centre contains a large amount of star-forming clouds, and the inner few parsecs host a few dusty structures like filaments and rings (see Section 3.2). However, the extinction towards the GC makes observations in the UV/visible bands impossible since it goes well above 30 magnitudes in the V band (centred around ~550 nm) [82]. The infrared band is heavily obscured up to a few microns [78], but it becomes relatively transparent above $15-20\mu$m thus allowing for the observations of structures orbiting around Sgr A*. Their 3D orbital parameters can be obtained by means of radio observations [213] and in the K-band [153]. This process requires a thorough modelling of both the dust emission (Section 3.1.1) and the 3D UV radiation field of the NSC (Section 3.4) in order to derive the energetics of UV photons absorbed by the dust, and subsequently re-emitted in MIR/FIR. As a result, we derive the mass of the dust and its temperature in the 3D space (Section 3.7), obtaining the 3D IR radiation field in the inner few parsecs (Section 3.8).

3.1 INTERSTELLAR DUST

The term “astrophysical dust” broadly refers to a variety of particles ranging in size from a few Ångströms to several microns, composed of chemically advanced elements[1] primarily synthesised in stars – mainly carbon and silicon. The cores of dust grains form either in the ejecta of supernovae, where the material is rather dense, or in the dense and relatively cold winds of giant stars like Asymptotic Giant Branch (AGB) stars, red supergiants, Wolf-Rayet stars and Luminous Blue Variables (LBVs). In both instances, shock or advection allows for a redistribution of the dust into the interstellar medium. Upon injection into the ISM, the grains are enriched with other common elements (hydrogen, oxygen, carbon, nitrogen) forming icy shells of simple molecules such as water, methane, ammonia, with basic organic compounds constituting a thin surface. However, these grains can also be destroyed, either through collisions or thermally, in the very environments where they are produced [181]. Consequently, modelling the rate of dust injection into the interstellar medium is far from straightforward.

The primary source of data on interstellar dust composition stems from infrared spectroscopy [63, 192]. Bands at 9.7 and 18 μm in the infrared spectrum dominate extinction (see for instance the model shown in Fig. 3.1) and are attributed to the vibrational modes of amorphous silicates. Hydrogenated Amorphous Carbon (HAC) dust is inferred by absorption bands at 3.4, 6.8, and 7.2 μm due to aliphatic CH groups. Moreover, Aromatic Infrared Bands are apparent at multiple wavelengths (e.g., 3.3, 6.2, 7.7, 8.6, 11.2, and 12.7 μm), alongside a strong interstellar extinction bump around 0.2 μm. Direct connections to their origins can be traced through isotopic signatures in stardust collected from meteorites, despite a severe selection effect that makes them not fully representative of the entire grain zoo.

Owing to its physical properties, astrophysical dust plays a pivotal role in various fields:

- In star formation. Dust assists in cooling gas clouds in several ways: by limiting ionising UV radiation, providing an additional cooling channel through infrared emission, and facilitating the formation of molecular hydrogen through the grains’ “adhesive” function [201]. All of this enables the clouds to achieve

---

[1] Since chemical elements are synthesised from hydrogen through stellar activity, and helium is the only other pre-existing common element, astrophysics classifies elements heavier than helium as “metals”, much to the chagrin of chemists.

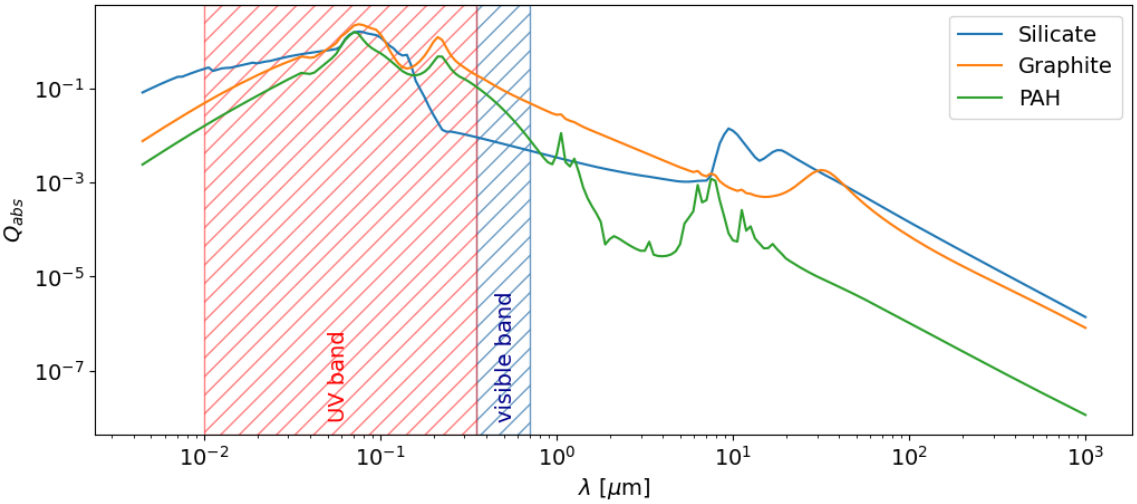

Figure 3.1: Example of dust absorption efficiency $Q_{\rm abs}$ for different chemical species, according to the model by Weingartner and Draine adopting $R_V = 3.1$ [205]. The dust grains shown here have a single size of 0.01 µm (silicate and graphite grains) and 0.003 µm (PAH grains).

the critical density needed to trigger gravitational collapse. At the same time, UV photons can extract photoelectrons from the dust, which heat the gas – thus working in the opposite direction. For more detailed information on the role of dust in star formation, a recommended preliminary read is [118].

- In the synthesis of complex organic molecules observed in molecular clouds and protoplanetary disks, thanks to its aforementioned aggregating and adhesive functions ([144]).
- In cosmology. Dust serves as an energy regulator in galaxies – including the earliest galaxies. Additionally, dust interacts with the Cosmic Microwave Background (CMB) and can distort our understanding of the primordial universe.

By far the most important property of a dust grain is its ability to absorb short-wavelength radiation (UV and visible) and re-emit it as black body emission in the IR. This absorption effect is strongly frequency-dependent, such that UV and blue radiation are absorbed more than red radiation, leading to a reddening in the emission obscured by the dust. Fig. 3.1 outlines the absorption efficiency spectrum of individual dust grains according to the Weingartner and Draine model with $R_V = 3.1$ [205]. It is evident that the grains tend to absorb most strongly around 0.1 µm, but could also be important for soft X-ray absorption and scattering (Section 3.1.2).

3.1.1 *Dust emission*

Let us assume a spherical dust grain of size a and temperature T_d absorbing photons with an absorption efficiency Q_abs (a dimensionless parameter measuring the ratio of the optical cross section to the geometric cross section), re-emitting photons in thermal equilibrium. Its luminosity density[2] at a frequency ν_em can be expressed as a *modified Planck function*:

$$L_\nu^\mathrm{sg}(a,\nu_\mathrm{em}) = 4\pi\cdot\pi a^2\cdot Q_\mathrm{abs}(a,\nu_\mathrm{em})\cdot BB_\nu(\nu_\mathrm{em},T_\mathrm{d}(a)). \tag{3.1.1}$$

Note that T_d in general depends on the grain size. The superscript "sg" stands for single grain, and $BB_\nu(\nu_\mathrm{em},T_\mathrm{d})$ is the Planck formula for the brightness of a black body at temperature T_d:

$$BB_\nu(\nu,T) = \frac{2h\nu^3}{c^2}\frac{1}{e^{h\nu/k_\mathrm{B}T}-1} \tag{3.1.2}$$

Note that in the case $Q_\mathrm{abs} = 1$ at all frequencies this formula, when integrated over frequency, yields the familiar expression for the total luminosity of a black body:

$$L_\mathrm{em} = 4\pi a^2\sigma_\mathrm{SB}T_\mathrm{d}^4 \tag{3.1.3}$$

where σ_SB is the Stefan-Boltzmann constant.

$Q_\mathrm{abs}(a,\nu_\mathrm{em})$ has a dependence on the frequency that, in case of wavelengths $c/\nu_\mathrm{em} \gg a$, can be roughly made explicit in the form

$$Q_\mathrm{abs}(a,\nu_\mathrm{em}) = \left(\frac{a}{a_\mathrm{ref}}\right)\cdot Q_\mathrm{abs,ref}\cdot\left(\frac{\nu_\mathrm{em}}{\nu_\mathrm{em,ref}}\right)^\beta. \tag{3.1.4}$$

It may in principle also depend on the grain temperature, but this is usually disregarded in most dust absorption models.

By defining an *absorption cross section per mass of dust* $k_\mathrm{abs}(a,\nu_\mathrm{em})$ for a given grain mass $M_\mathrm{d}(a)$ as

$$k_\mathrm{abs}(a,\nu_\mathrm{em}) = \pi a^2\cdot\frac{Q_\mathrm{abs}(a,\nu_\mathrm{em})}{M_\mathrm{d}(a)} \tag{3.1.5}$$

---

[2] Luminosity per unit frequency, sometimes also called spectral luminosity or even specific luminosity. For brevity, in this thesis we will use "luminosity", adopting a subscript ν in the formalism when it is a spectral density. The same goes for brightness and flux.

the dependence of the luminosity density on the dust mass becomes explicit:

$$L_\nu^{\mathrm{sg}}(a,\nu_{\mathrm{em}}) = 4\pi \cdot k_{\mathrm{abs}}(a,\nu_{\mathrm{em}}) \cdot M_{\mathrm{d}}^{\mathrm{sg}}(a) \cdot BB_\nu(\nu_{\mathrm{em}}, T_{\mathrm{d}}(a)). \tag{3.1.6}$$

The grain brightness, necessary to compare the modelled emission with observations, can be obtained assuming such emission to be isotropic. The common relation between brightness B_ν, flux S_ν and luminosity L_ν is as usual

$$B_\nu = \frac{S_\nu}{\Delta\Omega} = \frac{L_\nu}{4\pi d^2} \cdot \frac{d^2}{A} = \frac{L_\nu}{4\pi A} \tag{3.1.7}$$

where $\Delta\Omega$ is the subtended solid angle, d is the distance to the observer and A is the emission area presented towards the observer (e.g. πR^2 for a spherical grain or radius R).

In the most general case, the dust is composed of a mixture of different grain species i with their own size distributions, so that the number of grains per unit size can be written as

$$n^{(i)}(a) = \frac{\mathrm{d}N^{(i)}}{\mathrm{d}a} \tag{3.1.8}$$

which have yet to be normalised to be probability density functions. The size-averaged total brightness emitted by such a mixture would then be the sum of the brightness of each species $B_\nu^{(i)}$, integrated over the relative size distribution, and re-normalised:

$$B_\nu(\nu_{\mathrm{em}}) = \frac{\sum_i \int B_\nu^{(i)}(a,\nu_{\mathrm{em}}) n^{(i)}(a)\,\mathrm{d}a}{\sum_i \int n^{(i)}(a)\,\mathrm{d}a}. \tag{3.1.9}$$

Grains in thermal equilibrium with the radiation field

Under the simplistic assumption that the temperature of the dust grains does not depend on a (in other words, if a constant T_{d} for any grain in the mixture can be defined), then the properties of the black body emission become independent of the grain size. It is then very practical to integrate all the size-dependent quantities over the size distribution first. From Equation 3.1.6 it follows that, in order to calculate the total (size-integrated) dust mass M_{d}, one can define a mass-averaged mass absorption coefficient $\langle k_{\mathrm{abs}}(\nu_{\mathrm{em}})\rangle$:

$$\langle k_{\mathrm{abs}}(\nu_{\mathrm{em}})\rangle = \frac{\sum_i \rho^{(i)} \int k_{\mathrm{abs}}(a,\nu_{\mathrm{em}}) a^3 n^{(i)}(a)\,\mathrm{d}a}{\sum_i \rho^{(i)} \int a^3 n^{(i)}(a)\,\mathrm{d}a}. \tag{3.1.10}$$

$\rho^{(i)}$ is the mass density of the species i. This formulation allows for a simpler calculation of the emitted luminosity density and introduces a linear dependence on the total mass. This then leads to a compact expression of Equation 3.1.6 valid for the entire mixture:

$$L_\nu^{\mathrm{mix}}(\nu_{\mathrm{em}}, T_{\mathrm{d}}) = 4\pi \cdot \langle k_{\mathrm{abs}}(\nu_{\mathrm{em}})\rangle \cdot M_{\mathrm{d}} \cdot BB_\nu(\nu_{\mathrm{em}}, T_{\mathrm{d}}) \tag{3.1.11}$$

which describes the luminosity density as a simple function of the mass M_{d} and the temperature T_{d} of a dust mixture in thermal equilibrium, irrespective of the differences between the mixture components. Despite being handy at times[3], this approximation is not good on a general level since different chemical species have different grain size distributions, with T_{d} being strongly dependent on a.

Grains not in thermal equilibrium with the radiation field

Let us now take the general case where the grain temperature varies as a function of the grain size, assuming a mixture of different dust components. Since a unique dust temperature cannot be defined anymore, the luminosity density must be formally written as a function of dust mass, composition, and the total UV and visible radiation absorbed by the grains. An average $k_{\mathrm{abs}}(\nu_{\mathrm{em}})$ value cannot be defined as it was done in Equation 3.1.10, therefore there is no simple relation between the emitted luminosity density at frequency ν_{em} and the absorbed illumination at frequency ν_{abs}, since the grain re-processes the energy of the absorbed photons. Finding an analytical solution involves imposing energy conservation between absorption and emission, both integrated over the entire frequency spectrum. In other words, for a given position $\vec{r}$, it can be imposed:

$$L_{\mathrm{abs}}^{\mathrm{sg},(i)}(a, \vec{r}) = L_{\mathrm{em}}^{\mathrm{sg},(i)}(a, \vec{r}). \tag{3.1.12}$$

The integrated luminosity (both absorbed and emitted, since they are equal) becomes then

$$L^{\mathrm{sg}}(\vec{r}) = \sum_i \int L^{\mathrm{sg},(i)}(a, \vec{r})\, n(a)\, \mathrm{d}a. \tag{3.1.13}$$

---

[3] Not only when the dust is in thermal equilibrium with the radiation field, but also when modelling the emission deep in the Rayleigh-Jeans (RJ) regime where $L \propto T$ rather than T^4.

Now the two terms of Equation 3.1.12 must be evaluated. $L_{\rm abs}^{{\rm sg},(i)}(a,\vec{r})$ is a function of the radiation field density $u_{{\rm rad},\nu}$ absorbed by the grain:

$$L_{\rm abs}^{{\rm sg},(i)}(a,\vec{r}) = \int \pi a^2 Q_{\rm abs}^{(i)}(a,\nu) u_{{\rm rad},\nu}(\nu,\vec{r}) c \, {\rm d}\nu. \tag{3.1.14}$$

This last equation clarifies two points: first, defining a mass absorption coefficient as was done in Equation 3.1.5, which allowed for a compact luminosity formula (Equation 3.1.11), is not viable anymore since the integration of $Q_{\rm abs}^{(i)}(a,\nu)$ over the frequency range prevents it and forces a separate calculation of the absorbed luminosity for each value of a. Second, the luminosity dependence on the (3D) position is inherited from the spatial distribution of the UV radiation field.

Equation 3.1.14 could be solved analytically by imposing Equation 3.1.4 to make the dependence on the frequency explicit, obtaining

$$L_{\rm abs}^{{\rm sg},(i)}(a,\vec{r}) = C_1 a^3 \int u_{{\rm rad},\nu}(\nu,\vec{r}) \nu^\beta \, {\rm d}\nu \qquad C_1 = \pi c \left(\frac{Q_{\rm abs,ref}^{(i)}}{a_{\rm ref} \nu_{\rm ref}^\beta} \right). \tag{3.1.15}$$

However, since Equation 3.1.4 is an approximation and dust models provide tabulated values for $Q_{\rm abs}$ anyway, solving it numerically is definitely more precise.

On the other hand, from Equation 3.1.1 the emitted luminosity is simply

$$L_{\rm em}^{{\rm sg},(i)}(a,\vec{r}) = \int 4\pi^2 a^2 Q_{\rm abs}^{(i)}(a,\nu) BB_\nu(\nu, T_{\rm d}^{(i)}(a,\vec{r})) \, {\rm d}\nu. \tag{3.1.16}$$

Having analytical forms for both the absorbed (Equation 3.1.14) and the emitted total luminosity (Equation 3.1.16) allows for a solution of Equation 3.1.12 for each grain species and for each position with respect to the UV source. It basically comes down to a simple root-finding problem:

$$\int f(\nu, T_{\rm d}) \, {\rm d}\nu - D = 0 \tag{3.1.17}$$

and its solution yields the temperature $T_{\rm d}^{(i)}(a,\vec{r})$ of the dust grain. Again, the spatial dependence of the temperature reflects the position of the grain with respect to the radiation field.

To calculate the flux of a single grain, one can use the relation in Equation 3.1.7, the emission area being πa^2, obtaining:

$$S_\nu^{\mathrm{sg},(i)}(a, \nu_{\mathrm{em}}, \vec{r}) = \frac{\pi a^2}{d^2} Q_{\mathrm{abs}}^{(i)}(a, \nu_{\mathrm{em}}) BB_\nu(\nu_{\mathrm{em}}, T_{\mathrm{d}}^{(i)}(a, \vec{r})) \tag{3.1.18}$$

where the flux inherited its dependence on the position directly from the temperature of the dust grain. It is now possible to calculate the normalised flux density of the i-th species $S_\nu^{\mathrm{sg},(i)}(\nu_{\mathrm{em}}, \vec{r})$, by knowing the size distribution $n^{(i)}(a)$ (defined in Equation 3.1.8):

$$S_\nu^{\mathrm{sg},(i)}(\nu_{\mathrm{em}}, \vec{r}) = \int S_\nu^{\mathrm{sg},(i)}(a, \nu_{\mathrm{em}}, \vec{r}) n^{(i)}(a)\, \mathrm{d}a \tag{3.1.19}$$

and the total flux density for the mixture is finally

$$S_\nu^{\mathrm{sg}}(\nu_{\mathrm{em}}, \vec{r}) = \sum_i S_\nu^{\mathrm{sg},(i)}(\nu_{\mathrm{em}}, \vec{r}). \tag{3.1.20}$$

Lastly, this can be converted into the total dust brightness coming from a region of area A subtending a solid angle $\Delta\Omega = d^2/A$:

$$B_\nu^{\mathrm{sg}}(\nu_{\mathrm{em}}, \vec{r}) = \frac{\pi}{A} \sum_i \int B_\nu^{\mathrm{sg},(i)}(a, \nu_{\mathrm{em}}, \vec{r}) a^2 n^{(i)}(a)\, \mathrm{d}a. \tag{3.1.21}$$

3.1.2 *Line of sight extinction and scattering*

The generic term “light extinction” refers to the dimming of radiation due to absorption or scattering by the material in the line of sight (LoS). It is now well-established that interstellar dust is responsible for obscuring vast regions in the UV and visible bands, with strong emission in the MIR and FIR. However, the existence of interstellar dust and its role was postulated as far back as the early 1900s to explain the observed low stellar luminosity. It gained empirical support in the 1930s when Robert Julius Trumpler correlated the reddening and dimming of stellar clusters with their distance [195].

The characterisation of the wavelength-dependent extinction of a source – the amount of absorbing and scattering dust along the line of sight – is a fundamental requirement for understanding the source’s *intrinsic* (that is, un-obscured) luminosity. Moreover, the extinction spectrum provides additional information on the composition and size distribution of the grains [63]. Producing a synthetic extinction curve involves modelling both the grain distribution and composition while keeping into account observational constraints given by dust polarisation spectrum, extinction profile and astrochemistry in the ISM, infrared emission spectral features in galaxies, and more. Additional information may come from laboratory astrophysics, and even from the growing field of astrobiology.

Typically, to measure the extinction spectrum of a region, it is essential to know the intrinsic luminosity of a local source across the desired spectrum (for instance, by observing objects of known luminosity like red clump stars [152]). Another option is to apply a known extinction curve assumed to be valid in the region of interest [173]. Additionally, the extinction spectrum can be measured through hydrogen emission lines [78], which are numerous, well-known, and offer better uncertainties compared to stellar emission models. Obviously, this extinction curve must be paired with a calibration with respect to the intrinsic flux, which depends on the region distance. This often poses a challenge, except for regions at a known distance such as the Galactic Centre, which is therefore a privileged target when attempting to derive "universal" extinction laws.

The dust in the line of sight attenuates the flux F^0_λ from a source by a factor $e^{-\tau_\lambda}$, the optical depth τ_λ being

$$\tau_\lambda = N_\mathrm{d} \sigma Q_\mathrm{ext}(\lambda) \tag{3.1.22}$$

N_d being the number of grains per unit area, $\sigma = \pi a^2$ the wavelength-dependent geometrical cross section of the grain of radius a and $Q_\mathrm{ext}(\lambda) = Q_\mathrm{abs}(\lambda) + Q_\mathrm{sca}(\lambda)$ the dust extinction coefficient accounting for both absorption and scattering effects of the dust grains. However, the extinction coefficient A_λ is measured in magnitudes, and since the relation between a flux F and a magnitude m is the *Pogson's equation*[4] $F_1/F_2 = -2.512\, e^{-(m_1-m_2)}$, one gets

$$A_\lambda = 2.5 \log_{10}\left(\frac{F^0_\lambda}{F_\lambda}\right) \tag{3.1.23}$$

where the superscript 0 indicates the intrinsic flux. From Equation 3.1.22 one also obtains the relation between the extinction and the particle nature of the dust:

$$A_\lambda = -2.5 \log_{10} e^{-\tau_\lambda} = 1.086\tau_\lambda = 1.086 N_\mathrm{d} \sigma_\lambda Q_\mathrm{ext}(\lambda). \tag{3.1.24}$$

---

[4] Mainly due to historical reasons, today we still use the old logarithmic scale based on magnitude 5 being 100 times brighter than magnitude 6, so that a single magnitude corresponds to an increase of a factor of $\sqrt[5]{100} \simeq 2.512$.

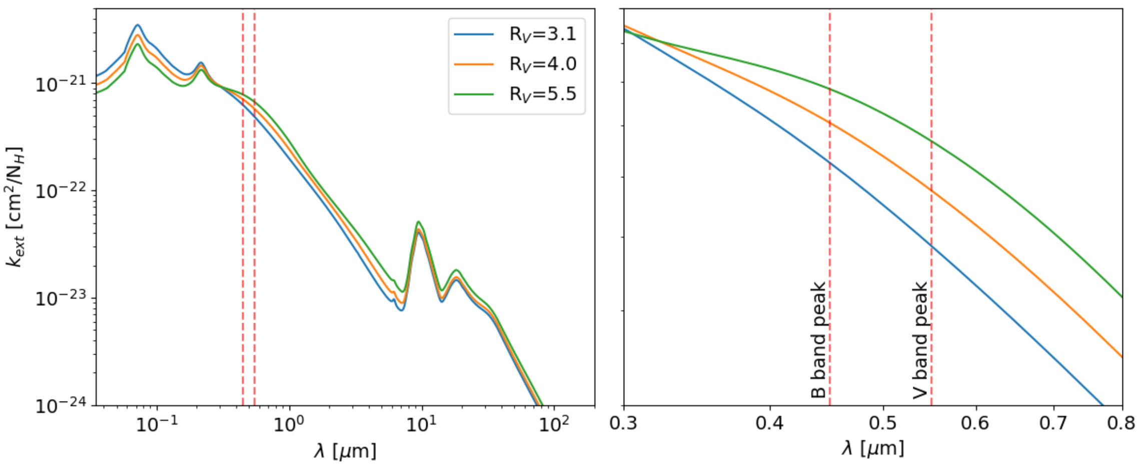

Figure 3.2: Extinction cross sections per hydrogen atom for the Weingartner and Draine dust models with $R_V = 3.1, 4.0$ and 5.5 [205]. A close-up in the visible range is shown, including the band where R_V is defined. The normalisation is discussed in the text.

Note that an extinction cross section per unit mass $k_{\rm ext}(\lambda)$ can be defined in a similar way as in Equation 3.1.5. The equation above then becomes

$$A_\lambda = 1.086 N_{\rm d} \sigma_\lambda Q_{\rm abs}(\lambda) = 1.086 N_{\rm d} M_{\rm d} k_{\rm ext}(\lambda) = 1.086 M_{\rm d}^{\rm tot} k_{\rm ext}(\lambda) \qquad (3.1.25)$$

correlating the LoS extinction with the dust column density.

The slope of the extinction curve in the visible band is commonly described by the parameter $R_{\rm V}$ [51], defined as

$$R_{\rm V} = \frac{A_{\rm V}}{A_{\rm B} - A_{\rm V}} \qquad (3.1.26)$$

where $A_{\rm V}$ and $A_{\rm B}$ are the extinctions in the V and B bands respectively, centred around 550 and 445 nm. Bearing in mind that absorption varies as a function of grain size [63], for grains much larger than $\lambda_{\rm vis}$ one finds $A_B \approx A_{\rm V}$ and hence $R_{\rm V} \to \infty$. In other words, $R_{\rm V}$ – which is an astrophysical observable – is correlated with the average size of the dust grains. For our Galaxy, the commonly observed value in diffuse clouds is $R_{\rm V} = 3.1$ [51], but values between 2 and 5.5 have been observed in different regions. Since denser clouds yield higher average $R_{\rm V}$ values, one possible explanation is that higher values of $R_{\rm V}$ indicate a more efficient accretion onto the dust grains.

Numerous extinction curves can be found in the literature, starting from the cornerstone Mathis et al. graphite-silicate model [141], and with the subsequent introduction of PAHs as small ($< 10^3$C) carbonaceous particles [205], refractory organic materials and ices. In general the dust models can be very different to each other depending on the particles' chemistry but also on their density and size distribution. Most of them fall roughly in three groups: the silicate-graphite-PAH model (e.g. [205]), the silicate core-carbonaceous mantle model (e.g. [130]) and the so-called composite model of silicate and carbonaceous particles (e.g. Zubko et al. [215], where they present composite dust models with and without icy and organic mantles, or with HAC replacing graphite in the cores).

In this thesis I make ample use of the synthetic curves introduced in [205] and revised in [64], produced for R_V values of 3.1, 4.0 e 5.5. In these models, dust grains are made of a mixture of graphite, silicates and both neutral and ionised PAHs. The extinction cross section per hydrogen atom k_{ext} for the three models is shown in Fig. 3.2. It can be converted into a dust column density assuming a dust-to-gas ratio (which for the Milky Way is around 100, but is subject to large variations [194]). In their model, they adopt the normalisation $A_{\mathrm{V}}/N_{\mathrm{H}} = 5.8 \times 10^{-22}\,\mathrm{cm}^2$ according to ISM observations in the solar neighbourhood. Since the scaling with N_{H} varies with metallicity and thus position, its application to different targets needs an appropriate re-normalisation, as will be shown in Section 3.2.3.

Concerning this last point, it should be kept in mind that applying an extinction law to regions with their own extinction normalisation can be tricky, because dust can scatter photons from different lines of sight into the LoS of the observed region, and the extinction normalisation through known intrinsic spectra cannot take this effect into account. This is one of the main differences between *extinction* and *attenuation*, and it can be neglected only at wavelengths long enough so that scattering is negligible[5]. In that regime attenuation, extinction, and absorption tend to converge – unless in that LoS there are un-extincted sources. A review on this topic can be found in [175].

---

[5] Scattering is more efficient when the radiation has a wavelength comparable to the grain size, hence up to a maximum of $\sim 10\,\mu\mathrm{m}$. Conversely, it can greatly affect UV and soft X-ray photons.

3.2 Gas and dust in the inner parsecs

The distribution of gas and dust within a few parsecs of Sgr A* has a complex morphology, featuring clumpy streamers, rings, and disks with non-axisymmetric motions [87]. Their distribution is of particular interest since the Galactic Centre is the only galactic nucleus close enough to study the dynamics of the surrounding gas. Their dynamics and shape are influenced by the gravitational potential of the central black hole [193], but also by the radiation pressure from the central cluster [79] and advection due to strong stellar winds. Last but not least, the pivotal role of local magnetic fields has emerged in recent years [106]. The origin of these gaseous macro-structures is unclear, but they could have formed from the tidal disruption of molecular clouds or from the accretion and infall of more distant structures [101]. Validating an evolutionary model for them is thus an extremely challenging task, inevitably linked to dynamics on a much larger scale (CMZ-like), and much of the difficulty arises from uncertainties in their relative positions in three dimensions along the line of sight [101].

3.2.1 *Observed gas structures*

Sgr A* is roughly at the centre of a cavity with a radius of 1-2 pc, known as the Central Cavity (CC), previously associated with a filamentous HII region called Sgr A West (see also Fig. 2.3, third and fourth panels), and most likely carved out by the activity of the NSC. Over the years, this cavity has been observed in detail in all its complexity (e.g., with VLA [127], SOFIA [125], ALMA [197], etc.). Most of the ionised gas in the CC is present in two filaments known as the Northern Arm (NA) and the Horizontal Branch (HB), which make up the so-called mini-spiral with tens of solar masses of ionised gas ($\approx 10^4$ K, [149]) and warm dust ($\approx 10^2$ K, [125]) and roughly ten times the amount in neutral atomic gas, more difficult to observe [75]. Their nature is debated: the gas could be spiralling towards Sgr A* [111] and be responsible for the moderate accretion onto it [149]. Alternatively, the generally accepted model is the so-called tidally stretched cloud (TSC) model [213], in which the structures are elliptical with Sgr A* at one of their foci, although with very different orbital parameters – the discussion of which is reported at the end of this section.

Outside the cavity lies a thick rotating torus of molecular gas, referred to in the

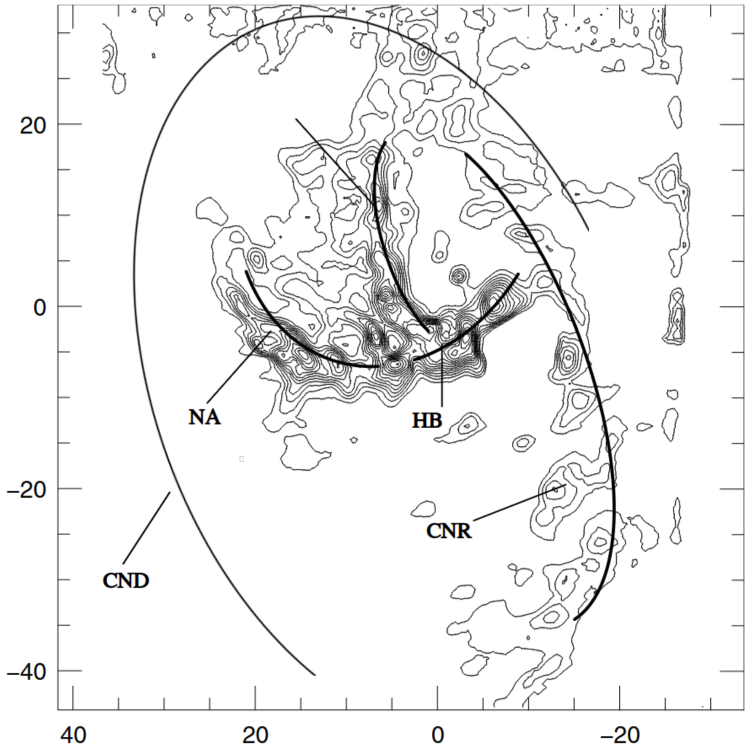

Figure 3.3: Map of the cloudlets in the Central Cavity. The contour lines trace the [NeII] emission with the TEXES spectrograph [123]. The axis values represent the offset from Sgr A* in equatorial coordinates. The structures described in text have been labelled and the curved lines are taken from [213]. Figure adapted from [111].

literature as both the Circum-Nuclear Disk (CND) and Circum-Nuclear Ring (CNR)[6]. In this thesis, the term "CND" is used to describe the structure that extends up to about ten parsecs away, and "CNR" to indicate its inner edge, ≈ 0.5 pc thick, bordering the CC and highly photo-ionised. Its mass in molecular gas amounts to $\sim 2{\times}10^5\,M_\odot$, with a prominent temperature gradient ranging from ∼ 300 K to ∼ 100 K in the peripheral parts [75]. The dust temperature decreases radially from 50-60 K to 15-20 K. The nature of this structure is unclear: on one hand, the most common interpretation is that it is an accretion disk around Sgr A* [75], but its asymmetry and low-density clumpiness – with molecular cores having densities on the order of $10^5\,\mathrm{cm}^{-3}$, well below the Roche limit[7] of $\sim 10^7\,\mathrm{cm}^{-3}$ – suggest a transient nature (see discussion in [87]). Whether or not accretion onto the SMBH occurs, the turbulent

---

[6] In the literature, the southwest part of the CNR is sometimes considered a separate filament, the Western Arc (WA), as it is denser, slightly closer to the centre than the rest of the ring, and whose inclination shows a small offset of about 5° with respect to the CND.

[7] The density needed by an orbiting object to sustain itself without being pulled apart by tides.

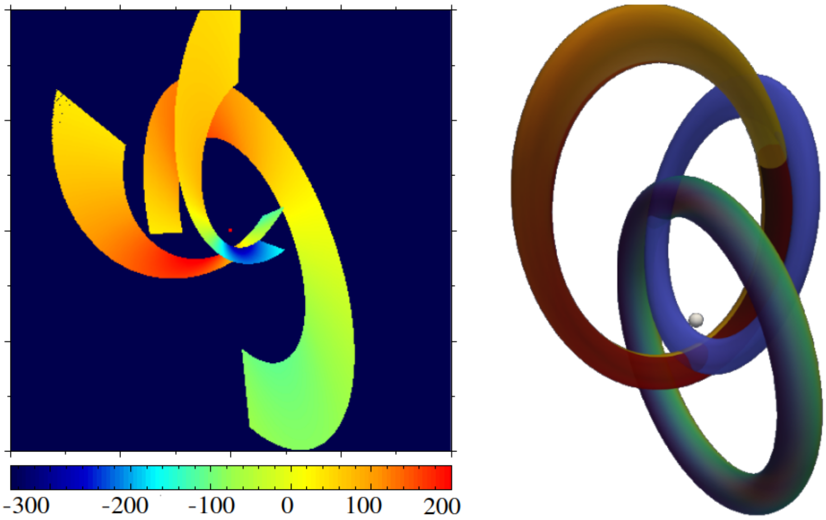

Figure 3.4: Left panel: radial velocities in km/s, smoothed and fitted into Keplerian orbits. The axes are the same as Fig. 3.3 and the red dot marks the position of Sgr A*. The figure is taken from [213]. Right panel: 3D spatial reconstruction of the same orbits. The NA is in blue, the CNR is in green, and the HB is in red (see text). Sgr A* is marked with a white dot.

nature of the CND allows gas to be transported towards the inner regions of the disk. The presence of molecular gas in the cavity – under theoretically prohibitive conditions for its survival given the UV and X-ray radiation fields, gravitational field, CR density, and stellar wind – could be a good indicator that some of the external material manages to fall inward. Molecular line emission within the cavity has indeed been observed [148], but it is not conclusive: it could come from embedded proto-stellar environments, therefore suggesting stellar formation activity within a parsec from Sgr A*.

3D mass distribution and orbital parameters

By combining VLA radio observations at 1.3 cm (H66α recombination line) and 3.6 cm (H92α recombination line) at different epochs, Zhao et al. [213] derived the proper motions of 71 ionised cloudlets in the CC and CNR. Additionally, the 3.6 cm observation allowed them to determine the radial velocities. By combining radial velocity and proper motions, they verified that the ionised gas in that region moves on three Keplerian orbits around Sgr A*. Both NA and HB have highly accentuated eccentricities (see Table 3.1), while the CNR is practically circular. The orbiting material has a counterclockwise motion as seen from Earth (inclination angles $i > 90°$), with orbital periods on the order of $10^4 – 10^5$ years. A few arcseconds

Parameter	Unit	NA	HB	CNR
Semi-major axis a	pc	1.01 ± 0.45	1.44 ± 0.70	1.14 ± 0.06
Period T	kyr	45	76	54
Eccentricity e	–	0.83 ± 0.10	0.82 ± 0.05	0.20 ± 0.15
Inclination i	deg	139 ± 10	122 ± 5	117 ± 3

Table 3.1: A few orbital parameters of the three streamers, according to [213]. The complete set is reported in their Table 5. The semi-major axis has been adjusted for the Galactic Centre distance value in [89].

south of Sgr A*, the NA and HB are very close in 3D space (henceforth synonymous with "de-projected space") and could collide. The left panel of Fig. 3.4 shows the radial velocities obtained in this way, smoothed and fitted onto Keplerian orbits. The red dot indicates the position of Sgr A*. The figure is taken from [213], and the axes are the same as in Fig. 3.3. The right panel shows the 3D depiction of the same orbits, with Sgr A* indicated by a white dot. The "collision region" between the NA (blue orbit) and the HB (red orbit) to the south is more markedly visible, as is the interaction to the north between the NA and the CNR (green orbit). Especially in the latter region, such collision could cause a deviation from the Keplerian orbits. A similar study has been approached by Nitschai et al. [153], using observations in K-band (1.934 µm – 2.460 µm) with KMOS [180] and adopting a Bayesian analysis. Besides their different modelling of the HB, which they divide into the Eastern Arm and the Bar, their results are overall compatible with the previous study, except for a slightly more elliptical and less inclined NA orbit. Throughout this thesis the orbital parametrisation by [213] is adopted.

3.2.2 *IR maps used*

To model the 3D infrared radiation field due to dust emission, three types of information are required:

- The dust mass M_d in each of its chemical components;
- The emission temperature T_d;
- The dust distribution in 3D space.

On this last point, the aforementioned orbital models by Zhao et al. [213] are very helpful because, assuming that dust correlates with gas, they allow for an axisymmetric treatment of the mass distribution, where the only further step involves de-projecting the column density (the total mass in the line of sight) onto the dimension perpendicular to the orbital plane (this step is covered in Section 3.7). As for the fundamental quantities of the first two points, the standard procedure involves deriving M_d and T_d from the observed emission, for example according to Equation 3.1.6 (here expressed as brightness through Equation 3.1.7):

$$B_\nu(a,\nu_\mathrm{em}) = \frac{k_\mathrm{abs}(a,\nu_\mathrm{em}) \cdot M_\mathrm{d}(a) \cdot BB_\nu(\nu_\mathrm{em}, T_\mathrm{d}(a))}{A} \tag{3.2.1}$$

Here A indicates the area of the emission region. The objective is to reconstruct the mass distribution and the emission temperature of the dust, and then to de-project the mass onto 3D volumes[8]. A single brightness map provides a spectral point for each pixel – in other words, for each LoS – sampling the entire region. The emission area A should then be understood as the area subtended by a single pixel.

For the choice of maps to use, several factors must be considered:

- The temperature of the dust within a radius of $4-5\,\mathrm{pc}$ from Sgr A* ranges from $25-30\,\mathrm{K}$ in the far-CND to about $150-200\,\mathrm{K}$ in the mini-spiral. This translates into a range of thermal emission peaks[9] respectively between 115 µm and 20 µm. Since the emission peak must be sampled by spectral points both at longer wavelengths (RJ regime) and shorter wavelengths (Wien regime), the chosen maps should cover at least the band between 20 and 120 µm.
- The minimum number of maps to use depends on two factors: how dense the wavelength range sampling needs to be, and how many different emission sources need to be handled simultaneously. Indeed, as previously mentioned, the structures in the CC contain both colder neutral gas and hotter ionised gas. Therefore, in the best-case scenario, one would expect that at least two populations of dust – corresponding to ionised and neutral gas – emit along the same line of sight. Consequently, the formula above becomes

$$B_\nu(a,\nu_\mathrm{em}) = \sum_i \frac{k_\mathrm{abs}(a,\nu_\mathrm{em}) \cdot M_\mathrm{d}^{(i)}(a) \cdot BB_\nu(\nu_\mathrm{em}, T_\mathrm{d}^{(i)}(a))}{A} \tag{3.2.2}$$

---

[8] Since the maps image the surface brightness (total brightness in the line of sight), what one obtains is a column density rather than a mass. Nevertheless, throughout the thesis, the terms "mass" and "brightness" will also be used in relation to projected quantities until the term becomes ambiguous, i.e., when performing the actual de-projection onto 3D volumes.

[9] Although the emission does not follow the Planck formula but the modified Planck formula (Section 3.1.1), the position of the peak does not change – unless the emission is dominated by the emission peaks of silicates (∼ 20 µm) or graphite (∼ 40 µm).

where the emission spectrum is the sum of multiple components (two for the simple warm-cold dust model). As there are two variables per component (mass and emission temperature), two dust populations introduce 4 variables and consequently require at least 4 spectral points[10]. A greater number of spectral points enhances the reliability of the fit and reduces the degeneracy of the result.

- The angular resolution of the maps is not strictly a fundamental parameter, as long as the entire region ($\sim 10\,\mathrm{pc} \simeq 250''$ in diameter) is not sampled by an excessive number of pixels. Furthermore, the IR radiation field is developed in view of a spatial gamma-ray analysis – which typically deals with resolutions of several arcminutes. Obtaining spatial gamma-ray information with a resolution of a few arcseconds would already be a notable achievement, virtually impossible for the vast majority of gamma-ray sources.
- The last constraint is set by the extinction due to dust in the line of sight. The greater the extinction the lower the reliability of the information collected, and as seen in Section 3.1 IR extinction increases rapidly as the wavelength decreases. Moreover, at wavelengths of a few microns, extinction and attenuation do not coincide because scattering becomes more relevant, and accounting for obscuration becomes more difficult. For this reason, choosing maps at wavelengths lower than 20 µm is not necessarily a good idea.

Combining these factors and the available GC maps, choosing SOFIA/FORCAST [103] maps at 19.7, 25.3, and 37.1 µm, and Herschel PACS [166] at 70, 100, and 160 µm seems a reasonable choice.

The Stratospheric Observatory For Infrared Astronomy (SOFIA [191]) is a joint American-German mission that operates a telescope mounted on a Boeing 747 SP, allowing observations across the MIR to FIR bands while minimising atmospheric contamination. The telescope employed is a 2.5 m diameter Cassegrain reflector featuring a parabolic primary mirror and a hyperbolic secondary mirror with a Nasmyth focal plane. To investigate a broad range (1 – 250 µm), SOFIA uses various instruments capable of imaging: the Faint Object infraRed CAmera for the SOFIA Telescope (FORCAST, various bands in the 5 – 40 µm range), the First Light Infrared Test CAMera (FLITECAM, 1 – 5 µm), and the High-resolution Airborne Wideband

---

[10] The number of independent observations, i.e., spectral points at different wavelengths, corresponds to the degrees of freedom (DoF) and therefore to the maximum number of parameters that can be obtained from a fit.

	l_{pix}	FWHM	σ_{B_ν}	λ_{ref} [μm]	width [μm]	FoV
19.7 μm	0.768″	2.5″	10%	19.712	5.706	3.4′ × 3.2′
25.3 μm	0.768″	2.1″	10%	25.248	1.807	3.4′ × 3.2′
37.1 μm	0.768″	3.4″	10%	37.144	3.284	3.4′ × 3.2′
70 μm	1.6″	5.45″ × 5.77″	5%	70.0	60 – 85	1.75′ × 3.5′
100 μm	1.6″	6.65″ × 6.87″	5%	100.0	85 – 125	1.75′ × 3.5′
160 μm	3.2″	10.50″ × 12.02″	5%	160.0	125 – 210	1.75′ × 3.5′

Table 3.2: Parameters for SOFIA FORCAST (first three rows) and Herschel PACS (last three rows) observations, from [103] and [166] respectively. Besides the first column, from left to right are: pixel size (or map sampling), PSF FWHM, brightness uncertainty, reference wavelength, bandwidth (band FWHM for FORCAST), field of view.

Camera-plus (HAWC+, 50 – 200 μm), along with the Focal Plane Imager Plus (FPI+) in the optical regime. Additionally, several spectrometers and spectrographs are available: the Field-Imaging Far-Infrared Line-Spectrometer (FIFI-LS, two channels in the 50 – 200 μm range), the Echelon-Cross-Echelle Spectrograph (EXES, 4 – 28 μm), and the German REceiver for Astronomy at Terahertz frequencies (GREAT, in submillimetre). Among these instruments, FORCAST [103] is a wide-field dual-channel camera that has been operational between 5 and 40 μm since 2010. It can function in imaging mode, in which case it has a field of view of 3.4′ × 3.2′, featuring 256x256 square silicon pixels each measuring 0.768″ on a side, and can operate at frame rates up to 500 Hz. It also serves as a spectrometer through the use of grisms and long-slits/short-slits (for low and high resolution, respectively). On one hand, it complements the wavelength range of Herschel; on the other, it overlaps with Spitzer's range but offers significantly better angular resolution despite having a comparable field of view. FORCAST has observed the GC in July 2019 [99].

The Herschel Space Observatory [164] is a space-based telescope with a Cassegrain mount that observes in the FIR/submm range between 55 and 670 μm. Orbiting at the second Lagrange point (L2), it was launched in 2009 in a partnership between ESA and NASA, and collected data for about 4 years before exhausting its reserves of liquid helium for cooling. Its primary mirror measures 3.5 m in diameter, and the payload houses two main instruments for broad-band photometric imaging: the Photodetector Array Camera and Spectrometer (PACS, peaking at 70, 100, and 160 μm) and the Spectral and Photometric Imaging REceiver (SPIRE, peaking at 250, 350, and 500 μm). Additionally, the Heterodyne Instrument for the Far Infrared (HIFI) provides high-resolution spectroscopy. PACS [166] employs various arrays of Ge:Ga and silicon to perform integral field spectroscopy and dual-channel imaging

	19.7 µm	25.3 µm	37.1 µm	70 µm	100 µm	160 µm
Measured flux [Jy]	1450	2620	4220	21900	14200	8180
ISO SWS flux [Jy]	1500	2600	4000	20000	15500	9000

Table 3.3: Flux calibration with respect to the ISO spectra (see text). The uncertainties for the FORCAST, PACS and ISO flux are assumed to be 10%, 5% and 15% respectively.

photometry. Its field of view is approximately 1.75′×3.5′, with an angular resolution of 1.6″ (at 70 and 100 µm) and 3.2″ (at 160 µm). Herschel has observed the GC between 2011 and 2012 [86], scanning the entire Galactic Plane with both PACS and SPIRE in the Herschel infrared GALactic plane survey (Hi-GAL) project.

Background calibration

The six selected maps must be calibrated before use. Prior to obtaining the final maps (displayed in Fig. 3.7), there is an initial sanity check plus two main corrections to consider:

- the flux photometric comparison to a known spectrum of the region;
- the background calibration of each map;
- the flux correction according to the expected LoS extinction.

As a sanity check, the total flux can be compared with the spectra provided by the Infrared Space Observatory (ISO) [120], which uses two single-aperture spectrometers in different bands: the Short Wavelength Spectrometer (SWS) [62] up to 45 µm and the Long Wavelength Spectrometer (LWS) [189] from 45 to 200 µm, both at high (R∼10000) and low (R∼200) resolution. The aperture of the SWS varies with the band: it is a 14″ × 27″ rectangle below 27 µm and 20″ × 33″ above. The LWS, on the other hand, has a circular aperture with a beam size of about 80″. Therefore, the fluxes to be compared to the ISO references must be convolved to the PSF of the SWS [182] and computed for the apertures corresponding to the chosen wavelengths. The results are reported in Table 3.3. Considering a 10% error on the FORCAST flux [102] and 5% for PACS [151], the flux appears to be in excellent agreement with the ISO spectrometers assuming a 15% uncertainty [112].

The FORCAST and PACS maps are already calibrated in real-time using a chopper, which, however, is not devoid of systematic uncertainties, especially when observing extended regions [102, 151]. Moreover, especially at longer wavelengths, the observations are contaminated by background and foreground Galactic emission.

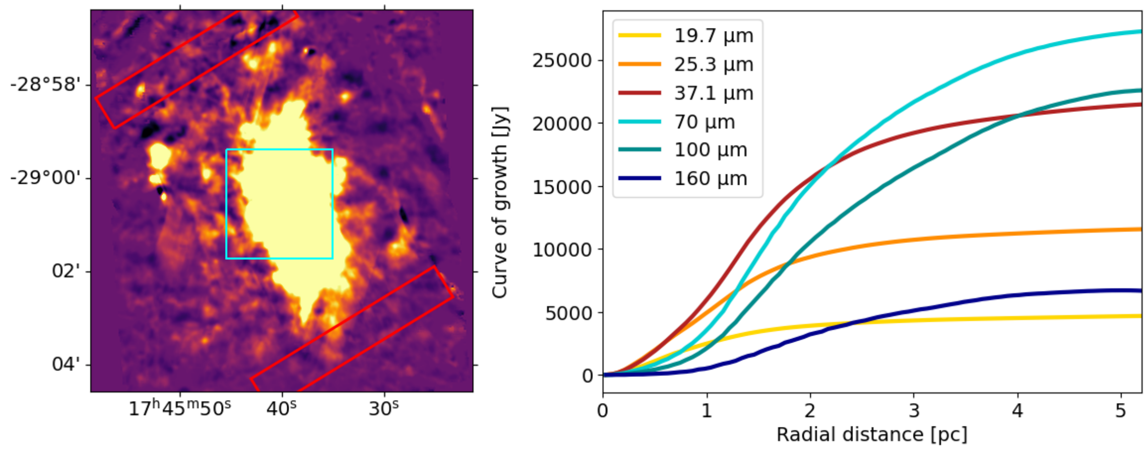

Figure 3.5: Left panel: Herschel 70 µm map. The colour scale (from −0.5 to 0.5 Jy/arcsec^2) has been chosen to highlight the brightness fluctuations. The two red rectangles mark the regions where the background has been evaluated (see text). The azure square corresponds to the inner 6 parsecs mapped in Fig. 3.7. Right panel: curve of growth of the maps after the background subtraction. The radial coordinate is the 3D distance to Sgr A* obtained by de-projecting the observed structures onto the CND orbital plane.

Consequently, it is necessary to assess the background of the region of interest to subtract it – and then verify that such correction is appropriate. It is crucial that the region where the background is evaluated (Infrared Background Region or IRBR) does not include local emission but is close enough to be affected by the same systematics. In the left panel of Fig. 3.5, the IRBRs are highlighted by two red rectangles within a rather expansive area ($7' \times 7'$, while the azure square outlines the inner 6 pc region of actual use displayed in Fig. 3.7). The simplest way to evaluate the background is to calculate the average emission in the IRBR and subtract it – however, this method does not account for a possible gradient in the background itself. To address this, two IRBRs are chosen on opposite sides, the average brightness is calculated in each sub-region, and background values are interpolated across the entire map. Since a variation with Galactic latitude is expected (although probably on larger scales than the ~ 10 pc considered), the IRBRs were taken orthogonal to the GP and divided into strips at different latitude values. In this way, the background becomes a grid of values aligned along the Galactic reference frame. The background corrections (in Jy/arcsec^2) for the position of Sgr A* are reported in order to provide an order of magnitude: $(1.5 \pm 1.8) \times 10^{-3}$ at 19.7 µm, $(1.1 \pm 1.1) \times 10^{-2}$ at 25.3 µm, $(4.5 \pm 2.0) \times 10^{-2}$ at 37.1 µm, $(7.8 \pm 4.3) \times 10^{-2}$ at 70 µm, $(8.2 \pm 3.3) \times 10^{-2}$ at 100 µm, $(8.1 \pm 3.0) \times 10^{-2}$ at 160 µm. No significant variations have been observed with Galactic latitude (at least on scales of a few arcminutes).

To verify that the background subtraction is appropriate, one can calculate the enclosed flux in concentric rings centred on Sgr A* (the so-called curve of growth or CoG). Ideally, after background subtraction, the large-scale emission should become negligible, and consequently the CoG should tend to flatten – if there is no flattening, either there is residual emission even at those scales, or the background has been underestimated. An overestimated background would manifest as a CoG with a negative slope. To derive the flux in the concentric rings, the maps were first de-projected onto the orbital plane of the CND, which is where the structures are expected to be located on a sufficiently large scale. The concentric rings thus obtained are actually ellipses on the original 2D maps. The right panel of Fig. 3.5 shows the CoG for all the maps: at a distance of about 5-6 pc, the background appears sufficiently flat.

3.2.3 *Local dust obscuration*

Since the GC is at the centre of the MW disk and the Sun is located in a rather peripheral region, the amount of dust along the line of sight – and consequently the extinction – is extremely high: it well exceeds 30 magnitudes in the visible range [82] and is also a limiting factor in the NIR [78, 177]. However, the unique situation of the GC also offers a significant opportunity. First, it lies a known distance, which facilitates the absolute calibration of flux through comparison with known sources like red clump stars – which are, moreover, abundant throughout the region, thus providing generous statistics. Second, such a high level of extinction accentuates the features in the absorption spectrum, greatly aiding the characterisation of dust properties. It is therefore unsurprising that the GC has long been a favoured target in the study of universal properties of dust extinction.

Numerous studies in the literature derive extinction laws for the GC. They primarily fall into two categories: those that utilise the "pair method" relative to known stellar sources [177, 82, 154], and those that employ spectral lines such as molecular hydrogen [138, 78]. The two methods have different strengths, and their results are somewhat complementary (if stars are abundant, one can obtain an extinction map with good resolution [177], whereas emission lines provide dense sampling of the extinction spectrum). However, the aim here is to determine the extinction between 20 and 160 μm, a range somewhat overlooked in the literature. While at 160 μm significant corrections are not anticipated, the situation between 20 and 70 μm is different.

For the purposes of this study, it was opted to use the extinction from Fritz et al. 2011 [78] (hereafter F11) up to 19 μm. Beyond this range, the extinction values at the six desired wavelengths were interpolated onto an absorption curve given by a dust model. The reasons motivating this choice are mainly two:

- F11 derives the hydrogen recombination lines using ISO-SWS [138], but also obtains absolute attenuation values using continuum VLA imaging of free-free emission at 2 cm of the mini-spiral, which are one of the subjects at the core of this study.
- Their attenuation curve extends up to 19 μm, conveniently close to the first spectral point needed (the FORCAST 19.7 μm).

By exploiting the fact that scattering beyond 20 μm should be negligible (hence extinction is dominated by absorption) and that attenuation should converge to extinction, it is feasible to use an absorption profile to extend F11's attenuation curve to longer wavelengths. It should be noted that this does not guarantee that the extinction is the same within a radius of 6 parsecs – a 20 μm extinction map would also be needed, which has never been derived.

The primary issue with this approach is that at 20 μm dust emission is dominated by a silicate feature. Thus, anchoring F11's attenuation data and a dust model's absorption curve right around that peak introduces a risk factor: the relevance of silicates in the chosen dust model. As previously extensively discussed, dust models can differ significantly from one another. F11 itself discusses several in relation to how well they fit their datapoints in the 1-19 μm range, finding the best fit to be the COMP-AC-S model in Zubko et al. [215], which is a composite model that includes ices and voids. Unfortunately, they do not consider the model of Weingartner and Draine 2001 (hereafter W&D[11]) [205] with $R_V = 5.5$, which is the best candidate among the W&D models for the GC, as it has been designed for superdense environments with intense UV radiation fields contributing to a larger average grain size (see Equation 3.1.26 and the discussion shortly thereafter).

In light of this, three different models are adopted: W&D with $R_V = 3.1$, 4.0, and 5.5 (the same ones used in Fig. 3.2), anchoring them to F11's highest wavelength datapoint (19.062 μm), and extrapolating the extinction values to the six wavelengths

---

[11] This designation also includes the revision in Draine and Li 2007 [64].

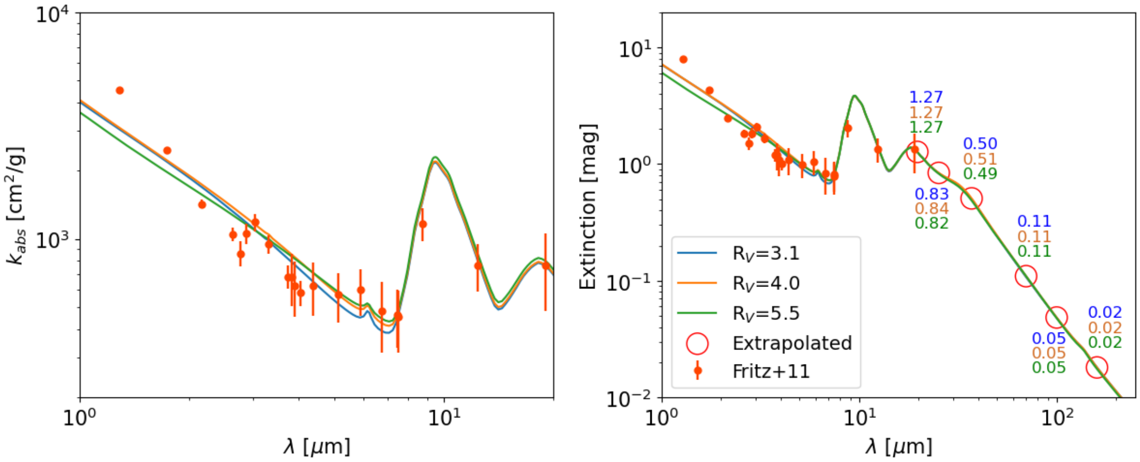

Figure 3.6: Left panel: absorption cross section per unit mass in the 1-20 μm range, calculated using W&D dust models with $R_V = 3.1$, 4.0 and 5.5 [205]. Additionally, the extinction values from Fritz et al. [78] are shown, normalised to the k_{abs} value at 19.062 μm ($R_V = 3.1$). The legend is the same as the right panel. Right panel: LoS extinction values for the GC, extrapolated up to 160 μm. The absorption curves are the same as in the left panel, and have been normalised to the extinction value at 19.062 μm. The values inferred at 19.7, 25.3, 37.1, 70, 100 and 160 μm are reported in the same colours as the dust models used for the extrapolation. The corresponding flux correction factors are reported in Table 3.4.

of the SOFIA and Herschel maps. The result is shown in Fig. 3.6 and the correction factors (calculated inverting Equation 3.1.23) are listed in Table 3.4. With the application of the corrections, one obtains[12] the maps shown in Fig. 3.7.

The prominence of the 20 μm silicate peak is apparent, yet the absorption curve remains a good fit for the F11 datapoints even down to a few microns (this includes the 10 μm silicate peak, whose slope could have led to larger deviations). This ensures that anchoring the absorption curves to the 20 μm peak should not pose significant challenges. To associate an uncertainty with the extinction values (and hence the correction factors), one could employ the uncertainty of the spectral joining point, which, however, is the largest in the entire dataset. To assess the impact of using the 19 μm point as the normalisation anchor, a straightforward chi-square test was conducted by varying the normalisation datapoint, using only datapoints above 5 μm. The 19 μm point proved to be the best but with minor variations across the entire range of cases. This is reassuring concerning the impact of the silicate bump and also allows to statistically calculate the uncertainty on the extinction values using the 7 spectral points above 5 μm. The absorption curve was

---

[12] The correction factors for the brightness are obviously the same.

Model	19.7 µm	25.3 µm	37.1 µm	70 µm	100 µm	160 µm
$R_V = 3.1$	3.220	2.157	1.584	1.104	1.045	1.017
$R_V = 4.0$	3.221	2.167	1.596	1.106	1.046	1.017
$R_V = 5.5$	3.217	2.138	1.565	1.106	1.045	1.016

Table 3.4: Flux correction factors accounting for LoS extinction, calculated according to W&D dust models [205], and corresponding to the values shown in Fig. 3.6. Their relative uncertainty amounts to 6.5% (see text).

used to fit such spectral points, yielding an uncertainty on the fit of 7% at 1σ, which was then used as the uncertainty δA on the extinction value. Consequently, error propagation yields an uncertainty on the flux correction factor δF equal to

$$\delta F = \left|\frac{\mathrm{d}F}{\mathrm{d}A}\right| \delta A = \frac{10^{\frac{A}{2.5}}\ln(10)}{2.5}\delta A = 0.92\,F\,\delta A \tag{3.2.3}$$

which translates to δF/F=6.4%, falling below the calibration uncertainty for the SOFIA/FORCAST maps (10%, using only the dual-channel runs, see figure 8 in [102]) and comparable to the nominal uncertainty for Herschel PACS (5% [151]). Since the differences between the values obtained with the three models are minimal (below 1%), only the W&D model with $R_V = 5.5$ is assumed when dealing with the LoS extinction. This argument is valid exclusively for the dust responsible for extinction: the dust emitting in the GC is in no way constrained by the analysis of dust in molecular clouds along the line of sight, as the environmental properties are entirely distinct. Concerning the emission, all three W&D models should be used for comparison.

3.2.4 *A preliminary investigation of the central heater scenario*

The maps in Figure Fig. 3.7 highlight different features across various bands. Generally, one would expect higher temperature emissions towards the centre, in proximity to the NSC. Indeed, the 20 µm map primarily displays the ionised filaments (NA and HB, labelled in Fig. 3.3). Even the CNR, which is also partially ionised, is barely visible at 20 µm. Between 25 and 37 µm, the CNR becomes more prominent, while conversely, the filaments tend to become increasingly less visible in the Herschel maps (note the different intensity scale). Investigating this trend quantitatively serves as a good check for the initial conditions to ascertain that the NSC is the primary source of UV photons. This is crucial, as understanding the radial variation

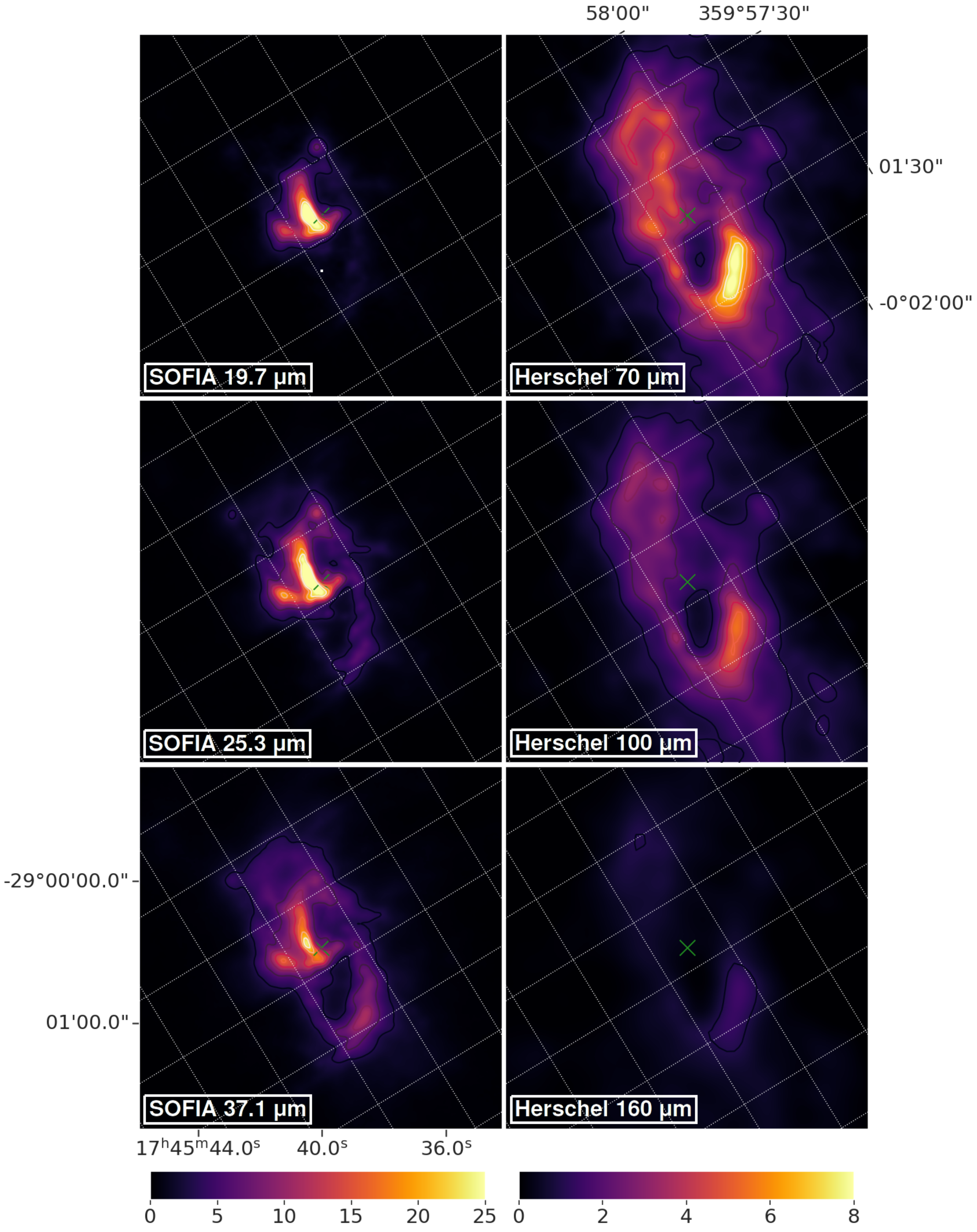

Figure 3.7: SOFIA/FORCAST [103] and Herschel PACS [166] brightness maps [in Jy/arcsec^2] in the inner 6 parsecs, background-subtracted and corrected for extinction. Each map group has its relative colour bar at the bottom. The green cross marks the position of Sgr A*. The coordinates are given both in equatorial (RA,Dec) frame (labelled on the bottom left panel) and in Galactic (l,b) frame (top right panel, also white grid). At the GC distance, 1′ corresponds roughly to 2.4 pc.

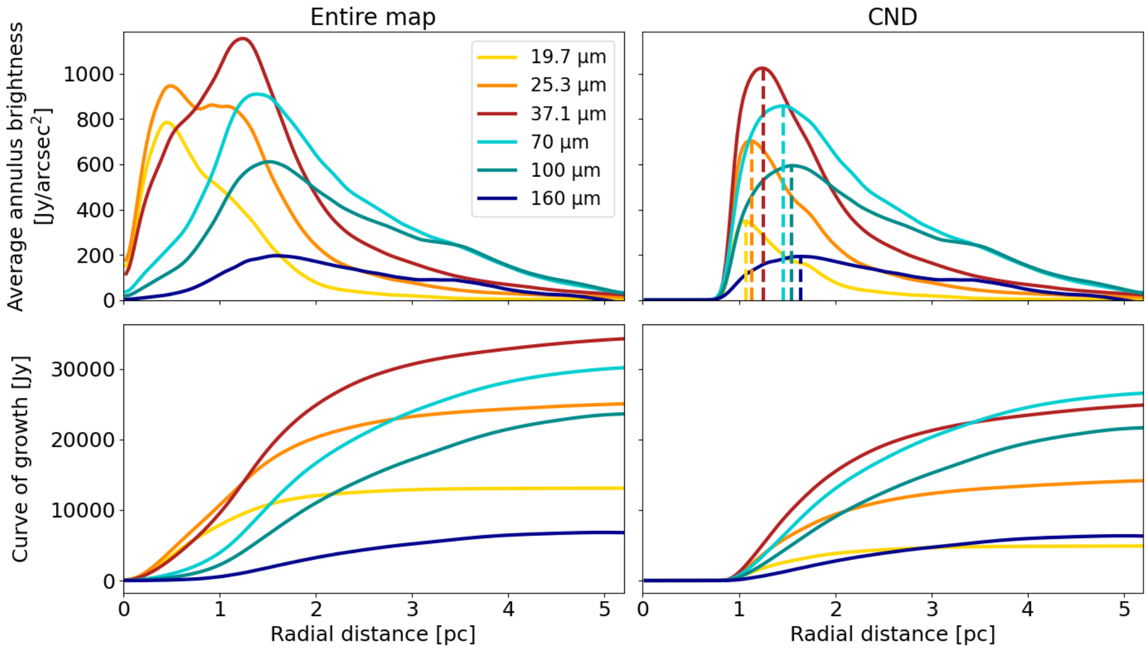

Figure 3.8: Average brightness in concentric annuli centred on Sgr A* and smoothed with a Gaussian profile (first row), and CoG accounting for the line of sight extinction (second row). The first column uses the entire maps, while the hot filaments in the central cavity have been masked off in the second column (for the mask used, see Appendix A). In the top right panel, the position of each peak has been marked to highlight the gradient in the dust temperature. As for Fig. 3.5 (in which LoS extinction is not accounted for), the radial distance to Sgr A* has been calculated in the orbital plane of the CND.

of the UV radiation field, the primary heater of the dust, is required to model the IR dust emission.

However, the presence of multiple structures on non-coplanar orbits complicates the study of the dust temperature gradient. The CNR/CND is well-suited for such an investigation as it is visible across all wavelengths and has a distinctly axisymmetric geometry. In contrast, the inner filaments within the CC display a more irregular morphology and too little dust, at too high temperatures for investigations at longer wavelengths. For this reason, the internal structures have been masked out (the masks are shown in Appendix A). The analysis conducted is very similar to what was done previously in evaluating the Galactic background: the total flux density as well as the enclosed flux density have been calculated for all concentric rings around Sgr A* on the orbital plane of the CND (elliptical in the 2D frontal projection). The result is shown in Fig. 3.8 and is rather encouraging: the emission peaks on the rings display a clear temperature gradient on the CND (from lower to higher wavelengths

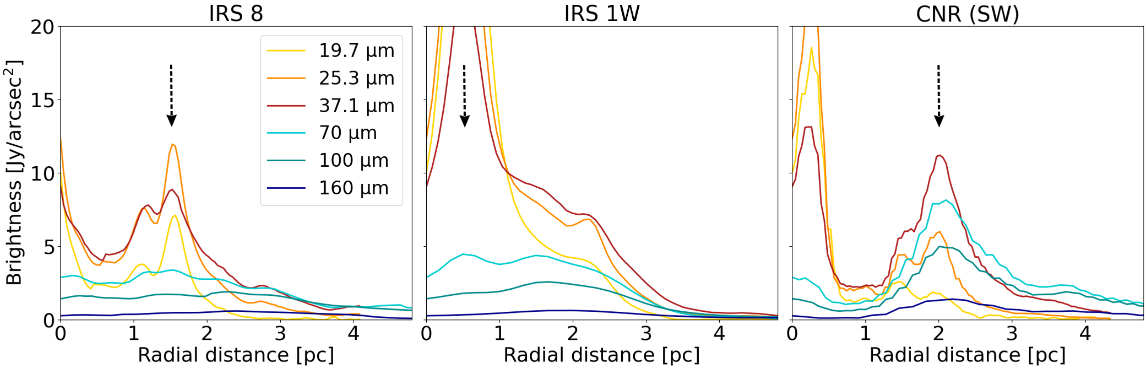

Figure 3.9: IR brightness obtained on linear slices from Sgr A*, at 93° (first panel), 170° (second panel) and −60° (third panel), respectively passing through IRS 8, IRS 1W, and the southwest part of the CNR). The distance has been calculated on the respective orbital planes – the NA in the first two panels, the CNR in the third.

moving outwards), while the CC is dominated by emissions at 20 – 25 μm. The CoG shown accounts for extinction corrections and allows for the evaluation of the un-obscured flux density of the CND, and for its comparison with the values found in literature. The total luminosity of the CNR obtained is $(2.2 \pm 0.3) \times 10^6\,L_\odot$, in good agreement, for example, with [125] and [124]. In conclusion, up to at least 6 parsecs the majority of UV illumination on the dust is likely due to a central source.

In addition to the structures already described, at least two stellar and quasi-stellar objects are clearly visible, especially at 25 μm: the source IRS 8 [83] (at the northern edge of the NA, where it intersects with the CNR), likely an advanced-stage O5/O6 star, and the source IRS 1W [176] embedded in the NA, a WR star that is partially responsible for the enhanced emission at shorter wavelengths. While their UV contribution does not seem to be dominant locally, their impact on local dynamics and energetics, particularly for IRS 1W, is far from negligible, as the expelled material heats the surrounding gas creating bow shocks [190, 176]. To get an idea, one can plot the brightness in each map along a direction that passes through both sources. The result is presented in Fig. 3.9, clearly showing that the emission around IRS 8 (first panel) is warmer compared to the CNR (third panel), despite similar angular distances. This contamination must be taken into account when constructing the model. Their IR emission has therefore been modelled using a Gaussian profile [176, 158] and subtracted from the maps.

3.3 2D MODIFIED PLANCK FITS FOR DUST GRAINS IN THERMAL EQUILIBRIUM

Now that the groundwork has been done (the theoretical formulation in Section 3.1.1 and the observational tools in the preceding section), it is finally time to proceed to the modelling. A simple approach employs a model of dust in thermal equilibrium and includes two broad components: a hot component that traces ionised gas, expected primarily in the inner filaments and in the CNR, and a cold component that traces neutral gas, anticipated mainly in the CNR/CND but also within the ionised filaments and in significantly larger quantities than the hot component [75]. All the grains of a single component have the same temperature, without accounting for size or chemistry.

In this formulation, following Equation 3.1.11, the equation for the total brightness in each map pixel becomes:

$$B_\nu^{\text{pix}}(\nu_{\text{em}}) = \sum_{i=1,2} \frac{\langle k_{\text{abs}}(\nu_{\text{em}})\rangle \cdot M_i \cdot BB_\nu(\nu_{\text{em}}, T_i)}{\Delta l^2} \tag{3.3.1}$$

The parameters to obtain are four: T_1 and M_1 for the hot component, and T_2 and M_2 for the cold component. Here, the brightness is calculated for a square pixel with a subtended area of Δl^2. For all six maps to be usable within the same pixel, they must be re-sampled to have the same angular resolution. The original maps have samplings of 0.78″ (FORCAST), 1.6″ (PACS 70 µm and 100 µm), and 3.2″ (PACS 160 µm). Accordingly, a unified sampling of 1.6″/pixel is chosen. This way, the introduction of oversampling noise into the PACS maps can be avoided, with the exception of the 160 µm map. For this map, however, significant variations in the examined region are not expected, and the 160 µm emission is always sub-dominant. As an additional test, it was verified that the RMS of the map remained unchanged (+0.3%) after resampling. The same test was performed for the FORCAST maps, confirming that the change in RMS in the investigated region does not exceed 2% and that there is no systematic huge variation from pixel to pixel that would be lost with the re-sampling. With this resolution, each pixel subtends a side of 0.063 pc and an area of 0.0040 pc^2.

The six spectral data points for each pixel of the re-sampled maps can be fitted with the modified Planck function[13] shown in Equation 3.3.1. It is important to note that 3D information is so far absent in this approach: the aim is to first obtain a 2D map

---

[13] This method will hereafter be referred to as *Planck fit* for brevity.

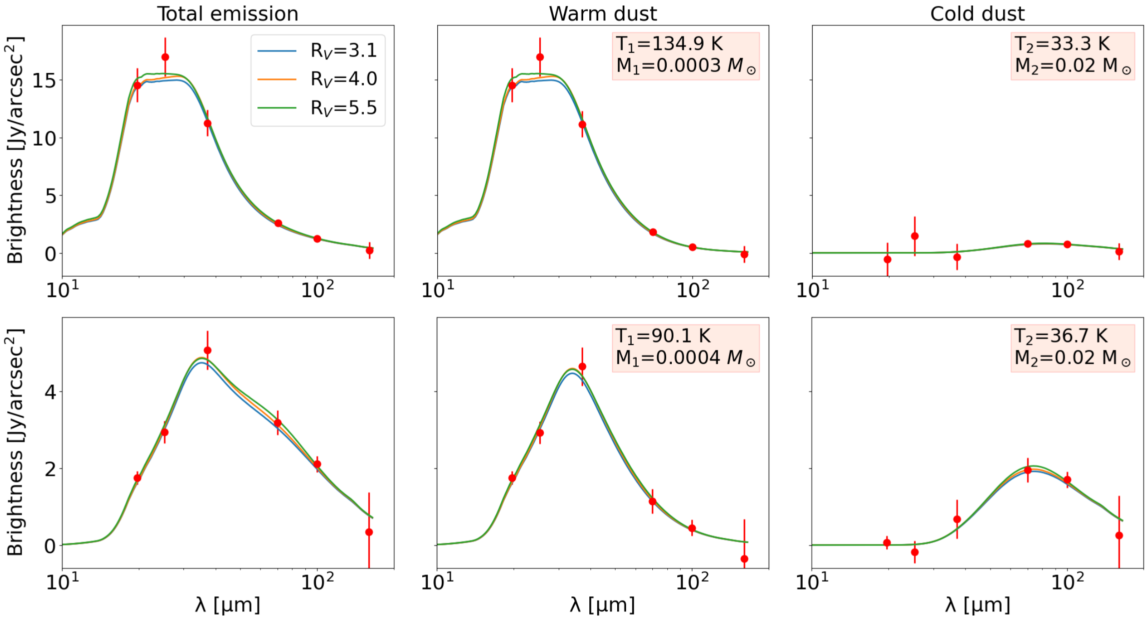

Figure 3.10: 2D Planck fits for different regions: close to Sgr A* (first row) and at the Eastern intersection of CNR and HB (second row). The total emission shown in the first column is divided between the contribution from the hot dust (second column) and from the cold dust (third column). The parameters extracted are reported in the red boxes. The datapoints from the IR maps are shown in red. The dust emission has been fitted using three W&D models [205].

of the distribution of each component, and only subsequently de-project them onto their respective orbital planes. An example of a Planck fit is depicted in Fig. 3.10, where emissions are fitted along two distinct lines of sight where significant variations in the four parameters are expected: one 4″ away from Sgr A* on the NA, and the other at the intersection between the CNR and the HB to the east, about 20″ away from Sgr A*. The results are promising for the potential of this investigation. In the first case, the emission emanates from a region internal to the NSC, which is strongly ionised, and the luminosity is dominated by the high-temperature component ($T_1 \approx 135\,\mathrm{K}$), despite its mass being two orders of magnitude lower than that of the cold component ($T_2 \approx 30\,\mathrm{K}$) along the same line of sight[14]. In the second case, the two emissions are comparable, as expected in a line of sight that traverses both an ionised filament (albeit rather peripheral, so not as warm) and a more massive and relatively colder structure like the CNR. The upper plot also provides a good example of how the dust chemistry influences the emission spectrum: black-body emission is not a good approximation for high-temperature dust emission, due to

---

[14] A reminder that $L \propto T^4$ for black body emission.

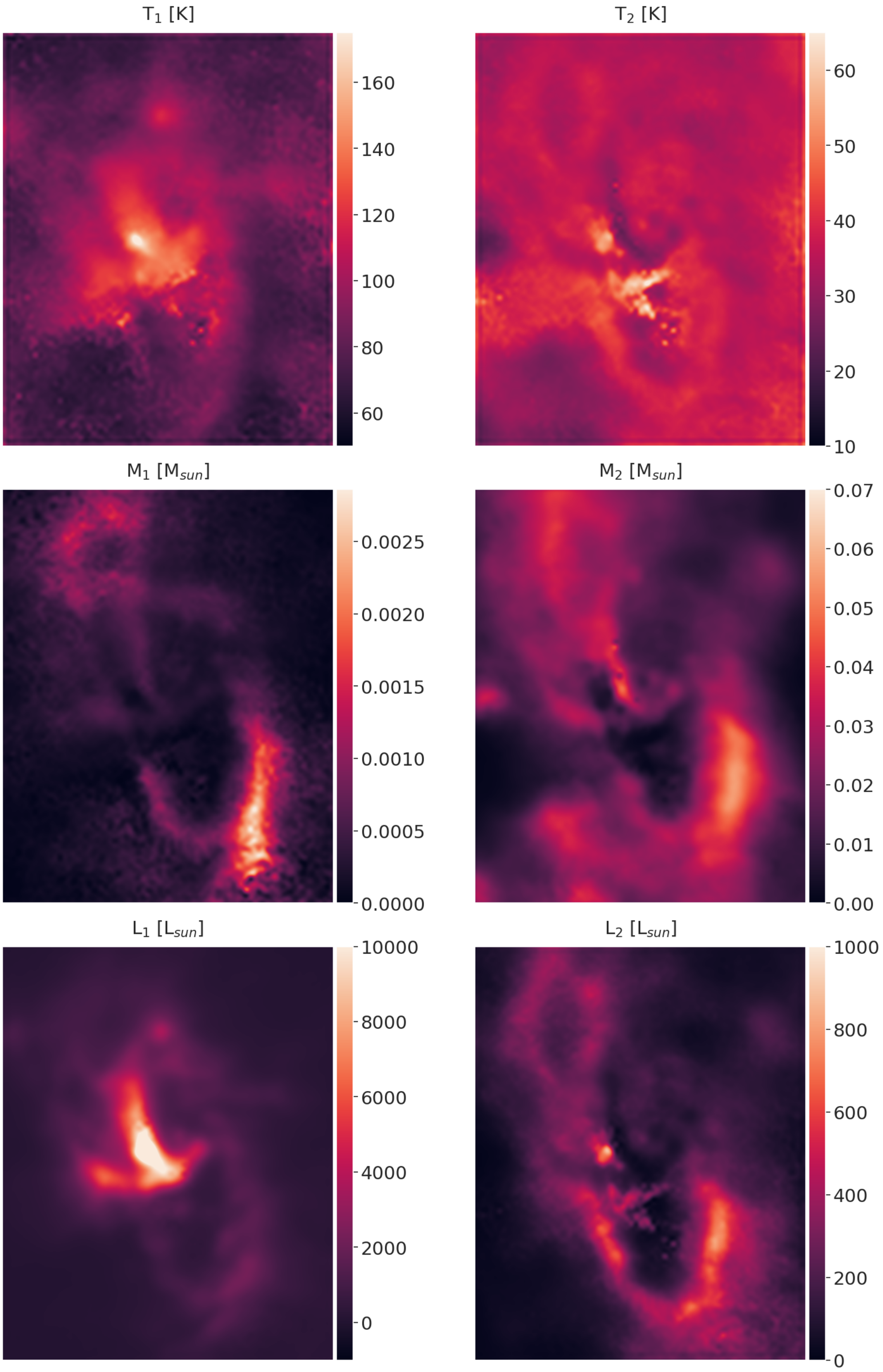

Figure 3.11: 2D maps of the main parameters obtained by means of Planck fits. The first column relates to the warm dust component, the second to the cold one. The model used for the dust emission is W&D with $R_V = 5.5$.

the peak of silicates at 20 μm.

Performing a Planck fit pixel-by-pixel across the field of view yields the 2D spatial parameter maps shown in Fig. 3.11. The integrated luminosity across the entire spectrum for both components (third row) is calculated using Equation 3.1.11. The total luminosity is dominated by the warm component (both in the CC and the CNR), but the mass of the cold dust is between 10 and 100 times greater, even within the inner filaments. Furthermore, the southern part of the central cavity appears to contain very little dust. Lastly, on the southern edge of the CNR, there is a significant amount of mass in both components, the origin of which remains unclear. It is unlikely to be an accumulation due to the dynamics of the streamer, given that the orbital period of the CNR is on the order of $10^4 - 10^5$ years, and the average lifetime of the clumps containing most of the dust is much shorter ($\sim 10^4$ years [87]) due to photo-evaporation from the stellar radiation field, collective stellar winds, and strong gravitational shears. When this figure was generated the emission from IRS 1W had not yet been subtracted, leaving visible features in all the maps and highlighting the importance of appropriate noise subtraction[15].

The next step involves de-projecting the 2D mass distributions onto the orbital planes of NA, HB, and CNR. The greatest challenge arises in regions where multiple structures emit along the same line of sight. Since cold dust is present in both the central filaments and the ring, the intersecting zones[16] between CNR and NA (north) and between CNR and HB (east and west) contain emissions – both hot and cold – from both structures, with no straightforward way to disentangle their respective contributions. One approach is to model the emission from the inner filaments so that it can be subtracted in the more congested lines of sight. In theory, the CC should offer a reasonably uncluttered environment devoid of further neutral emission from other orbital planes, with the exception of the area immediately south of Sgr A* where NA and HB intersect (sometimes referred to as the Bar) – the complication is that most of the HB lies in the same line of sight as CNR (to the east) and NA (the Bar), except for the western extremity, and it is also hard to say whether the NA lies in front of the CNR or not. The starting approach, therefore, is to model NA first – between the Bar and the northern intersecting region (roughly where IRS 8 is located) – and potentially use the same modelling for HB, given that the two filaments share similar energetics, geometry, and dynamics. The biggest unknown is

---

[15] One of the many lessons learned using these 2D maps for a preliminary investigation.

[16] Intersecting in projection, not in 3D.

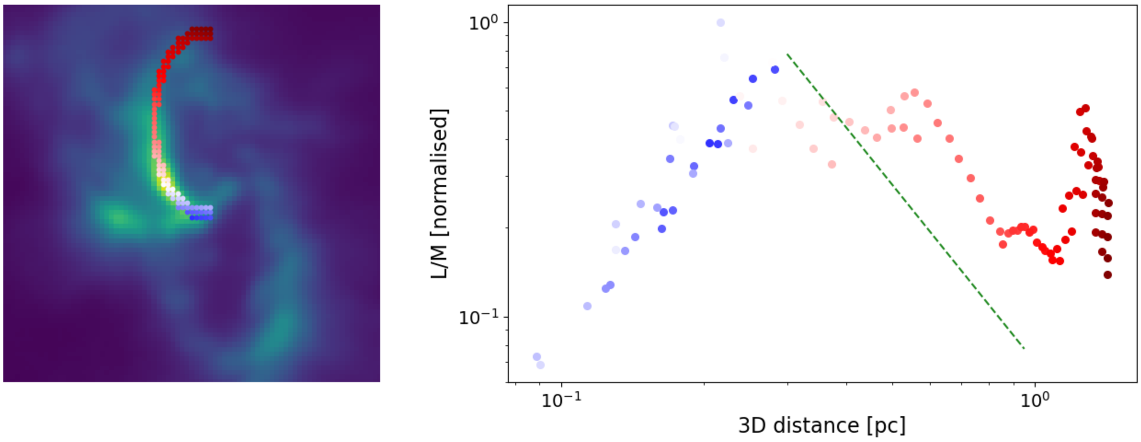

Figure 3.12: Illumination radial profile in the NA after de-projection of the 2D maps obtained from Planck fits. The points in the right panel keep the same colour as the ones overplotted onto the SOFIA 37.1 µm map in the left panels. The green line marks the inverse square law.

the ratio between warm and cold dust, which depends as much on the dynamics as on the energetics of individual dust cloudlets – making it position-dependent.

To test the de-projection of dust onto the orbital plane, a necessary yet straightforward check is to ensure that the luminosity per unit mass of dust (hereafter referred to as ’illumination’) follows a flux-like law at sufficiently large distances from the heating source: $L/M \propto r^{-2}$, where r is the actual 3D distance from Sgr A*. Indeed, while the luminosity is dominated by hot emission, cold dust accounts for the bulk of the mass. Consequently, investigating the illumination profile serves as a good test to ensure that the amount of cold dust de-projected onto NA is not, in fact, “background” – dispersed in the CC, possibly on the orbital plane of the CNR.

The outcome is depicted in Fig. 3.12: the profile does not conform to a radial flux law (as illustrated by the dashed green line) but exhibits an irregular trend with real distance. While an irregular trend is expected for the Bar region (blue points) due to multiple structures in the field of view – although the consistent upward trend suggests that most of the dust resides in the HB’s orbital plane – the region north of the Bar displays bumps that cannot be correlated with any specific features (not even with IRS 1W, which affects the PFs so that the estimated mass is lower and hence should lead to greater illumination). This suggests that a non-negligible amount of cold dust may exist on a different orbital plane within the same line of sight of the NA. This is a crucial piece of information to consider when constructing the 3D infrared radiation field: the de-projection of dust along the line of sight must account for all structures simultaneously. Furthermore, one cannot assume that the dust along a given line of sight will be at a uniform temperature, since the temperature is influenced by local UV illumination and thus varies with distance from the NSC. It becomes evident that 3D distance is another factor to consider already in the Planck fitting phase. The solution is discussed in Section 3.6.

3.4 POWERING THE DUST EMISSION: SIMULATIONS OF THE NSC

The NSC (see Section 2.1.1, page 45) is the primary source of UV[17] emission within the central parsec and consequently the source of the re-emitted energy from the dust. To obtain a 3D model of the dust IR emission, a 3D model of the UV radiation field is essential, and hence the emission of the youngest and most massive stars, which are concentrated within a radius of $\sim 13''$ ($\sim 0.5\,\mathrm{pc}$). However, although the NSC displays a triaxial symmetry with an elongation along the Galactic Plane, the more than 100 inner massive stars exhibit a very different geometry, with an isotropic distribution within the first 0.03 pc (the so-called S-stars) and a more flattened one beyond – with large deviations – with projected orbits in both clockwise and counter-clockwise directions (heavy reliance was placed on [71] regarding the geometry of the NSC stars).

The total mass of the young stars has been constrained to a range between 12 000 and 36 000 $\mathrm{M}_\odot$ [71, 136] depending on the IMF and the maximum mass of a single star, which in turn depends on the age of the last starburst – constrained between 3 and 8 Myr [136, 155] – and is found to be greater than or equal to 80 $\mathrm{M}_\odot$. Their IMF has been found to be top-heavier compared to the "standard" value of 2.3, with a spectral index of 1.7 ± 0.2 [136].

For the simulation of the NSC's young population, it was decided to keep both the IMF spectral index α_{IMF} and the total mass[18] of the NSC M_{NSC} as free parameters (ranging between 1.3 – 2.3 and 4000 –36 000 $\mathrm{M}_\odot$, respectively), in part to assess the potential of this study as a predictive tool for the cluster physical properties. On the other hand, the maximum stellar mass was fixed to 80 $\mathrm{M}_\odot$, which according to [71] should yield a M_{NSC} value between 12 000 and 16 000 $\mathrm{M}_\odot$ depending on the IMF.

The cluster radial profile adopted is an isotropic King profile:

$$f(r) = k\left[\left(1 + r^2/r_{\mathrm{c}}^2\right)^{-1/2} - \left(1 + r_{\mathrm{t}}^2/r_{\mathrm{c}}^2\right)^{-1/2}\right]^2 \tag{3.4.1}$$

where r_{c} is the core radius and r_{t} the tidal radius. The cumulative probability distribution is given by the integrated density:

$$n(r) = \pi r_{\mathrm{c}}^2 k\left[\ln(1 + r^2/r_{\mathrm{c}}^2) - 4\frac{(1 + r^2/r_{\mathrm{c}}^2)^{1/2} - 1}{(1 + r_{\mathrm{t}}^2/r_{\mathrm{c}}^2)^{1/2}} + \frac{r^2/r_{\mathrm{c}}^2}{1 + r_{\mathrm{t}}^2/r_{\mathrm{c}}^2}\right] \tag{3.4.2}$$

---

[17] And also visible, of course. In this thesis, it is implied in "UV" for brevity.

[18] Throughout the thesis, NSC's "total mass" means total mass of young stars.

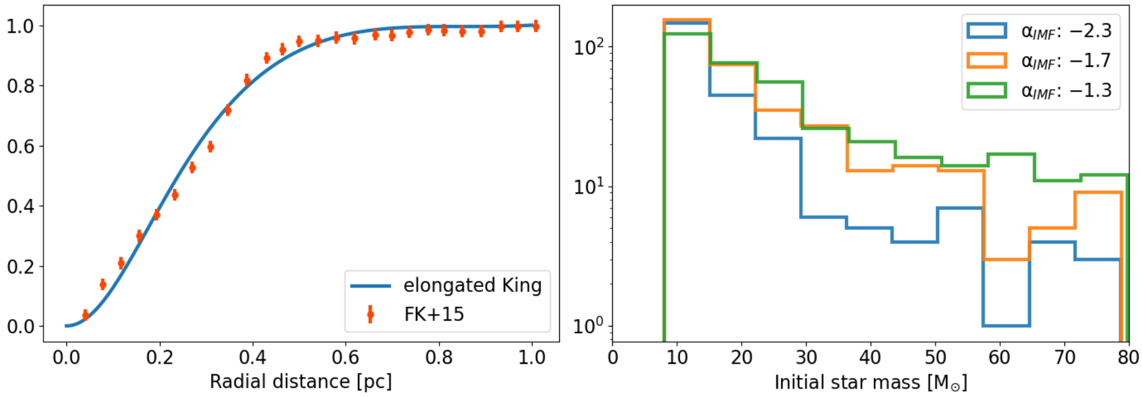

Figure 3.13: Distribution of initial parameters for the NSC simulation. The chosen elongated King distribution (left panel) is compared to the radial profile found by Feldmeier-Krause+15 [71]. The initial mass distribution of the evolved population (right panel) is shown for three different IMFs and for a NSC total stellar mass of 16 000 M$_\odot$, including only stars with initial mass above 8 M$_\odot$.

The values assumed were $r_c = 0.25$ pc and $r_t = 0.85$ pc. The distribution is then elongated along the Galactic Plane according to the map in [71] with a/b=1.5. The obtained profile is shown in Fig. 3.13 (left panel) where the profile measured in [71] is also shown. The assumed profile fits the data with a chi-square per DoF equal to 1.7. The distribution of the angles (θ, ϕ) is instead assumed to be flat.

The stars are evolved singularly, following the prescriptions of the evolutionary population synthesis (EPS) code SeBa [169] without accounting for binary interactions. The 3D space is populated randomly with the evolved sample until the population reaches $M_{\rm NSC}$. The number of stars simulated depends on the assumed IMF, as shown in the right panel of Fig. 3.13. This procedure has been done for different combinations of $\alpha_{\rm IMF}$ and $M_{\rm NSC}$.

3.4.1 *UV radiation field*

The stellar emission has been modelled as a black body. In order to calculate the energy density $u_{\rm rad}(\nu, T)$ in a position $\vec{r}$, assuming a star with radius r_s in $\vec{r_0}$, the spectral radiance from Equation 3.1.2 must be multiplied by $4\pi \cdot \pi r_s^2$ obtaining the star luminosity, which must then be divided by $4\pi c|\vec{r} - \vec{r_0}|^2$, yielding

$$u_{\rm rad}(\nu, T, \vec{r}) = \frac{2\pi h\nu^3}{c^3} \frac{1}{e^{h\nu/k_B T} - 1} \frac{r_s^2}{|\vec{r} - \vec{r_0}|^2} \qquad (3.4.3)$$

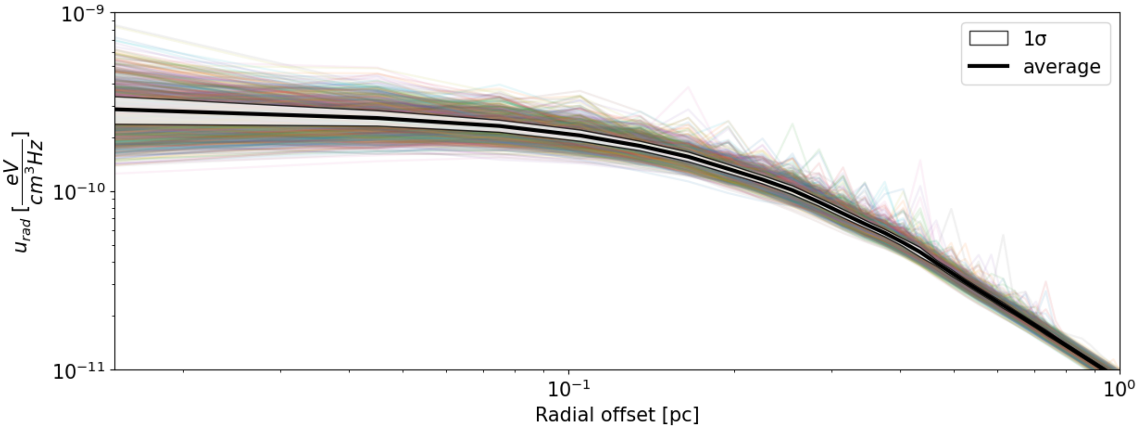

Figure 3.14: Radial profile of the UV radiation field at 0.1 μm in the direction of the NSC elongation, assuming $M_{\mathrm{NSC}} = 16\,000\,\mathrm{M}_{\odot}$ and $\alpha_{\mathrm{IMF}} = 1.7$. The black line is the average of the 1000 simulations plotted, and the white area corresponds to one standard deviation. $r = 0$ corresponds to the position of Sgr A*.

The radiation field was calculated over the entire volume enclosed within the inner 6 parsecs as the sum of contributions from all simulated stars, with a spatial binning of 0.03 pc (thus finer than the one chosen for the IR maps). Sgr A* was assumed to be in $r = 0$. Given the crowding of stars on spatial scales below 0.5 pc, it is plausible for a star to randomly be near the point where u_{rad} is computed, dominating its emission. Since the objective of this simulation is to assess an average field, the choice was made to mitigate local effects by running an appropriate number of simulations – a suitable compromise was found at 1000. A radial profile obtained in the direction of the NSC elongation is displayed in Fig. 3.14, calculated in the near UV at the frequency of $3 \times 10^{15}\,\mathrm{Hz} = 0.1\,\mu\mathrm{m}$. All 1000 simulations are shown: spikes are relatively frequent, but the average profile is rather smooth. This behaviour has been checked in 14 radial directions (for 4 values of both θ and ϕ, plus the two poles). The radiation field exhibits a turnover between 0.2 and 0.3 pc, as expected from the choice of $r_c = 0.25\,\mathrm{pc}$. Beyond 0.5-0.6 pc, the profile is log-linear. It should be noted that an average UV radiation field scales with the total mass of the cluster. Throughout this thesis, the "standard simulation set" assumes $\alpha_{\mathrm{IMF}} = -1.7$ and $M_{\mathrm{NSC}} = 16\,000\,\mathrm{M}_{\odot}$.

3.5 Composite dust model: emission temperature and brightness

As discussed in the previous section, a simplified dust model (consisting of two different mixed components, each in thermal equilibrium) is not adequate for the objectives of this study. It is crucial to reach a detailed understanding of the dust energetics, which is evidently dependent on its position relative to the UV source, and is also heavily influenced by its micro-chemistry. Specifically, dust grains can vary in size by orders of magnitude for each chemical species in the mixture. It is generally incorrect to assume that grains with such diverse physical and chemical properties would have identical energetics – that is, they would reach the same temperature when exposed to the same UV radiation field. Consequently (see the discussion on page 58), the emission temperature should not be derived during the fitting phase but should be calculated as a function of the distance from the UV sources by enforcing thermal equilibrium between absorption and emission for each grain of each chemical species. Explicitly, referring to Equation 3.1.14 and Equation 3.1.16, the equation to be solved is:

$$\int \pi a^2 Q^{(i)}_{\mathrm{abs}}(a,\nu) u_{\mathrm{rad},\nu}(\nu,\vec{r}) c \, \mathrm{d}\nu = \int 4\pi^2 a^2 Q^{(i)}_{\mathrm{abs}}(a,\nu) BB_\nu(\nu, T^{(i)}_{\mathrm{d}}(a,\vec{r})) \, \mathrm{d}\nu. \tag{3.5.1}$$

in which both $Q_{\mathrm{abs}}(a,\nu)$ for each species i (from the dust model [205]) and the radiation field (calculated in Section 3.4) are now known. To understand what to expect from the calculation of $T(a,\vec{r})$, it is advisable to investigate the composition of the dust to gain qualitative insights into its properties.

The W&D model assumes that the dust is a mixture of silicates, graphite, and both ionised and neutral PAHs. The sizes of PAH grains range from a few Å to 10 nm, seamlessly transitioning to graphite, which extends the size range up to 1 µm. The silicates range from a radius[19] of 1 nm up to 1 µm. The assumed density is 2.24 g/cm^3 for carbonaceous grains and 3.5 g/cm^3 for silicates. The abundance of the various components in the model is illustrated in Fig. 3.15: more than 99% of the dust exists in the form of very small PAH grains, yet their mass ($\propto a^3$) accounts for a little less than 80% of the total. Furthermore, the average grain size is 1.8×10^{-3} µm for the silicates, 1.8×10^{-2} µm for the graphite, 5.7×10^{-4} µm for the ionised PAHs and 5.1×10^{-4} µm for the neutral PAHs. Considering that PAHs, being small, heat up

---

[19] As it is probably clear from the formulas already discussed, grains are assumed to be spherical in this treatment. This is, of course, not strictly accurate – an empirical demonstration is provided, for example, by dust polarisation [165].

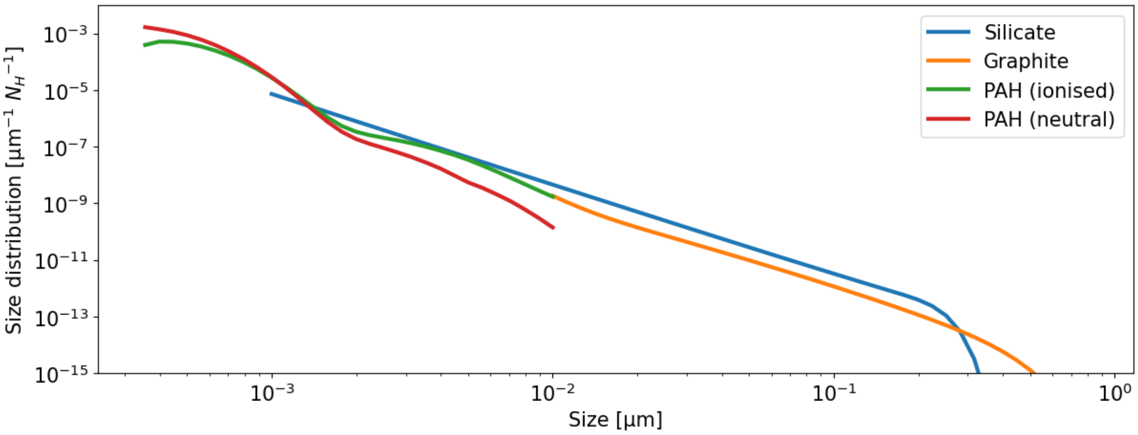

Figure 3.15: Dust size distribution according to the W&D model adopted [205].

more quickly upon absorption, this offers an alternative microphysical explanation for why the dust component that dominates in luminosity does not dominate as much in mass. This point has already been noted both in Section 3.3 and in the introduction under Section 3.2.1 [75].

The absorption properties for each species are clearly highlighted in Fig. 3.16, where the dependence of $Q_{\mathrm{abs}}(a, \nu)$ on grain size and the wavelength of the incident radiation is plotted. Generally, it can be seen that silicates and graphite have a higher average absorption efficiency (first column) and they absorb more efficiently at both high (1 μm) and low (10^{-2} μm) wavelengths (second column). However, the absorption efficiency in the UV for the typical grain size (marked with a vertical dashed line on the left plots and basically corresponding to the darkest dashed line on the right plots) makes the difference, since it is noticeably different for graphite (~1), silicates (0.3) and PAHs (0.1), hinting at the fact that the larger grains have a higher chance to absorb and re-emit the UV radiation.

The transition between PAHs and graphite is not entirely smooth: this is evident both in the PAH profile with size, which shows a sudden rise in Q_{abs} above 6×10^{-3} μm, and in the PAH spectrum for $a = 10^{-2}$ μm, where the spectral lines around 10 μm are lost. Moreover, both ionised and neutral PAHs converge towards the graphite profile, but ionised PAHs are noticeably more efficient at emitting in the infrared bands due to the forest of emission lines around 10 μm (see the intermediate dashed red line on the left). This means that ionised PAHs can emit in a broader band, and therefore reach a lower equilibrium temperature, with respect to the neutral PAHs. A vertical blue dashed line marks the ionisation energy of H atoms: inside

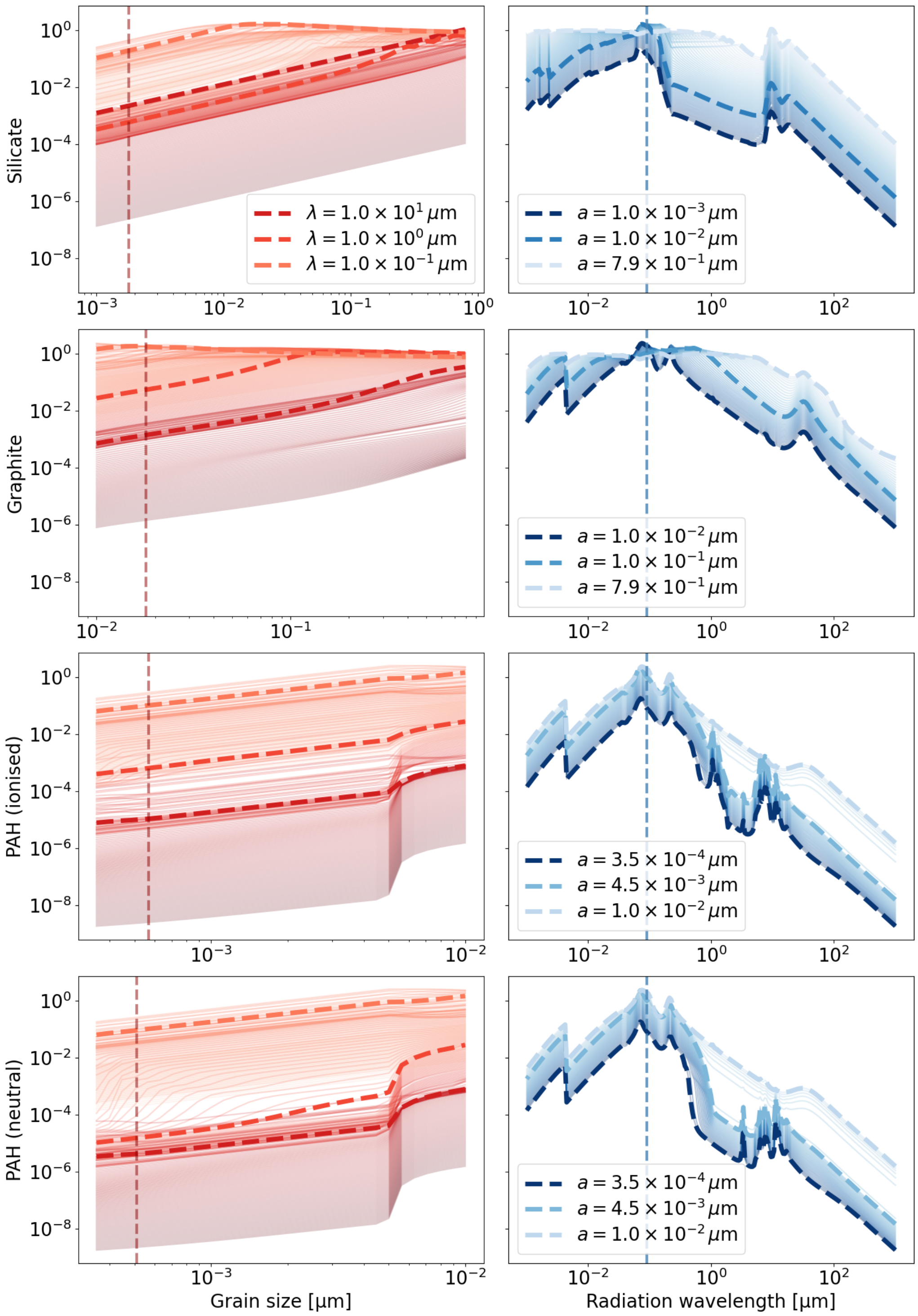

Figure 3.16: Absorption efficiency $Q_{\mathrm{abs}}(a, \nu)$ for all dust species, as a function of grain size (first column) and radiation wavelength (second column). The colour gradient in the first column scales with radiation wavelength, while the spectra adopt a blue gradient scaling with the grain size. The vertical dashed lines on the left mark the average grain size, while the vertical dashed line on the right marks the H ionisation limit at 13.6 eV = 912 Å.

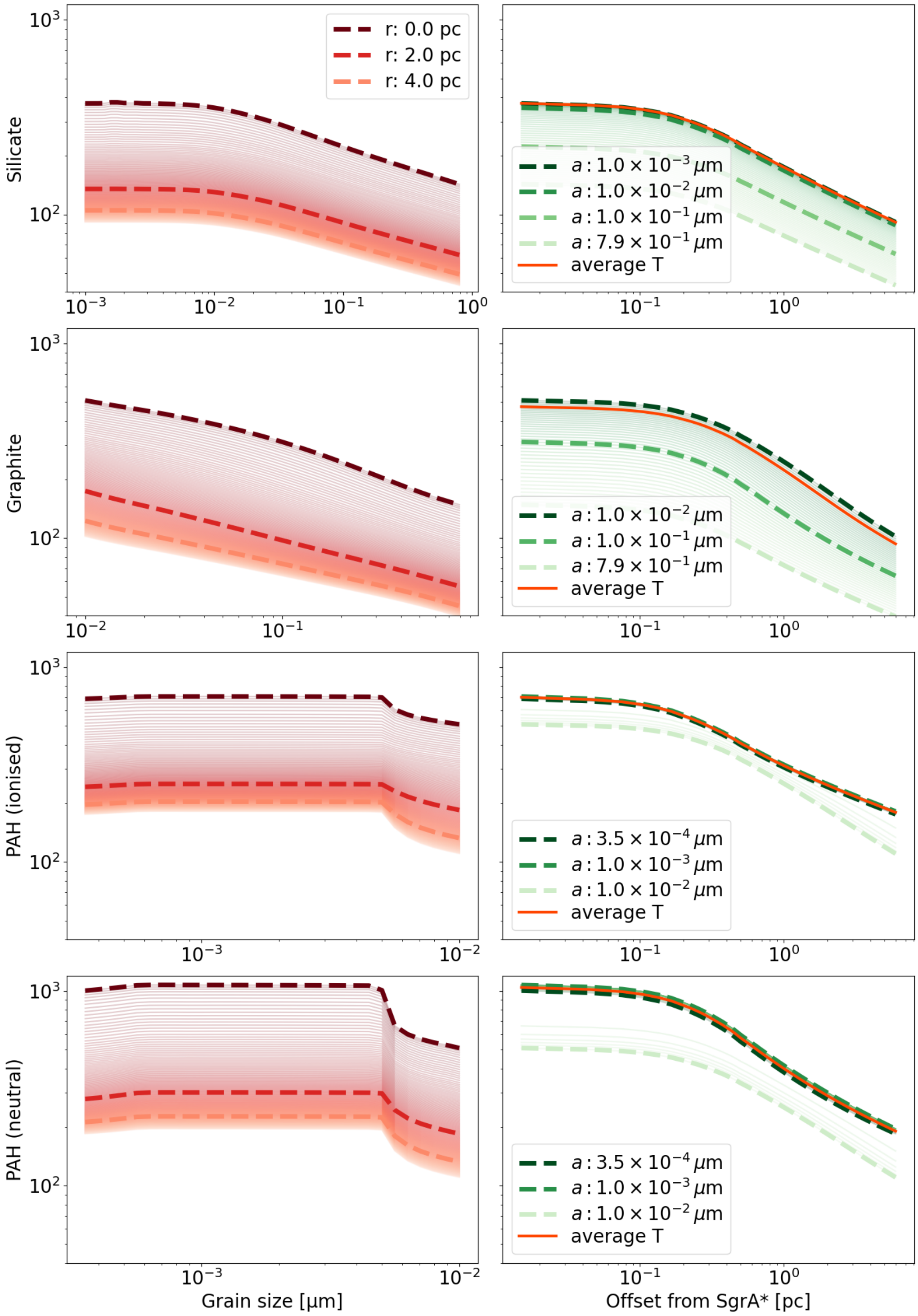

Figure 3.17: Dust temperature [K] as a function of grain size (first column) and distance to Sgr A* along the elongation of the NSC distribution (second column), assuming the same $u_{\rm rad}$ as Fig. 3.14. The logic of the gradients is the same as Fig. 3.16. The red lines on the right plots mark the average temperature, calculated assuming the grain size distribution observed in the solar neighbourhood.

the clouds, photons with energy $> 13.6\,\mathrm{eV}$ are likely to be absorbed by the H atoms, effectively removing all wavelengths to the left of that line from the dust energy balance.

Now that the dust has been characterised, the next step is solving Equation 3.5.1 to get $T_\mathrm{d}(a,\vec{r})$. The result is depicted in Fig. 3.17. Due to their small sizes and their comparatively lower Q_abs in the infrared band, PAHs are much hotter than graphite and silicates. Neutral PAHs in particular tend do be 30% hotter than ionised ones under the strongest UV radiation field. Given that temperature is essentially a monotonic function of grain size, and for all species the average size is very close to the lower limit, the temperatures averaged over the size distribution are essentially coincident with the highest temperatures. Consequently, PAHs are expected to consistently exhibit warmer emissions compared to graphite and silicates. The temperature profiles finally allow to calculate the dust emission and investigate the contributions from different species. The brightness of a grain B_ν^sg is:

$$B_\nu^\mathrm{sg}(a,\nu_\mathrm{em},\vec{r}) = Q_\mathrm{abs}(a,\nu_\mathrm{em}) \cdot BB_\nu(\nu_\mathrm{em}, T_\mathrm{d}(a,\vec{r})). \tag{3.5.2}$$

In this case, the absorption efficiency should be considered as the emission efficiency. Although the temperature dictates the black body emission, the efficiency of a grain to transmit in a particular band – defined by Q_abs – greatly shapes it. This is not a minor detail, as in the infrared Q_abs varies by several orders of magnitude (see Fig. 3.16). For ease of visualisation, Fig. 3.18 displays the brightness profiles as a function of distance from Sgr A* at various spectral wavelengths (first column), and the emission spectra at different distances (second column). The brightness shown here is obtained through an average over the size distribution:

$$B_\nu^{(i)}(\nu_\mathrm{em},\vec{r}) = \frac{\int B_\nu^{(i)}(a,\nu_\mathrm{em},\vec{r})a^2 n^{(i)}(a)\,\mathrm{d}a}{\int n^{(i)}(a)\,\mathrm{d}a}. \tag{3.5.3}$$

It is important to note that the normalisation relative to the distribution of the individual species i does not take into account the abundance of the species in question.

From the profiles, it is evident that the high temperature of PAHs (approximately twice that of silicates and graphite) is mitigated by their relative inefficiency in emitting in the IR. Their Q_abs is, in fact, two orders of magnitude lower on average, and consequently the brightness is reduced by a factor of $\Delta T/\Delta Q_\mathrm{abs} = 2^4/100$, that

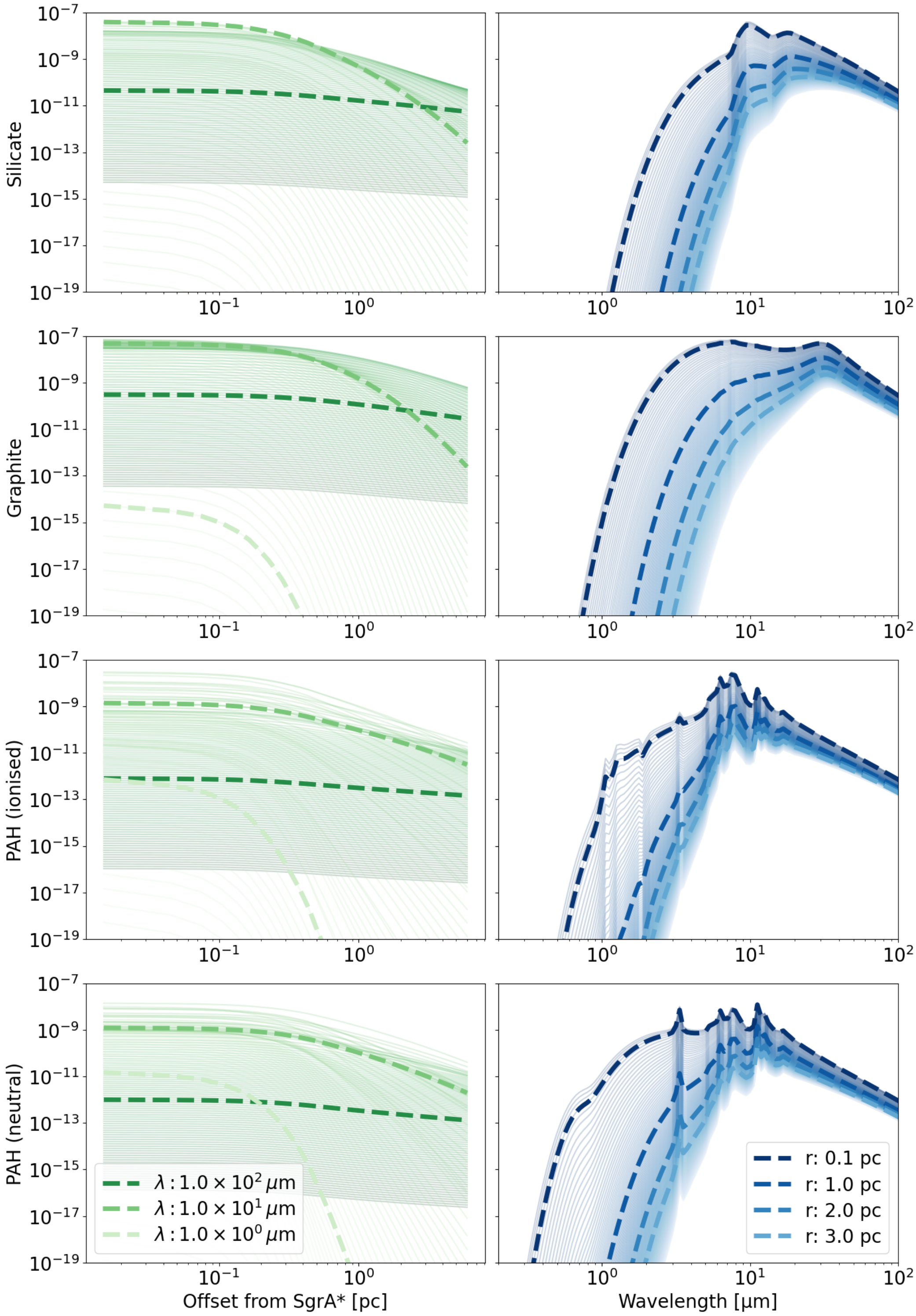

Figure 3.18: Dust brightness in W/(Hz m^2 sr) averaged over their size distribution, as a function of the distance to Sgr A* (first column) and emission wavelength (second column), under the same assumptions as the previous plots. Note that the plotted quantities do not take the species' abundance into account.

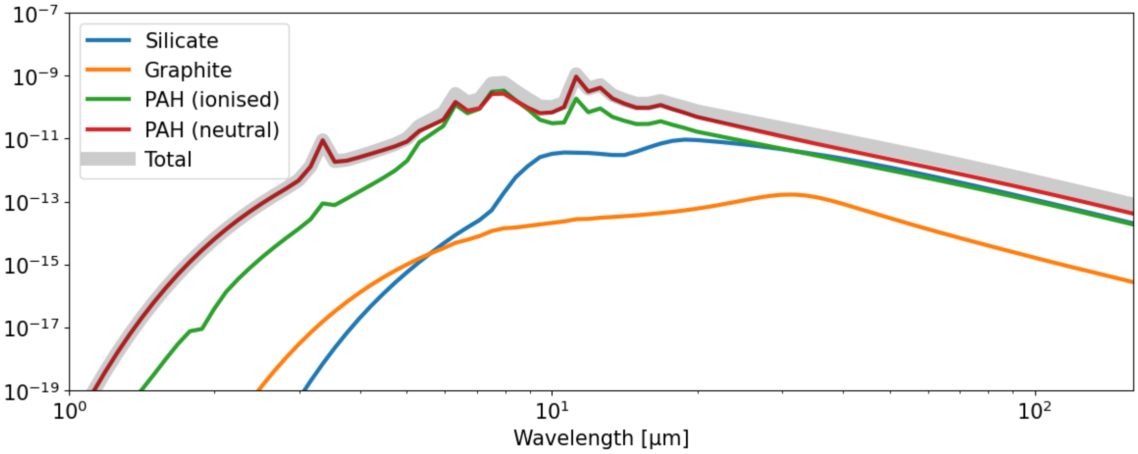

Figure 3.19: Total brightness in W/(Hz m^2 sr) from a single dust grain at 1 pc from Sgr A*.

is roughly a factor of 6.

Naturally, for the purposes of the complete emission from the dust, the brightness of individual species should be treated as a fractional quantity:

$$B_\nu^{(i)}(\nu_{\rm em}, \vec{r}) = \frac{\int B_\nu^{(i)}(a, \nu_{\rm em}, \vec{r}) a^2 n^{(i)}(a)\,\mathrm{d}a}{\sum_i \int n^{(i)}(a)\,\mathrm{d}a} \tag{3.5.4}$$

with obviously

$$B_\nu(\nu_{\rm em}, \vec{r}) = \sum_i B_\nu^{(i)}(\nu_{\rm em}, \vec{r}). \tag{3.5.5}$$

This is formally equivalent to defining a luminosity-averaged grain of dust. It is worth reminding that the term a^2 in the integral comes from the conversion from brightness to luminosity and back after summation (as brightness is not an additive quantity), as has been shown in the derivation of Equation 3.1.21. The emission profile thus calculated is shown in Fig. 3.19. It is interesting to note that the emission above 20 μm is essentially divided between neutral and ionised PAHs and silicates, with a negligible contribution from graphite (under 1%).

For this particular set of simulations ($\alpha_{\rm IMF}$ and $M_{\rm NSC}$), the temperatures reached by the PAHs – the neutral PAHs in particular, as they are noticeably higher – are substantially above the temperatures one would expect within a radius of one parsec (150 – 200 K). Silicates and graphite exhibit sufficiently low $T_{\rm d}$ emissions, but it still seems challenging to account for a 30 K emission as is the case for the CND at a distance of 4 – 5 pc from Sgr A*. Moreover, it is not at all obvious that the dust in the GC includes PAHs: for example, ISO-SWS spectra do not detect PAH emission lines in this region [138]. One plausible hypothesis is that the radiation field is so intense that it disintegrates such small grains [138]. Yet even in the absence of PAHs, the predicted temperature for the grains seems to be higher than observed – see the red line in the radial temperature profile corresponding to a grain-size-averaged temperature, calculated as

$$\langle T_\mathrm{d}(\vec{r})\rangle_a = \frac{\int T_\mathrm{d}(a,\vec{r})\, a^2 n(a)\, \mathrm{d}a}{\int n(a)\, \mathrm{d}a}. \tag{3.5.6}$$

This temperature excess is confirmed for all simulated environments, as it will be shown in Section 3.6). From these profiles, the need for an additional dust cooling mechanism becomes apparent. On one hand, altering the size distribution could lower the temperature – but for now, no changes in composition will be introduced; this will be explored and discussed in Section 3.6.3.

Another source of cooling could stem from a clumpy distribution of grains. In this scenario, grains within the clumps would be shielded from UV radiation, resulting in cooler emissions. The size of these clumps must be sufficiently small to evade detection at a 1″ pixel scale, yet large enough to facilitate substantial shielding for a large number of grains. This hypothesis has observational backing: it is already documented in the literature that interstellar dust in the GC may be organised into clumps – see for instance [58]. Besides, a clumpy dust distribution is much better than a diffuse dust model, optically thick in UV, at fitting the observed SED of dust emission and specifically at reproducing a wider range of emission temperatures. The effects of dust clumpiness are discussed in Section 3.6.4.

3.6 MODIFIED PLANCK FITS IN 3D SPACE

The key lesson gleaned from Section 3.3 is that the strategy of carrying out a 2D PF to determine dust mass and temperature, followed by de-projecting these distributions into 3D, proved unfeasible. The stumbling block arises from the impossibility of defining a singular temperature for the dust mixture, thus hindering the accurate connection of emission energetics (including dust mass) to their 3D spatial distribution. As a result, a different approach is warranted, where the particle energetics are not parameters derived from the fit but are modelled as functions of their 3D positions (Section 3.4 and Section 3.5). Consequently, the parameters to be obtained from the fits are no longer the dust mass and temperature, but rather the dust mass and its 3D spatial distribution.

3.6.1 *Fitting function*

To arrive at a formal definition a simple case is assumed first – a single source at a 3D position $\vec{r}$ in the line of sight k. The modelled brightness is by definition

$$\overset{\text{model}}{B^k_\nu}(\nu_{\text{em}},\vec{r}) = \frac{dB^k_\nu(\nu_{\text{em}},\vec{r})}{dM_{\text{d}}} \cdot M^k_{\text{d}}(\vec{r}) \tag{3.6.1}$$

If the first term on the right-hand side were known, the fitting process would yield the dust mass $M^k_{\text{d}}(\vec{r})$ at the 3D position $\vec{r}$, and this is all that is needed to calculate the emission since a model for the brightness at a distance $\vec{r}$ is now known. Therefore, all that is left to do is to model the term dB_ν/dM_{d}, which has already been referred to as “illumination”[20].

From Equation 3.2.1, it is clear that the brightness is proportional to the emitting mass, provided that the dust is transparent in the considered band (which is substantially true for MIR/FIR, the band of interest). Since B_ν and M_{d} are proportional, it makes no difference whether it is a single grain or an extended source. The total mass of all species i is obviously defined as:

$$M_{\text{d}}(\vec{r}) = \sum_i M^{(i)}_{\text{d}}(\vec{r}). \tag{3.6.2}$$

---

[20] It does not really matter whether it means luminosity per unit mass (as was the case for instance in Fig. 3.12) or brightness per unit mass (as is the case here), since they are proportional.

Introducing the operation $\langle x \rangle^{(i)}$ which subtends an average over the size distribution:

$$\langle x \rangle = \int x n(a)\,\mathrm{d}a \tag{3.6.3}$$

the total mass of the i-th species $M_\mathrm{d}^{(i)}$ can be expressed as a function of the number of dust grains N_d, the grain density $\rho^{(i)}$, and its average volume $\langle V \rangle^{(i)}$:

$$M_\mathrm{d}^{(i)} = N_\mathrm{d} \cdot \langle M_\mathrm{d}^{\mathrm{sg},(i)} \rangle = N_\mathrm{d} \cdot \rho^{(i)} \langle V \rangle^{(i)} = N_\mathrm{d} \cdot \frac{4\pi}{3} \rho^{(i)} \langle a^3 \rangle^{(i)}. \tag{3.6.4}$$

On the other hand the brightness $B_\nu(\nu_\mathrm{em}, \vec{r})$ is expressed in Equation 3.1.21 for a single grain. By multiplying it by N_d and putting it all together, one finds:

$$\frac{d\mathrm{B}_\nu^k(\nu_\mathrm{em}, \vec{r})}{\mathrm{d}M_\mathrm{d}} = \frac{3}{4A} \frac{\sum_i \int B_\nu^{\mathrm{sg},(i)}(a, \nu_\mathrm{em}, \vec{r}) a^2 n^{(i)}(a)\,\mathrm{d}a}{\sum_i \rho^{(i)} \int a^3 n^{(i)}(a)\,\mathrm{d}a} \tag{3.6.5}$$

which yields the total IR illumination of the dust at a position $\vec{r}$ as a function of the physical properties of the grains and the UV radiation field. Here the superscript k is only related to the solid angle through the emission area – for instance, k could indicate a single pixel of the IR maps used, and $A = \Delta l^2 = 0.0040\,\mathrm{pc}^2$ (see page 80). It should be noted that the dependence on the number of grains is gone, as did any non-standard normalisation for the distribution $n(a)$ (the number of hydrogen atoms, in the case of W&D). A noteworthy implication is that there is no formal difference between working with columnar or volumetric quantities in the fitting phase.

Now that the model in Equation 3.6.1 has been defined, it can be generalised to extend to a more useful test case. Indeed, along a given line of sight, there are typically multiple dusty structures at different 3D positions, and the assumption of a single emitter is inadequate. Moreover, one of the most crucial lessons learned from the 2D attempt is that even within the CC, there is a significant amount of dust that is considerably colder and lies in an orbital plane different from that of the filaments. As a result, it is appropriate to define an additional background term (also including the foreground). A more general formulation would be:

$$\overset{\mathrm{model}}{B_\nu^k}(\nu_\mathrm{em}) = \sum_s \frac{\mathrm{d}B_\nu(\nu_\mathrm{em}, \vec{r}_s^{\,k})}{\mathrm{d}M_\mathrm{d}} \cdot M_\mathrm{d}(\vec{r}_s^{\,k}) + B_\nu^{\mathrm{BG},k}(\nu_\mathrm{em}) \tag{3.6.6}$$

such that each structure s is located at a position $\vec{r}_s^k$ along the line of sight k. However, to avoid adding further degrees of freedom to the model, $\vec{r}_s^k$ must be known – this approach only works because a 3D model of the spatial distribution of the structures already exists (Section 3.2.1). The local background[21] contribution to the total SED is denoted by $B_\nu^{\mathrm{BG},k}(\nu_{\mathrm{em}})$ and it is defined as

$$B_\nu^{\mathrm{BG},k}(\nu_{\mathrm{em}}) = B_\nu^{\mathrm{BG}}(\nu_{\mathrm{em}}) \cdot \Lambda^k. \tag{3.6.7}$$

with the scalar Λ^k representing the background intensity, and the term $B_\nu^{\mathrm{BG}}(\nu_{\mathrm{em}})$ indicating its spectrum. This formulation implies a strong assumption, namely that the SED of the local background can be considered constant throughout the region. Although in principle this is not true, as the emission temperature depends on distance, the variation could be sufficiently small.

Equation 3.6.6 can be finally rewritten in a rigorous way:

$$\overset{\text{model}}{B_\nu^k}(\nu_j) = \sum_s \frac{\mathrm{d}B_\nu(\nu_j, \vec{r}_s^k)}{\mathrm{d}M_\mathrm{d}} \cdot M_\mathrm{d}(\vec{r}_s^k) + B_\nu^{\mathrm{BG}}(\nu_j) \cdot \Lambda^k \tag{3.6.8}$$

which expresses the modelled brightness in a line of sight k as a function of $s+1$ variables: s mass values $M_\mathrm{d}(\vec{r}_s^k)$ plus a single Λ^k value. These values are obtained through the minimisation of a chi-square function:

$$\chi_k^2 = \sum_{j=1}^{\text{maps}} \frac{\left| \overset{\text{model}}{B_\nu^k}(\nu_j) - \overset{\text{data}}{B_\nu^k}(\nu_j) \right|^2}{\sigma_{j,k}^2} \tag{3.6.9}$$

where the total number of data points j corresponds to the number of brightness measurements in that line of sight (that is, six), and with $\sigma_{j,k}$ being the uncertainty on the brightness at the j-th frequency. Our six data points per pixel are then enough to fit up to five known structures in the same line of sight, plus the local background – and this is more than enough for the three structures in the inner few parsecs.

---

[21] The term "background" here indicates an additional emitting component which is not in the modelled orbital planes (NA, HB, CNR) and thus constitutes a "local" background or foreground by its very definition. Obviously, it is a completely different layer from the Galactic background subtracted in Section 3.2.2, although having two different background layers might come off a bit confusing.

Local background emission

To extract the SED of the local background, emission from three concentric rings at varying distances was considered, ensuring they did not intersect strongly emitting structures. These rings are depicted in Fig. 3.20, top right panel, overlaid on the background-subtracted Herschel 70 µm map where the colour scale has been chosen to highlight sub-dominant structures. The average SED for each wavelength computed over these rings is presented in the top left panel. While the outer ring displays an SED dominated by small brightness variations after the Galactic background subtraction, the inner ones exhibit remarkably similar SEDs – specifically, the ratio between the two SEDs never deviates from the average by more than 7%. Naturally, there is no guarantee that this trend holds true in the more central regions, but it is a promising indication that this emission has a local origin. If it were linked to the CND, the background calculated at distances greater than the CNR would tend towards zero, whereas scrutiny of the inner filaments should be able to detect the cold component along the same line of sight. This will be verified a posteriori. To determine whether the background is locally valid or subject to larger fluctuations, one can study the spatial distribution of the emission colour. For this investigation, only the two inner shells are selected. The distribution is illustrated in the lower panels, for the colours 160 µm/100 µm, 100 µm/70 µm, and 70 µm/37 µm, as a function of Galactic coordinates. From the colour fluctuations on scales of approximately $\sim 10''$, it is evident that the selection includes some structures – some of which are also visible on the map, in the inner shell to the west – but no specific trends are observed, except perhaps for a weak dependence of the 160/100 colour on latitude which is not unexpected since the CND projected axis is tilted by only 20° with respect to the Galactic Plane. Generally, adopting the SED of the inner shell as the local background seems reasonable.

Model uncertainties

Since the modelled luminosity has been calculated in a semi-empirical manner, the total uncertainty is not solely constituted by the uncertainty on the datapoints (which includes the de-obscuration term, see Table 3.4). There are at least other two sources to consider: the calibration of the background SED $B_\nu^{\mathrm{BG}}(\nu_{\mathrm{em}})$, and the IR illumination term (see Equation 3.6.5). The contribution from the latter in particular needs to be detailed:

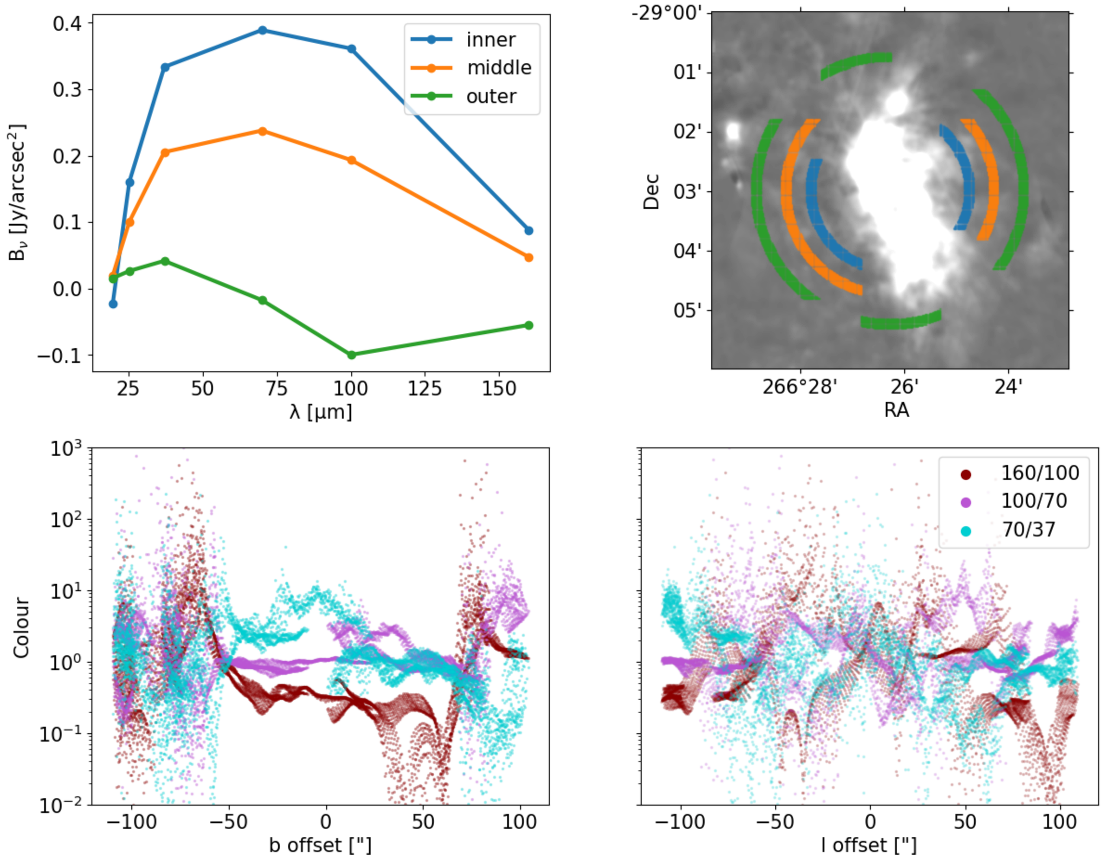

Figure 3.20: Local background average SED extracted in the three annuli (top left panel) defined at different distances from Sgr A* (top right panel). The 160 µm/100 µm, 100 µm/70 µm, and 70 µm/37 µm emission colours for all pixels in the three annuli are shown in the bottom panels, as function of their Galactic latitude (left panel) and longitude (right panel).

- The size distribution $n^{(i)}(a)$ has been evaluated in the local environment but is expected to vary significantly, especially being so close to a compact and luminous source of ionising radiation and CRs;
- The simulated UV radiation field density u_{rad} influences the grain temperature T_{d}. This is a key factor, as the goodness of the fit depends on how effectively contributions from structures at different positions along the same line of sight can be discerned, and such information stems from the temperature – in fact, as mentioned a few times, $B_\nu^{(i)}(a, \nu_{\mathrm{em}}, \vec{r}) = B_\nu^{(i)}(a, \nu_{\mathrm{em}}, T_{\mathrm{d}}^{(i)}(a, \vec{r}))$. Hence, an uncertainty term on brightness due to temperature deviations should be considered.

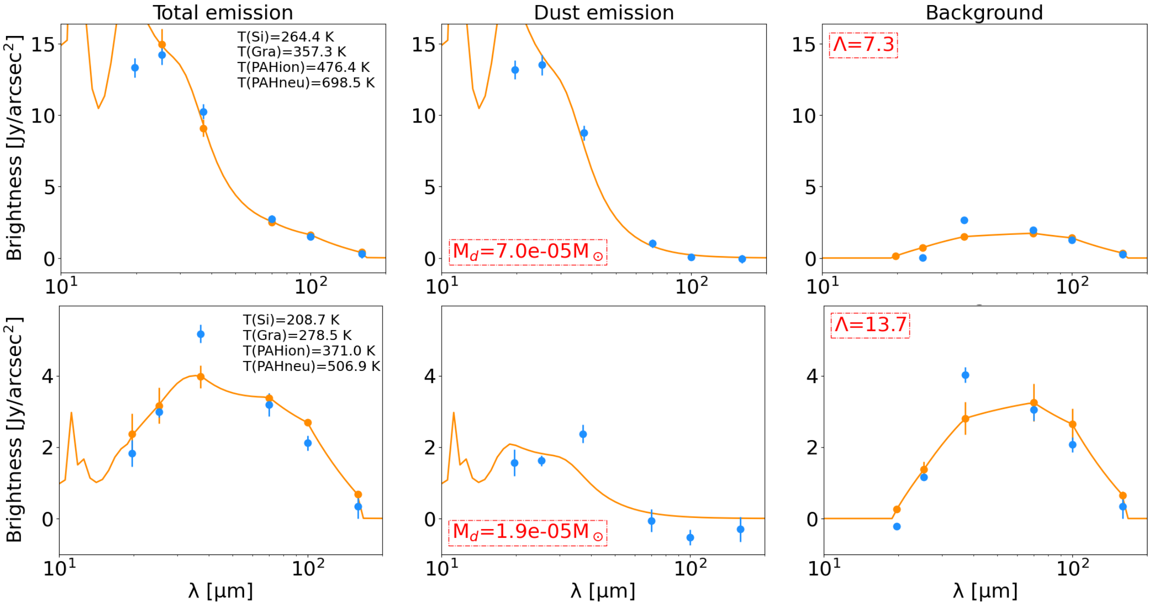

Figure 3.21: 3D Planck fits for different regions: close to Sgr A* on the NA (first row) and close to the Eastern intersection of CNR and HB (second row), exactly the same as Fig. 3.10. The total emission shown in the first column is divided between the modelled contribution from the dust (second column) and from the background (third column). The parameters extracted are reported in the red boxes. The datapoints from the IR maps are shown as blue points. The temperatures of the dust components are reported in the first column. These fits do not account for any additional cooling mechanism (see Section 3.6.2).

It is practically impossible to directly address the uncertainty on the size distribution in the chi-square, as brightness varies greatly depending on the smallest grain assumed in the dust mixture. It is more convenient to perform separate calculations assuming different compositions and to directly verify in the chi-square map whether a model is preferred. A similar argument can be made about temperature uncertainties: it is better to perform separate calculations for different NSC simulations and consider only the uncertainty arising from deviations in the modelled UV radiation field (which are calculated statistically, and thus can be minimised through a large number of simulations) given a certain set of NSC parameters.
To sum it up, the total variance used in the chi-square formula is

$$\sigma_{j,k}^2 = \sigma_{j,k}^2\big|_{\text{data}} + \sigma_{j,k}^2\big|_{\text{BG}} + \sigma_{j,k}^2\big|_{\text{T}}. \tag{3.6.10}$$

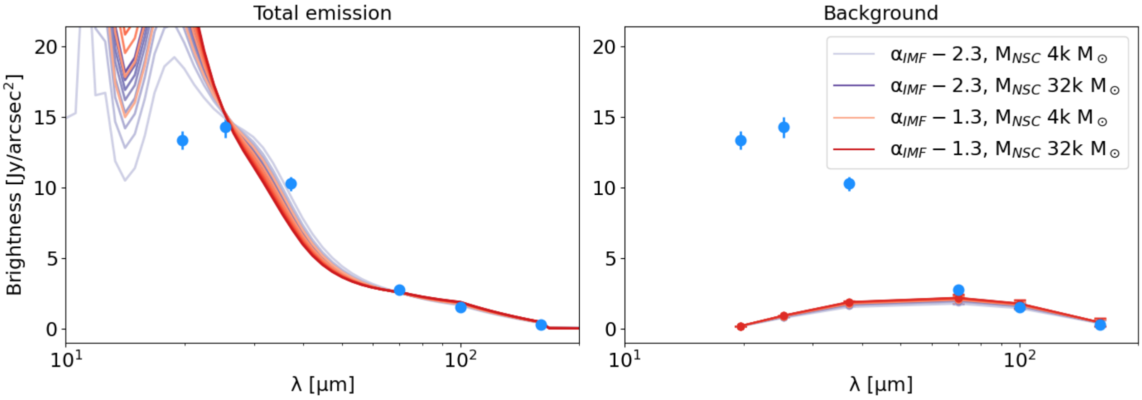

Figure 3.22: 3D Planck fits in the same line of sight as Fig. 3.21 (top panel) but adopting different NSC simulations: using $\alpha_{\rm IMF} = -1.3$ in red and using $\alpha_{\rm IMF} = -2.3$ in purple, and 8 $M_{\rm NSC}$ values each. The larger the mass of the NSC, the brighter the hue. Only the largest and the smallest NSC masses have been labelled in the legend.

3.6.2 *3D Planck fits on the NA without additional cooling*

In an analogous way to what was done in Section 3.3, the first step is to verify that the model works in a simple case – in a region where only one structure is presumed to be present along the line of sight. In this case, selecting the NA becomes an almost obligatory step, given that this is where the 2D fit failed. But for an initial visual comparison between the two methods, Fig. 3.21 shows a fit in the same pixels as in Fig. 3.10. The total emission is shown in the first column, and is divided between the dust contribution at the 3D position $\vec{r}^k$ and the background. The parameters obtained from the fit (M^k and Λ^k) are displayed in their respective panels. The substantial difference from the 2D fits is that temperatures are obtained for each species and each grain size, and the background temperature is fixed (Λ^k can be converted to a mass, as will be seen in Section 3.6.6).

The concerns raised in the previous section, noting that the modelled temperatures seemed too high, are confirmed by the profiles observed in the figure. The temperatures are significantly higher both compared to the results of the 2D fit and to the values found in the literature [75]. There is no way the model can reproduce both the emission colour ratios of 25.3/19.7 μm and 37.1/25.3 μm. If it fits the latter (top part of the figure, line of sight closer to Sgr A*), the spectral point at 19.7 μm is not fitted, and the emission peak is misinterpreted at shorter wavelengths – implying hotter emissions – and likely underestimating the background. Conversely, if the model fits the spectral points at 19.7 μm and 25.3 μm, it tends to lower the dust mass to compensate for such high temperatures – resulting in an overestimation of the background instead. This effect is evident in all lines of sight, on each orbital plane, and for any set of NSC simulations: see for instance Fig. 3.22, where the fit is attempted by using a few different NSC simulations, and indeed the best fit is found for the least hot illumination: $\alpha_{\mathrm{IMF}} = -2.3$, $M_{\mathrm{NSC}} = 4000\,\mathrm{M}_{\odot}$ – but the emission is still too hot, with an evident background underestimation. It is clear that the adopted dust model is not suitable for describing the observed IR emission unless physically motivated temperature corrections are introduced, as mentioned at the end of the previous section.

Just as in Section 3.3, one might want to devise a test to verify that the 3D mass allocation is appropriate. However, it is no longer possible to perform a radial profile test of the illumination, as it is now one of the model parameters (in other words, its profile is $1/r^2$ by construction). It is important to note that this is true only within a single parameter set. Allowing one of the parameters to freely vary in each pixel does not guarantee that the system will compensate for this variation while maintaining the theoretical illumination profile; verifying this serves as a good stability test for the entire procedure.

The best parameter to vary is the mass of the NSC, for several reasons: it is a scalar, the system's energy scales linearly with the stellar mass, and varying it does not alter the SED of the UV/optical emission (as it would happen, for example, with the IMF). Furthermore, allowing it to be a free parameter in all lines of sight allows for an exploration of the capabilities of IR SED fitting in constraining the stellar mass of the NSC. However, the illumination is modelled from a UV radiation field obtained from thousands of simulations, so M_{NSC} cannot vary during the fitting process. Therefore, a grid of NSC simulations was set up, varying the mass between 4000 and 32 000 $\mathrm{M}_{\odot}$ in steps of 4000 $\mathrm{M}_{\odot}$, and the IMF index between −1.3 and −2.3 in steps of 0.2. It was realised that the system is not sensitive to such small spectral index variations, so only the two extreme values of −1.3 and −2.3 were retained. For each IMF value, the preferred M_{NSC} value was investigated in a pixel-by-pixel fit.

The result is predictable when looking at Fig. 3.22: due to the temperature excess, the fit always prefers the lowest possible stellar mass, making the test inconclusive. Without additional cooling sources, the M_{NSC} value preferred by the data in all lines of sight is consistently 4000 $\mathrm{M}_{\odot}$.

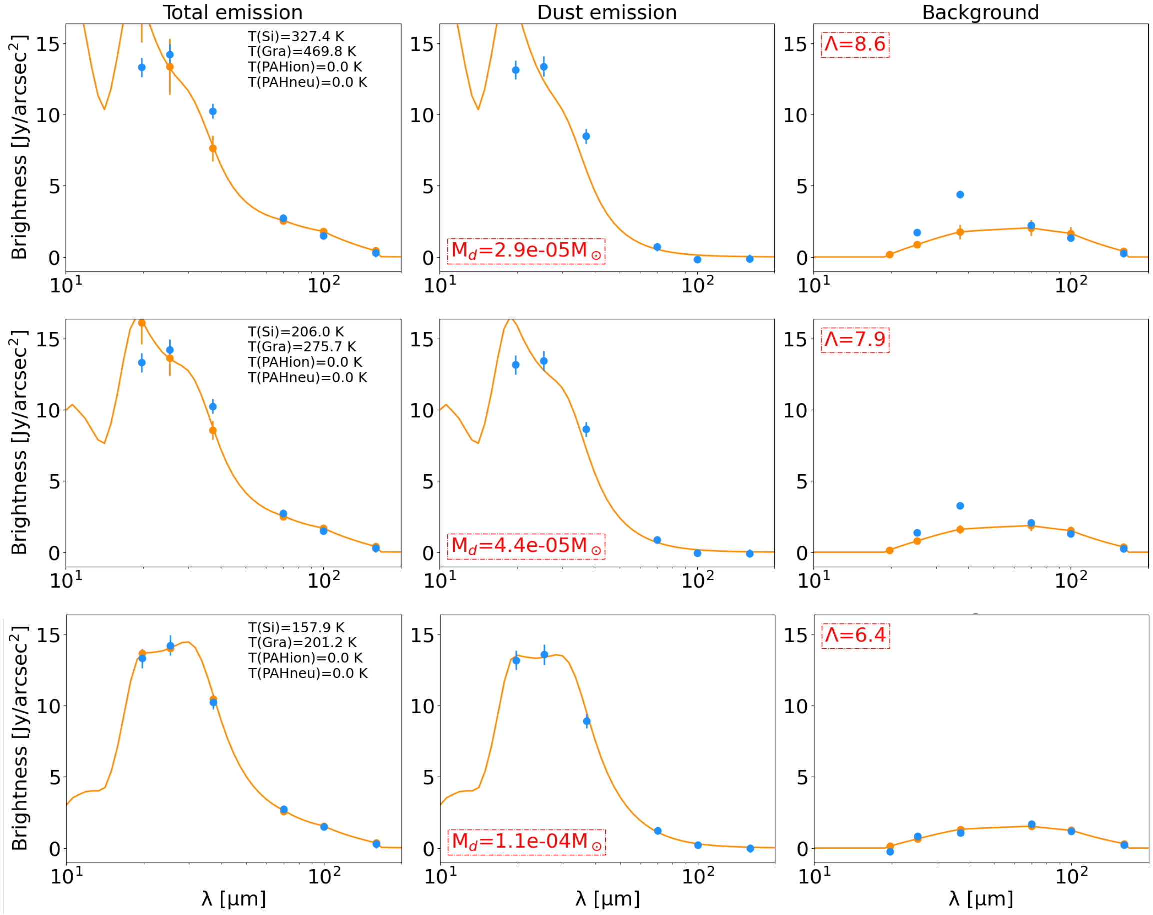

Figure 3.23: 3D Planck fits in the same line of sight as the top panels in Fig. 3.21, but varying the minimum grain size to 0.01 μm(top panels), 0.10 μm (mid panels) and 0.22 μm (bottom panels). From top to bottom, the reduced chi square values are 18, 10, and 0.65.

3.6.3 *Minimum grain size*

In the quest to identify physical mechanisms for the cooling of dust, one is naturally inclined to modify the grain size distribution in order to obtain grains that are, on average, larger and consequently colder (see Fig. 3.17). On one hand, it could be justified by a radiation field so intense that it photo-evaporates smaller grains. After all, the composition of the W&D model has been calibrated in the local interstellar medium (LISM), and expecting the same one in environments that appear vastly different in terms of physical conditions, chemical makeup, and star formation history, does not sound convincing. Additionally, various interstellar processes can affect grain distribution [63] (such as sputtering, photolysis, coagulation, vaporisation and shattering due to collisions, atom accretion, and interaction with CRs and high-

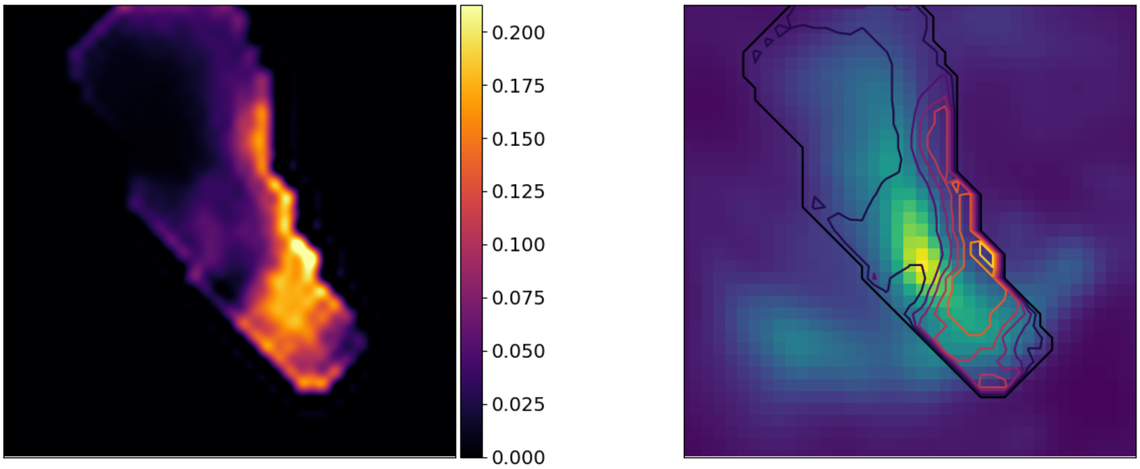

Figure 3.24: Spatial distribution of the minimum grain size on the NA, obtained by relaxing the constraints on the minimum grain size in the Planck fits. The distribution is also plotted on the right panel as contour lines onto the SOFIA 25.3 µm map. The grain size is in µm.

energy radiation). A size-dependent separation of components due to anisotropic starlight is also possible [63]. At the same time, altering the chemical composition in the models is a delicate task because it radically changes the energetics of the emission. Consequently, despite all the caveats introduced, it is not advisable to make changes unless they are strongly motivated by observations (as in the case of PAHs [138]).

The effect on the SED of imposing a lower limit on grain size has been studied along the same line of sight depicted in Fig. 3.21, that is, a few arcseconds away from Sgr A*. The result is shown in Fig. 3.23. The minimum grain size was initially set to 0.01 µm to exclude PAHs from the mixture (Fig. 3.17). By raising the minimum size to 0.10 µm – a value much higher than what is normally expected – temperatures approach 200 K (graphite is subdominant, see Fig. 3.19), but a very high threshold (0.2 µm) is required to reach the expected temperatures on the NA so close to Sgr A* and to reduce the effect of the silicate emission at 20 µm which complicates fitting the lower-wavelength SOFIA datapoint. In the process, the reduced chi-square decreases from 18 to 10 to 0.65.

The value of 0.22 µm arises from setting the minimum grain size as a free parameter in the fit. It results in a rather high value (though not completely unreasonable considering that it lies at only 2″ from Sgr A*: a lower limit of 0.1 µm in extreme UV radiation fields is hypothesised, for example, in [159]), but it allows for temperatures to be found within the correct range. This allows for the stability test introduced and attempted in Section 3.6.2, since a pixel-by-pixel fit on a M_{NSC} grid should not converge on the smallest value anymore but should assemble a M_{NSC} "map" of the values preferred by data, thus enabling the exploration of the illumination profile. Furthermore, even though it was conceived as a tool to lower temperature, the map of the minimum grain size values reported in Fig. 3.24 shows a rather reassuring result for its physical significance: the higher values are found in proximity to the NSC or at the edges of filaments facing it (see the right panel), suggesting that dust in the low mass density cavity is more easily destroyed, but that within the filaments the shielding is highly effective.

The spatial distributions on the NA of the main parameters obtained are presented in Fig. 3.25. The mass distribution is very encouraging: it shows an outflow in which the density increases radially, as one would expect in an orbiting filament. The quantities are comparable to those obtained with the 2D fit (Fig. 3.11). The background parameter Λ shows a slight displacement relative to the dust mass: although it might appear as a non-physical feature of the fit, it is due to the geometry of the CNR behind it, as will be seen in Section 3.6.6.

The obtained illumination map looks promising: it is almost centred around Sgr A*, with an extent that seems comparable to the NSC, yet the contour profiles ultimately do not deviate much from a central symmetry. This is encouraging, as a difference in the 3D orientation of two structures projected along the same line of sight would result in a mismatch, dependent on the direction on the 2D map, between the modelled 3D distance and its projection. Naturally, the definitive test consists of plotting its radial profile with respect to the 3D distance, which is shown in Fig. 3.26. The behaviour at distances above $0.2-0.3\,\mathrm{pc}$ follows a flux law, which is the desired outcome. This means that the method of fitting the SED in 3D works well for lines of sight where there is a single emission beyond a standard background. It should be noted that in the southern part of the NA there is actually an overlap with the HB, so this could account for the greater spread in illumination up to $0.5\,\mathrm{pc}$, even though so close to Sgr A* the actual distance should not be too different from the projected one.

On the other hand, a rather high spread of the values for M_{NSC} is observed, covering the entire range spanned by the simulations, except perhaps for $32\,000\,\mathrm{M}_{\odot}$ which is only reached at distances where the material is no longer on the NA but on the CNR. Given the greater de-projected distance, the illumination decreases. Regions within one parsec tend to select higher values for the NSC, whereas at greater distances –

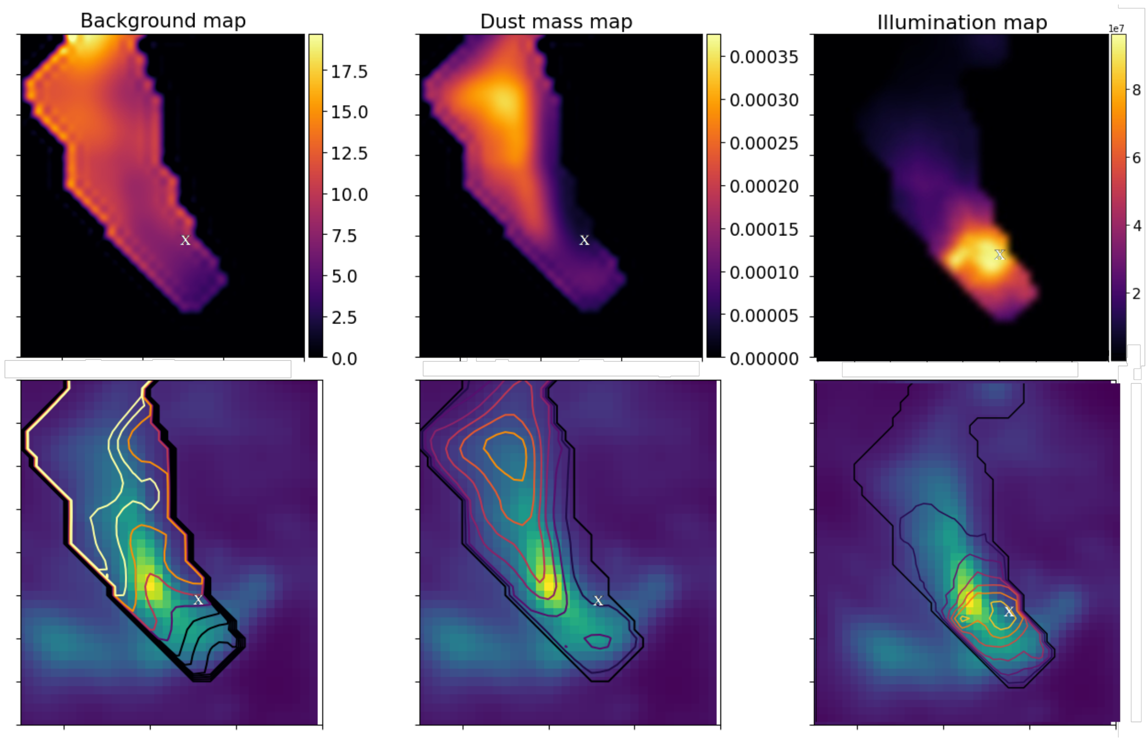

Figure 3.25: Spatial distributions on the NA of local background Λ, dust mass M_{d} and illumination dB_{ν}/dM, obtained through 3D Planck fits adopting the minimum grain size distribution in Fig. 3.24, in a 1.36 pc × 1.60 pc region. The distributions on top are plotted as contour lines on the bottom onto the SOFIA 25.3 μm map. The dust mass in a pixel of area 1.6×10^{-3} pc^2 is in solar mass units, while the illumination is in $\mathrm{L}_{\odot}/\mathrm{M}_{\odot}$. The position of Sgr A* is marked with a white cross.

perhaps the most indicative test for the NSC mass, as it is less affected by the stellar distribution in the cluster and by variations in minimum grain size – the value lies between 8000 and 24 000 $\mathrm{M}_{\odot}$, and is relatively uniformly distributed. In conclusion, the SED fitting of dust emission fails to constrain the mass of the NSC beyond a rather large interval 16 000 ± 8000 $\mathrm{M}_{\odot}$, although this measurement is merely a byproduct of this investigation.

In conclusion, adopting a variable minimum grain size greatly aids the fitting process, and the result can be coherently interpreted from a physical standpoint as well. However, the fit is far from perfect: the spread in the illumination profile (or in the derived dust masses) is rather significant, and the accumulation towards the profile corresponding to 4000 $\mathrm{M}_{\odot}$ indicates that a single Planck function cannot often describe the 37.1/25.3 μm and 25.3/19.7 μm colours simultaneously, as seen in Section 3.6.2. This is not an issue that can be resolved by further adjusting the grain size since the emission from PAHs has already been eliminated, unless

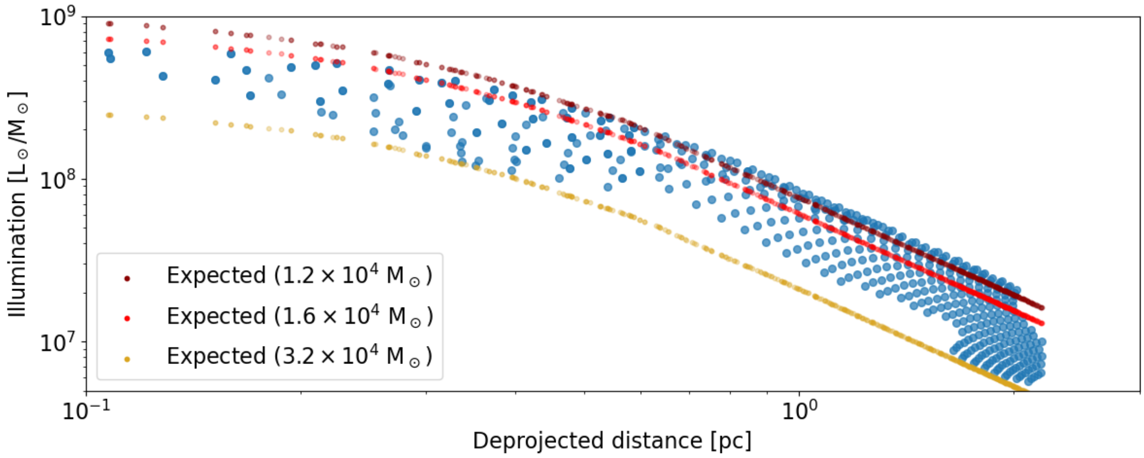

Figure 3.26: Illumination radial profile in the NA after minimum size corrections. Expected profiles calculated for different values of M_{NSC} are also shown, while $\alpha_{\mathrm{IMF}} = -1.7$.

one also wants to completely remove the contribution of silicates around 20 µm. Consequently, there is a need for an additional mechanism that allows for better fitting – specifically, one that reduces emission at shorter wavelengths more than at longer wavelengths. This mechanism is related to the opacity of the dust clumps, as described in the following part.

3.6.4 *Dust clumpiness and opacity*

Up to this point, one of the implicit assumptions has been that the UV radiation field could propagate throughout the 3D space without obstacles – in other words, that dust is transparent to UV radiation, and that absorption by the dust affects only the dust's energetics and not the energetics of the radiation field. This is quite adequate if the dust is homogeneously distributed and provided it remains optically thin to UV, but not if it tends to aggregate into clumpy structures. In the latter case, one would expect that the internal dust within the clump is partially shielded from UV radiation, leading to a consequent alteration of the energy balance and emission temperature. A simple "universal" model for the grain brightness $B_\nu^{\mathrm{pix}}(a, \nu_{\mathrm{em}}, \vec{r})$ is no longer sufficient, because the straightforward relationship between position and emission temperature no longer holds – it must take into account the nature of the clumps (mainly the density distribution of the dust). Therefore, the main difference compared to the previous formulation is the introduction of a single new parameter

x that describes the grain's position within the clump:

$$B_\nu^{\rm pix}(a, \nu_{\rm em}, \vec{r}) \Longrightarrow B_\nu^{\rm pix}(a, \nu_{\rm em}, \vec{r}, x) \tag{3.6.11}$$

where it is assumed that the clump has spherical symmetry. Since the physical size of the clump is much smaller than the pixel size, when calculating the IR emission along a line of sight one must perform an average over the entire clump using a distribution function $\xi(x)$:

$$B_\nu^{\rm pix}(a, \nu_{\rm em}, \vec{r}) = \frac{\int B_\nu^{\rm pix}(a, \nu_{\rm em}, \vec{r}, x)\xi(x)\,{\rm d}x}{\int \xi(x)\,{\rm d}x}. \tag{3.6.12}$$

In this formula, there is a reasonable implicit assumption: that the grain size distribution is the same everywhere within the clump – in other words, that $n^{(i)}(a)$ is not a function of x. The question now is how to model the dependence on x. Since, as stated, the physical parameter varying within the clump is the temperature, the conservation law in Equation 3.1.12 must be modified not just for $(a, \vec{r})$ but also for x, to obtain $T_{\rm d}^{(i)}(a, \vec{r}, x)$. In other words, one must solve:

$$L_{\rm abs}^{{\rm sg},(i)}(a, \vec{r}, x) = L_{\rm em}^{{\rm sg},(i)}(a, \vec{r}, x) \tag{3.6.13}$$

where the emitted luminosity is evidently given by:

$$L_{\rm em}^{{\rm sg},(i)}(a, \vec{r}, x) = \int 4\pi^2 a^2 Q_{\rm abs}^{(i)}(a, \nu) BB_\nu(\nu, T_{\rm d}^{(i)}(a, \vec{r}, x))\,{\rm d}\nu. \tag{3.6.14}$$

Therefore, in the end, it all boils down to modelling the dependence of the UV radiation field on x or, from a purely physical perspective, the attenuation of UV illumination due to the clump's opacity. Assuming that the properties of the radiation field outside the clump are not influenced by the clump seems reasonable, so the previous calculation of $u_{{\rm rad},\nu}(\nu, \vec{r})$ remains valid externally. Thus, in general, one can write:

$$u_{{\rm rad},\nu}^{(i)}(\nu, \vec{r}, x) = u_{{\rm rad},\nu}^{\rm out}(\nu, \vec{r})\Phi^{(i)}(\nu, x) \tag{3.6.15}$$

where the contribution from opacity Φ depends not only on the position of the clump but also on the frequency – as one would expect from dust extinction. To make explicit the analytic form of $\Phi^{(i)}(\nu, x)$, it is necessary to clarify its physical meaning. Up to now, it is clear that x is either a physical distance (a radial distance in

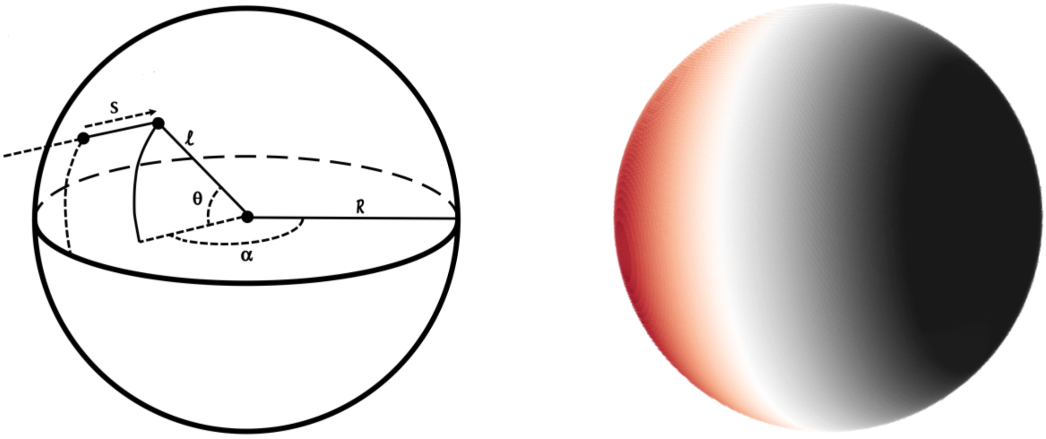

Figure 3.27: Left panel: depiction of a spherical clump illuminated by a single source in the direction of s. Right panel: high-transparency simulation of the temperature inside a clump when the UV radiation comes from a single direction, calculated using Equation 3.6.25.

the spherical clump, or a chord) or a quantity related to it. A rather straightforward physical interpretation naturally arises by noting that:

- from Equation 3.6.15, the function $\Phi^{(i)}(\nu, x)$ is the ratio between internal and external illumination, where the attenuation is due to dust extinction – hence it should be in the form of exponential decay;
- the physical properties of the dust grains are assumed to be the same everywhere within the clump – in other words, the dependence on x and ν is separable within Φ.

Consequently, one obtains

$$\Phi^{(i)}(\nu, x) = \exp\left(-\tau^{(i)}(\nu, x)\right) = \exp\left(-\psi(x) \cdot \zeta^{(i)}(\nu)\right). \tag{3.6.16}$$

To define the analytic forms of $\psi(x)$ and $\zeta^{(i)}(\nu)$, it is necessary to model the clump. For a visual representation of the geometric quantities, refer to Fig. 3.27. Let R be the radius of the spherical clump, and l the radial distance. A single UV source illuminating the clump from a direction $\hat{s}$ is assumed. To model the decrease in illumination in the direction $\hat{s}$ within the clump, the penetration distance s must be defined. Finally, for convenience, the scaled variables $\tilde{l} = l/R$ and $\tilde{s} = s/R$ are introduced. The radiation field density then becomes

$$u^{(i),\hat{s}}_{\mathrm{rad},\nu}(\nu, \tilde{s}) = u^{\mathrm{out},\hat{s}}_{\mathrm{rad},\nu}(\nu) \exp\left(-\tilde{s} \cdot \frac{\mathrm{d}\tau^{(i)}(\nu)}{\mathrm{d}\tilde{s}}\right). \tag{3.6.17}$$

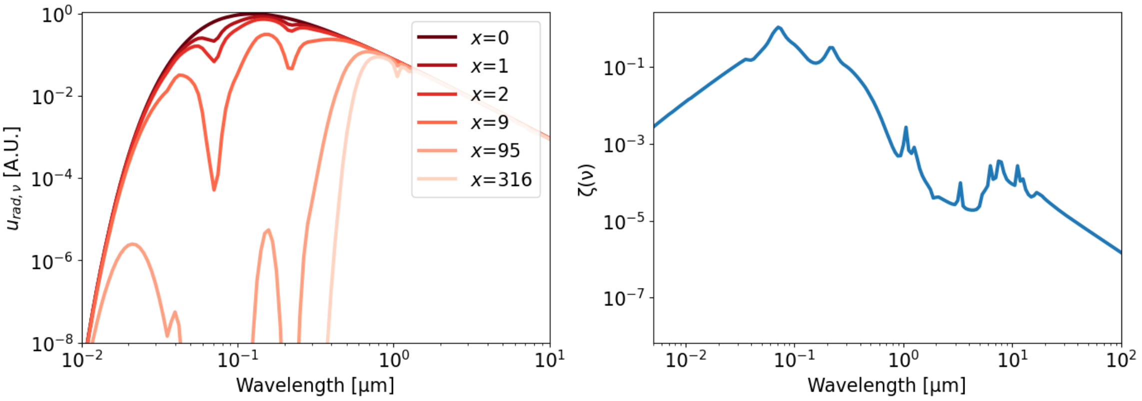

Figure 3.28: Left panel: radiation field density at different opacity values, calculated according to Equation 3.6.22 and normalised to the peak value. The integrated radiation field densities are lower by a factor 1, 0.71, 0.52, 0.15, 0.01 and 0.005 respectively. Right panel: the function $\zeta(\nu)$ (Equation 3.6.21), which accounts for the dependence of opacity on frequency.

$\tau(\nu)$ must be calibrated for a reference value $\nu_{\rm ref}$, for a species i and at a specific position – chosen to be the centre of the clump. The calibrated value is denoted by $\tau^{\rm c}_{\rm ref}$:

$$\tau^{\rm c}_{\rm ref} = \tilde{s}^{\rm c} \cdot \frac{{\rm d}\tau(\nu_{\rm ref})}{{\rm d}\tilde{s}} = \frac{{\rm d}\tau(\nu_{\rm ref})}{{\rm d}\tilde{s}} \tag{3.6.18}$$

($\tilde{s}^{\rm c} = 1$ by definition), and therefore

$$\tau^{\rm c}(\nu) = \frac{{\rm d}\tau(\nu_{\rm ref})}{{\rm d}\tilde{s}} \cdot \frac{{\rm d}\tau^{(i)}(\nu)}{{\rm d}\tau(\nu_{\rm ref})} = \tau^{\rm c}_{\rm ref} \cdot \zeta^{(i)}(\nu) \tag{3.6.19}$$

so that Equation 3.6.17 becomes

$$u^{(i),\hat{s}}_{{\rm rad},\nu}(\nu,\tilde{s}) = u^{{\rm out},\hat{s}}_{{\rm rad},\nu}(\nu)\exp\left(-\tilde{s} \cdot \tau^{\rm c}_{\rm ref} \cdot \zeta^{(i)}(\nu)\right). \tag{3.6.20}$$

Now, the variables and functions can be explicitly defined:

$$x = \tilde{s} \cdot \tau^{\rm c}_{\rm ref} \qquad \zeta^{(i)}(\nu) = \frac{Q^{(i)}_{\rm ext}(\nu)}{Q^{(i)}_{\rm ext}(\nu_{\rm ref})}. \tag{3.6.21}$$

Given our choice of parameterisation, x corresponds to the optical depth at a reference value $\nu_{\rm ref}$. Its value is 0 outside the clump and an unknown value $x_{\rm max}$, which must be probed by data, at its centre. The frequency dependence is given by the dust extinction efficiency $Q^{(i)}_{\rm ext}(\nu)$ and must be normalised to the same reference value

ν_{ref} for all chemical species i. Additionally, since $Q_{\text{ext}}^{(i)}$ is also a function of grain size – and the radiation field should not depend on individual species but on the mixture – Equation 3.6.21 implicitly averages over the grain size distribution, according as usual to Equation 3.6.3. It should be noted that the normalisation of x depends heavily on the choice of ν_{ref}, since x is proportional to $Q_{\text{ext}}(\nu_{\text{ref}})$ and the extinction varies by orders of magnitude. For simplicity, the frequency of maximum scattering was chosen as reference value ($\nu_{\text{ref}} = 0.13\,\mu\text{m}$), which means that ζ is very low on average, with x consequently large.

In the end, from Equation 3.6.15, a specific formula for the radiation field density is obtained:

$$u_{\text{rad},\nu}^{(i)}(\nu,\vec{r},x) = u_{\text{rad},\nu}^{\text{out}}(\nu,\vec{r})\exp\left(-x\cdot\frac{Q_{\text{ext}}^{(i)}(\nu)}{Q_{\text{ext}}^{(i)}(\nu_{\text{ref}})}\right) \tag{3.6.22}$$

where an integration over all directions $\hat{s}$ containing UV sources is assumed:

$$u_{\text{rad},\nu}^{(i)}(\nu,\vec{r},x) = \sum_{\hat{s}} u_{\text{rad},\nu}^{(i),\hat{s}}(\nu,\vec{r},x). \tag{3.6.23}$$

An integral formula for the absorbed UV luminosity is finally obtained:

$$L_{\text{abs}}^{\text{sg},(i)}(a,\vec{r},x) = \int \pi a^2 Q_{\text{abs}}^{(i)}(a,\nu)u_{\text{rad},\nu}^{\text{out}}(\nu,\vec{r})\exp\left(-x\cdot\frac{Q_{\text{ext}}^{(i)}(\nu)}{Q_{\text{ext}}^{(i)}(\nu_{\text{ref}})}\right)c\,\mathrm{d}\nu. \tag{3.6.24}$$

By solving the thermal equilibrium (Equation 3.6.13), temperatures can be calculated for various optical depths (an example is shown in Fig. 3.29), obtaining $B_\nu^{\text{pix}}(a,\nu_{\text{em}},\vec{r},x)$.

The meaning of the functional form $\xi(x)$ introduced in Equation 3.6.12 can now be explored. Generally speaking, the illumination within the clump depends on the direction of UV sources (see the right panel in Fig. 3.27), the size of the clump, and the distribution of dust within it. Calculating it would require a 3D model of each clump to determine the value of the radiation field at each position $u_{\text{rad},\nu}^{(i),\hat{s}}(\nu,\vec{r},l,\alpha,\theta)$:

$$u_{\text{rad},\nu}^{(i),\hat{s}}(\nu,\vec{r}) = \int_0^R \int_0^{2\pi} \int_0^{\pi} u_{\text{rad},\nu}^{\text{out},\hat{s}}(\nu,\vec{r})e^{-\tau^{(i)}(\hat{s},\nu,l,\alpha,\theta)}\mathrm{d}l\,\mathrm{d}\alpha\,\mathrm{d}\theta \tag{3.6.25}$$

and then a sum over all UV sources. Even imposing symmetries on the clump and the sources distribution does not reduce the number of variables by more than one. In a simplified approach, the parameter x accounts for the sum over all directions,

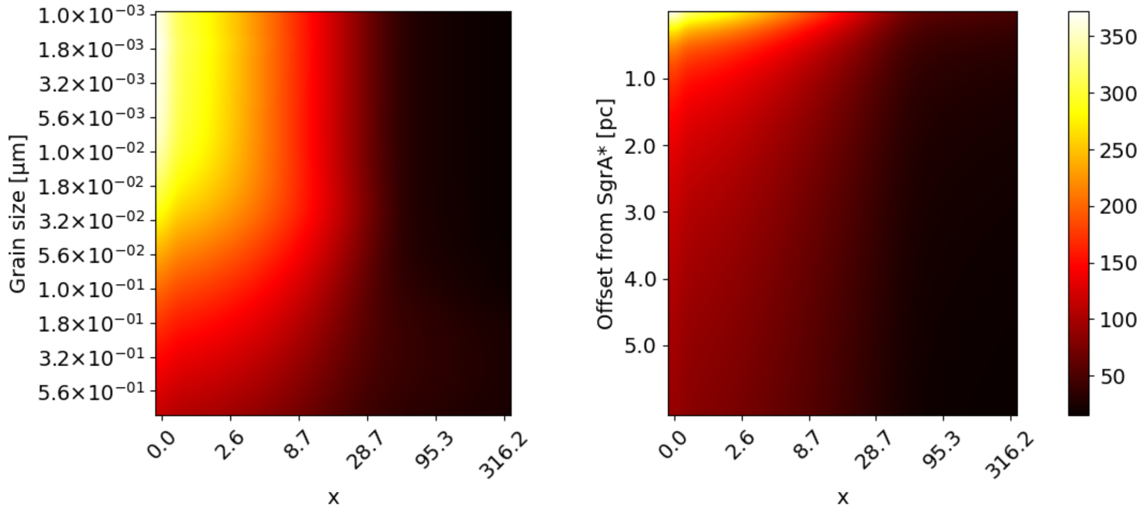

Figure 3.29: Left panel: silicate temperature map depending on grain size and opacity x, calculated in the position of Sgr A*. The column at $x = 0$ corresponds to the dashed dark red line in Fig. 3.17. Right panel: temperature map assuming a "standard" silicate grain, at different offsets from Sgr A* along the NSC elongation.

as well as the dependence of optical depth on angles. The density profile of the radiation field within the clump is so complex that using the distribution function $\xi(x)$ to obtain a distribution of optical depths seems to be a reasonable approach, especially considering that clumps are contained in quantity within the solid angle subtended by the pixels. $\xi(x)$ allows for the distribution of clump opacity everywhere with a single parameter, assuming that its form and domain (i.e., the value $x_{\max}$) are understood.

In Fig. 3.30, some examples are shown. Outside the clump ($s = 0$) or in a completely transparent clump ($\tau^{c}_{\mathrm{ref}} = 0$, blue line), the value of x is zero, and therefore the radiation field is unaffected at any point, resulting in a Dirac delta at $\Phi = 1$. However, in an opaque clump (red, green and yellow lines), due to the internal shielding, the total value of $u_{\mathrm{rad},\nu}$ ends up being lower, with the minimum value $u_{\min}$ corresponding to $x_{\max}$. Therefore, when lowering the temperature of some of the grains, the value of $x_{\max}$ is critical.

In Fig. 3.29 it is evident how the opacity of the clumps can dramatically lower their temperatures. A clearer perspective on how and why this allows for fitting both the emission colours 37.1/25.3 µm and 25.3/19.7 µm is also visually depicted in Fig. 3.31. This illustrates a simple case: a grain in which half of the mass is assumed to be on the opaque clump region with $x = 300$ (dark red line), while the other half

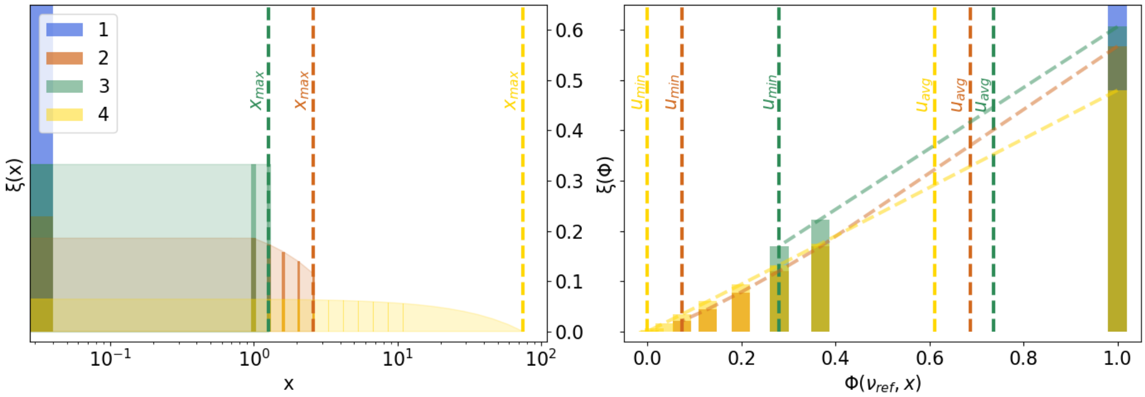

Figure 3.30: Dust distribution in the clump in four cases. 1: $\tau = 0$ (blue); 2: ξ linearly decreasing with x with $x_{\text{max}} \sim 3$ (red); 3: flat distribution with $x_{\text{max}} \sim 1$ (green); 4: ξ linearly decreasing with x with $x_{\text{max}} \sim 80$ (yellow). The distribution functions for the corresponding attenuation Φ are plotted in the right panel, calculated for the reference frequency value ν_{ref}. Vertical dashed lines indicate both the minimum attenuation u_{min} and the average value u_{avg}.

is not shielded from UV radiation at all (orange line). Consequently, their average – plus the local background given by Λ – allows for a model that fits all the points well, something impossible with a single dust temperature profile assuming a “standard” chemical composition. While lowering the temperature, the effect from dust clumps differs from that achieved by increasing the minimum grain size because the grain’s chemistry remains unchanged, and consequently, its SED would display different features at the appropriate temperatures. The fact that clump opacity lowers temperatures masks this, resulting in a similar profile. However, there is one parameter that is affected in a very different manner: the dust mass derived from the fit. Both methods increase it to compensate for the lower temperature, but opacity assumes that part of the dust mass is “hidden”, leading to a much greater increase – potentially infinite, considering a clump in which UV radiation does not penetrate beyond a certain distance. As a result, accounting for dust in clumps is a powerful but extremely delicate tool. The difference is not enormous for the purposes of calculating the IR radiation field, as what matters is the luminosity of the dust – but the situation changes for investigations where the dust mass is significant, for instance, if one wishes to infer the amount of gas.

This concept is closely related to the opacity distribution function. In the figure, a simple case has been presented, but generally the function ζ assumes different values over a large range, resulting in a more gradual and continuous variation of the

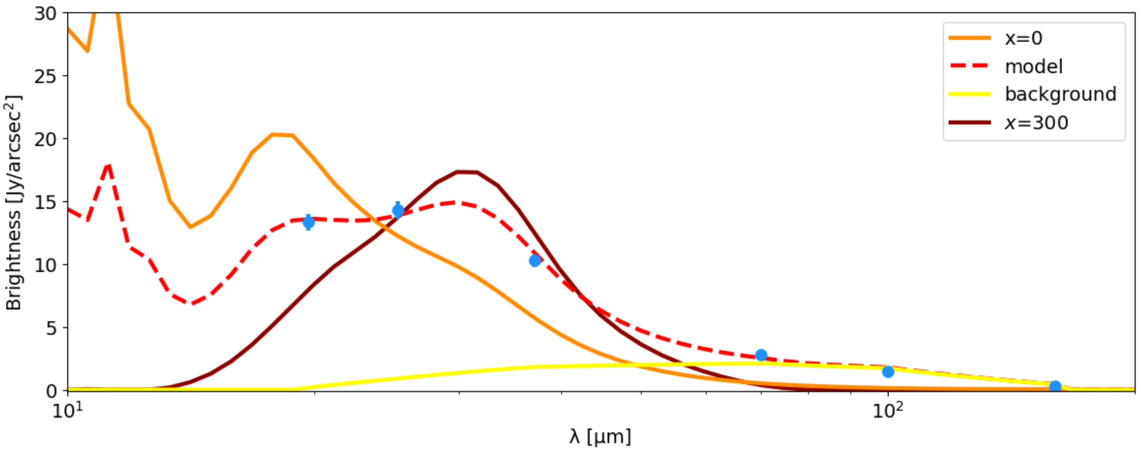

Figure 3.31: 3D Planck fit accounting for opacity corrections in the simple case of a single opacity value, for the usual test LoS (same as Fig. 3.23). The $x = 0$ orange curve is the standard non-opaque one, while the dark red curve is obtained for a very opaque clump ($x \simeq 300$). The resulting model (red line, dashed) is the sum of the local background and the average of the opaque and non-opaque emission.

SED. This alters the distribution of the dust mass within the clump and its relative contribution to the total SED, with either a decrease or an increase in the total mass depending on the assumed radial profile of opacity. In front of such complexity that cannot be constrained by the data, adopting the simplest and most effective case – namely the simple average between the central and peripheral emission as shown in the figure, which corresponds to flat profile #3 in Fig. 3.30 – seems to be a reasonable choice.

It is worth emphasising that, from a physical standpoint, clumpiness is not an alternative to the variation in grain size distribution, but it is rather complementary. Furthermore, applying opacity corrections on top of altering the grain size distribution minimises the impact of clumpiness on the derived mass. Consequently, since in Fig. 3.26 a significant spread in the illumination distribution around the value of $M_{\mathrm{NSC}} = 16\,000\,\mathrm{M}_\odot$ was observed, it is interesting to examine the interplay of the two cooling mechanisms. The result, extremely encouraging, is shown in Fig. 3.32: corrections for clumpy dust (on the right) considerably reduce the spread and provide an independent verification of the 3D emission distribution, with an average opacity $x = 103$. The fact that the opacity of the clumps is similar in limited regions of space (for instance, the highest corrections occur between 0.2 and 0.4 pc) may depend on the conditions of the interstellar medium (as an example, it is more likely that more compact clumps survive UV radiation within the NSC [58, 207, 208]).

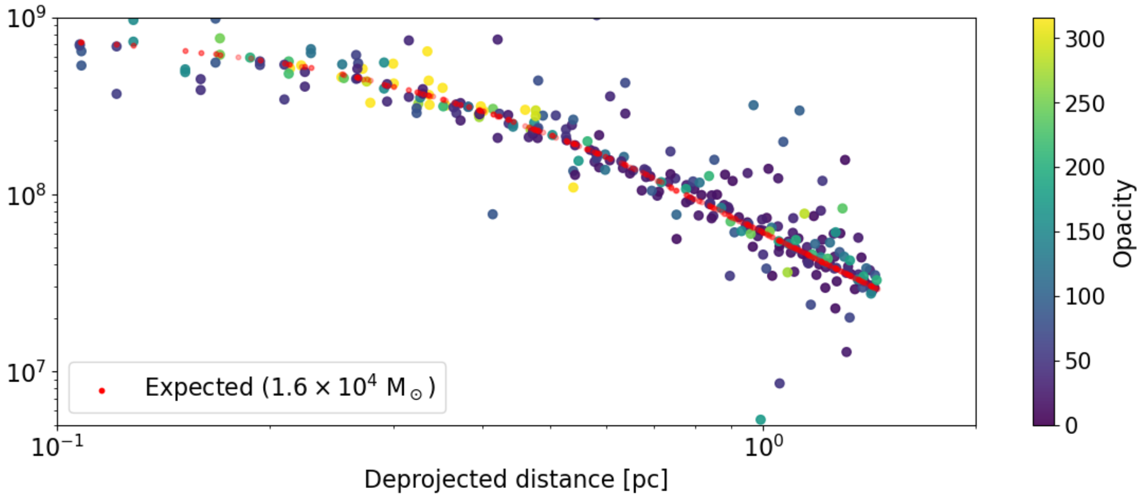

Figure 3.32: Illumination radial profile for the NA after correcting for the minimum grain size distribution (as in Fig. 3.26) and also accounting for a clumpy dust distribution. The datapoints have been coloured according to their $x_{\max}$ value.

One might consider investigating the mass of the NSC preferred by the data when accounting for clumpiness. In general, a less massive NSC produces lower temperatures, and therefore the corrections are simply less necessary on average. Unfortunately, in the absence of an independent measurement of local clumpiness, there is no way to ascertain whether the fit should favour higher or lower opacity values.

In conclusion, fitting the SED with a modified Planck function in 3D works well in lines of sight that contain a single known source, especially when adopting corrections on grain size and assuming that the dust is distributed in clumps. Naturally, the other known structures must also be investigated; however, most of the HB lies in the same projected direction as the CNR/CND to the east or the NA in the centre. While the overlap between HB and CNR poses no issues as their emissions are easily distinguishable, a different situation arises in the area south of Sgr A*, also known as the Bar, where HB and NA are very close to each other and consequently have very similar emissions. Modelling their intersection is the final refinement needed to ensure that the 3D maps of the entire region (Section 3.7) are reliable. The next section will address this specific point.

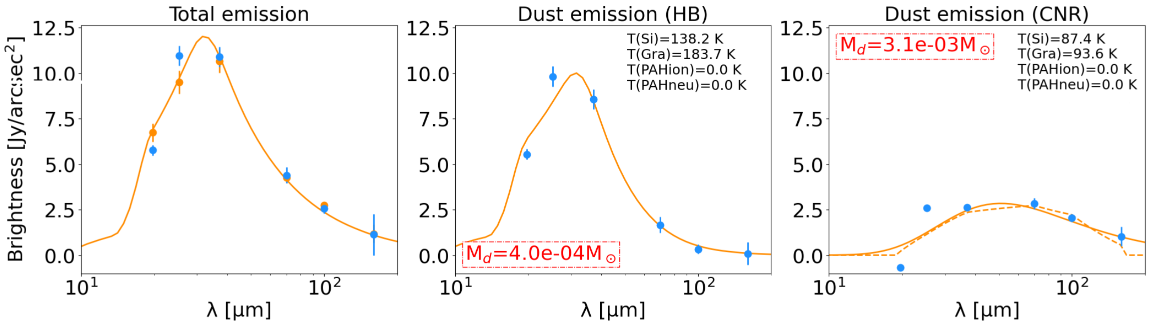

Figure 3.33: 3D Planck fits in the HB/CNR overlap region. The first column shows as usual the total dust emission, while the second and the third show the separate contributions from the two structures. The local background obtained with the fit is zero. The profile that would have been obtained without including the emission from the CNR is plotted with a dashed line and corresponds to $\Lambda = 11.5$.

3.6.5 *Multiple structures in the line of sight*

Modelling the overlap region between the CNR and the HB does not really pose a problem: their emission profiles are easily distinguishable because the inclinations of their respective orbital planes, and hence their 3D distances, are different. Consequently, the temperatures in the CNR are significantly cooler than those in the HB (this is not surprising when considering the IR maps in Fig. 3.7), and the emission is less affected by silicate and graphite features. Instead, the CNR is expected to contain the vast majority of the dust mass along the line of sight. Fig. 3.33 shows, as an example, the result of a fit obtained at the extremity of the eastern arm of the HB. In this case, the fitting formula used (compared to the general one in Equation 3.6.8) considers two structures simultaneously plus the background. The emission is dominated by the ionised filament with a temperature of about 140 K[22], but with approximately $\sim 20\%$ of the mass. The rest is distributed over the CNR. Moreover, whenever the CNR/CND are part of the line of sight, the local background is practically zero because the high-wavelength spectral points are already fitted by the low-temperature component. This reinforces the belief that the SED of the background in the lines of sight internal to the cavity traces the CNR. For comparison, the local background that would have been obtained without simultaneously fitting the CNR is shown with a dashed line. Even more so than in the case of the NA, the decisive test for ensuring that the mass fraction attributed to the HB is correct is checking the illumination inverse square law. However, this will

---

[22] Silicates dominate the emission when PAHs are cut out, as seen in Fig. 3.19

be addressed after dealing with the overlap in the Bar.

The overlap between the HB and NA is not as straightforward. As already mentioned, the temperatures of the two filaments in the Bar are similar because this is the region where the distance from Sgr A* is minimal, at the centre of the NSC. As a result, discerning their respective contributions to the total emission is not achievable through simultaneous fitting on the two orbital planes. One solution is to model the SED of one of the two structures and subtract it from the data points, in order to fit the residuals on the other. The choice was made to model the NA because it is longer, making it easier to observe trends in the profile and extrapolate them into the overlap region. Furthermore, the overlap region lies at a constant distance from Sgr A*: this suggests that the temperature should be quite constant, and therefore the modelled SED should not vary much. To check this, the SED was first evaluated on a few slices orthogonal to the direction of the filament. For convenience, a new coordinate has been defined – the "ridge coordinate" – which runs along the central axis of the filament, increasing from top to bottom. The slices were thus taken at various values of the ridge coordinate.

At sufficiently high distances from the source of the UV field, a fairly uniform temperature across an orthogonal slice is expected, and this is what is observed in the upper half of the NA. The colour of the emissions does not vary significantly in the selected pixels – with the exception of the spectral points at 19.7 μm on the western edge (to the right, in the convention of these maps). In other words, the 19.7/25.3 μm emission colour drops noticeably on the inner edge facing the CC. This trend is reinforced as one approaches Sgr A*, and may be related to the photo-evaporation effect due to the NSC at both low distances and material density (see the map in Fig. 3.24). In Fig. 3.34, the average SED on the reference slices is illustrated in the left panel, where the colour of the line gets darker the more the pixel is to the west. The position where it was extracted from is marked by the blue band in the right panel. While at any wavelength the ratio relative to the emission at 25.3 μm is constant, the 19.7/25.3 μm emission colour drops approaching the edge – with the exception of the last pixel, which is well outside the filament, in an area of very low density in the cavity, immersed in the radiation field of the NSC and therefore highly non-standard. Since it is external to the filament, the SED in that line of sight was not considered.

In addition to a valid SED model for the "latitudinal" directions (orthogonal to the ridge), constructing an emission model valid for all pixels in the region also requires

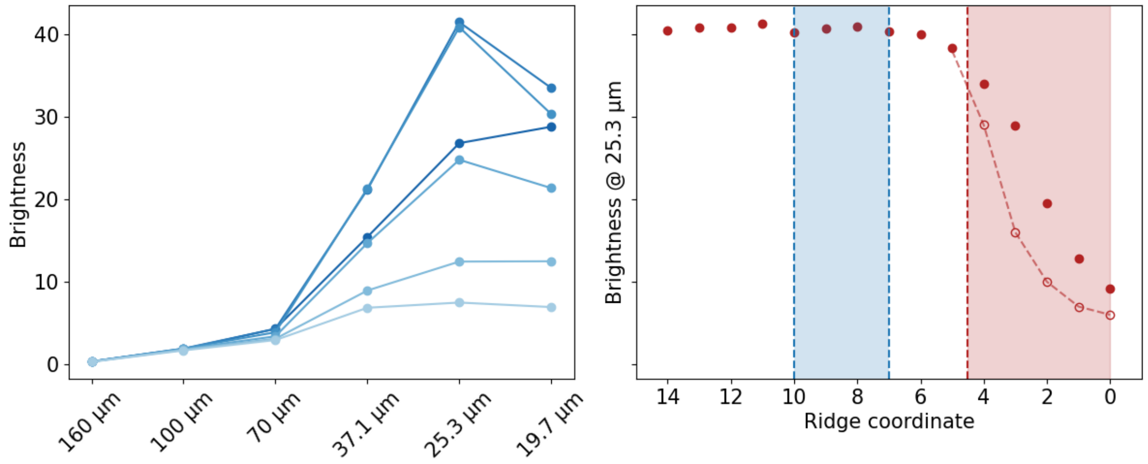

Figure 3.34: SED (left panel) and 25 μm profile (right panel) along the central and southern part of the NA (see text). The SEDs in the left panel are average values extracted from four orthogonal slices starting at a distance of 2 – 3 pixels from the Bar, and whose position is marked with a blue band in the right panel. The 6 profiles correspond to 6 pixels in a slice: the marker colour gets darker from left to right (from east to west). The red band marks the Bar position in the ridge coordinate. The ridge coordinate is in map pixels, the 0 corresponding to the bottom part of the Bar.

a "longitudinal" normalisation of the emission along the ridge. In this way, one can subtract the NA emission pixel-by-pixel and fit the residuals, assuming that the remaining dust resides on the HB. For the SED normalisation, the idea is to take the value of the 25.3 μm emission on the ridge and extrapolate its behaviour within the overlap region. The profile of the 25.3 μm emission along the ridge coordinate is shown in the right panel: the brightness is approximately constant until just before the overlap region (marked with a red band), followed by a sharp drop due to mass depletion in the area. This makes it difficult to extrapolate the expected amount of dust mass on the NA in the region, an operation that must therefore be performed iteratively between NA and HB, ensuring that the calculated mass profile is continuous with respect to the rest of the filament. For the initial normalisation (represented by the empty circles in the figure), a variable fraction of the observed brightness was chosen, compatible with the expected mass profile on the HB (in the intersection region, the ridge coordinate on the NA roughly corresponds to a latitudinal slice on the HB).

To verify that the intersection has been handled appropriately, one possibility is to check the SED on the HB's ridge in an analogous study to the one performed on the NA, and confirm that the behaviour on the latitudinal slices is similar in the

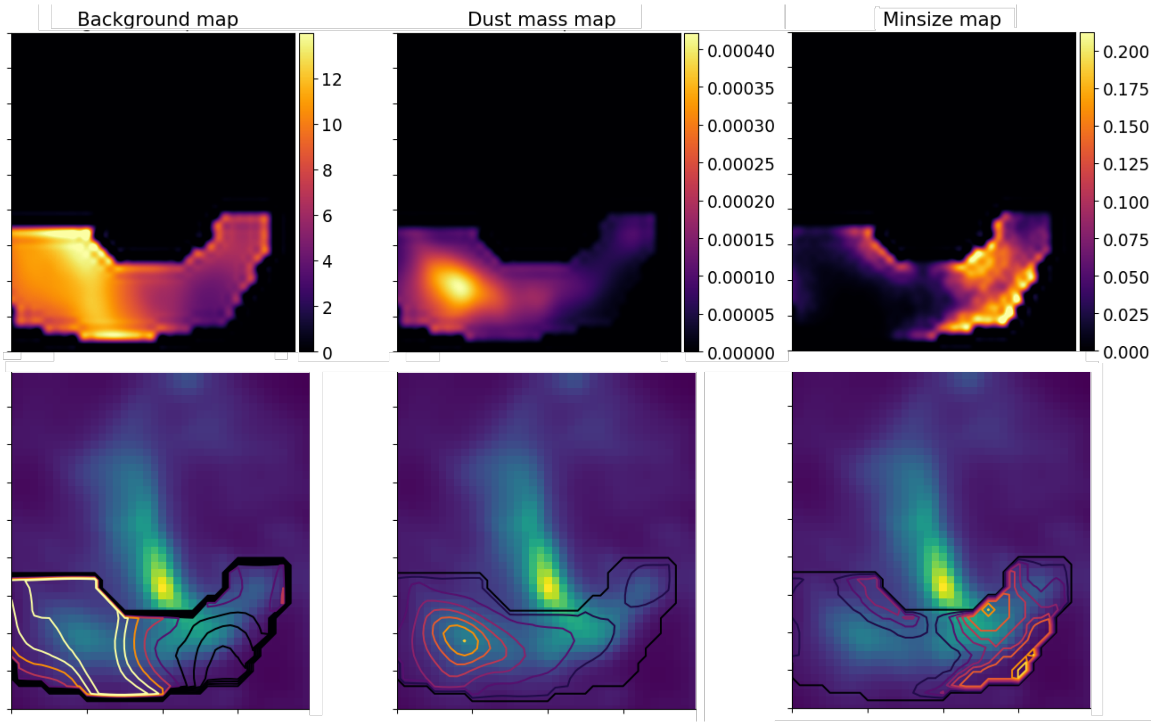

Figure 3.35: Spatial distributions on the HB of local background Λ, dust mass M_{d} and minimum grain size, obtained through 3D Planck fits. The distributions on top are plotted as contour lines on the bottom onto the SOFIA 25.3 μm map. The dust mass is in solar mass units.

modelled area. The HB is a filament very similar to the NA, with a nearly fixed SED in its eastern part, while it shows the same 19.7/25.3 μm colour trend on its northern edge as the NA showed on its western edge. This already serves as a positive test to verify that the intrinsic SED of the HB has not been altered. Another test involves plotting the profile of the obtained dust mass along the ridge coordinate, taking advantage of the fact that the intersection region is in an intermediate sector of the HB, and thus can be compared with both the eastern and western sections. As seen in Fig. 3.35, the mass shows a slight inflection in the intermediate section. This actually reflects a depletion in the Bar that has already been observed [122], and is perhaps due to its proximity to Sgr A*.

In Fig. 3.35, the spatial distributions of dust mass, local background, and minimum grain size for the HB are presented. The latter, in particular, shows the same trend observed for the NA, with the edges of the filament being highly photo-evaporated. The mass distribution exhibits a noticeable accumulation towards the west, away from Sgr A*, again similar to the pattern observed in the NA. The local background,

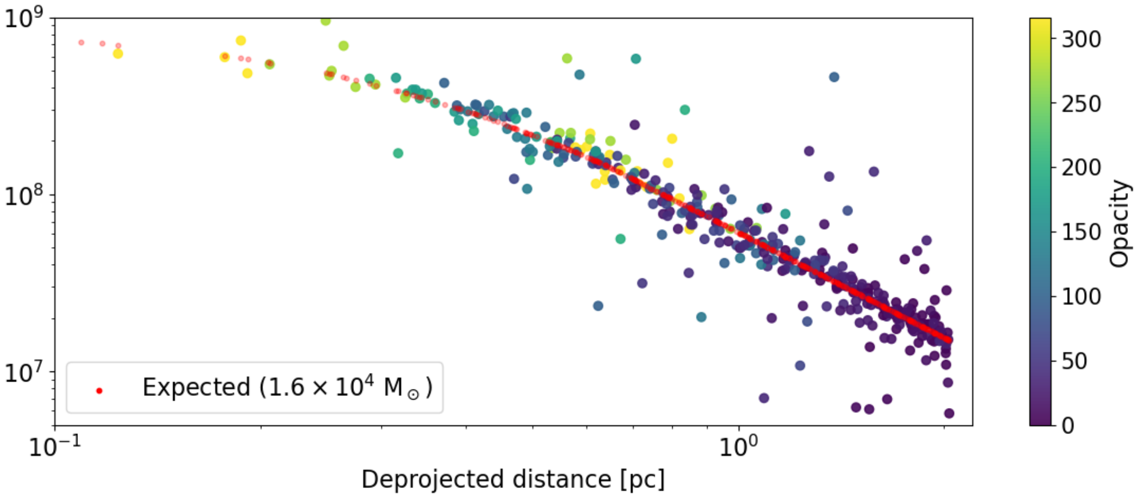

Figure 3.36: Illumination radial profile for the HB, after correcting for both the minimum grain size distribution and accounting for a clumpy dust distribution as well. The datapoints have been coloured according to their $x_{\max}$ value.

on the other hand, reveals a structure that appears contiguous to that already observed in the NA (Fig. 3.25), providing a clue in favour of its physical nature rather than being a feature of the fit induced by the filament's geometry. The final validation of the model is provided by a test of the inverse square law of illumination for the HB. The profile is shown in Fig. 3.36: the data points extracted from each pixel are decidedly compatible with the expected behaviour. As anticipated, the highest opacity occurs for regions immersed in the UV radiation field (up to 0.3 pc) or those at the southern and northern edges of the filament, suggesting that the high UV radiation tends to select denser clumps at the expense of diffuse dust, which is more easily destroyed or swept away [63].

3.6.6 *Local background map*

Before moving on to the 3D mass distribution, one may inquire into how the local background distribution appears across the entire field of view considered, especially in light of the fact that there are seemingly contiguous 2D structures on different 3D structures (Fig. 3.25, Fig. 3.35). The profile is shown in Fig. 3.37 and is decidedly interesting: the first thing that strikes the eye is that the parameter Λ traces the profile of the CNR even where the CNR had not been fitted, that is, on the internal filaments. In other words the local background, calibrated at ap-

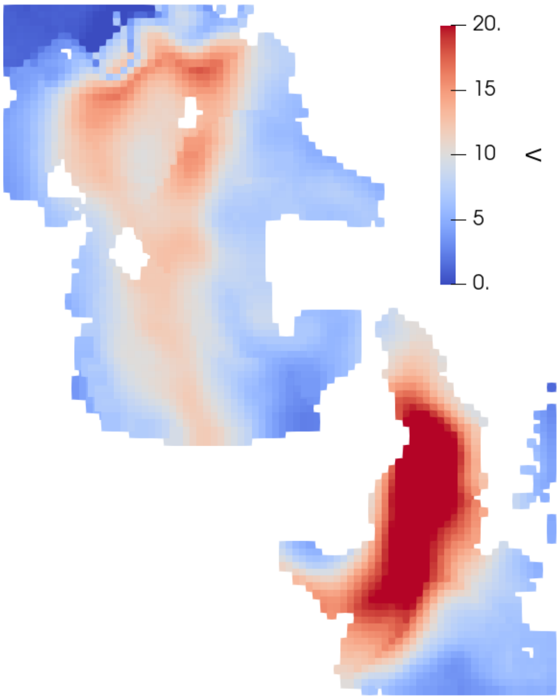

Figure 3.37: Map of the local background traced by the parameter Λ. Part of the CNR has been cropped, namely the pixels with $M_{\mathrm{CNR}} < 10^{-2}\,\mathrm{M}_{\odot}$.

proximately 3-4 parsecs from Sgr A* (Fig. 3.20), seems to be effective in tracing the CNR component obscured by the filaments which was erroneously thought to lie on the orbital plane of the NA (the contiguity of the projection onto the HB rules out this hypothesis). This is most likely the reason why the PF in 2D could not separate the hot component from the cold one on the NA: indeed, the distribution in Fig. 3.11 shows a longitudinal asymmetry along the NA in the cold temperature map (top-right panel) — not in the hot one, which is independent from the CNR emission — and consequently in the extracted masses (central panels). There is also a partially visible diffuse local background component towards the centre. One does not expect diffuse and relatively cold clouds in the orbital plane of the CNR so close to Sgr A*, thus it is anticipated to be either background or foreground emission on a shell at a 3D distance between 1.5 pc and 4 pc, where the local background has been calibrated (indeed, the SED of the outer ring in Fig. 3.20 is different).

To test this theory, the entire field of view was refitted, assuming it to be on the orbital plane of the CNR, but subtracting the emission from the mini-spiral and excluding the possibility of a local background. The fit external to the CC yielded very good results (average reduced $\chi^2 = 0.8$), demonstrating that the additional component belongs to the CND, but was not as good inside the cavity (average reduced $\chi^2 = 4.1$). Fitting the internal dust at a fixed 3D distance of 2 pc yields significantly better results (average reduced $\chi^2 \simeq 1.8$). Consequently, the dust within the CC has been assumed to be uniformly distributed in a spherical shell between 1.5 and 4 pc, and with a temperature of 40 K inferred from the 2D maps of the cold component for an average distance of 3 pc.

3.7 3D MAPS OF THE INNER 6 PARSECS

As anticipated in the footnote on page 68, up to this point the term “mass” has referred to the integral of the mass along the line of sight, that is, a column density. This stems from the fact that the maps used are actually surface brightness maps. The 3D column density distributions that have been obtained with the PFs correspond to the total mass projected onto an orbital plane in 3D space, which then needs to be de-projected into a volume. The direction of de-projection must not be orthogonal to the orbital plane, because column density presupposes integration along the line of sight – namely along the z-axis, orthogonal to the 2D maps. Fig. 3.38 shows the NA as an example, illustrating on the left the mass distribution on the (x,y) plane, and the corresponding 3D de-projection from the 2D orbital plane along the z-axis (indicated by the blue arrow). It should be noted that the distribution of the volume, shown in high transparency, is not symmetric with respect to the orbital plane.

To de-project the volume, some assumptions about the geometry of the structures are required. For instance, the CND is a disk that can be modelled with a single parameter: the opening angle ω (see for example [125] for a visual depiction). Given a distance D from the centre of a circular disk (and the CND is a good approximation of one), the disk's thickness would trivially be $D\tan(\omega)$, if ω is defined as the full opening angle. In [125] they calculate $\omega = 14^\circ \pm 3^\circ$ – at a distance of 1 pc, the thickness of the CNR is $h_{\text{CNR}} = (0.25 \pm 0.05\,\text{pc})$.

From a mathematical standpoint, given the observed distribution of 2D column density $M_{2\text{D}}(x,y)$, calculating the mass distribution $M_{3\text{D}}(x,y,z)$ on the disk is rather straightforward. When viewing the disk face-on, the mass enclosed in a 3D pixel with a depth δh is:

$$M_{3\text{D}}(x,y,z) = M_{2\text{D}}(x,y)\frac{\delta h}{r\tan(\omega)} \tag{3.7.1}$$

Upon considering the disk's rotation by an angle ϕ in 3D with respect to z-axis, the only variation is that $\delta z = \delta h/\cos(\phi)$.

In the case of the two internal filaments, the structure is usually assumed to have axial symmetry, with a lateral extent that is generally not constant along the axis. Mathematically, given the pixel coordinate of the ridge $R(x,y)$ (assuming that the ridge defines the points along the axis) and the lateral extent $L(R(x,y))$ which pro-

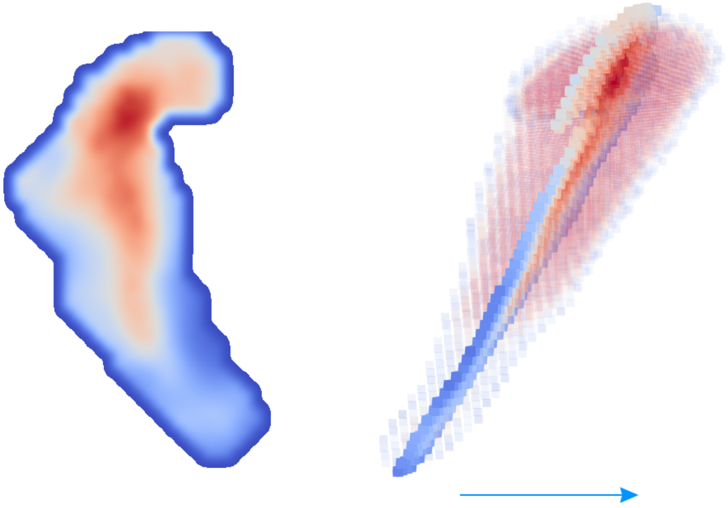

Figure 3.38: 3D de-projection of surface density, from the projected distribution (on the left) to the 2D distribution on a orbital plane, de-projected along the z-axis (on the right). The axis is indicated with a blue line.

vides the radius around the ridge, the mass distribution is generally:

$$M_{\rm 3D}(x,y,z) = M_{\rm 2D}(x,y) \times f(d,z) \tag{3.7.2}$$

where $f(d,z)$ represents the mass profile and describes how the mass of the 2D pixel is distributed in volume, and where $d(x,y)$ is the distance of the pixel from the ridge R. For a uniform mass distribution, $f(d,z) = 1/V_{\rm cyl}$, where $V_{\rm cyl}$ is the volume of the cylindrical section at depth z. For a Gaussian distribution along the radial direction [28], one has

$$f(d,z) = \frac{1}{\sqrt{2\pi\sigma^2}} e^{-\frac{d^2}{2\sigma^2}}. \tag{3.7.3}$$

It was chosen to define $\sigma = L(x,y)/2$, thereby encompassing 95% of the mass on the filament. The mass that remains outside the filament is considered a small separate cloud lying on the orbital plane.

In both cases (CND and mini-spiral), very small values of δz (0.1″) were taken to sample depth. The final result was aggregated (for the mass distribution) or interpolated (for the temperature) and then re-sampled onto a grid of (100×100×100) cubic pixels, each with a side length of 1″ in the (x,y) projection. The obtained 3D mass distribution is shown in Fig. 3.39, where a minimum threshold of $10^{-5}\,M_\odot$ for the mini-spiral and $10^{-3}\,M_\odot$ for the CND has been adopted for the mass to be

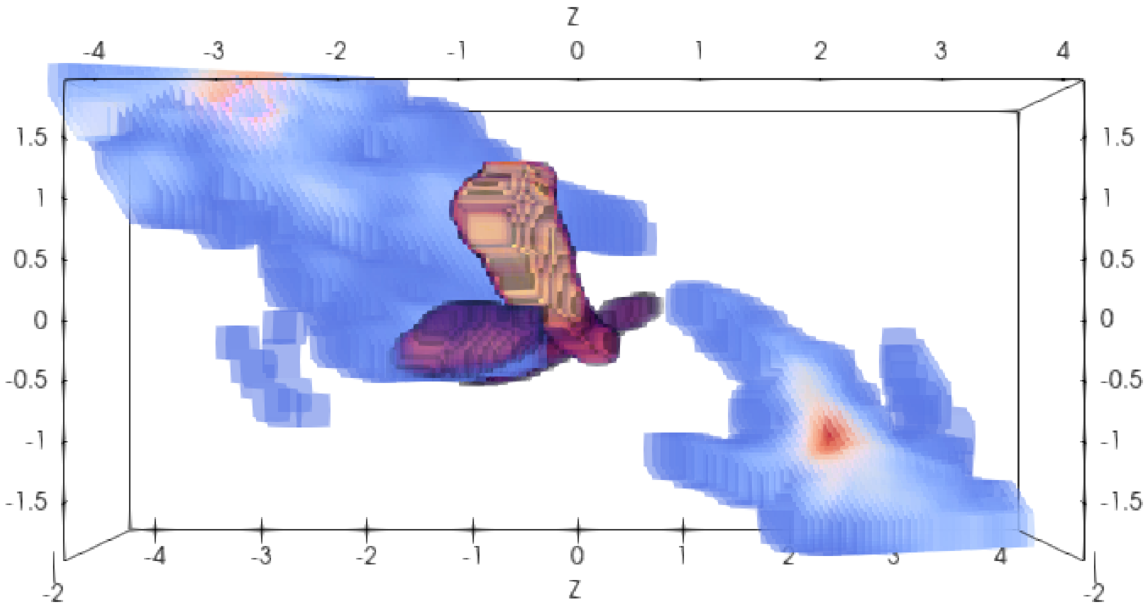

Figure 3.39: 3D map of the dust mass distribution in the inner few parsecs of the Galactic Centre, seen from the side. The observer lies to the right (positive z values). Sgr A* is at the centre, behind the NA. The CNR has been cropped on one side for ease of visualisation. Also, a mass threshold of $10^{-5}\,M_\odot$ for the mini-spiral and $10^{-3}\,M_\odot$ for the CND has been chosen for the mass to visualise, masking out most of the smallest diffuse clouds. The inner filaments and the CNR adopt different colour maps. The grid units are in parsec, where 1 pc corresponds to about 25 pixels.

visualised. Sgr A* is at the centre of the map, obscured behind the NA in this side perspective. The observer is to the right, in the direction of the increasing z-axis. The HB orbits around Sgr A* almost horizontally, remaining consistently behind it (as viewed from the observer's position), which has a significant impact on the calculation of the vectorial IR radiation field around Sgr A*, and particularly in its capability to absorb gamma-rays travelling towards Earth. This point will be discussed in detail in Chapter 4.

In the figure, the colour-code has not been reported because it serves no practical utility in visualising the volumetric distribution. The total mass of dust in the NA is $(0.126 \pm 0.020)\,M_\odot$, which, assuming the gas-to-dust ratio of 124 [129] at the basis of the dust model used, translates to $(15.0 \pm 2.5)\,M_\odot$ in total. Similarly, for the HB, $(0.093 \pm 0.014)\,M_\odot$ or $(11.3 \pm 1.7)\,M_\odot$ between gas and dust is found, remarkably similar to the $\sim 0.25\,M_\odot$ found for the dust mass in [122] using the VISIR telescope at ESO's VLT. The CNR within a radius of 2 pc yields $(4.11 \pm 0.62)\,M_\odot$ of dust, or $(512 \pm 77)\,M_\odot$ when considering the gas as well. Note that the gas-to-dust ratio in

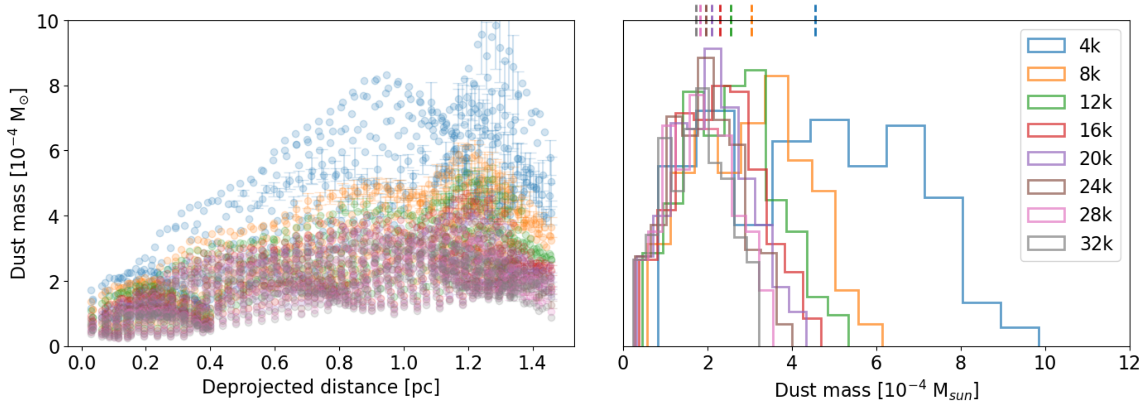

Figure 3.40: Dust mass-distance relation and histograms assuming different NSC masses. For ease of visualisation, only the dust on the NA has been included. The vertical dashed segments on the right represent the average values for each distribution.

the region could be lower by a factor of 4 – 5 when accounting for its Galactocentric variation [85] or even by a factor of 10 [122]. The gas mass of the CNR is consistent with what was found in [125] using SOFIA/FORCAST, which reports 610 $M_\odot$ under similar assumptions on the gas-to-dust ratio. [111] reports several tens of solar masses in ionised gas and hundreds in neutral gas as well. Meanwhile, [68] reports a gas mass of 1.56×10^4 $M_\odot$ for the CC and also including the first pc from the inner edge of the CNR. However, their result assumes a single grey body at 90 K for the CC, which is lower by a factor of more than 2 in the brightest part of the mini-spiral – that would result in a factor of up to 16 less for the mass. A good overview of the mass distribution of the structures in the inner 10 pc is given in [75], finding on average higher gas mass values than those found in this work.

The temperature in the CC, both for the emission of silicates and that of graphite, is slightly higher than reported by [125] using the 37.1/25.2 μm colour. However, they

	NA	HB	CNR
Dust M [$M_\odot$]	$(12.6 \pm 2.0) \times 10^{-2}$	$(9.3 \pm 1.4) \times 10^{-2}$	4.11 ± 0.62
Gas M_{124} [$M_\odot$]	15.0 ± 2.5	11.3 ± 1.7	512 ± 77
Gas M_{30} [$M_\odot$]	3.63 ± 0.60	2.73 ± 0.41	123 ± 19
Gas M_{10} [$M_\odot$]	1.26 ± 0.20	0.93 ± 0.14	41.1 ± 6.2

Table 3.5: Dust and gas mass values found for the three structures. The CNR accounts for the dust and gas between the inner edge and 2 pc from Sgr A*. The gas mass has been calculated assuming different gas-to-dust mass ratios: 124 [129], 30 [85] and 10 [122], see discussion in the text.

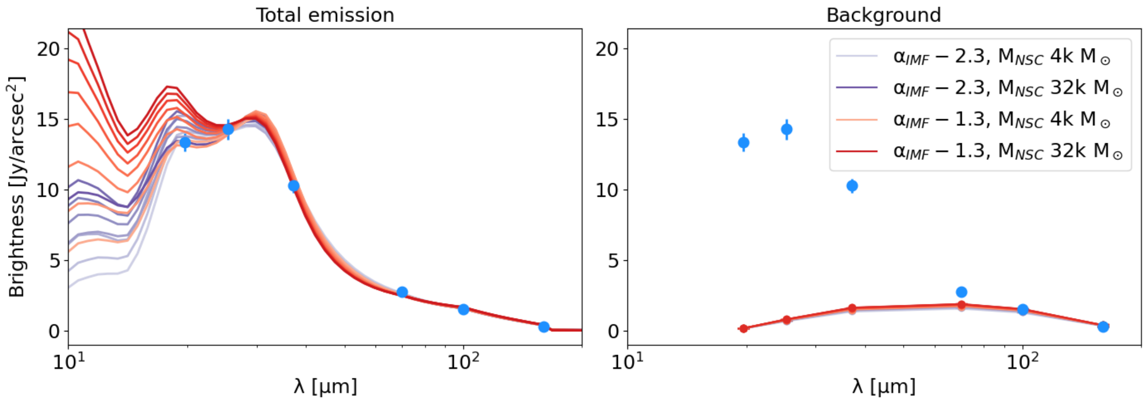

Figure 3.41: 3D Planck fit in the same line of sight as Fig. 3.22, this time accounting for both grain size distribution modification and dust clumpiness. The colour-code convention is the same: the larger the mass of the NSC, the brighter the hue.

use this colour to fit the CNR, finding a much lower temperature (~ 60 K compared to the ~ 90 K found here). 90 K is also the temperature reported by [68].

As previously stated, in all the calculations a NSC with a total mass $M_{\mathrm{NSC}} = 16\,000\,\mathrm{M}_\odot$ and a spectral index $\alpha_{\mathrm{IMF}} = -1.7$ was assumed. On one hand, a more massive NSC results in a greater illumination and thus in a lower dust mass. On the other hand, the opacity corrections introduced by adjusting the grain size distribution are undoubtedly effective in fitting the SED. However, they have the drawback of altering the dust mass values in a manner that is not always easily quantifiable (particularly for opacity), and adapt rather well to any NSC simulation. By adopting these corrections, one forgoes the opportunity to use the SED to constrain the NSC mass – and especially so for the spectral index, which affects the SED mainly at shorter wavelengths where opacity corrections are most sensitive. The dependence on M_{NSC} is shown in Fig. 3.40, where the mass distribution of the NA's pixels is shown. The dust mass found varies according to the illumination provided, which is not surprising. However, it does not vary by more than a factor of 2 between $4000\,\mathrm{M}_\odot$ and $16\,000\,\mathrm{M}_\odot$. By comparison, adjustments due to dust clumpiness and grain size alterations could change the mass found by a factor 3-4 depending on the assumptions. Moreover, a value as low as $4000\,\mathrm{M}_\odot$ for the NSC stellar mass is not likely, and it is disregarded in literature (e.g. [71, 179]), which reduces the possible spread to a factor 1.18 at most. Consequently, a 15% uncertainty on the dust mass values has been adopted.

How much the dust mass is affected by the NSC's IMF spectral index after applying the additional cooling mechanisms can be seen in Fig. 3.41, which is analogous to

Fig. 3.22: the minimum grain size value adopted here is 0.08 µm, and the fit favours a spectral index of −2.3 or intermediate-NSC masses with $\alpha_{\rm IMF} = -1.3$. However, simply adopting a different size threshold changes the results sensibly – the peak at 20 µm can be easily lowered by altering the average size of silicate grains – so that finding a favoured model is impossible unless the parameters involved are physically constrained. For this reason, the minimum grain size values adopted in the radiation field calculations were the ones that provided the best fit to the data, with the constraint that the minimum grain size cannot exceed 0.2 µm. With such modifications, the spread in the mass values found adopting different NSC simulations does not exceed the 15% value even for the regions most affected by grain size modifications or dust clumpiness (such as the closest to Sgr A*). Consequently, no additional uncertainty has been applied when altering the grain size distribution or when accounting for dust clumpiness.

3.8 INFRARED RADIATION FIELD COMPUTATION

The 3D mass distribution, along with the dust temperature, allows the calculation of the emission at a given position and its effects in every other cell within the volume illustrated in Fig. 3.39. Iterating this process for all cells, the total value of the spectral radiation field density at each point P^i is obtained under the assumption that the medium between the clumps is optically thin to IR light:

$$u^i_{\mathrm{rad},\nu} = \sum_j \frac{L^j_\nu}{4\pi c r^2_{ij}} \tag{3.8.1}$$

Here, L_ν is calculated directly from Equation 3.1.1, assuming the appropriate minimum grain size (Section 3.6.3) and averaging over the grain size distribution for all species (silicates and graphite). The emission from the low-temperature mass introduced to model the opacity of the clump is taken into account (Section 3.6.4). r_{ii} would be 0 by definition, but it is set as the distance to the closest cell in order to correct for singularity when accounting for $u^i_{\mathrm{rad},\nu}$ contributions from the same cell i. To assess the frequency values required for sampling the SED, different emission scenarios were examined: hot regions near Sgr A*, in the overlap zone between HB and CNR, and on the CND. The selected sampling ensured an error of less than 2% in the ratio between the integrated modelled emission and the integrated sampled emission. The chosen sampling frequencies were 20: 1.875, 3, 4, 5, 7×10^{12} Hz, and from 1×10^{13} to 3.6×10^{13} Hz at steps of 0.2×10^{13} Hz, plus 3×10^{14} Hz (respectively 160, 100, 75, 60, 43, and 30 to 8 µm, plus 1 µm), which ensures good sampling of the emission peaks between 15 and 30 µm. Having removed the PAH emission features, the range 1 – 8 µm can be interpolated to a good precision.

Moreover, from the knowledge of the 3D spatial distribution of emitting structures one can obtain the vector field distribution, crucial information for appropriately studying gamma-gamma absorption given the vectorial nature of the reaction. Introducing the unit vector $\hat{\mathbf{n}}$ such that

$$\mathbf{u}^j_{\mathrm{rad},\nu}(\hat{\mathbf{n}}_j) = \frac{L_{\nu,j}}{4\pi c r^2_{ij}} \hat{\mathbf{n}}_j \qquad \hat{\mathbf{n}}_j = \frac{\mathbf{r}_{ij}}{r_{ij}} \tag{3.8.2}$$

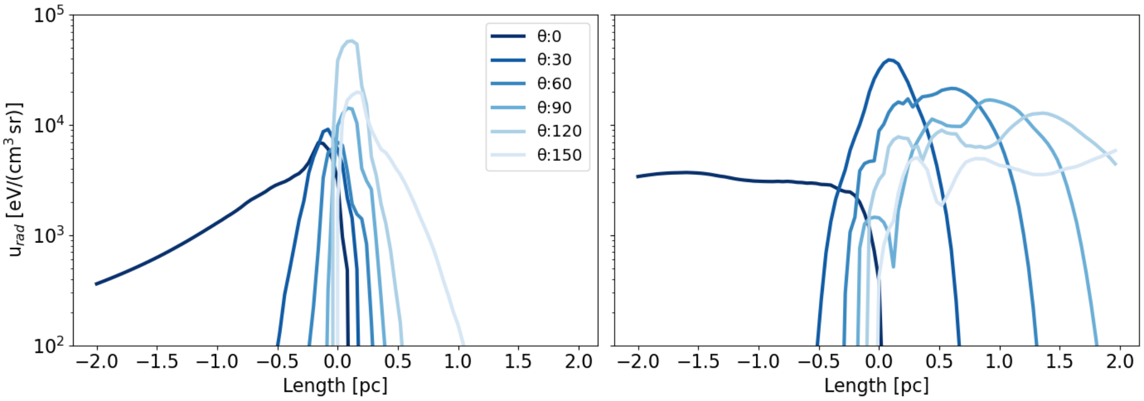

Figure 3.42: Left panel: infrared radiation field density collected in a solid angle of 0.044 sr, moving along the z-axis away from the observer, looking at on $\phi = 15°$ to the left. Right panel: infrared radiation field density collected in the same solid angle moving diagonally on the $z = 0$ plane, looking at $\phi = 15°$ to the right, passing below the arching NA. Sgr A* is at length = 0. $\theta = 0$ looks to the front horizontally.

the total spectral radiation field density for a given direction k is

$$\mathbf{u}_{\mathrm{rad},\nu}(\hat{\mathbf{n}}_k) = \sum_{j=1}^{N} \frac{L_{\nu,j}}{4\pi c r_{ij}^2} \hat{\mathbf{n}}_j \delta(\hat{\mathbf{n}}_k - \hat{\mathbf{n}}_j) \tag{3.8.3}$$

The field of view needs to be binned in the two polar angles ϕ (rotation relative to the x-axis) and θ (rotation relative to the z-axis). For the needs of this thesis, the most constraining aspect arises from the properties of vector interactions in pair production reactions, which are illustrated in Fig. 4.1. A grid of ϕ, θ with bins of 15 degrees samples the full solid angle with 0.044 sr bins and is a good compromise between the required precision and computational complexity. This latter factor must be taken into account, as the obtained radiation field is a 6-dimensional vector:

- 3 spatial dimensions (volume 100x100x100);
- 1 spectral dimension (20);
- 2 angular dimensions (24x12).

Fig. 3.42 provides an example of the information nested in such a matrix. The SED has been integrated in the frequency spectrum. Rather than throughout the entire volume, it has been calculated along two different trajectories: along the z-axis, moving away from the observer (left panel), and on a horizontal plane along a 45° trajectory moving away towards the west (right panel). In the first case, $\phi = 15°$

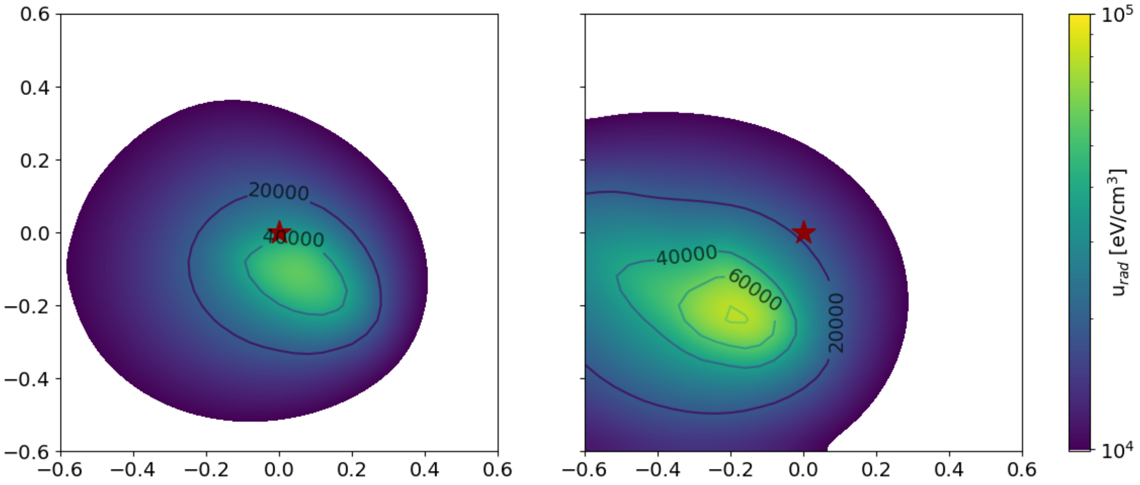

Figure 3.43: Radiation field density maps of the inner 0.6 pc, integrated over all emission angles and selecting only the emission $> 10^4$ eV/cm^3, at $z = 0$ pc (left panel) and $z = -0.2$ pc (right panel, closer to the observer). The contour lines are plotted for $u_{\rm rad}$ values of 2×10^4, 4×10^4, 6×10^4, 8×10^4 eV/cm^3. The projected position of Sgr A* is marked with a red star.

to the left from the observer point of view. At the beginning (from −2 to −0.5 pc) only photons from the HB come from that direction, practically at the same height ($\theta = 0$). As one approaches Sgr A* (at $z = 0$), very close structures (high $u_{\rm rad}$ values) are rapidly encountered at various height positions, thanks to the NA that wraps the trajectory from above. Note that, by the definition of θ adopted, $\theta = 150°$ means a height of +30° in the opposite direction. In the second case, the observer "looks" 15° to the right and moves almost parallel to the HB before "passing into" the space between the HB and NA, with close emissions at all heights in the northern hemisphere.

Discarding the vectorial information and integrating over all possible angles, one obtains the integrated radiation density throughout the entire volume. The maximum value, 8.15×10^4 eV/cm^3, is achieved at 0.3 pc from Sgr A*, deep inside the HB – and such an incredible density of photons is to be considered a lower limit, because of the singularity correction in the very cell. The value at the position of Sgr A* is roughly 4×10^4 eV/cm^3.

In the literature, various references can be found concerning the IR luminosity enclosed within different galactocentric radii. Here, reference is made to Mezger et al. [143], and to the references listed in their Table 6. The luminosity enclosed within 1 pc is reported to be $5.8 \times 10^6\, L_\odot$, while for a radius of 0.5 pc the value reported is $4.2 \times 10^6\, L_\odot$. Assuming an isotropic distribution of luminosity (which is not appropriate in this case), one would obtain a radiation field density at the position of Sgr A* of 1.1×10^4 eV/cm^3. If the luminosity distribution is more concentrated towards the centre, the value would naturally increase. In this work, it has been calculated that the dust in the NA emits about $1.4 \times 10^6\,\mathrm{L}_\odot$ within the inner pc, while the dust in the HB – which orbits around Sgr A* within a radius of 0.6 pc – emits approximately four times as much: $5.8 \times 10^6\,\mathrm{L}_\odot$. This is the reason not only for a maximum value that is about 7 times greater than the value calculated for an isotropic distribution, but also for the rather extensive area of the radiation field above 10^4 eV/cm^3 shown in Fig. 3.43. In this figure two slices at different values of z in a small cubic volume 1.2 pc long centered on Sgr A* have been shown. The projected (x,y) position of Sgr A* is marked with a red cross – in the left panel, it corresponds to its real 3D position. While the radiation field is maximum inside the filaments, an impressively large area exhibits radiation field densities above the threshold even in voids. Such values are comparable to an energy density of a magnetic field of 1 mG, effectively dominating the energetics in the CC except for the filaments themselves where the magnetic fields are known to reach a few mG [24]. Depending on the vectorial geometry of such a radiation field, it could greatly affect the SED of a gamma-ray source passing through or embedded in that region, as will be shown in the next chapter.

4

GAMMA-GAMMA ABSORPTION IN THE GALACTIC CENTRE

The previous chapter has shown that at the heart of the GC there is an extremely high diffuse radiation field, which has been calculated vectorially. This field can interact with a high-energy radiation field, resulting in the creation of particle/antiparticle pairs[1] (first discussed in 1934 in [46]). In this light, the energetics and geometry of gamma-ray absorption from a source embedded in the region can be studied, for various assumptions about the shape and spectrum of the source. Using the reverse argument, the absorption can be studied to investigate the geometry and spectrum of HESS J1745–290, starting from an intrinsic spectrum coinciding with that of the diffuse source, which is equivalent to assuming that the central source absorption drives the difference between the two spectra observed by H.E.S.S. (discussed in detail in Section 2.2). In such an analysis one must carefully evaluate the galactic gamma-ray background, because the solid angle subtended by the absorption region is much smaller than the PSF of H.E.S.S. ($\sim 5'$ at 1 TeV), and consequently the background is largely un-absorbed (discussed in Section 4.2.3). Instruments with better sensitivity and resolution like CTA, however, could resolve the source and thus discriminate between different emission and absorption scenarios.

---

[1] As a logical consequence of this approach, in this chapter the 3D IR field will be referred to as the “target” radiation field.

4.1 GAMMA-RAY ABSORPTION BY PAIR PRODUCTION

Consider a high-energy photon (whose energy is labelled with E_γ) interacting with a local "soft" radiation field (whose photons have energy E_ϵ) with a collision angle ψ, producing an electron-positron pair $\mathrm{e}^+\mathrm{e}^-$. The energy of each lepton is E_e. The metric tensor is chosen so that the four-momentum vector $\mathbf{p}$ is $(E/c, -\vec{p})$, thus $E = \sqrt{p^2c^2 + m^2c^4}$. From conservation of energy and momentum it follows that

$$E_\gamma + E_\epsilon = 2E_\mathrm{e} \quad \rightarrow \quad E_\gamma^2 + E_\epsilon^2 + 2E_\gamma E_\epsilon - 4E_\mathrm{e}^2 = 0 \tag{4.1.1}$$

$$\vec{p_\gamma} + \vec{p_\epsilon} = \vec{p}_{\mathrm{e}^+} + \vec{p}_{\mathrm{e}^-} = 0 \quad \rightarrow \quad E_\gamma^2 + E_\epsilon^2 + 2E_\gamma E_\epsilon \cos(\psi) = 0. \tag{4.1.2}$$

Putting (4.1.1) and (4.1.2) together:

$$E_\gamma E_\epsilon (1 - \cos(\psi)) = 2E_\mathrm{e}^2 \tag{4.1.3}$$

and since $E_\mathrm{e} = \gamma_\mathrm{L} m_\mathrm{e} c^2 = m_\mathrm{e} c^2 / \sqrt{1 - \beta^2}$ where γ_L is the Lorentz factor and $\beta = v/c$ is the scaled electron[2] velocity, one finds

$$\beta = \sqrt{1 - \frac{2m_\mathrm{e}^2 c^4}{E_\gamma E_\epsilon (1 - \cos(\psi))}}. \tag{4.1.4}$$

It is opportune to stress that this equation is valid in any reference frame[3] – but the angle ψ changes depending on the reference frame velocity β_F according to

$$\cos(\psi') = \frac{\cos(\psi) + \beta_\mathrm{F}}{1 + \beta_\mathrm{F} \cos(\psi)}. \tag{4.1.5}$$

which tends to 1, since the Lorentz factor of the CoM frame velocity with respect to the lab frame is proportional to E_γ / E_ϵ. The privileged frame is obviously the observer's, so a coordinate transformation would be needed later if one wants to study the effects induced by the leptons created. As it is evident from Equation 4.1.4, this process has a threshold energy and can occur only when

$$E_\gamma E_\epsilon (1 - \cos(\psi)) \geq 2m_\mathrm{e}^2 c^4 \tag{4.1.6}$$

---

[2] On the formal standpoint the same calculations apply to the positron unless they depend on charge. Throughout this chapter, the created particle will generally be labelled "electron" unless specified differently.

[3] In this thesis, the quantities in the CoM frame are denoted with ′.

and for a head-on collision ($\psi = \pi$) the condition then becomes

$$E_\epsilon \geq 0.26\,\mathrm{eV}\left(\frac{E_\gamma}{1\,\mathrm{TeV}}\right)^{-1}. \tag{4.1.7}$$

As a first practical example, a 10 TeV photon can interact with a 0.026 eV (48 µm) soft photon, but a 1 TeV photon is not absorbed by photons with energies lower than 0.26 eV (wavelengths larger than 4.8 µm), which could have a large relevance in a photon field peaking around 10-20 µm as the one modelled in the previous chapter. The absorption of the gamma-ray flux I_γ passing through a region with a soft photon density $n_\epsilon(E_\epsilon, \vec{r})$[4] can be described by the local absorption fraction f_γ (absorption per unit length):

$$f_\gamma(\vec{r}) = \int_{\epsilon_{\min}}^{\epsilon_{\max}} \sigma_\epsilon(E_\epsilon)\, n_\epsilon(E_\epsilon, \vec{r})\, \mathrm{d}E_\epsilon \tag{4.1.8}$$

where the differential cross section σ_ϵ is a function of the angle and of the energy of both photons E_ϵ and E_γ, and the integral is calculated for fixed values of E_γ. The photon density is related to the radiation field density through

$$n_\nu = u_{\mathrm{rad},\nu}/\nu \qquad\qquad n_\epsilon = n_\nu/h. \tag{4.1.9}$$

If the absorption is proportional to the flux, then it is straightforward to find:

$$\frac{\mathrm{d}I_\gamma}{\mathrm{d}r} = -f_\gamma\, I_\gamma \quad\Longrightarrow\quad \int_{I_\gamma(0)}^{I_\gamma(R)} \frac{\mathrm{d}I_\gamma}{I_\gamma} = -\int_0^R \int_{\epsilon_{\min}}^{\epsilon_{\max}} \sigma_\epsilon n_\epsilon\, \mathrm{d}E_\epsilon\, \mathrm{d}r \tag{4.1.10}$$

which has a simple solution given a travel distance R in the form

$$I_\gamma(R) = I_\gamma(0)e^{-\tau} \tag{4.1.11}$$

where the definitions of optical depth τ and spectral optical depth τ_ϵ have been used:

$$\tau = \int_{\epsilon_{\min}}^{\epsilon_{\max}} \tau_\epsilon\, \mathrm{d}E_\epsilon \qquad\qquad \tau_\epsilon = \int_0^R \sigma_\epsilon n_\epsilon\, \mathrm{d}r. \tag{4.1.12}$$

The last missing piece is that the interaction probability of the gamma-ray is proportional to $(1-\cos(\psi))$, since the interaction is favoured when it is head-on. A more

---

[4] In gamma-ray astrophysics, the spectra are usually calculated per unit energy rather than frequency or wavelength. This is the reason for the approach adopted in this chapter.

complete formulation is then:

$$\tau(E_\gamma) = \int_0^R \mathrm{d}r \int_{\Delta\Omega} (1 - \cos(\phi))\,\mathrm{d}\Omega \int_{\epsilon_{\mathrm{min}}}^{\epsilon_{\mathrm{max}}} n_\epsilon(E_\epsilon, \Omega, \vec{r})\,\sigma_\epsilon(E_\gamma, E_\epsilon, \psi)\,\mathrm{d}E_\epsilon. \tag{4.1.13}$$

σ_ϵ contains the information about the specific interaction – in the case under consideration, the creation of electron-positron pairs has a much larger cross section than the creation of pairs of other leptons [157] or mesons [183]. Its mathematical formulation as a function of the velocity of the produced electron is

$$\sigma_\epsilon = \frac{3}{16}\sigma_\mathrm{T}(1-\beta^2)\left[2\beta(\beta^2-2) + (3-\beta^4)\ln\frac{1+\beta}{1-\beta}\right] \tag{4.1.14}$$

which has been adapted from eq. 13-40 of [114]. There are two limit cases when the cross section can be written in a simplified way: 1) $E_\gamma \sim E_\epsilon \sim 0.511$ MeV, and 2) $E_\gamma \cdot E_\epsilon >> (0.511\ \mathrm{MeV})^2$. In the first case $\beta \ll 1$. Since $\lim_{\beta\to 0} \ln\left(\frac{1+\beta}{1-\beta}\right) = 2\beta$ at first order, it results

$$\sigma_\epsilon = \frac{3\sigma_\mathrm{T}}{8}\beta \tag{4.1.15}$$

In the latter case $\beta \sim 1$, and the cross section can be written as

$$\sigma_\epsilon = \frac{3}{8\gamma_\mathrm{L}^2}\sigma_\mathrm{T}\left(\ln(4\gamma_\mathrm{L}^2) - 1\right) \tag{4.1.16}$$

which means (from Equation 4.1.3) that the cross section goes down with E_γ. Its maximum value amounts to $\sim 1.6 \times 10^{-25}\,\mathrm{cm}^2$, approximately a quarter of the Thomson cross section, and it is a much higher value than other physical processes involving photons – e.g., Delbrück scattering is about 10^{-4} times smaller, and even photo-nuclear processes at MeV-GeV energies do not exceed a few $10^{-26}\,\mathrm{cm}^2$ for some nuclei during giant dipole resonance [119]. This is the reason why absorption by pair production is considered so relevant in astrophysics (see for example [21]). The profile of σ_ϵ is reported in Fig. 4.1 as a function of the velocity of the produced electron (left panel) and the energy of the soft photon (central and right panel) by means of Equation 4.1.4, where the dependence on the gamma-ray energy and on the collision angle ψ is investigated. As shown in the last two panels, gamma-ray photons of different energies or with different collision angles interact with targets in different spectral ranges. The maximum of the cross section occurs at energies approximately two times the threshold energy. Furthermore, at 1 TeV the interaction

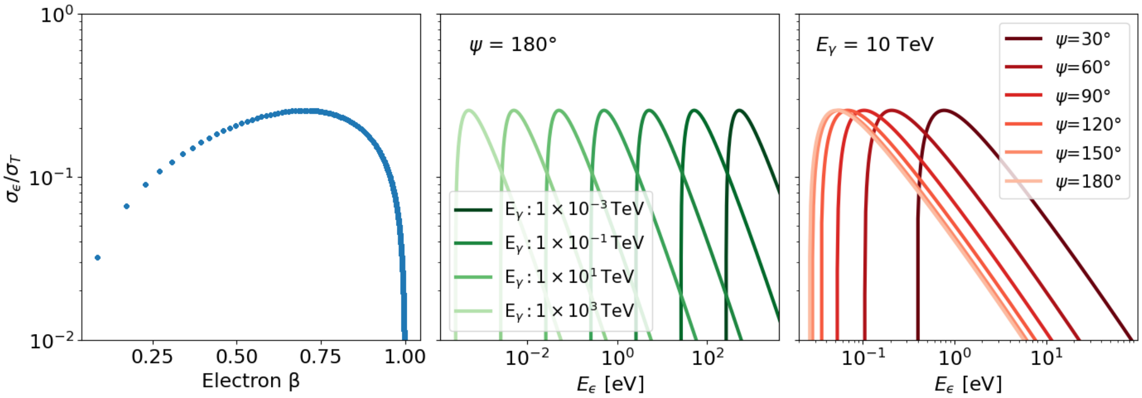

Figure 4.1: Pair production cross section as a function of the electron velocity (left panel) and of the soft photon energy (central and right panels). In the central panel a collision angle $\psi = 180°$ has been assumed and gamma-ray energies from 1 GeV to 1 PeV have been investigated. The right panel assumes $E_\gamma = 10\,\text{TeV}$ and explores the dependence on ψ.

is centred around 0.5 eV (2.5 µm), while at 10 TeV it is centred around 5 eV (25 µm). In the GC radiation field modelled (see for example the SED in Fig. 3.23), an emission peak at 20 µm is typical of the CC in the inner parsec, whereas the emission around 5 µm is disfavoured by the spectral points at 19.7 µm. This means that, without considering the interaction angles, it is expected that photons at energies around 10 – 20 TeV are much more absorbed in the CC, also considering the intensity of the fields in that region. Photons of 40 – 50 TeV, on the other hand, have a maximum cross section around 100 µm. This is not typically the emission found in the centre, but in the cold and extended structures such as the CND that contain enough material in the line of sight to compensate for radiation field densities lower by orders of magnitude.

In the right panel, the dependence of the cross section on the collision angle is illustrated for $E_\gamma = 10\,\text{TeV}$. The first evident property is that for the cross section there is very little difference between a head-on collision ($\psi = 180°$) and one with $\psi = 120°$. Indeed, from Equation 4.1.4 it follows that once a value of β is fixed – that is, a value of σ_ϵ – one obtains $E_\epsilon \propto (1 - \cos(\phi))^{-1}$, which is equivalent to saying that varying the collision angle is akin to shifting the cross section to other soft energies. The difference between a head-on collision and an almost parallel one ($\psi = 30°$) is that the cross section moves to energies about 10 times higher – this results in more or less the same probability and the same energy range of interaction as a frontal collision of a gamma-ray photon with one tenth of the energy. The considerations made previously about the application to the GC radiation field apply in the same way, with an additional piece of information: since the direction of the photons determines the energy range of interaction, the signature of the absorption on the gamma-ray source spectrum changes substantially if the gamma-ray photon source is in front of or behind the ionised filaments relative to the observer. If one identifies the gamma-ray source with Sgr A*, for example, most of the filaments are behind or around it, thus the energies absorbed the most in the observer direction are much higher compared to the case of a gamma-ray source located a parsec further away from the Earth, behind the filaments.

4.2 LOCAL GAMMA RAYS ABSORPTION BY RADIATION FIELDS ON DIFFERENT SCALES

Since gamma rays can be absorbed by radiation fields over different scales – depending on the ease of absorption (expressed by the cross section) and the quantity of absorbers along the line of sight (expressed by the radiation field density) – it is necessary to evaluate which radiation fields can absorb them. Before investigating the main contribution given by dust emission in the MIR/FIR, the absorption due to the NSC's UV radiation field and that due to the optical/IR emission of the Galactic bulge are studied below. These are two diametrically opposed cases: while UV absorption is effective only for extremely intense emissions and is therefore localised very close to individual stars, the second is diffuse over scales greater than 1 kpc.

4.2.1 *Absorption by the local UV field*

Equation 4.1.11 can be applied in a simple case for ease of visualisation, which can be extended to a more practically useful case. A gamma-ray source located at 300 AU from a UV point source emits photons in two different directions with respect to the UV source's position – at 20° and at 40°. A star is assumed as the UV source: η Carinae A as modelled in [206] using $T = 2.58 \times 10^4\,\mathrm{K}$. The assumed black body emission is obtained from Equation 3.4.3. The resulting optical depth is shown in Fig. 4.2, integrated over the distance, over the spectrum, and over both. The resulting absorbed flux can be seen in the bottom right panel. The trajectory passing closest ($\simeq 100\,\mathrm{AU}$) is indicated by solid lines, while the other ($\simeq 200\,\mathrm{AU}$) by dashed lines. As seen in the top right panel, while the opacity of the lower-energy gamma rays (10 GeV, dark line) decreases rapidly when the interaction is no longer head-on ($\psi = 90°$ at 230 AU and 280 AU in the two cases, respectively), the opacity for the higher-energy gamma rays increases when $\psi < 90°$, as they can interact with the soft spectral range where the radiation is most intense. In this case, the typical UV field generated by a young, massive star tends to absorb primarily between 0.1 and 1 TeV. Absorption is only important if the trajectory passes sufficiently close to the star: indeed $200\,\mathrm{AU} \simeq 0.001\,\mathrm{pc} \simeq 0.025''$, that is 1/40 of the pixel size of the SOFIA maps (and a negligible fraction of the angular resolution of H.E.S.S.). It makes sense to investigate whether, besides the IR field, the radiation field of the NSC is capable of absorbing the radiation from the central gamma-ray source. From a qualitative point of view, the answer is “almost certainly not”, for at least two reasons:

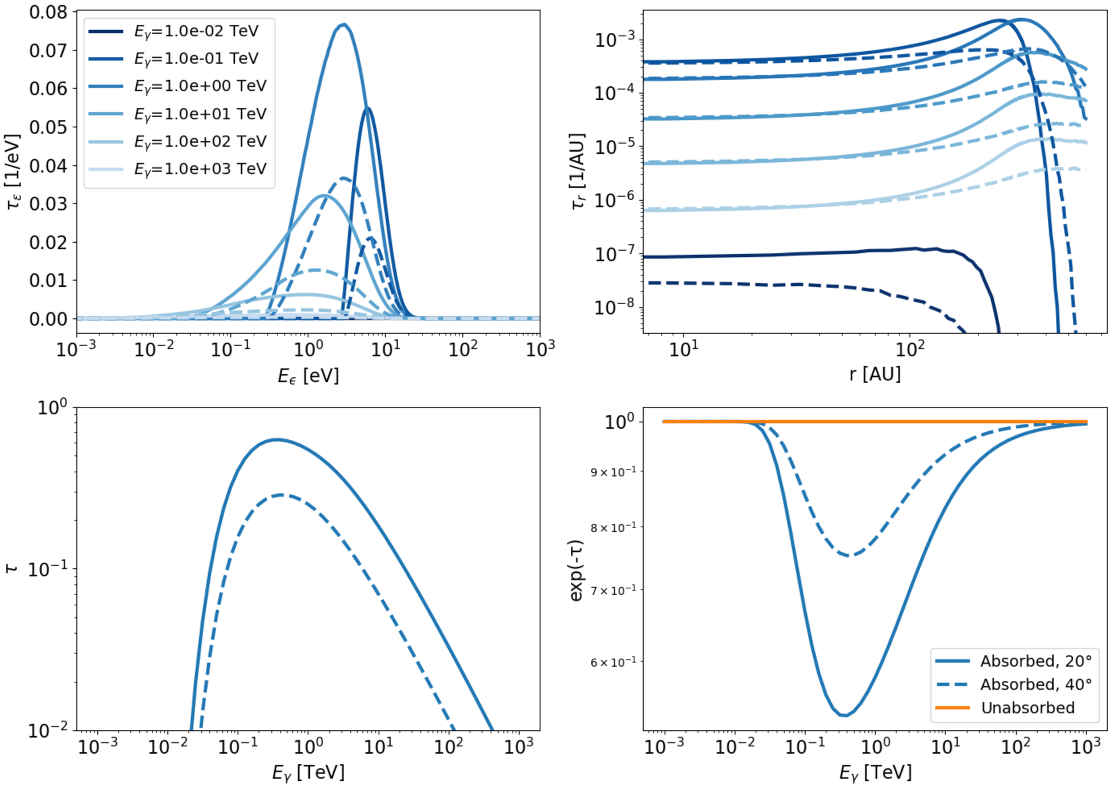

Figure 4.2: Pair production optical depth for gamma rays in a UV field, integrated over the trajectory (top left), over the spectrum (top right), and over both (bottom left), and relative gamma-ray spectrum absorption (bottom right). The details on the radiation field used and the two trajectories assumed are reported in the text. The colour code, reported only for the 20° trajectory, is the same for the other.

- the absorption by the UV field affects primarily gamma-ray energies between 0.1 and 1 TeV, but the H.E.S.S. spectrum does not show large deviations from a power-law in that range, and it would be strange to expect a gamma-ray emission peak balanced by an absorption effect that is completely independent;
- as already mentioned, the fraction of the area "covered" by the absorbing UV field is negligible compared to the projected region where the stars are distributed (a circle of radius 0.5 pc). It is very likely that some stars are along the line of sight of the H.E.S.S. maps – assuming that the central gamma-ray source is not in the foreground, with respect to the NSC – but the overall absorption effect is practically null if one assumes that the gamma-ray source is not point-like (in other words, that it can't be fully absorbed by a single star's radiation field).

As an additional check, the 1000 simulations of the NSC described in Section 3.4 were used to verify statistically how many stars would be in front of Sgr A*. Only in 3 simulations out of 1000 was a star found in the foreground within a radius of 200 AU, and never at less than 100 AU, determining a modest and statistically very unlikely absorption. All of this shows that the UV field in the GC, although extremely intense, does not play any direct[5] role in shaping the gamma-ray SED of the central source.

4.2.2 *Absorption by the Galactic bulge*

The term "galactic bulge" generally refers to a clustering of stars towards the central part of a galaxy, on scales of kpc. The stars are typically Pop II stars, "old" and low-mass. Their 3D orbits do not lie on the GP, randomised by the large number of (collisionless) encounters that occur over sufficiently long timescales in crowded environments. This gives the bulge its typical ellipsoidal shape that in some cases (e.g., M31) is even visible to the naked eye. The luminosity distribution peaks towards the centre of the galaxy, and follows a Sérsic profile:

$$I(r) = I(r_\mathrm{e})e^{\left[-b_n\left[\left(\frac{r}{r_\mathrm{e}}\right)^{1/n}-1\right]\right]} \tag{4.2.1}$$

where r_e is the half-light radius, n is the Sérsic index, $b_n(n)$ is a constant given by n and I is a surface brightness (or any projected quantity). It can be shown that b_n satisfies the condition $\Gamma(2n) = 2\gamma(2n; b_n)$ where the gamma function and the incomplete gamma function have been used respectively. The Sérsic profile is empirical, suited to describe the luminosity profile of a galaxy seen face-on. In the case of the MW, the centre of the Galaxy is seen in projection and has a typical Boxy/Peanut (B/P) shape, which today is well known to be part of the Galactic Bar seen from the GP, although a spheroidal component towards the centre has been recently observed [88]. Given the geometry of the observation, the bulge of our Galaxy is not easily comparable morphologically with the features observed in similar galaxies seen face-on, although today it is the most common investigation to understand the structure of the MW [126].

The long timescales necessary for the randomisation of the orbits select less massive

---

[5] The secondary e+/e- pairs produced can interact with the UV field by IC emission, starting a pair production/IC cascade that does modify the SED. This effect has not been taken into account here.

stars, resulting in a radiation field of the bulge with a peak in the NIR [199]. This is an energy above the pair creation threshold if $E_\gamma \gtrsim 0.1\,\mathrm{TeV}$, thus absorption is possible and must be quantified. To determine the radiation field of the Galactic bulge, the profile developed by Popescu and Tuffs 2017 [168] (hereinafter P&T17) was used, based on observations from NIR to sub-mm using COBE, IRAS, and Planck maps. The SED does not vary with the wavelength, and its dependency on the spectral index is shown in [167]. However, the resolution of the calculations in P&T17 is $\sim 50\,\mathrm{pc}$, effectively cutting out the part with the highest emissivity. Its extrapolation to shorter distances is dangerous, as at very short distances the dependence on the assumed Sérsic index is very strong. Another problem is the singularity at the centre given by the Sérsic profiles according to Equation 4.2.1, which must be resolved. Consequently, a theoretical model for the behaviour up to the central parsecs was developed, connecting it to the P&T17 profile at around 50 pc. With an additional complication: the Sérsic profile describes the behaviour of a surface brightness, that is, a quantity projected in the direction of the observer – in the case of Earth, the view is edge-on. To use it as an extension of P&T17 towards the innermost region, it needs to be de-projected radially. Appendix B illustrates the geometry of the process and derives the de-projected Sérsic profile:

$$\rho(s) = -\frac{e^{b_n} b_n}{\pi\, s^{(1-1/n)}} \int_1^\infty \frac{e^{-b_n \tau s^{1/n}}\,\mathrm{d}\tau}{\sqrt{\tau^{2n}-1}} \tag{4.2.2}$$

where s is the radially de-projected coordinate.

Regarding the singularity at the centre, one possibility to define a physically motivated non-zero inner limit of the bulge is to define a core radius r_c for which the frequency of scattering of the orbits becomes equal to the crossing time of the central region, so that stars do not further accumulate towards the centre in their random motion. The crossing time t_cr is of the order of

$$t_\mathrm{cr} \sim \frac{r_\mathrm{c}}{v_\mathrm{vir}} \tag{4.2.3}$$

where $v_\mathrm{vir}(r)$ is the virial velocity:

$$v_\mathrm{vir} = \sqrt{\frac{GM_\mathrm{e}}{r}} \tag{4.2.4}$$

with M_e mass enclosed within r. The scattering timescale t_sca, defined as the time in which a star has a sufficient number of interactions N_int so that its orbit is significantly altered, is of the order of

$$t_\mathrm{sca} \sim (v_\mathrm{vir}\, n_\mathrm{s}\, \sigma_\mathrm{sca}\, N_\mathrm{int})^{-1} \tag{4.2.5}$$

where $n_\mathrm{s}(r)$ is the density of stars at a certain radius, and $\sigma_\mathrm{sca}(r)$ is the scattering cross section for star-star interactions assuming stars travelling at $v_\mathrm{vir}(r)$:

$$\sigma_\mathrm{sca} = \pi b_*^2 \left(1 + \frac{2Gm_\mathrm{s}}{b_* v^2}\right) = \pi b_*^2 \left(1 + 4\frac{m_\mathrm{s}}{M_\mathrm{e}}\frac{r}{b_*}\right). \tag{4.2.6}$$

The impact parameter b_* – namely the minimum distance of interaction – is the most uncertain variable. It depends on both the kinematics of the encounter and the gravitational attraction. In general it must be

$$b_* \gg \frac{Gm_\mathrm{s}}{v_\mathrm{vir}^2}. \tag{4.2.7}$$

For values around $v_\mathrm{vir} = 250\,\mathrm{km/s}$ [200], the condition on b_* becomes $b_* \gg 0.01\,\mathrm{AU}$, which is a very weak constraint. In the end $b_* = 3$ AU was chosen. For values of such magnitude, the cross section is more or less constant within a couple parsecs, since $M_\mathrm{e}/m_\mathrm{s} \gg r/b_*$, so that $\sigma_\mathrm{sca} \simeq \pi b_*^2$.

Finally, it can be demonstrated that, statistically, a single interaction does not significantly modify the trajectory of a star, but a number of encounters $N_\mathrm{int} \approx 0.1 N_\mathrm{e}/\ln(N_\mathrm{e})$ is required, with $N_\mathrm{e}(r)$ being the number of stars contained in the region (which is exactly the reason why only stars with a sufficiently long life populate the bulge).

The equilibrium is reached when

$$t_\mathrm{tr} \sim t_\mathrm{sca} \Longrightarrow r_\mathrm{c} \sim (n_\mathrm{s}\, \sigma_\mathrm{sca}\, N_\mathrm{int})^{-1}. \tag{4.2.8}$$

Thus, a set of equations has been found that can be solved iteratively starting from a set of initial values. All variables depend on r_c: the number of crossings, the cross section, the enclosed mass, and the local star density. Regarding the last two, in principle their value can be calculated from the profile in Equation 4.2.2, scaling it with respect to a known luminosity density profile (P&T17) and making assumptions about the mass/luminosity ratio. In the case of the number of stars, it

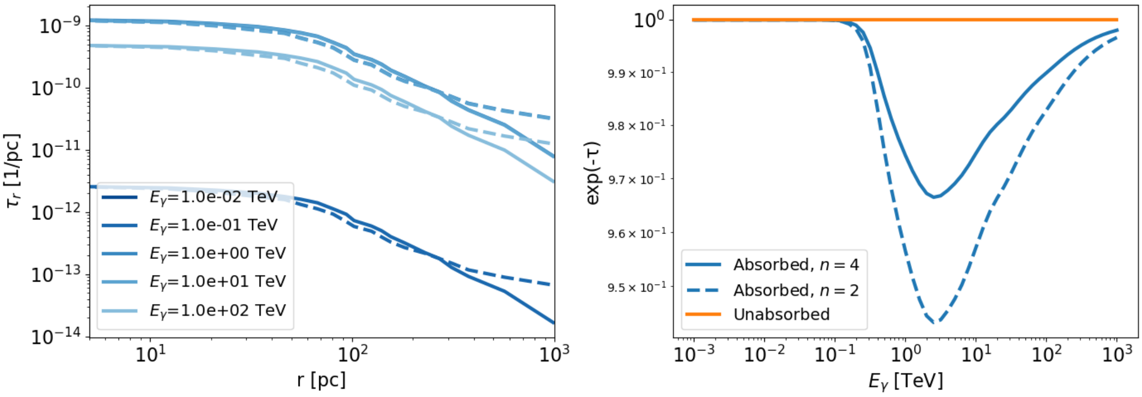

Figure 4.3: Pair production opacity in the Galactic bulge (left panel) and gamma-ray absorption by the bulge radiation (right panel), assuming a Sérsic index $n = 2$ (solid line) and $n = 4$ (dashed line).

is also necessary to calculate an average stellar mass, which is obtained by averaging the density over an IMF. For the IMF and the mass/luminosity ratio, the values in [214] were used, which give an average mass of $0.75\,\mathrm{M}_\odot$.

The equilibrium is reached at $r_c = 5 \pm 2\,\mathrm{pc}$, at which one finds $M_e = 4 \times 10^7\,\mathrm{M}_\odot$ and $n_s = 10^4\,\mathrm{pc}^{-3}$. These values are in agreement with those found for example in [199]. Compared to the single UV source scenario, the geometry of gamma-ray absorption by the bulge radiation field is significantly different because the direction of the soft photons is random at each point of the trajectory. This means that there is a relative abundance of soft photons in all the "effective directions" for absorption (head-on for the lower gamma-ray energies, at large angles for the higher ones), determining a rather wide range of affected energies – from a few tens of TeVs to 10^3 TeV – but at the same time a more moderate absorption. The profile is shown in the right panel of Fig. 4.3, while the optical depth integrated over the frequency spectrum is reported in the left panel. Two cases were analysed: $n = 4$, adopting the bulge profile in P&T17, and $n = 2$, obtained by making the appropriate changes to the radiation field according to [167]. As can be expected (see for example their Figure 13), a lower Sérsic index results in a greater concentration of stars at large distances, but not near the centre. In both cases, the absorption is very modest.

4.2.3 *Gamma-ray background in the inner few parsecs*

Before studying the gamma-ray absorption by the MIR/FIR radiation field, it is necessary to quantify how much of the intrinsic flux should be included in the absorption calculations. Indeed, the FWHM of H.E.S.S.'s PSF at 1 TeV is about 5′, which therefore corresponds to the apparent extension of a point source – as HESS J1745–290 was modelled [19]. Thus, regardless of the real extension of HESS J1745–290, the background lying in the same LoS would need to be evaluated in the solid angle subtended by the PSF. However, the H.E.S.S. flux is extracted using the forward folding method [19], which means that the spectrum shown is associated exclusively with HESS J1745–290, and therefore there is no need to worry about the background when modelling the flux absorption.

Even considering the scenario in which the spectrum of HESS J1745–290 was obtained through aperture photometry, and where the flux must therefore be considered as the sum of the source and the various background contributions, the situation does not change drastically. The flux of the diffuse emission enclosed within the FWHM of H.E.S.S. is 9 times lower than the central source's. If one assumes that absorption is significant for $u_{\rm rad} > 10^3\,{\rm eV/cm^3}$, the absorbing region corresponds to the central 2′ ($\sim 5\,$pc), which is $5^2/2^2 = 6.25$ times smaller than the area subtended by the PSF. In this case, the spectrum of HESS J1745–290 is the sum of the intrinsic flux of the central source plus the remaining 1/9, part of which (15%) is absorbed because it lies near Sgr A*, and only a total of less than 10% of the flux lies in the outer part and should be subtracted before the absorption calculations.

4.2.4 *Absorption by the local IR field*

To study the absorption towards the observer of the emission from the central gamma-ray source, both its geometry and intrinsic (non-absorbed) spectrum have been modelled. The former was studied in terms of three parameters: position of the centre, shape, and size. Once its 3D spatial distribution was obtained, absorption was calculated using a ray-tracing approach: Equation 4.1.13 was solved in every cell traversed moving towards the observer. By performing this calculation for each ray starting from every cell inside the source (utilising the spatial resolution of the 3D IR radiation field map), one obtains the average absorption for each value of E_γ and for that specific geometry. Several sets of parameters were investigated:

- For the source shape, two possibilities were assumed – either a sphere or a shell.
- Regarding its size, four external radii were considered (point-like, 0.3 pc, 0.7 pc, 1.3 pc). In the case of shells, the internal radius was taken as 4/5 of the

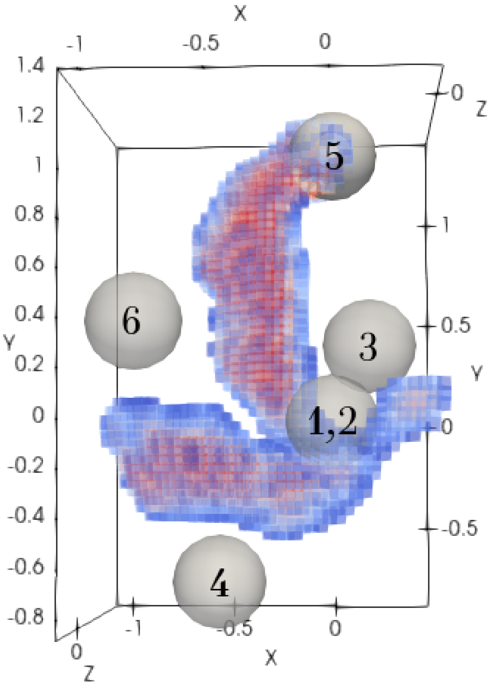

Figure 4.4: The 6 regions defined in the text. Their 3D offsets from Sgr A* are reported in Table 4.1, and their absorption spectra are shown in Fig. 4.5. Regions #1 and #2 lie on the same LoS. The grid is in units of parsecs.

external radius. Additionally, a large shell with radii from 1.5 pc to 2.5 pc was considered (tailoring the radii of the CNR).

- For the centre, a grid of values (x, y, z) between −0.5 pc and 1.5 pc with a spacing of 0.5 pc was initially taken. The area corresponding to the centroid of H.E.S.S. (see Fig. 2.3) was sampled with a spacing of 0.2 pc. Around the regions that are more “interesting” from a spectral point of view (see below), the spacing was refined to 0.1 pc.

To study the absorption spectrum, a simple flat emission profile was assumed (a power-law with index 0, as in the case of Fig. 4.2), calculating the absorption for each adopted geometry. To qualitatively assess the dependence of absorption on the shape and position of the gamma-ray source, six regions were selected (highlighted and numbered in Fig. 4.4) and various source shapes modelled. The regions are: 1) Sgr A*; 2) in the same LoS as Sgr A*, but 1 pc further away from the observer; 3) inside the cavity, coinciding with the position of G359.95–0.04; 4) below the HB; 5) within the NA, at the intersection with the CNR; 6) above the HB, to the left of the NA. The coordinates are reported in Table 4.1. Five different shapes were chosen: a point source, the small, medium, and large spheres previously introduced, and the largest shell. The absorption towards the observer for each combination of shape and position is plotted in Fig. 4.5. The values at 10 TeV and 40 TeV are reported in Table 4.1.

To understand the spectra in the figure, one needs to keep in mind the morphology of the UV radiation field on one hand, and how the gamma-gamma interaction depends on the collision angle on the other. Regarding the first point, the intensity of the radiation strongly depends on the distance from the ionised filaments (see Fig. 3.43). As for the second, the spectral range of absorption depends on the relative position of the source and filaments with respect to the observer (see the third panel of Fig. 4.1 and related discussion). The gamma rays reaching the Earth from a source positioned in front[6] of the filaments interact at very low collision angles with the soft photons, resulting in the absorption of higher E_γ. A source positioned behind the filaments, in addition to this absorption, "sees" them in front – i.e., the photons must traverse the high-radiation region head-on, with the consequent absorption of lower gamma-ray energies, before interacting with the soft photons coming "from behind". Consequently, the absorption of gamma-ray radiation at $5-10$ TeV and 40 TeV is determined, more than by variations in the IR emission temperature (not very broad in the ionised filaments), by whether a source is beyond the hot structures – as well as by how close it is to them in projection.

This point is especially valid for point sources, whose photons all intercept the same structures and are absorbed in the same way. For extended sources, the total absorption is the average of the contributions from each small volume that constitutes the source. For a source with a radius greater than 0.5 pc (compare again to Fig. 3.43), even if centred in a region with a high density of IR radiation, the gamma-ray flux sums contributions from regions with much lower radiation densities, resulting in a flattening of the absorption profile.

The comparison between the absorption spectra #1 and #2, namely from two regions of high intensity of warm radiation but positioned on opposite sides of the filaments, is highly illustrative. The substantial difference for point-like sources, as expected, is given by the absorption between 2 and 15 TeV and by the fact that photons emitted from region 2 travel through the filaments. As the size of the source increases, the effect diminishes because part of the volume is in less absorbed lines of sight.

The CNR/CND is clearly another source of absorption, but its radiation density is

---

[6] "As seen by the observer" is implied from now on.

#	3D offset [pc]	shape	abs_{10} [%]	abs_{40} [%]
1	$\Delta x = 0$ $\Delta y = 0$ $\Delta z = 0$	point-like	0.43	0.67
		small sphere	0.49	0.65
		medium sphere	0.34	0.53
		large sphere	0.10	0.27
		large shell	0.03	0.13
2	$\Delta x = 0$ $\Delta y = 0$ $\Delta z = -1$	point-like	0.65	0.69
		small sphere	0.63	0.68
		medium sphere	0.47	0.56
		large sphere	0.13	0.27
		large shell	0.03	0.13
3	$\Delta x = 0.15$ $\Delta y = 0.3$ $\Delta z = 0$	point-like	0.29	0.62
		small sphere	0.23	0.51
		medium sphere	0.23	0.37
		large sphere	0.16	0.24
		large shell	0.08	0.12
4	$\Delta x = -0.5$ $\Delta y = -0.7$ $\Delta z = 0$	point-like	0.35	0.58
		small sphere	0.29	0.47
		medium sphere	0.22	0.30
		large sphere	0.14	0.18
		large shell	0.09	0.11
5	$\Delta x = 0$ $\Delta y = 1.2$ $\Delta z = -0.5$	point-like	0.52	0.58
		small sphere	0.43	0.50
		medium sphere	0.30	0.38
		large sphere	0.14	0.26
		large shell	0.05	0.12
6	$\Delta x = -0.8$ $\Delta y = 0.4$ $\Delta z = 0.5$	point-like	0.18	0.51
		small sphere	0.14	0.43
		medium sphere	0.17	0.32
		large sphere	0.12	0.24
		large shell	0.06	0.12

Table 4.1: Modelled gamma-ray sources defined spatially in Fig. 4.4. The columns indicate respectively: centre position with respect to Sgr A*, shape (see the text for the source size), and expected absorption at 10 and 40 TeV. The full absorption spectra are shown in Fig. 4.5.

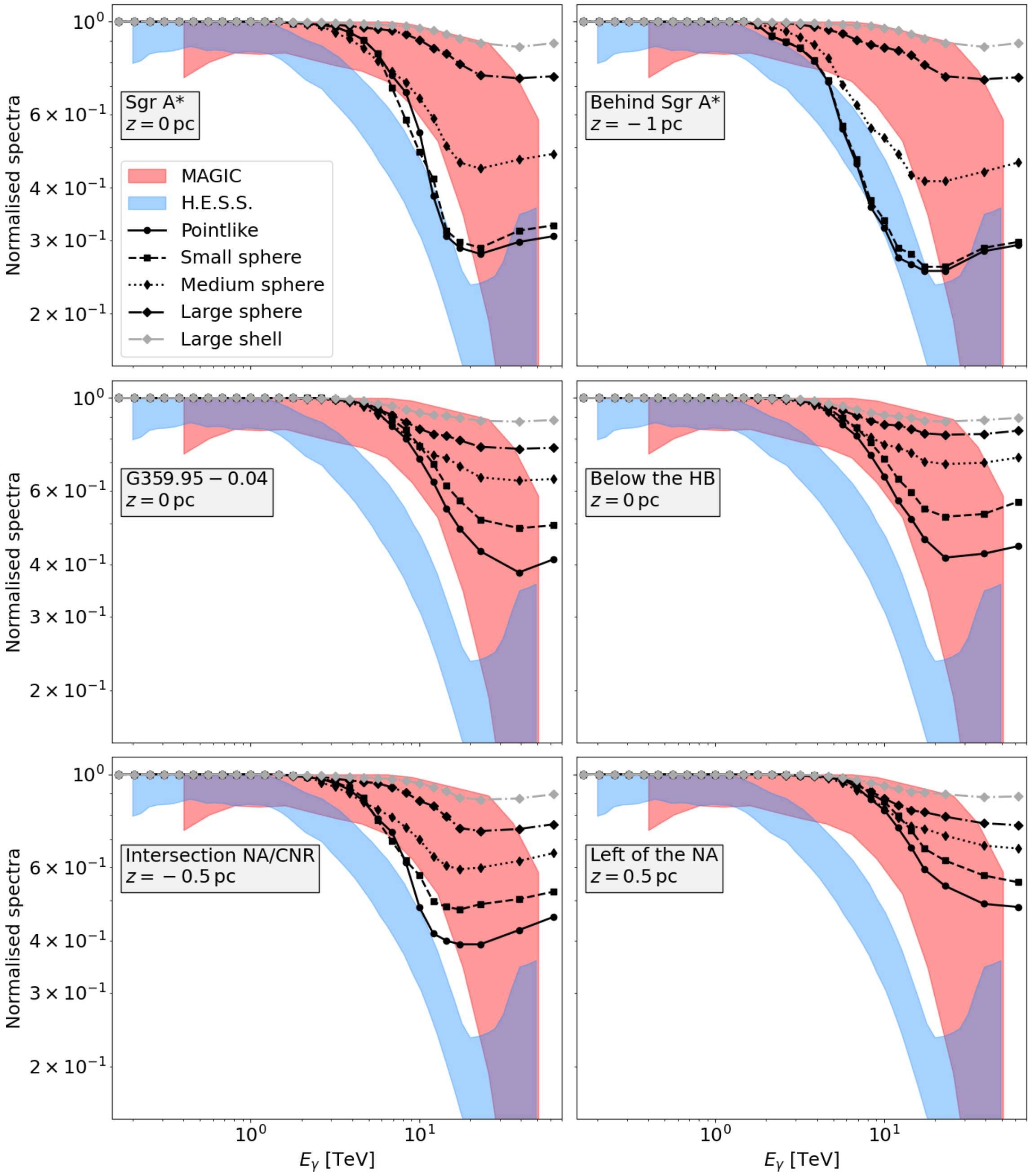

Figure 4.5: Absorbed spectra in the GC regions listed in Table 4.1 and shown in Fig. 4.4, under different assumptions on the source shape and extent. The corresponding numbering (1 – 6) goes from left to right and from top to bottom, so that the region #3 corresponds to the mid-left panel. If $z > 0$, the source is closer to the observer. The shaded areas correspond to the ratio of the H.E.S.S. (blue) and MAGIC (red) bands fitting the central source emission (the shaded areas shown in Fig. 2.2) to the respective bands fitting the diffuse emission (see [93] for H.E.S.S. – also shown in Fig. 2 – and [139] for MAGIC).

significantly lower. Furthermore, the disk is rather inclined relative to the direction of the observer, with the consequence that there is not much cold material (which would absorb around 40 TeV) in the line of sight of the entire CC. As an example, the region #5 in the bottom left of Fig. 4.5 (the intersection between NA and CNR) falls in the LoS of both, and indeed shows relatively high absorption both at 10 TeV – as expected from a source embedded in the NA – and at 40 TeV due to both the photons from the NA towards the observer and the absorption by the CND.

The regions #3, #4 and #6 have been chosen as probes for a gamma-ray source in different positions inside the CC, even if only #3 corresponds to a known gamma-ray candidate (G359.95–0.04). They all show the spectra one could expect given the similar MIR/FIR intensities, including #6 which is slightly shifted towards the observer and shows an absorption peak around 60 TeV, as expected from an IR radiation field emitted by structures located behind. Obviously, being clearly of leptonic origin (as discussed in Section 2.1.1), G359.95–0.04 is not linked to the diffuse gamma-ray emission – at least not through its CR accelerator. This will be further investigated in Section 4.4).

In general, sources with an offset $z < 0$ have greater absorption between 10 and 20 TeV compared to those with $z > 0$. The spectral profiles of the shells are rather independent of the position of the centre since the fraction of volume behind and in front of the $z = 0$ plane is practically the same, with few variations, and a similar argument can be made for the large spheres, although in the latter case the ratio of the absorption values at 10 and at 40 TeV (listed in Table 4.1) is more sensitive to the offset. As expected, more compact sources show a larger variability in their absorption profiles depending on their position, and it is not surprising that the most absorbed source is a point source positioned right behind the filaments (#2).

To assess the likelihood of each scenario, it is necessary to discuss the relationship between their geometry and the possible physics of associated CR acceleration and gamma-ray emission. This will be discussed in the next section.

4.3 CONSTRAINTS ON THE GAMMA-RAY SOURCE GEOMETRY

In the previous section, absorption spectra were calculated depending solely on the morphology of the gamma-ray source, regardless of the underlying physics. However, the physics of CR acceleration and gamma-ray emission have characteristic lengthscales and shapes depending on the mechanism invoked (for example, scales of Sgr A*'s Schwarzschild radius for p+γ emission, or the shell of $50-100$ pc radius associated with the Cygnus Cocoon [7]), which can be taken into account in order to evaluate from a physical standpoint the gamma-ray sources presented above. The central questions of this thesis were anticipated in Section 2.3: is it possible to assume that the central gamma-ray source HESS J1745–290 and the diffuse emission on scales of 250 pc share the same CR accelerator and consequently the same intrinsic gamma-ray spectrum? In this case, could it be possible that the differences between the two spectra (namely, the cut-off of HESS J1745–290 above a few TeVs) are due to gamma-gamma absorption? Which sources are compatible with this hypothesis, assuming the spectra observed by H.E.S.S. and MAGIC?

Regarding this last point, it should be noted that the two scenarios (H.E.S.S. and MAGIC) represent significantly different paradigms as MAGIC claims that the spectrum of the diffuse emission presents a cut-off at 17.4 TeV [139], unlike H.E.S.S. (see the discussion in Section 2.2). Consequently, the two absorption scenarios are substantially different above $2-3$ TeV. To visualise this, two different bands, corresponding to the ratio between central and diffuse emission, have been superimposed onto the absorption spectra in Fig. 4.5. As the central emission model, the band given in [93] and the band given for Sgr A* in [23] were used for H.E.S.S. and MAGIC respectively, both also shown in Fig. 2.2; as the intrinsic spectrum model, the bands of the diffuse emission reported in the same two papers were used. Both bands in the figure correspond to 1σ deviations. The uncertainty of the spectral points comes mainly from the uncertainty of the dust mass values and is 15% of the flux at $\tau = 1$ (hence for an absorbed flux $I_\nu^{\mathrm{abs}} = e^{-1} = 0.37$, in which case $\sigma_I = 0.05$) and tends to 0 at $\tau = 0$.

The most significant result is that, apart from region #2, no gamma-ray source – and in particular no source centred on Sgr A*– is compatible with the H.E.S.S. scenario. In other words, if one assumes that the CR accelerator at the centre of our Galaxy is capable of accelerating protons to energies around the PeV, the physics of the central source must be uncorrelated with that of the diffuse emission. Given the abundance of possible local CR accelerators within the H.E.S.S. centroid (Sgr A*, G359.95–0.04, the NSC – and these are just the known ones), this conclusion is perfectly reasonable. Regarding region #2, it should be noted that it represents a point-like or very compact source in the same line of sight as Sgr A*, but conveniently located beyond the ionised filaments. Although theoretically possible, it is clear that the probability of having such a source is decidedly low.

Another non-trivial point is that the compact sources centred on Sgr A* are not compatible within the error with any absorption scenario. Sgr A* and the NSC can still be CR accelerators, but then the source cannot be compact[7]. For more extended structures (spheres with radius ≥ 0.7 pc), the data are compatible with a MAGIC absorption scenario. In other words, a spherical source coinciding with the NSC or with a radius of up to 1.3 pc can be powered by the same proton accelerator that fuels the diffuse gamma-ray emission in the CMZ, assuming a cut-off around 17 TeV. Similarly, a spherical-shaped source located in the CC is compatible with MAGIC. By extension, since the scenario holds from point-like sources to spheres with a radius of 1.3 pc, it holds for a source of any shape (as long as it is not hollow, like shells), although no significant hadronic candidates are known in the CC besides Sgr A* and the NSC.

Wide shells (radius $r > 1$ pc) are too weakly absorbed to validate an absorption scenario. On the other hand, from a phenomenological point of view, thin shells of smaller size are unlikely, and increasing their thickness tends to converge them to spheres. This is not a trivial remark – one of the main candidate accelerators responsible for the diffuse gamma-ray emission is the NSC. Although no termination shock (TS) is observed, by analogy with YMSCs with similar properties (Westerlund 1 [8], Cygnus Cocoon [7, 43]), one might expect acceleration at a distance of 5 – 10 pc and possibly gamma-ray emission from the fraction of the CND contained within. However, in this case one would not expect the gamma-ray luminosity to be concentrated in the central parsec. Consequently, if the NSC is the central accelerator responsible for the diffuse gamma-ray emission, either the CR acceleration is well confined within the cluster itself (approximately 0.5 pc in radius), or HESS J1745–290 is due to another accelerator. The possibility that the central source is due to Colliding Wind Binaries (CWBs) is ruled out by the fact that the flux of HESS J1745–290 extends beyond 20 TeV [92].

---

[7] Or the observed cut-off is simply not due to gamma-gamma absorption, as already discussed in Section 2.3. Although this chapter focuses on absorption, one should keep this caveat in mind.

4.4 Implications for the local gamma-ray and cosmic-ray source

The “geometric” constraints from the absorption spectrum have isolated two categories of sources – extended structures centred on Sgr A*, and variously shaped structures in the CC – but the intense absorption in the CC has a few implications even if the central gamma-ray source does not share a common origin with the diffuse gamma-ray emission, as will be discussed later in the section. The information from gamma-ray emission physics can now be exploited to assess the best candidates for HESS J1745–290. In the next part, a few possible emission models for HESS J1745–290 are discussed, and later in the chapter the constraints based on both physical and geometrical arguments will be put together.

4.4.1 *Sgr A**

The gamma-ray emission from the central source can in principle be modelled through both hadronic and leptonic emission processes. One main difficulty when choosing an emission model is that very little is known of the spatial scale of either the CR acceleration and their gamma-ray emission – and on different scales, the environmental conditions change dramatically:

- On so-called “magnetospheric” scales (on the order of the Schwarzschild radius $R_S \sim 4 \times 10^{-7}\,\mathrm{pc}$), magnetic fields have a disordered geometry and show a large variability on timescales of less than a hour [115], with flux densities constrained to tens of Gauss. We would expect synchrotron emission from protons, perhaps IC emission (predicting the electric fields under those gravitational conditions is currently next to impossible), and possibly even emission through p+γ interactions ($\mathrm{p} + \gamma \rightarrow \mathrm{p} + \pi^0$), with VHE emission due to pion decay.
- On the scale of the accretion disk (Bondi radius $\sim 10^5 R_S$ [204]), one would definitely expect hadronic emission from proton-proton collisions. However, depending on the electric fields, the energy transferred to electrons on these scales and the magnetic fields, IC emission could also be important. Similar considerations should be made again for $\mathrm{p} - \gamma$ interactions.

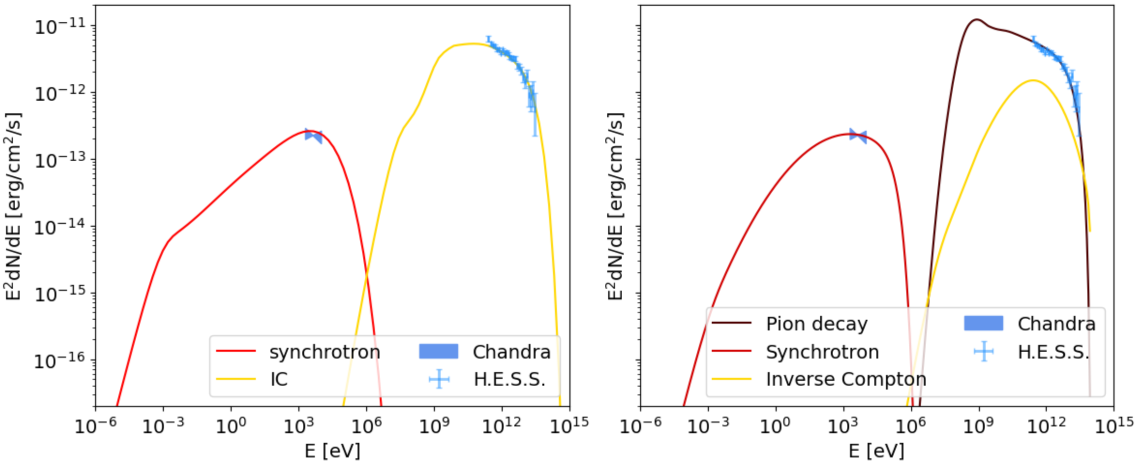

Figure 4.6: SED of HESS J1745–290 fitted with a leptonic (left panel) and a hadronic (right panel) emission model, assuming Sgr A* is the accelerator. Besides the flux reported by H.E.S.S., the X-ray flux constraints by Chandra are shown (taken from [90]). For the IR radiation field density in FIR and NIR, we used the values calculated in Section 3.8 in the inner arcsecond, corresponding to a maximum distance of 0.04 pc from Sgr A*. The relatively low B field value of 90 μG assumes that the emission is generated far from the black hole. All spectra have been calculated using GAMERA [98]. The parameters used in both cases are given in Table 4.2.

- On scales smaller than a parsec, the NSC could be responsible for the acceleration of particles up to several TeV, both through hadronic and leptonic emission processes.
- On scales larger than $\sim$ 1.2 pc, well beyond the centroid radius of H.E.S.S. but within its FWHM, the CND provides a significant number of protons distributed rather symmetrically around Sgr A*, leading to emission through pp collisions. Similarly, on the same scale, there are dozens of unresolved non-thermal sources – for instance in the Chandra catalogue[8] – such as PWNe and hot magnetised filaments, which could contribute to leptonic emission.

It is then not surprising that the H.E.S.S. data can be fitted with both hadronic and leptonic emission models. An example is shown in Fig. 4.6. Modelling the emission on the smallest scales has been avoided, since the physics of particle interactions becomes too complicated for this kind of study. The parameters used in the figure are described in the caption and listed in Table 4.2. On one hand, the data can be fitted assuming electron acceleration in a termination shock around the SMBH, but the gamma rays need to be produced far enough from it to justify a magnetic

---

[8] https://cxc.cfa.harvard.edu/csc/.

	FIR u_{rad} [ev/cm^3]	NIR u_{rad} [ev/cm^3]	E^e_{min} [GeV]	α_e	W_e [erg/s]	B [μG]	E^p_{max} [GeV]	α_p	W_p [erg/s]
Sgr A*, leptonic	5×10^3	5×10^4	10	2.0	4×10^{35}	90	-	-	-
Sgr A*, hadronic	5×10^3	5×10^4	10	2.0	10^{35}	200	10^5	2.2	5×10^{35}
G359.95–0.04	3×10^3	2×10^4	20	2.0	5×10^{35}	100	-	-	-
GeV bump, hadronic	-	-	-	-	-	100	3×10^3	2.4	10^{36}

Table 4.2: Parameters used in fitting HESS J1745–290 SED for different scenarios, plus the Fermi SED in the last row. From left to right: energy density in FIR, energy density in NIR, minimum energy of injected electrons, electron distribution spectral index, total power of injected electrons, magnetic field flux density, maximum energy of injected protons, proton distribution spectral index, total power of injected protons. The maximum energy of injected electrons is set to 1 PeV, while the minimum energy of injected protons is set to 1 GeV. The gas density is set to 4×10^4 cm^{-3}. Lastly, the injection age is set to 10^4 years.

field of 90 μG (left panel), which allows for synchrotron emission to fit the Chandra observations during a quiescent phase. At the same time, the TeV component is fitted by the IC scattering of the electrons on the intense IR radiation fields at less than 1″ from the black hole. The radiation field density calculated in Chapter 3 has an angular resolution of 1″, so the values reported must be regarded as a lower limit. Even if the injected electrons reach an energy of 1 PeV, the IC peak energy does not depend drastically on the maximum electron energy (see Fig. 1.7).

On the other hand, the TeV data can be fitted assuming proton acceleration on small scales followed by collision with the orbiting material, leading to pion production and decay (right panel). Given the intense radiation fields, the power injected in the electrons needs to be much lower or IC would dominate, which in turn leads to a larger required value for the magnetic field in order to fit the Chandra data. The radio constraints on the flux determine a lower limit of 20 GeV for the electron energy. Contrary to the leptonic case where the H.E.S.S. turn-off at 5–10 TeV did not put major constraints on the maximum electron energy, the pp emission profile is very sensitive to the turn-off position, setting an an upper limit of 100 TeV for the maximum proton energy.

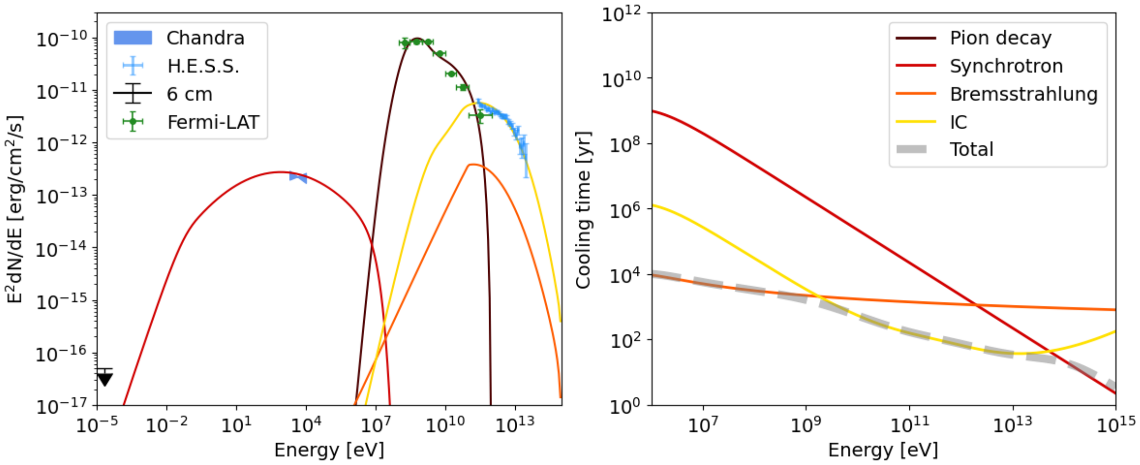

Figure 4.7: Left panel: SED of HESS J1745–290 fitted by modelling the TeV source as the PWN G359.95–0.04. The Chandra constraints to the flux are taken from [203]. The radio flux at 6 cm [127] is also included. The parameters used are reported in Table 4.2. For the IR radiation field density in FIR and NIR, the values used are the ones found in Section 3.8 assuming that the PWN projected distance to Sgr A* is its real distance (see discussion in there). The Fermi points from 100 MeV to 300 GeV are also shown and fitted with a separate hadronic component, even if a IC GeV scenario is also possible. Right panel: cooling timescales of the TeV electrons.

4.4.2 *G359.95–0.04*

This PWN has been found in 2005 using Chandra observations [203] and has been immediately considered a candidate for HESS J1745–290 [105]. A small introduction to it has been given in Section 2.1.1. Since its X-ray spectrum softens at larger distances from the pulsar instead of hardening as it would be expected in case of IC scattering in the Klein-Nishina regime, in [105] they assume synchrotron emission in the surrounding halo and find a lower limit of 100 μG for the magnetic field. By modelling its TeV emission, they showed that this source could account for the flux and the spectrum measured by H.E.S.S.

However, the Fermi observations complicate this scenario. While for Sgr A* an additional past flaring phase could be invoked, this is not the case for PWN models. At the same time, no hadronic emission is expected. Therefore, PWNe can only explain the TeV emission if it is assumed that the GeV emission is due to other sources – most likely to Sgr A* rather than Sgr A East since the centroid of the GeV emission moves even further away from the SNR [49]. This additional component is shown in the same figure, and it is modelled as pion decay due to protons with energies lower than $\sim 3\,\text{TeV}$. In other words, the additional accelerator needs to be quite inefficient. It should be noted that this additional GeV hadronic component could also fit the Sgr A* IC TeV scenario shown in Fig. 4.6.

The cooling time around 10 TeV is about 30 yr, dominated by IC cooling despite being in KN regime. This allows placing a constraint on the maximum size of the TeV source using Equation 1.1.22. The result is strongly dependent on the diffusion coefficient used: if one appropriate for Galactic CRs ($D \simeq 2 \times 10^{30}\,\mathrm{cm}^2/\mathrm{s}$) is used, a source radius of 21 pc for 10 TeV electrons and 16 pc for 1 TeV electrons is obtained. For a Kraichnan-type turbulence spectrum (Section 1.1.4), distances of about 12 pc and 10 pc are obtained, which are lower than the FWHM of the H.E.S.S.'s PSF. Invoking Bohm diffusion $D \propto E \times B^{-1}$ yields a much lower distance (1.1 pc), but it is a scenario excluded by the energy-dependent morphology of the X-ray distribution [105]. Finally, in a rather varied case study of PWNe with different ages (VelaX, Geminga, Monogem) diffusion appears to be suppressed, with coefficients lower by two orders of magnitude [107, 170]. Adopting a value of $D = 10^{28}\,\mathrm{cm}^2/\mathrm{s}$ at 10 TeV a source radius of 1.5 pc is obtained, corresponding to a source radius smaller than $1'$. In this case, the TeV source is relatively compact, moderately absorbed (around 20% between 20 and 50 TeV), and point-like for H.E.S.S.

4.4.3 *Constraints from the gas in the CNR*

In the absorption scenario, the source must obviously be hadronic: in order to have the same intrinsic gamma-ray spectrum, the emission from the central source must be due to the same population of protons that fuels the diffuse emission. This includes the possibility that the gamma rays are produced very close to Sgr A* (on magnetospheric scales or on the accretion disk). On the other hand, the proton injection rate required to power the diffuse gamma-ray emission is $10^{37} - 10^{38}$ erg/s [93], which is two orders of magnitude higher than the bolometric luminosity of Sgr A*– an unlikely but not impossible value. However, the analysis of the absorption spectra excludes within 1σ that a compact gamma-ray source centred on Sgr A* is linked to the diffuse emission. If there is proton acceleration and gamma-ray production on such small scales, these protons do not power the gamma-ray luminosity of the CMZ.

On another note the gas distribution, and therefore the gamma-ray luminosity of HESS J1745–290, could help further constrain the possible options under certain assumptions about CR diffusion in the inner 10 pc. However, the fact that the CC does not contain molecular gas constitutes a problem – the mini-spirals contain around ten solar masses, while much more is required to account for the HESS J1745–290 luminosity $L_\gamma \simeq 7.8 \times 10^{34}$ erg/s (calculated from the H.E.S.S. data shown in Fig. 2.2). One can roughly estimate the amount of the necessary gas mass M_γ from

$$L_\gamma(E) = L_\mathrm{p}(E)\, n_\mathrm{p} \sigma_\mathrm{pp}\, l\, F_{\mathrm{p}-\gamma} \quad \Longrightarrow \quad M_\gamma = \frac{3}{4}\pi R_\mathrm{g}^3\, n_\mathrm{p}(l, L_\mathrm{p})\, m_\mathrm{p} \tag{4.4.1}$$

assuming a sphere with radius R_g. The variable quantities that need to be assessed are the (diffusion-dependent) path length l and the proton luminosity L_p. The cross-section σ_pp for $\mathrm{p} + \mathrm{p} \to \mathrm{p} + \mathrm{p} + \pi^0$ for a TeV proton is about $1.4 \times 10^{-25}\,\mathrm{cm}^2$ and varies very little across the TeV range [156]. The fraction of energy transferred to the gamma-ray photon $F_{\mathrm{p}-\gamma}$ is around 10% [116]. Given a pp interaction timescale $t_\mathrm{pp} \simeq 1.6 \times 10^8\,\mathrm{yr}/n_\mathrm{p}$ [93], L_p can be found from

$$\eta_\mathrm{CR}\, E_\mathrm{p} = L_\gamma \times t_\mathrm{pp} \quad \Rightarrow \quad L_\mathrm{p} = \frac{E_\mathrm{p}}{t_\mathrm{d}} \tag{4.4.2}$$

with E_p being the total proton energy, t_d the diffusion timescale and $\eta_\mathrm{CR} \approx 1.5$ a coefficient accounting for the diverse chemical composition in the CRs and in the ISM. t_d and the path length $l = c \times t_\mathrm{d}$ are obtained by solving $t_\mathrm{d} = R_\mathrm{g}^2/6D$ for a diffusive environment (the slight difference from Equation 1.1.22 is due to scattering being modelled in 3D). The diffusion timescale has been calculated for 150 TeV protons, responsible for the emission of 15 TeV gamma rays.

Adopting a tentative value $R_\mathrm{g} = 2\,\mathrm{pc}$, one obtains the value $M_\gamma \simeq 650\,\mathrm{M}_\odot$. This value is of the same order of magnitude as the value reported in Table 3.5 for the CNR, adopting a gas-to-dust mass ratio of 124. Furthermore, the adopted value of R_g is smaller than the extent of the gamma-ray source, which is $1.3' \simeq 3\,\mathrm{pc}$ in radius [11]. This confirms that the CNR can be the origin of the emission from HESS J1745–290, as it has enough gas available to fuel the gamma-ray emission.

However, the value of the gas-to-dust mass ratio used is not calibrated for the GC. Using the more realistic values provided in Table 3.5, the available gas mass is significantly reduced. Extending the diffusion radius of the protons up to 3 pc, which is still compatible with the extent given by H.E.S.S., and using a gas-to-dust mass ratio of 30, results in a total mass of about $450\,\mathrm{M}_\odot$ which is not sufficient for the required gamma-ray luminosity. A possible solution is to use the gas mass values derived directly by tracing the gas itself (e.g., CO [45], HCN [146]), thus freeing oneself from the uncertainties on the gas-to-dust ratio. In general, the gas mass values found in this way are much higher ($\sim 10^4\,\mathrm{M}_\odot$), providing a solution to the problem.

On the other hand, the condition $t_\mathrm{d} \gg R_\mathrm{g}/c$ places a strong constraint on the diffusion coefficient due to the reduced scale of diffusion: $D \ll 4.6 \times 10^{28}\,\mathrm{cm}^2/\mathrm{s}$ at 10 TeV, which is already an order of magnitude lower than that used in [93] or the value assumed for TeV CRs in the Galactic disk (Equation 1.1.21). Since the magnetic field in the CC is rather intense (a few 10s of μG in the cavity and a few mG in the mini-spiral [74]), an enhanced diffusion with $D = 5 \times 10^{24}\,\mathrm{cm/s} \times (E/1\,\mathrm{GeV})^{1/2}$ [15] could be invoked, or even Bohm diffusion considering that in this case the limit for the mean free path is given by the Larmor radius, which for a 10 TeV proton in a magnetic field $B = 100\,\mu\mathrm{G}$ is about 10^{-4} pc (see [109] for a discussion on the limits of this assumption). A better geometry of the gamma-ray source can also be taken into consideration: since most of the protons are on the CNR, the comparison of the excape timescale to the pp-interaction timescale should be considered only in the 1.5 pc-thick external layer, in which case the gas density is not averaged on the sphere but sensibly higher ($N_\mathrm{H} = 2 \times 10^5\,\mathrm{cm}^{-3}$ [75]).

Assuming the former case (diffusion with a Kraichnan-type turbulence spectrum), the path length increases considerably. Using the gas density calculated on the shell yields an escape time of 8×10^2 yr which gives a value around $L_\mathrm{p} = 5 \times 10^{35}$ erg/s. Such a value is lower than the bolometric luminosity of Sgr A* and constitutes a negligible amount of the power due to the accretion onto the SMBH. Notably, it is the same proton luminosity value used to fit the emission from Sgr A* in Fig. 4.6 and reported in Table 4.2.

Although the CNR contains enough gas within 2.5 pc, the geometric distribution of the gamma-ray emission is that of a thick shell[9] which is not compatible with the absorption scenario (see the grey profile in Fig. 4.5). Consequently, if the emission from HESS J1745–290 is due to the interaction of protons accelerated on Sgr A* or the NSC, the CR accelerator responsible for the gamma-ray emission in the CMZ must be another – unless gamma-ray absorption and fast diffusion at higher energies are invoked at the same time.

Considering that the incompatibility between the CNR as the gamma-ray source and the geometry of the absorption scenario is only due to a $10-15\%$ missing flux

---

[9] One should not forget that the CC is noticeably under-dense outside the mini-spirals, which means that even if a space-averaged volume has been considered, the gas is way denser on the CNR and the gamma-ray luminosity is expected to trace it.

at 40 TeV, this option looks very reasonable. Moreover, the runaway of 400 TeV protons can be easily explained with the enhanced diffusion assumed previously. Indeed the escape time is 1100 yr compared to an interaction time of 800 yr, which gives a fraction of escaped protons of 24% and, added to the 10% absorption at 40 TeV (minus 2.4% to account for the non-emitted, and thus non-absorbed, gamma radiation from escaped protons), allows meeting the constraints imposed by the observations of MAGIC. For a 200 TeV proton, responsible for the production of 20 TeV gamma rays, the escape time is 1500 yr, giving a fraction of escaped protons of 15%.

In conclusion, by adopting a physical model of gamma-ray emission compatible with the geometry imposed by absorption, with the amount of available gas, and with the gamma-ray luminosity of HESS J1745–290, a proton source centered on Sgr A* can explain both local and diffuse gamma-ray emission through the interplay of gamma-ray absorption and diffusion of the more energetic CRs.

4.4.4 *Future investigation with CTA*

CTA, the next-generation gamma-ray detector, represents an upgrade in all aspects compared to current IACTs, particularly in terms of its angular resolution and flux sensitivity [56]. Compared to H.E.S.S., and for an equal observation time, the southern array of CTA exhibits a sensitivity that is improved by a factor of 10 at 10 TeV, while its energy range extends to over 100 TeV. Simultaneously, the Point Spread Function (PSF) of CTA has a 95% containment radius that is approximately one-third better than that of H.E.S.S. Consequently, CTA has the potential to test the absorption models presented in the previous section, both spatially and spectrally. In Fig. 4.8, the sensitivity of CTA for observations of 50 h and 100 h is shown. The dotted line represents the extension of the HESS J1745–290 spectrum to high energies, assuming it is due to pp interactions with the CNR. The absorption by the shell is rather low as it assumes a cutoff even for the diffuse emission (see Fig. 4.5), and consequently, a recovery around 100 TeV is not expected. The case of a gamma-ray source centred on Sgr A* confined within a radius on the order of the Bondi radius represents an opposite limit case for the absorption scenario. In this instance the diffuse spectrum of H.E.S.S. was assumed, and the de-absorbed profile has a recovery that CTA is capable of detecting with a targeted observation – indeed, the GC is among the most important Key Science Projects (KSPs) of CTA [55]. If CTA

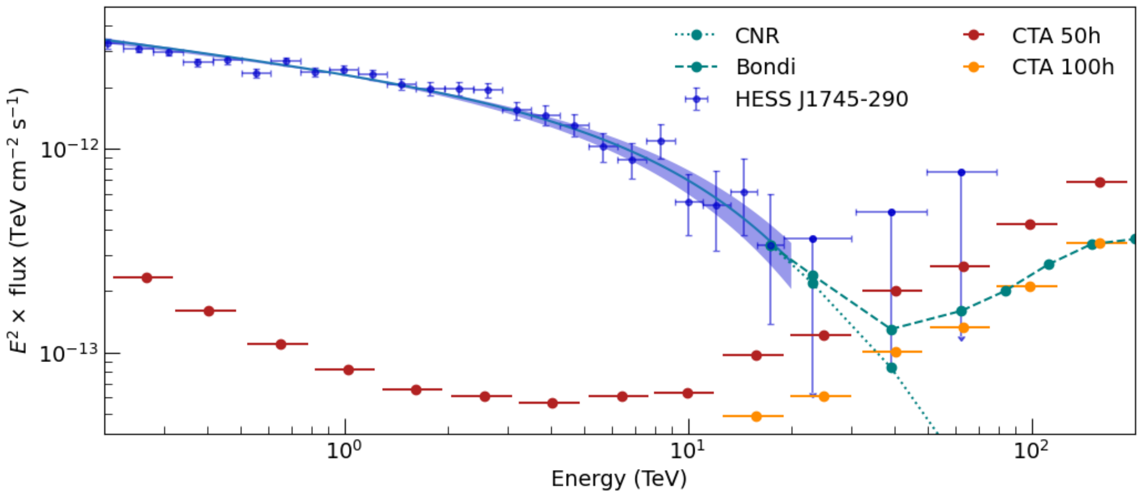

Figure 4.8: CTA Southern Array sensitivity to different scenarios for HESS J1745–290. The dotted line assumes that the gamma-ray emission is due to the pp interaction with the gas in the CNR. The dashed line assumes gamma-ray production on the Bondi radius of Sgr A*, and the diffuse gamma-ray emission of H.E.S.S. [93] as the intrinsic spectrum. CTA would be able to detect the flux recovery at 100 TeV in less than 100 hours of observations.

observes the such flux recovery, it would be a clear indication of the hadronic nature of the central gamma-ray source and its common origin to the diffuse emission. It should be noted that the results found in the previous section rule out the absorption scenario of H.E.S.S.

Even more interesting, and decisive in any case, will be the ability of CTA to discern the position and extent of HESS J1745–290. Indeed, CTA will be able to differentiate between a compact source contained within the CC, such as G359.95–0.04, and the emission from the gas of the CNR. In the latter case, while a spectral analysis alone would not be conclusive, CTA would observe the ring, which has an outer radius of approximately 6 pc, equivalent to about 2.5′, as an extended source. This would definitively identify the counterpart of HESS J1745–290. Furthermore, in that scenario CTA would be able to investigate the CR propagation and density with greater resolution compared to H.E.S.S., being capable of testing the connection of the CNR to the gamma-ray emission from the CMZ.

CONCLUSION

Although they appear connected, in this thesis I present two distinct achievements. I have explored the possibility that HESS J1745–290, the gamma-ray source at the centre of our Galaxy, is connected to the high-energy emission coming from the Central Molecular Zone, a complex of clouds that extends over more than 250 pc around the dynamic centre of the Milky Way. My results allowed me to isolate two specific cases in which this scenario is possible. The next-generation gamma-ray observatory, the Cherenkov Telescope Array, will be able to test all hypotheses.
To attain this, I leveraged the ability of infrared fields to absorb gamma-ray photons to exploit the absorption morphology, developing a 3D model of dust IR emission in the central parsecs around the supermassive black hole Sgr A*. The development of this model is effectively the second achievement of this thesis. Its potential applications extend beyond the case study presented in this thesis, which has nevertheless led to unexpected results.

The radiation field density was calculated in a volume of 6 pc × 6 pc × 6 pc, with a resolution of approximately 0.04 pc. The MIR/FIR emission from the dust is due to the processing of UV radiation emitted by the Nuclear Star Cluster and approaches a radiation field density value of 10^5 eV/cm^3 near Sgr A* and the ionised gas filaments orbiting it within the Central Cavity, a region of very low gas density carved out by the activity of the NSC and bounded by the Circumnuclear Disk. This is the environment that hosts the gamma-ray source HESS J1745–290 and the CR accelerator that powers it, although their association with astrophysical subjects in the region is not known yet.
For the dust emission, the model of Weingartner and Draine [205] and of Li and Draine [64] were used, while the SED in the field of view was sampled by means of 20, 25, and 37 μm observations of SOFIA/FORCAST and 70, 100, and 160 μm observations of Herschel PACS. The UV emission of the NSC was simulated based on its total stellar mass in young stars and the spectral index of the IMF, which are still not well constrained in the literature [136, 71]. However, the predictive power of SED fitting on the properties of the UV field was limited by the lack of a survey

at $10-15\,\mu\mathrm{m}$ with a field of view and angular resolution similar to the six used. The problem is effectively illustrated in Fig. 3.41. This method fails to constrain the mass of the NSC beyond a wide interval $16000 \pm 8000\,\mathrm{M}_\odot$. This creates a degeneracy in the calculated dust mass values and consequently in the intensity of the radiation field. However, as evident in Fig. 3.40, the uncertainty on the dust mass is fairly contained.

To account for a wider range of emission temperatures, the dust was modelled in clumps capable of partially shielding the UV radiation – a hypothesis that, in addition to improving the quality of the fit, has observational backing [58]. The observed trend of clumpiness with proximity to the core of the NSC, visible for example in Fig. 3.36, confirms that the intense UV radiation is capable of removing diffuse dust and smaller clumps, effectively operating a selection of the more compact clumps.

The assumption of a variable minimum grain size in the fitting process determined a significant lack of small grains closer to the centre of the UV field, and in particular on the border of the ionised structures facing Sgr A*, as one would expect in the transition between low-density to high-density regions [159]. This result, highlighted in Fig. 3.24, is encouraging, and could motivate a follow-up study to investigate in greater detail the behaviour of clumpy dust grains in the presence of intense astrophysical UV radiation fields and strong gravitational pull. In addition to allowing a better fit of the emission SED, the removal of smaller grains explains the lack of emission from PAH molecules, in perfect agreement with the observations of ISO-SWS [138].

The obtained dust masses are reported in Table 3.5. The amount of dust in the ionised filaments amounts to $(21.9 \pm 3.4) \times 10^{-2}\,\mathrm{M}_\odot$, in agreement with [122]. The derived amount of gas depends on the gas-to-dust mass ratio chosen. The W&D model assumes a value of 124, but it has been calibrated for the solar neighbourhood. For the GC, the ratio is predicted to be much lower [85, 122]. The dust mass on the inner ridge of the CND is about $4.11 \pm 0.62\,\mathrm{M}_\odot$, which even in the best-case scenario does not exceed $500\,\mathrm{M}_\odot$ of gas. Although this value is in agreement with [125], who derived it in a very similar way but using only two spectral points and similar assumptions about the mass-to-dust ratio, it is consistently at least an order of magnitude lower than the estimates of the gas mass obtained by directly tracing the gas itself [45, 146, 75]. No satisfactory explanation has yet been found for this systematic discrepancy between the two methods.

The uncertainty on the radiation field density is dominated by the uncertainty on the dust mass, as the SED fitting is quite sensitive to the position of the emission peak and thus to the temperature. The uncertainty on the mass is 15%, and that on the radiation field density it is 20%. It should be noted that both altering the minimum grain size and introducing dust clumpiness affect the dust mass, as they lower its effective temperature and consequently increase the mass – even by a factor of 5, if the emission is dominated by silicate features around 20 μm. Section 3.7 contains a detailed discussion on how such modifications affect the uncertainty on dust mass, and therefore on the IR emissivity.

The application to gamma-ray emission from the central parsecs of the GC has yielded interesting results. If it is assumed that the emission from HESS J1745–290 is powered by the same CR accelerator responsible for the gamma-ray luminosity in the Central Molecular Zone, and that the difference in the gamma-ray spectra between the two sources (central and diffuse) is due to the absorption of the latter by the local IR radiation field, then two compatible scenarios emerge: either the accelerator is roughly centred on the position of Sgr A*– besides the black hole, this constraint includes the NSC – and then the gamma-ray luminosity can only be due to proton injection onto the Circumnuclear Ring (the inner edge of the Circumnuclear Disk), or the accelerator is an unidentified astrophysical object of maximum size $\sim 1.5\,\mathrm{pc}$ located within the inner parsec of the Central Cavity. In all likelihood, the gamma-ray emission would still be localised on the inner disk, unless other mechanisms are invoked, such as $\mathrm{p}+\gamma$ interactions in the local X-ray radiation field. In both cases, the absorption scenario is not compatible with the observations of H.E.S.S. [93] – which require very high gamma-ray absorption both at 10 TeV and 40 TeV – but rather with the observations of MAGIC [139]. In other words, the possibility that the central gamma-ray source shares the same accelerator with the diffuse gamma-ray emission implies abandoning the "PeVatron scenario" hypothesised by H.E.S.S.

In the case of a hadronic accelerator centred on Sgr A*, emission on the scale of the Bondi radius is disfavoured due to excessive absorption at 10 TeV. However, the Circumnuclear Ring contains enough gas to account for the luminosity of HESS J1745–290 within a radius of $3\,\mathrm{pc} \simeq 1.3'$, which corresponds to the upper limit given by H.E.S.S. to its size [11]. Nonetheless, confining protons at very high energies in such a compact region requires a very low diffusion coefficient ($D = 5 \times 10^{24}\,\mathrm{cm/s} \times (E/1\,\mathrm{GeV})^{1/2}$) to ensure effective containment [15]. Under these assumptions, HESS J1745–290 can be described by the interaction of protons accelerated inside the Central Cavity with the gas contained in the Circumnuclear Ring. The morphology of the emission, a thick shell modelled on the distances of the CNR, is not compatible with the absorption scenario due to excessive emission at 40 TeV. However, the adopted diffusion predicts that about 25% of protons at 400 TeV escape from the region without interacting. This additional contribution to the missing flux around 40 TeV makes the modelled gamma-ray source compatible with the absorption scenario. Moreover, the required rate of proton injection is relatively low ($L_p = 5 \times 10^{35}$ erg/s) and negligible compared to the value calculated by H.E.S.S. ($L_p = 10^{37} - 10^{38}$ erg/s [93]) necessary to power the diffuse gamma-ray emission.

As a summary, a compact accelerator centred on Sgr A*, with a turn-off in the proton spectrum around 180 TeV [139], is capable of explaining both the emission of HESS J1745–290 and the corresponding gamma-ray luminosity of the Central Molecular Zone. Moreover, CTA would see the gamma-ray emission from the CNR as an extended source, so it will be able to prove this scenario. At the same time, the energy sensitivity of CTA is unlikely to be decisive: since the absorption by the local IR field is rather modest, no flux recovery is expected at energies close to 100 TeV.

Clearly, it is always possible that the central TeV emission, the GeV emission from the Fermi-LAT source 4FGL J1745.6 – 2859 [6], and the diffuse TeV emission are due to three different CR accelerators. Various models of GeV and TeV emission can explain the observed data, both of leptonic and hadronic origin (two examples are shown in Fig. 4.7 and Fig. 4.6, while the table is given in Table 4.2). One possibility, for instance, is that the central GeV emission is due to the interaction of energetic protons with the X-ray radiation field on scales very close to Sgr A*, HESS J1745–290 is instead due to IC emission with the central parsec's intense IR fields of TeV electrons accelerated by the PWN G359.95–0.04 [105], and the diffuse emission comes from to particle acceleration at a hypothetical termination shock associated with the NSC at a distance of 10 – 20 pc from the centre. Unlike other young massive star clusters with similar conditions, such as Westerlund 1 [8] or the cluster at the centre of the Cygnus Cocoon [7], the NSC can feed the acceleration at the termination shock only if the Circumnuclear Disk does not hinder it. Since the disk lies almost parallel to the Galactic plane, the Central Cavity opens in the direction of Galactic latitude. Since H.E.S.S. and MAGIC have extracted the CR density in regions lying longitudinally on the Galactic plane, any possible latitudinal gradient due to acceleration at a distance of 20 pc would not have been recognised. It should be noted that this geometry allows the NSC to feed the diffuse emission without constraining the accelerator responsible for HESS J1745–290, which could be Sgr A*. The inverse scenario does not seem probable: if Sgr A* fuels the gamma-ray emission from the Central Molecular Zone, and if HESS J1745–290 is localised on the Circumnuclear Ring, then Sgr A* has enough power to feed both HESS J1745–290 and the diffuse gamma-ray emission.

ACKNOWLEDGEMENTS

This thesis simply would not have been possible without Dr. Richard J. Tuffs, to whom goes my deepest gratitude for his daily dedication, commitment, support, and attention to detail in all our discussions. Our conversations were always honest, and for this reason not always relaxed – something that in time I came to appreciate.

I consider myself fortunate to have had Prof. Dr. Jim Hinton as my supervisor, not just for his careful guidance and his reliable expertise in our discussions, but also for his personal support in challenging times and his general positivity in our interactions. Working under these conditions makes everything easier.

I sincerely thank Dr. Makarim Bouyahiaoui, Dr. Mischa Breuhaus, Dr. Lars Mohrmann, Dr. Natalia Oreshkina, Dr. Quentin Rémy and Dr. Rainer Schödel for their valuable comments, and all the people I worked with in the CHEC group.

Dr. Richard White deserves a special mention for his patient supervision in my first year. Finally, my heartfelt gratitude goes to Valeria, my personal typo-hunting bird of prey, circling my thesis over and over and over.

PERSONAL BIBLIOGRAPHY

In preparation:

P1. **Conte, F.**, Tuffs. R.J. and Hinton, J.A. 3D infrared radiation field in the inner few parsecs of the Galactic Centre, *in preparation*

P2. **Conte, F.**, Hinton, J.A. and Tuffs, R.J. The gamma-ray central source in the Galactic Centre: constraints on its spectrum and geometry through $\gamma - \gamma$ absorption, *in preparation*

Conference contributions

C1. **Conte, F.** CHEC – LED flashers' performance on the ASTRI-Horn telescope, *contributed talk* at "CTAC meeting", Bologna, Italy, October 2019

C2. **Conte, F.** CHEC – LED flashers' performance on the ASTRI-Horn telescope, *contributed talk* at "SST-CAM meeting", Heidelberg, Germany, January 2020

C3. **Conte, F.** and Tuffs, R.J. γ–γ absorption in the Galactic Centre, *poster* at "MW-Gaia Workshop 2021", Heidelberg, Germany, February 2021

C4. **Conte, F.** γ–γ absorption in the Galactic Centre: insights on the 3D geometry of HESS J1745–290, *invited talk* at "RICAP-22 Rome International Conference on AstroParticle Physics", Rome, Italy, September 2022

C5. **Conte, F.** γ–γ absorption in the Galactic Centre, the 3D IR radiation field in the inner few parsecs and its effects on the central gamma-ray source, *contributed talk* at "Galactic Center Workshop", Granada, Spain, April 2023

REFERENCES

[1] Aab, A. et al. Depth of maximum of air-shower profiles at the Pierre Auger Observatory. I. Measurements at energies above $10^{17.8}$ eV. *Phys. Rev. D*, 90:122005, 2014.

[2] Aab, A. et al. Inferences on mass composition and tests of hadronic interactions from 0.3 to 100 EeV using the water-Cherenkov detectors of the Pierre Auger Observatory. *Phys. Rev. D*, 96:122003, 2017.

[3] Aartsen, M.G. et al. A combined maximum-likelihood analysis of the high-energy astrophysical neutrino flux measured with IceCube. *The Astrophysical Journal*, 809(1):98, 2015.

[4] Aartsen, M.G. et al. Cosmic ray spectrum and composition from PeV to EeV using 3 years of data from IceTop and IceCube. *Phys. Rev. D*, 100(8):082002, 2019.

[5] Abbasi, R.U. et al. First observation of the Greisen-Zatsepin-Kuzmin suppression. *Phys. Rev. Lett.*, 100:101101, 2008.

[6] Abdollahi, S. et al. Fermi Large Area Telescope fourth source catalog. *The Astrophysical Journal Supplement Series*, 247(1):33, 2020.

[7] Abeysekara, A.U. et al. HAWC observations of the acceleration of very-high-energy cosmic rays in the Cygnus Cocoon. *Nature Astronomy*, 5:465–471, 2021.

[8] Abramowski, A. et al. Discovery of extended VHE γ-ray emission from the vicinity of the young massive stellar cluster Westerlund 1. *Astronomy & Astrophysics*, 537:A114, 2012.

[9] Abreu, P. et al. Search for first harmonic modulation in the right ascension distribution of cosmic rays detected at the Pierre Auger Observatory. *Astroparticle Physics*, 34(8):627–639, 2011. ISSN 0927-6505.

[10] Acciari, V.A. et al. Proton acceleration in thermonuclear nova explosions revealed by gamma rays. *Nature Astronomy*, 6:689–697, 2022.

[11] Acero, F. et al. Localizing the VHE γ-ray source at the Galactic Centre. *Monthly Notices of the Royal Astronomical Society*, 402(3):1877–1882, 2010.

[12] Adams, C.B. et al. VERITAS observations of the Galactic Center region at multi-TeV gamma-ray energies. *The Astrophysical Journal*, 913(2):115, 2021.

[13] Aguilar, M. et al. Precision measurement of the proton flux in primary cosmic rays from rigidity 1 GV to 1.8 TV with the Alpha Magnetic Spectrometer on the International Space Station. *Phys. Rev. Lett.*, 114:171103, 2015.

[14] Aguilar, M. et al. Precision measurement of the boron to carbon flux ratio in cosmic rays from 1.9 GV to 2.6 TV with the Alpha Magnetic Spectrometer on the International Space Station. *Phys. Rev. Lett.*, 117:231102, 2016.

[15] Aharonian, F. and Neronov, A. TeV gamma rays from the Galactic Center: direct and indirect links to the massive black hole in Sgr A. *Astrophysics and Space Science*, 300(1-3):255–265, 2005.

[16] Aharonian, F. et al. Very high energy gamma rays from the direction of Sagittarius A^*. *Astronomy & Astrophysics*, 425:L13–L17, 2004.

[17] Aharonian, F. et al. Discovery of very-high-energy γ-rays from the Galactic Centre ridge. *Nature*, 439(7077):695–698, 2006.

[18] Aharonian, F. et al. HESS observations of the Galactic Center region and their possible dark matter interpretation. *Phys. Rev. Lett.*, 97:221102, 2006.

[19] Aharonian, F. et al. Spectrum and variability of the Galactic center VHE γ-ray source HESS J1745-290. *Astronomy & Astrophysics*, 503(3):817–825, 2009.

[20] Aharonian, F.A. Proton-synchrotron radiation of large-scale jets in active galactic nuclei. *Monthly Notices of the Royal Astronomical Society*, 332(1):215–230, 2002. ISSN 0035-8711.

[21] Aharonian, F.A. Very high energy cosmic gamma radiation: a crucial window on the extreme Universe. World Scientific, 2004.

[22] Aharonian, F.A., Coppi, P.S. and Voelk, H.J. Very high energy gamma rays from active galactic nuclei: cascading on the cosmic background radiation fields and the formation of pair halos. *The Astrophysical Journal Letters*, 423:L5, 1994.

[23] Ahnen, M.L. et al. Observations of Sagittarius A* during the pericenter passage of the G2 object with MAGIC. *Astronomy & Astrophysics*, 601:A33, 2017.

[24] Aitken, D.K. et al. Mid-infrared polarization studies of SgrA: a three-dimensional study of the central parsec. *Monthly Notices of the Royal Astronomical Society*, 299(3):743–752, 1998.

[25] Albert, J. et al. Observation of gamma rays from the Galactic Center with the MAGIC telescope. *The Astrophysical Journal Letters*, 638(2):L101–L104, 2006.

[26] Aloisio, R. Propagation and energy spectrum of ultra high energy cosmic rays. *Nuclear Physics B - Proceedings Supplements*, 239-240:169–175, 2013. ISSN 0920-5632.

[27] Amenomori, M. et al. The all-particle spectrum of primary cosmic rays in the wide energy range from 10^{14} to 10^{17} eV observed with the Tibet-III air-shower array. *The Astrophysical Journal*, 678(2):1165–1179, 2008.

[28] André, P.J., Palmeirim, P. and Arzoumanian, D. The typical width of Herschel filaments. *Astronomy & Astrophysics*, 667:L1, 2022.

[29] Apel, W.D. et al. The KASCADE-Grande experiment. *Nucl. Instrum. Meth. A*, 620:202–216, 2010.

[30] Archer, A. et al. Very-high energy observations of the Galactic Center region by VERITAS in 2010-2012. *The Astrophysical Journal*, 790(2):149, 2014.

[31] Archer, A. et al. TeV gamma-ray observations of the Galactic Center ridge by VERITAS. *The Astrophysical Journal*, 821(2):129, 2016.

[32] Atwood, W.B. et al. The Large Area Telescope on the Fermi gamma-ray space telescope mission. *The Astrophysical Journal*, 697(2):1071–1102, 2009.

[33] Baade, W. and Zwicky, F. Cosmic rays from super-novae. *Proceedings of the National Academy of Sciences*, 20(5):259–263, 1934.

[34] Barkat, Z., Rakavy, G. and Sack, N. Dynamics of supernova explosion resulting from pair formation. *Phys. Rev. Lett.*, 18:379–381, 1967.

[35] Bell, A.R. Cosmic ray acceleration. *Astroparticle Physics*, 43:56–70, 2013. ISSN 0927-6505.

[36] Bell, A.R. et al. Cosmic-ray acceleration and escape from supernova remnants. *Monthly Notices of the Royal Astronomical Society*, 431(1):415–429, 2013. ISSN 0035-8711.

[37] Berezinskii, V.S. et al. Astrophysics of cosmic rays. North Holland, 1990.

[38] Berezinsky, V. and Kalashev, O. High-energy electromagnetic cascades in extragalactic space: physics and features. *Phys. Rev. D*, 94(2):023007, 2016.

[39] Bethe, H. and Heitler, W. On the stopping of fast particles and on the creation of positive electrons. *Proceedings of the Royal Society of London Series A*, 146(856):83–112, 1934.

[40] Binns, W.R. et al. Abundances of ultraheavy elements in the cosmic radiation: results from HEAO 3. *The Astrophysical Journal*, 346:997, 1989.

[41] Bjorklund, R. et al. High energy photons from proton-nucleon collisions. *Physical Review*, 77(2):213–218, 1950.

[42] Blandford, R.D. and Ostriker, J.P. Particle acceleration by astrophysical shocks. *The Astrophysical Journal Letters*, 221:L29–L32, 1978.

[43] Blasi, P. and Morlino, G. High-energy cosmic rays and gamma-rays from star clusters: the case of Cygnus OB2. *Monthly Notices of the Royal Astronomical Society*, 523(3):4015–4028, 2023.

[44] Braccesi, A., Ceccarelli, M. and Salandin, G. Search for γ radiation from the Cygnus A radiosource. *Il Nuovo Cimento*, 17(5):691–694, 1960. ISSN 1827-6121.

[45] Bradford, C.M. et al. Warm molecular gas traced with CO J = 7→6 in the Galaxy's central 2 parsecs: dynamical heating of the Circumnuclear Disk. *The Astrophysical Journal*, 623(2):866, 2005.

[46] Breit, G. and Wheeler, J.A. Collision of two light quanta. *Phys. Rev.*, 46:1087–1091, 1934.

[47] Breuhaus, M. et al. Galactic gamma-ray and neutrino emission from interacting cosmic-ray nuclei. *Astronomy & Astrophysics*, 661:A72, 2022.

[48] Burbidge, G.R. On synchrotron radiation from Messier 87. *The Astrophysical Journal*, 124:416, 1956.

[49] Cafardo, F., Nemmen, R. and Fermi LAT Collaboration. Fermi-LAT observations of Sagittarius A*: imaging analysis. *The Astrophysical Journal*, 918(1):30, 2021.

[50] Cao, Z. et al. The first LHAASO catalog of gamma-ray sources. *arXiv e-prints*, arXiv:2305.17030, 2023.

[51] Cardelli, J.A., Clayton, G.C. and Mathis, J.S. The relationship between infrared, optical, and ultraviolet extinction. *The Astrophysical Journal*, 345:245, 1989.

[52] Celli, S., Palladino, A. and Vissani, F. Neutrinos and γ-rays from the Galactic Center region after H.E.S.S. multi-TeV measurements. *European Physical Journal C*, 77(2):66, 2017.

[53] Cembranos, J., Gammaldi, V. and Maroto, A. Antiproton signatures from astrophysical and dark matter sources at the galactic center. *Journal of Cosmology and Astroparticle Physics*, 2015(03):041, 2015.

[54] Cerutti, B. et al. Modeling the three-dimensional pair cascade in binaries. Application to LS 5039. *Astronomy & Astrophysics*, 519:A81, 2010.

[55] Cherenkov Telescope Array Consortium et al. Science with the Cherenkov Telescope Array. 2019.

[56] Cherenkov Telescope Array Observatory and Cherenkov Telescope Array Consortium, version prod5 v0.1. https://zenodo.org/records/5499840, 2023. Accessed: 2023-11-22.

[57] Chernyakova, M. et al. The high-energy, arcminute-scale Galactic Center gamma-ray source. *The Astrophysical Journal*, 726(2):60, 2011.

[58] Ciurlo, A. et al. Clumpiness of the interstellar medium in the central parsec of the Galaxy from H_2 flux-extinction correlation. *Astronomy & Astrophysics*, 621:A65, 2019.

[59] Compton, A.H. A quantum theory of the scattering of x-rays by light elements. *Physical Review*, 21:483–502, 1923.

[60] Cristofari, P., Blasi, P. and Caprioli, D. Cosmic ray protons and electrons from supernova remnants. *Astronomy & Astrophysics*, 650:A62, 2021.

[61] Cummings, A.C. et al. Galactic cosmic rays in the local interstellar medium: Voyager 1 observations and model results. *The Astrophysical Journal*, 831(1):18, 2016.

[62] de Graauw, T. et al. Observing with the ISO Short-Wavelength Spectrometer. *Astronomy & Astrophysics*, 315:L49–L54, 1996.

[63] Draine, B.T. Interstellar dust grains. *Annual Review of Astronomy & Astrophysics*, 41:241–289, 2003.

[64] Draine, B.T. and Li, A. Infrared emission from interstellar dust. IV. The silicate-graphite-PAH model in the post-Spitzer era. *The Astrophysical Journal*, 657(2):810–837, 2007.

[65] Drury, L.O. An introduction to the theory of diffusive shock acceleration of energetic particles in tenuous plasmas. *Reports on Progress in Physics*, 46(8):973–1027, 1983.

[66] Drury, L.O., Aharonian, F.A. and Voelk, H.J. The gamma-ray visibility of supernova remnants. A test of cosmic ray origin. *Astronomy & Astrophysics*, 287:959–971, 1994.

[67] Eckart, A. and Genzel, R. Stellar proper motions in the central 0.1 PC of the Galaxy. *Monthly Notices of the Royal Astronomical Society*, 284(3):576–598, 1997.

[68] Etxaluze, M. et al. The Galactic Center in the far-infrared. *The Astronomical Journal*, 142(4):134, 2011.

[69] Event Horizon Telescope Collaboration et al. First Sagittarius A* Event Horizon Telescope results. I. The shadow of the supermassive black hole in the center of the Milky Way. *The Astrophysical Journal Letters*, 930(2):L12, 2022.

[70] Feenberg, E. and Primakoff, H. Interaction of cosmic-ray primaries with sunlight and starlight. *Physical Review*, 73(5):449–469, 1948.

[71] Feldmeier-Krause, A. et al. KMOS view of the Galactic Centre. I. Young stars are centrally concentrated. *Astronomy & Astrophysics*, 584:A2, 2015.

[72] Feldmeier-Krause, A. et al. Triaxial orbit-based modelling of the Milky Way nuclear star cluster. *Monthly Notices of the Royal Astronomical Society*, 466(4):4040–4052, 2016. ISSN 0035-8711.

[73] Fermi, E. On the origin of the cosmic radiation. *Phys. Rev.*, 75:1169–1174, 1949.

[74] Ferrière, K. Interstellar magnetic fields in the Galactic center region. *Astronomy & Astrophysics*, 505(3):1183–1198, 2009.

[75] Ferrière, K. Interstellar gas within ~ 10 pc of Sagittarius A*. *Astronomy & Astrophysics*, 540:A50, 2012.

[76] Fixsen, D.J. et al. The Cosmic Microwave Background spectrum from the full COBE FIRAS data set. *The Astrophysical Journal*, 473:576, 1996.

[77] Foschini, L. Notes on the data analysis in high-energy astrophysics. *arXiv: Instrumentation and Methods for Astrophysics*, 2009.

[78] Fritz, T.K. et al. Line derived infrared extinction toward the Galactic Center. *The Astrophysical Journal*, 737(2):73, 2011.

[79] Fritz, T.K. et al. The Nuclear Cluster of the Milky Way: total mass and luminosity. *The Astrophysical Journal*, 821(1):44, 2016.

[80] Funk, S. Ground- and space-based gamma-ray astronomy. *Annual Review of Nuclear and Particle Science*, 65(1):245–277, 2015.

[81] Gaggero, D. et al. Diffuse cosmic rays shining in the Galactic Center: a novel interpretation of H.E.S.S. and Fermi-LAT γ-ray data. *Phys. Rev. Lett.*, 119:031101, 2017.

[82] Gao, J., Li, A. and Jiang, B.W. Modeling the infrared extinction toward the Galactic Center. *Earth, Planets and Space*, 65(10):1127–1132, 2013.

[83] Geballe, T.R. et al. The K-band spectrum of the hot star in IRS 8: an outsider in the Galactic Center? *The Astrophysical Journal*, 652(1):370, 2006.

[84] Ghez, A.M. et al. Stellar orbits around the Galactic Center black hole. *The Astrophysical Journal*, 620(2):744, 2005.

[85] Giannetti, A. et al. Galactocentric variation of the gas-to-dust ratio and its relation with metallicity. *Astronomy & Astrophysics*, 606:L12, 2017.

[86] Goicoechea, J.R. et al. Herschel far-infrared spectroscopy of the Galactic Center. Hot molecular gas: shocks versus radiation near Sgr A*. *The Astrophysical Journal Letters*, 769(1):L13, 2013.

[87] Goicoechea, J.R. et al. High-speed molecular cloudlets around the Galactic Center's supermassive black hole. *Astronomy & Astrophysics*, 618:A35, 2018.

[88] Gonzalez, O.A. and Gadotti, D. The Milky Way bulge: observed properties and a comparison to external galaxies. In E. Laurikainen, R. Peletier and D. Gadotti, editors, Galactic Bulges, volume 418 of *Astrophysics and Space Science Library*, page 199. 2016.

[89] GRAVITY Collaboration et al. A geometric distance measurement to the Galactic Center black hole with 0.3% uncertainty. *Astronomy & Astrophysics*, 625:L10, 2019.

[90] GRAVITY Collaboration et al. Constraining particle acceleration in Sgr A* with simultaneous GRAVITY, Spitzer, NuSTAR, and Chandra observations. *Astronomy & Astrophysics*, 654:A22, 2021.

[91] Greisen, K. End to the cosmic-ray spectrum? *Physical Review Letters*, 16(17):748 – 750, 1966. Cited by: 2681.

[92] Grimaldo, E. et al. Proton acceleration in colliding stellar wind binaries. *The Astrophysical Journal*, 871(1):55, 2019.

[93] H. E. S. S. Collaboration et al. Acceleration of petaelectronvolt protons in the Galactic Centre. *Nature*, 531(7595):476–479, 2016.

[94] H. E. S. S. Collaboration et al. Characterising the VHE diffuse emission in the central 200 parsecs of our Galaxy with H.E.S.S. *Astronomy & Astrophysics*, 612:A9, 2018.

[95] H. E. S. S. Collaboration et al. The H.E.S.S. Galactic plane survey. *Astronomy & Astrophysics*, 612:A1, 2018.

[96] H. E. S. S. Collaboration et al. Revealing x-ray and gamma ray temporal and spectral similarities in the GRB 190829A afterglow. *Science*, 372(6546):1081–1085, 2021.

[97] H. E. S. S. Collaboration et al. Time-resolved hadronic particle acceleration in the recurrent nova RS Ophiuchi. *Science*, 376(6588):77–80, 2022.

[98] Hahn, J. GAMERA - a new modeling package for non-thermal spectral modeling. In 34th International Cosmic Ray Conference (ICRC2015), volume 34 of *International Cosmic Ray Conference*, page 917. 2015.

[99] Hankins, M.J. et al. SOFIA/FORCAST Galactic Center legacy survey: overview. *The Astrophysical Journal*, 894(1):55, 2020.

[100] Hayakawa, S. Propagation of the cosmic radiation through intersteller space. *Progress of Theoretical Physics*, 8(5):571–572, 1952. ISSN 0033-068X.

[101] Henshaw, J.D. et al. Star formation in the Central Molecular Zone of the Milky Way. *arXiv e-prints*, arXiv:2203.11223, 2022.

[102] Herter, T.L. et al. Data reduction and early science calibration for FORCAST, A mid-infrared camera for SOFIA. *Publications of the Astronomical Society of the Pacific*, 125(933):1393–1404, 2013. ISSN 00046280, 15383873.

[103] Herter, T.L. et al. FORCAST: a mid-infrared camera for SOFIA. *Journal of Astronomical Instrumentation*, 07(04):1840005, 2018.

[104] Heywood, I. et al. The 1.28 GHz MeerKAT Galactic Center mosaic. *The Astrophysical Journal*, 925(2):165, 2022.

[105] Hinton, J.A. and Aharonian, F.A. Inverse Compton scenarios for the TeV gamma-ray emission of the Galactic Center. *The Astrophysical Journal*, 657(1):302–307, 2007.

[106] Hu, Y., Lazarian, A. and Wang, Q.D. Multiscale magnetic fields in the Central Molecular Zone: inference from the gradient technique. *Monthly Notices of the Royal Astronomical Society*, 511(1):829–842, 2022.

[107] Huang, Z.Q. et al. Inefficient cosmic-ray diffusion around Vela X: constraints from H.E.S.S. observations of very high-energy electrons. *The Astrophysical Journal*, 866(2):143, 2018.

[108] Hulsizer, R.I. and Rossi, B. Search for electrons in the primary cosmic radiation. *Physical Review*, 73(11):1402–1403, 1948.

[109] Hussein, M. and Shalchi, A. Detailed investigation of the Bohm limit in cosmic ray diffusion theory. *The Astrophysical Journal*, 785(1):31, 2014.

[110] Hutchinson, G.W. LXXX. On the possible relation of galactic radio noise to cosmic rays. *The London, Edinburgh, and Dublin Philosophical Magazine and Journal of Science*, 43(343):847–852, 1952.

[111] Irons, W.T., Lacy, J.H. and Richter, M.J. Ionized gas in the Galactic Center: new observations and interpretation. *The Astrophysical Journal*, 755(2):90, 2012.

[112] ISO Handbook – the Short Wavelength Spectrometer. ISO Handbook – the Short Wavelength Spectrometer. https://www.ipac.caltech.edu/iso/sws/idum/sws_hb.pdf, 1995. Accessed: 2023-10-10.

[113] Jansky, K.G. A note on the source of interstellar interference. *Proceedings of the Institute of Radio Engineers*, 23:1158–1163, 1935.

[114] Jauch, J.M. and Rohrlich, F. The theory of photons and electrons. The relativistic quantum field theory of charged particles with spin one-half. Texts and Monographs in Physics. Springer, Berlin, 2nd ed. edition, 1976. ISBN 978-3-642-80953-8, 978-3-642-80951-4.

[115] Johnson, M.D. et al. Resolved magnetic-field structure and variability near the event horizon of Sagittarius A*. *Science*, 350(6265):1242–1245, 2015.

[116] Kafexhiu, E. et al. Parametrization of gamma-ray production cross sections for *pp* interactions in a broad proton energy range from the kinematic threshold to PeV energies. *Phys. Rev. D*, 90:123014, 2014.

[117] KASCADE Cosmic Ray Data Centre (KCDC). https://kcdc.ikp.kit.edu/, 2023. Accessed: 2023-06-08.

[118] Käufl, H.U. and Siebenmorgen, R., editors. The role of dust in the formation of stars. Proceedings of the ESO workshop in Garching, Germany. Springer, 1995. ISBN 978-3-540-68594-4.

[119] Kawano, T. et al. IAEA photonuclear data library 2019. *Nuclear Data Sheets*, 163:109–162, 2020.

[120] Kessler, M.F. et al. The Infrared Space Observatory (ISO) mission. *Astronomy & Astrophysics*, 315(2):L27–L31, 1996.

[121] Klebesadel, R.W., Strong, I.B. and Olson, R.A. Observations of Gamma-Ray Bursts of cosmic origin. *The Astrophysical Journal Letters*, 182:L85, 1973.

[122] Kunneriath, D. et al. The Galactic centre mini-spiral in the mm-regime. *Astronomy & Astrophysics*, 538:A127, 2012.

[123] Lacy, J.H. et al. TEXES: a sensitive high-resolution grating spectrograph for the mid-infrared. *Publications of the Astronomical Society of the Pacific*, 114(792):153–168, 2002.

[124] Latvakoski, H.M. et al. Kuiper widefield infrared camera far-infrared imaging of the Galactic Center: the Circumnuclear Disk revealed. *The Astrophysical Journal*, 511(2):761, 1999.

[125] Lau, R.M. et al. SOFIA/FORCAST imaging of the circumnuclear ring at the Galactic Center. *The Astrophysical Journal*, 775(1):37, 2013.

[126] Laurikainen, E., Peletier, R. and Gadotti, D., editors. Galactic Bulges. Astrophysics and Space Science Library. Springer Cham, 2016.

[127] Law, C.J., Yusef-Zadeh, F. and Cotton, W.D. A wide-area VLA continuum survey near the Galactic Center at 6 and 20 cm wavelengths. *The Astrophysical Journal Supplement*, 177(2):515–545, 2008.

[128] Lhaaso Collaboration et al. Peta-electron volt gamma-ray emission from the Crab Nebula. *Science*, 373:425–430, 2021.

[129] Li, A. and Draine, B.T. Infrared emission from interstellar dust. II. The diffuse interstellar medium. *The Astrophysical Journal*, 554(2):778–802, 2001.

[130] Li, A. and Greenberg, J.M. A unified model of interstellar dust. *Astronomy & Astrophysics*, 323:566–584, 1997.

[131] Lingenfelter, R.E. Cosmic rays from supernova remnants and superbubbles. *Advances in Space Research*, 62(10):2750–2763, 2018. ISSN 0273-1177. Origins of Cosmic Rays.

[132] Lipari, P. Spectral shapes of the fluxes of electrons and positrons and the average residence time of cosmic rays in the Galaxy. *Phys. Rev. D*, 99(4):043005, 2019.

[133] Lipari, P. and Vernetto, S. The shape of the cosmic ray proton spectrum. *Astroparticle Physics*, 120:102441, 2020.

[134] Liu, R.Y. et al. Modeling the gamma-ray emission in the Galactic Center with a fading cosmic-ray accelerator. *The Astrophysical Journal*, 833(2):200, 2016.

[135] Longair, M.S. High energy astrophysics. Cambridge University Press, 2011.

[136] Lu, J.R. et al. Stellar populations in the central 0.5 pc of the Galaxy. II. The initial mass function. *The Astrophysical Journal*, 764(2):155, 2013.

[137] Lucek, S.G. and Bell, A.R. Non-linear amplification of a magnetic field driven by cosmic ray streaming. *Monthly Notices of the Royal Astronomical Society*, 314(1):65–74, 2000. ISSN 0035-8711.

[138] Lutz, D. et al. SWS observations of the Galactic Center. *Astronomy & Astrophysics*, 315:L269–L272, 1996.

[139] MAGIC Collaboration et al. MAGIC observations of the diffuse γ-ray emission in the vicinity of the Galactic Center. *Astronomy & Astrophysics*, 642:A190, 2020.

[140] Malyshev, D. et al. Leptonic origin of the 100 MeV γ-ray emission from the Galactic centre. *Astronomy & Astrophysics*, 582:A11, 2015.

[141] Mathis, J.S., Rumpl, W. and Nordsieck, K.H. The size distribution of interstellar grains. *The Astrophysical Journal*, 217:425–433, 1977.

[142] Maurin, D. et al. Cosmic-Ray Database update: ultra-high energy, ultra-heavy, and antinuclei cosmic-ray data (CRDB v4.0). *Universe*, 6(8), 2020. ISSN 2218-1997.

[143] Mezger, P.G., Duschl, W.J. and Zylka, R. The Galactic Center: a laboratory for AGN? *Astronomy and Astrophysics Review*, 7(4):289 – 388, 1996. Cited by: 184.

[144] Minissale, M. et al. Dust as interstellar catalyst. I. Quantifying the chemical desorption process. *Astronomy & Astrophysics*, 585:A24, 2016.

[145] Molinari, S. et al. Hi-GAL: The Herschel Infrared Galactic plane survey. *Publications of the Astronomical Society of the Pacific*, 122(889):314, 2010.

[146] Montero-Castaño, M., Herrnstein, R.M. and Ho, P.T.P. GAS INFALL TOWARD Sgr A* FROM THE CLUMPY CIRCUMNUCLEAR DISK. *The Astrophysical Journal*, 695(2):1477, 2009.

[147] Morris, M. and Serabyn, E. The Galactic Center environment. *Annual Review of Astronomy and Astrophysics*, 34(1):645–701, 1996.

[148] Moser, L. et al. Approaching hell's kitchen: molecular daredevil clouds in the vicinity of Sagittarius A*. *Astronomy & Astrophysics*, 603:A68, 2017.

[149] Murchikova, E.M. et al. A cool accretion disk around the Galactic Centre black hole. *Nature*, 570(7759):83–86, 2019.

[150] Murgia, S. The Fermi–LAT Galactic Center Excess: evidence of annihilating dark matter? *Annual Review of Nuclear and Particle Science*, 70(1):455–483, 2020.

[151] Nielbock, M. et al. The Herschel PACS photometer calibration. A time dependent flux calibration for the PACS chopped point-source photometry AOT mode. *Experimental Astronomy*, 36(3):631–660, 2013.

[152] Nishiyama, S. et al. The distance to the Galactic Center derived from infrared photometry of bulge red clump stars. *The Astrophysical Journal*, 647(2):1093–1098, 2006.

[153] Nitschai, M.S., Neumayer, N. and Feldmeier-Krause, A. Three-dimensional analysis of the minispiral at the Galactic Center: orbital parameters, periods, and the mass of the black hole. *The Astrophysical Journal*, 896(1):68, 2020.

[154] Nogueras-Lara, F., Schödel, R. and Neumayer, N. Distance and extinction to the Milky Way spiral arms along the Galactic Centre line of sight. *Astronomy & Astrophysics*, 653:A33, 2021.

[155] Nogueras-Lara, F., Schödel, R. and Neumayer, N. The Nuclear Star Cluster and Nuclear Stellar Disk of the Milky Way: different stellar populations and star formation histories. *The Astrophysical Journal*, 920(2):97, 2021.

[156] Norbury, J.W. Pion cross section parametrizations for intermediate energy, nucleus-nucleus collisions. *Phys. Rev. C*, 79:037901, 2009.

[157] Ogrodnik, A. Photon-photon fusion and tau g-2 measurement in ATLAS. *arXiv e-prints*, arXiv:2209.15506, 2022.

[158] Ott, T., Eckart, A. and Genzel, R. Variable and embedded stars in the Galactic Center. *The Astrophysical Journal*, 523(1):248–264, 1999.

[159] Owen, J.E. and Lin, D.N.C. The evolution of circumstellar discs in the Galactic Centre: an application to the G-clouds. *Monthly Notices of the Royal Astronomical Society*, 519(1):397–417, 2023.

[160] Pacini, F. and Salvati, M. The nature of the energy source in radio galaxies and Active Galactic Nuclei, pages 247–253. Springer Netherlands, Dordrecht, 1982. ISBN 978-94-009-7781-5.

[161] Parker, E. The passage of energetic charged particles through interplanetary space. *Planetary and Space Science*, 13(1):9–49, 1965. ISSN 0032-0633.

[162] Perlow, G.J. et al. Rocket determination of the ionization spectrum of charged cosmic rays at $\lambda = 41°$N. *Phys. Rev.*, 88:321–325, 1952.

[163] Peterson, L.E. and Winckler, J.R. Gamma-ray burst from a solar flare. *Journal of Geophysical Research*, 64(7):697–707, 1959. ISSN 0148-0227.

[164] Pilbratt, G.L. et al. Herschel Space Observatory. An ESA facility for far-infrared and submillimetre astronomy. *Astronomy & Astrophysics*, 518:L1, 2010.

[165] Planck Collaboration et al. Planck 2018 results. XI. Polarized dust foregrounds. *Astronomy & Astrophysics*, 641:A11, 2020.

[166] Poglitsch, A. et al. The Photodetector Array Camera and Spectrometer (PACS) on the Herschel Space Observatory. *Astronomy & Astrophysics*, 518:L2, 2010.

[167] Popescu, C.C. and Tuffs, R.J. Radiation fields in star-forming galaxies: the disc, thin disc and bulge. *Monthly Notices of the Royal Astronomical Society*, 436(2):1302–1321, 2013.

[168] Popescu, C.C. et al. A radiation transfer model for the Milky Way: I. Radiation fields and application to high-energy astrophysics. *Monthly Notices of the Royal Astronomical Society*, 470(3):2539–2558, 2017. ISSN 0035-8711.

[169] Portegies Zwart, S.F. and Verbunt, F. Population synthesis of high-mass binaries. *Astronomy & Astrophysics*, 309:179–196, 1996.

[170] Porth, O. et al. Diffusion in pulsar wind nebulae: an investigation using magnetohydrodynamic and particle transport models. *Monthly Notices of the Royal Astronomical Society*, 460(4):4135–4149, 2016. ISSN 0035-8711.

[171] Predehl, P. et al. Detection of large-scale X-ray bubbles in the Milky Way halo. *Nature*, 588(7837):227–231, 2020.

[172] Prosin, V. et al. Tunka-133: results of 3 year operation. *Nuclear Instruments and Methods in Physics Research Section A: Accelerators, Spectrometers, Detectors and Associated Equipment*, 756:94–101, 2014. ISSN 0168-9002.

[173] Rieke, G.H. and Lebofsky, M.J. The interstellar extinction law from 1 to 13 microns. *The Astrophysical Journal*, 288:618–621, 1985.

[174] Ruszkowski, M. and Pfrommer, C. Cosmic ray feedback in galaxies and galaxy clusters – A pedagogical introduction and a topical review of the acceleration, transport, observables, and dynamical impact of cosmic rays. *arXiv e-prints*, arXiv:2306.03141, 2023.

[175] Salim, S. and Narayanan, D. The dust attenuation law in galaxies. *Annual Review of Astronomy & Astrophysics*, 58:529–575, 2020.

[176] Sanchez-Bermudez, J. et al. Properties of bow-shock sources at the Galactic Center. *Astronomy & Astrophysics*, 567:A21, 2014.

[177] Schödel, R. et al. Peering through the veil: near-infrared photometry and extinction for the Galactic nuclear star cluster. Accurate near infrared H, Ks, and L' photometry and the near-infrared extinction-law toward the central parsec of the Galaxy. *Astronomy & Astrophysics*, 511:A18, 2010.

[178] Schödel, R. et al. Surface brightness profile of the Milky Way's nuclear star cluster. *Astronomy & Astrophysics*, 566:A47, 2014.

[179] Schödel, R. et al. The Milky Way's nuclear star cluster: old, metal-rich, and cuspy. structure and star formation history from deep imaging. *Astronomy & Astrophysics*, 641:A102, 2020.

[180] Sharples, R. et al. First light for the KMOS multi-object integral-field spectrometer. *The Messenger*, 151:21–23, 2013.

[181] Slavin, J.D. et al. The dynamics, destruction, and survival of supernova-formed dust grains. *The Astrophysical Journal*, 902(2):135, 2020.

[182] Sloan, G.C. et al. A uniform database of 2.4-45.4 micron spectra from the Infrared Space Observatory Short Wavelength Spectrometer. *The Astrophysical Journal Supplement*, 147(2):379–401, 2003.

[183] Smith, J.R. et al. Pion pair production from $\gamma\gamma$ collisions at PEP. *Phys. Rev. D*, 30:851, 1984.

[184] Spurio, M. Probes of multimessenger astrophysics: charged cosmic rays, neutrinos, γ-rays and gravitational waves. Astronomy and Astrophysics Library. Springer, 2018.

[185] Stone, E.C. et al. Cosmic ray measurements from Voyager 2 as it crossed into interstellar space. *Nature Astronomy*, 3:1013 – 1018, 2019.

[186] Strong, A.W., Moskalenko, I.V. and Ptuskin, V.S. Cosmic-ray propagation and interactions in the Galaxy. *Annual Review of Nuclear and Particle Science*, 57(1):285–327, 2007.

[187] Strong, A.W., Moskalenko, I.V. and Reimer, O. Diffuse continuum gamma rays from the Galaxy. *The Astrophysical Journal*, 537(2):763–784, 2000.

[188] Su, M., Slatyer, T.R. and Finkbeiner, D.P. Giant gamma-ray bubbles from Fermi-LAT: Active Galactic Nucleus activity or bipolar Galactic wind? *The Astrophysical Journal*, 724(2):1044–1082, 2010.

[189] Swinyard, B.M. et al. In-orbit performance of the ISO long-wavelength spectrometer. In A.M. Fowler, editor, Infrared Astronomical Instrumentation, volume 3354 of *Society of Photo-Optical Instrumentation Engineers (SPIE) Conference Series*, pages 888–899. 1998.

[190] Tanner, A. et al. Stellar bow shocks in the Northern Arm of the Galactic Center: more members and kinematics of the massive star population. *The Astrophysical Journal*, 624(2):742–750, 2005.

[191] Temi, P. et al. SOFIA at full operation capability: technical performance. *Journal of Astronomical Instrumentation*, 7(4):1840011-186, 2018.

[192] Tielens, A. Dust formation in astrophysical environments: the importance of kinetics. *Frontiers in Astronomy and Space Sciences*, 9, 2022. ISSN 2296-987X.

[193] Trani, A.A., Mapelli, M. and Ballone, A. Forming circumnuclear disks and rings in galactic nuclei: a competition between supermassive black hole and Nuclear Star Cluster. *The Astrophysical Journal*, 864(1):17, 2018.

[194] Tricco, T.S., Price, D.J. and Laibe, G. Is the dust-to-gas ratio constant in molecular clouds? *Monthly Notices of the Royal Astronomical Society*, 471(1):L52–L56, 2017.

[195] Trumpler, R.J. Preliminary results on the distances, dimensions and space distribution of open star clusters. *Lick Observatory Bulletin*, 420:154–188, 1930.

[196] Tsuboi, M., Handa, T. and Ukita, N. Dense molecular clouds in the Galactic Center region. I. Observations and data. *The Astrophysical Journal Supplement*, 120(1):1–39, 1999.

[197] Tsuboi, M. et al. ALMA view of the circumnuclear disk of the Galactic Center: tidally disrupted molecular clouds falling to the Galactic Center. *Publications of the Astronomical Society of Japan*, 70(5):85, 2018. ISSN 0004-6264.

[198] Tsuchiya, K. et al. Detection of sub-TeV gamma rays from the Galactic Center direction by CANGAROO-II. *The Astrophysical Journal*, 606(2):L115, 2004.

[199] Valenti, E. et al. Stellar density profile and mass of the Milky Way bulge from VVV data. *Astronomy & Astrophysics*, 587:L6, 2016.

[200] Valenti, E. et al. The central velocity dispersion of the Milky Way bulge. *Astronomy & Astrophysics*, 616:A83, 2018.

[201] Vidali, G. H2 formation on interstellar grains. *Chemical Reviews*, 113(12):8752–8782, 2013.

[202] Vieu, T. and Reville, B. Massive star cluster origin for the galactic cosmic ray population at very-high energies. *Monthly Notices of the Royal Astronomical Society*, 519(1):136–147, 2023.

[203] Wang, Q.D., Lu, F.J. and Gotthelf, E.V. G359.95-0.04: an energetic pulsar candidate near Sgr A*. *Monthly Notices of the Royal Astronomical Society*, 367(3):937–944, 2006.

[204] Wang, Q.D. et al. Dissecting X-ray-emitting gas around the center of our Galaxy. *Science*, 341(6149):981–983, 2013.

[205] Weingartner, J.C. and Draine, B.T. Dust grain-size distributions and extinction in the Milky Way, Large Magellanic Cloud, and Small Magellanic Cloud. *The Astrophysical Journal*, 548(1):296–309, 2001.

[206] White, R. et al. Gamma-ray and X-ray constraints on non-thermal processes in η Carinae. *Astronomy & Astrophysics*, 635:A144, 2020.

[207] Witt, A.N. and Gordon, K.D. Multiple scattering in clumpy media. I. Escape of stellar radiation from a clumpy scattering environment. *The Astrophysical Journal*, 463:681, 1996.

[208] Witt, A.N. and Gordon, K.D. Multiple scattering in clumpy media. II. Galactic environments. *The Astrophysical Journal*, 528(2):799–816, 2000.

[209] Workman, R.L. et al. Review of Particle Physics. *Prog. Theor. Exp. Phys.*, 2022:083C01, 2022.

[210] Yanasak, N.E. et al. Measurement of the secondary radionuclides ^{10}Be, ^{26}Al, ^{36}Cl, ^{54}Mn, and ^{14}C and implications for the Galactic cosmic-ray age. *The Astrophysical Journal*, 563(2):768, 2001.

[211] Yoon, Y.S. et al. Proton and helium spectra from the CREAM-III flight. *The Astrophysical Journal*, 839(1):5, 2017.

[212] Zatsepin, G.T. and Kuz'min, V.A. Upper limit of the spectrum of cosmic rays. *Soviet Journal of Experimental and Theoretical Physics Letters*, 4:78, 1966.

[213] Zhao, J.H. et al. Dynamics of ionized gas at the Galactic Center: Very Large Array observations of the three-dimensional velocity field and location of the ionized streams in Sagittarius A West. *The Astrophysical Journal*, 699(1):186–214, 2009.

[214] Zoccali, M. et al. The Initial Mass Function of the Galactic Bulge down to $\sim$0.15 M_{solar}. *The Astrophysical Journal*, 530(1):418–428, 2000.

[215] Zubko, V., Dwek, E. and Arendt, R.G. Interstellar dust models consistent with extinction, emission, and abundance constraints. *The Astrophysical Journal Supplement*, 152(2):211–249, 2004.

A

MASKED GC MAPS

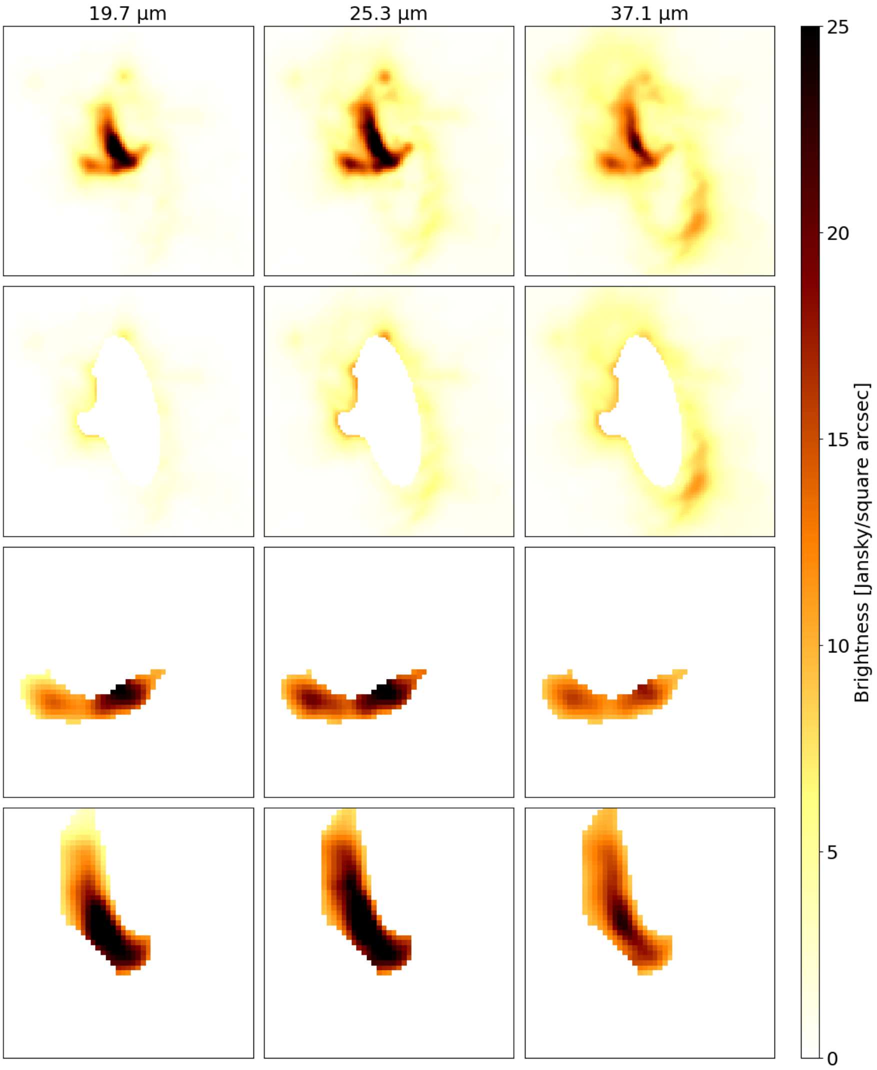

Figure A.1: SOFIA/FORCAST masked maps. From top to bottom: full map, CNR/CND, HB, NA. The hot filaments in the CC have a different magnification.

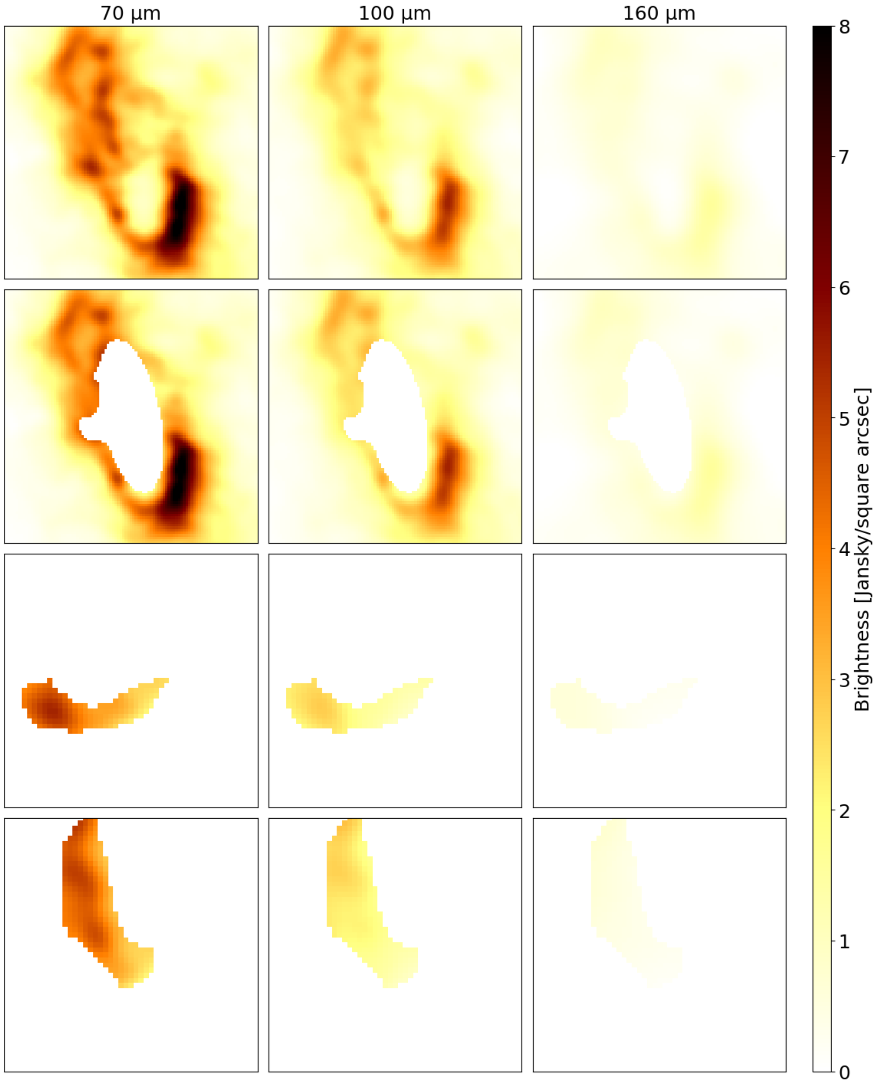

Figure A.2: Herschel PACS masked maps. From top to bottom: full map, CNR/CND, HB, NA. The hot filaments in the CC have a different magnification.

B

DE-PROJECTION OF THE SÉRSIC PROFILE

The Sérsic empirical profile models the radial profile of the bulge surface brightness as

$$I(r) = I_0\, e^{b_n(1-r^{1/n})} \tag{B.0.1}$$

where I_0 is a normalisation value, b_n is a constant that depends on the Sérsic index n and r is the radial coordinate. This formula is valid when describing a galaxy face-on – that is, it assumes a de-projected coordinate and the possibility to describe any point of the Galaxy through a set of polar coordinates. Our Galaxy is seen edge-on – which means that one cannot distinguish between r and s since they are on the same line of sight (see Fig. B.1). In the following, $f(r)$ and $F(r)$ are used to indicate a de-projected and a projected density respectively[1].

In order to get $F(r)$, a sum of $f(r)$ over all the corresponding l values is needed:

$$F(r) = \int_{-\sqrt{R^2-r^2}}^{\sqrt{R^2-r^2}} f(\sqrt{l^2+r^2})\,\mathrm{d}l = 2\int_r^R \frac{f(s)\,s}{\sqrt{s^2-r^2}}\mathrm{d}s. \tag{B.0.2}$$

---

[1] All the calculations shown in this appendix come from personal communications with Dr. Richard J. Tuffs.

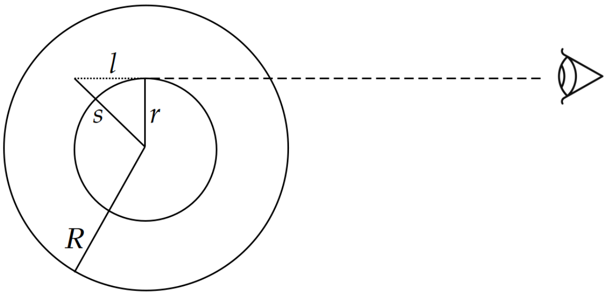

Figure B.1: Schematics of the de-projection of the Sérsic profile. R is the radius of the Bulge.

By setting

$$h = R^2 - r^2 \qquad x = R^2 - s^2 \qquad F(r) = \psi(h) \qquad f(s) = \frac{\mathrm{d}\psi}{\mathrm{d}x} = \psi'(x) \tag{B.0.3}$$

the equation can be rearranged to the form of Abel's integral equation:

$$\psi(h) = \int_0^h \frac{\psi'(x)}{\sqrt{h-x}}\,\mathrm{d}x \tag{B.0.4}$$

which can be solved for $\psi(x)$:

$$\phi(x) = \frac{1}{\pi}\int_0^x \frac{\phi(h)}{\sqrt{x-h}}\,\mathrm{d}h. \tag{B.0.5}$$

Integrating by parts yields:

$$\psi(x) = \frac{1}{\pi}(-2)\sqrt{x-h}\;\phi(h)\Big|_{h=0}^{x} + \frac{1}{\pi}\int_0^x 2\sqrt{x-h}\;\phi'(h)\,\mathrm{d}h = \frac{1}{\pi}\int_0^x 2\sqrt{x-h}\;\phi'(h)\,\mathrm{d}h \tag{B.0.6}$$

as the first term equals 0 for both $h = 0$ and $h = x$. To find the density $f(s)$ a differentiation of $\psi(x)$ is needed, as $f(s) = \psi'(x)$:

$$f(s) = \frac{\mathrm{d}\psi}{\mathrm{d}x} = \frac{1}{\pi}\int_0^x \frac{\phi'(h)\,\mathrm{d}h}{\sqrt{x-h}} = \frac{1}{\pi}\int_R^s \frac{F'(r)\,\mathrm{d}r}{\sqrt{r^2-s^2}}. \tag{B.0.7}$$

Replacing $F(r) = I(r)$ (since a surface brightness is by definition projected) and switching limits:

$$f(s) = -\frac{1}{\pi}\int_s^\infty \frac{I'(r)\,\mathrm{d}r}{\sqrt{r^2-s^2}}. \tag{B.0.8}$$

Substituting first $t = r^{1/n}$ and then $j = s^{1/n}$ results in

$$f(j) = -\frac{1}{\pi}\int_j^\infty \frac{I'(r)\,\mathrm{d}t}{\sqrt{t^{2n}-j^{2n}}} \tag{B.0.9}$$

and using Equation B.0.1:

$$f(j) = -\frac{I_0\,e^{b_n}b_n}{\pi}\int_j^\infty \frac{e^{-b_n t}\,\mathrm{d}t}{\sqrt{t^{2n}-j^{2n}}}. \tag{B.0.10}$$

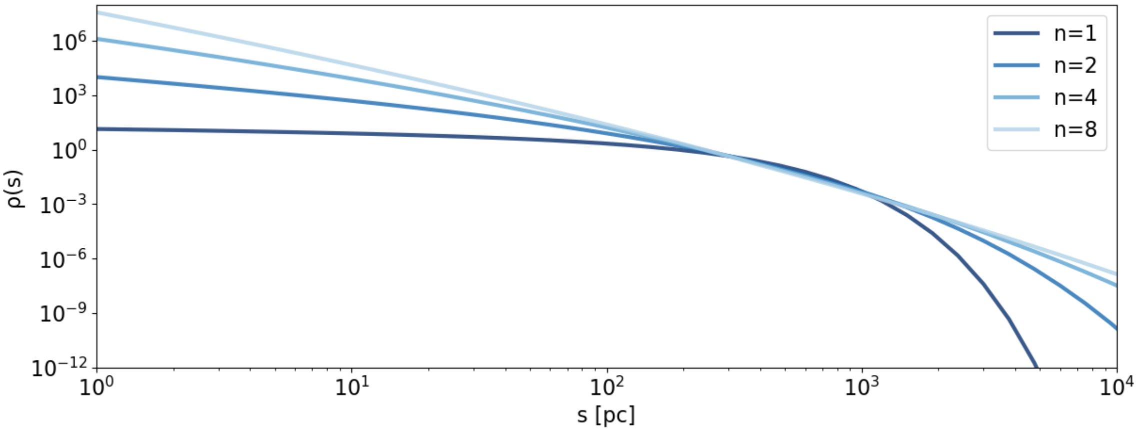

Figure B.2: Sérsic de-projected profiles for different indices. The function plotted is the scaled density, so that each profile can be normalised to match the P&T17 empirical profile around 50 TeV to extend it towards the inner region.

Taking $t = j\tau$ lets $1/j^{n-1}$ be taken out of the integral, and by switching back to the s variable the de-projected density is obtained:

$$f(s) = -\frac{I_0\, e^{b_n} b_n}{\pi\, s^{(1-1/n)}} \int_1^{\infty} \frac{e^{-b_n \tau s^{1/n}}\, \mathrm{d}\tau}{\sqrt{\tau^{2n} - 1}}. \tag{B.0.11}$$

Finally, the scaled density $\rho(s) = \dfrac{f(s)}{I_0}$ can be introduced, yielding

$$\rho(s) = -\frac{e^{b_n} b_n}{\pi\, s^{(1-1/n)}} \int_1^{\infty} \frac{e^{-b_n \tau s^{1/n}}\, \mathrm{d}\tau}{\sqrt{\tau^{2n} - 1}}. \tag{B.0.12}$$